

UNIVERSITY OF LIVERPOOL

Shining Light on Electrode Interfaces

*Thesis submitted in accordance with the requirements of the University of Liverpool for the
Degree of Doctor in Philosophy*

Tom Galloway

September 2017

Supervisor: Laurence J. Hardwick

Industrial supervisors: Sarah Ball and Mark Copley



Johnson Matthey

STEPHENSON INSTITUTE FOR RENEWABLE ENERGY
Battery and Electrified Interfaces Group



UNIVERSITY OF
LIVERPOOL

Abstract

The metal-oxygen battery is the pinnacle of beyond Li-ion battery technologies, providing a very high theoretical specific energy relative to current battery chemistries. However, the practical use of alkali metals (Li and Na) in the presence of oxygen species and carbon cathodes provides substantial problems in the development of this technology. The highly nucleophilic and reactive nature of the reduced alkali-oxygen species causes degradation of the electrolyte and cathode. In order to overcome these factors, the fundamental reaction mechanism taking place at the solid/electrolyte interface need to be understood. In this thesis, a range of electrochemical and spectroscopic techniques have been used to help elucidate the reaction pathways and products.

Initial studies have been conducted using shell isolated nanoparticles for enhanced Raman spectroscopy (SHINERS) to allow surface enhanced Raman studies on previously inaccessible electrode materials. The use of SHINERS utilised the localised surface plasmon from the gold nanoparticles without any additional effect from the particle surface, due to the Raman inactive silica shell. This allowed the vibrational modes of nearby molecules adsorbed on the surface to be enhanced. A comprehensive characterisation and analysis of SHINERS, as well as their functionality on a range of different electrode morphologies has been presented.

SHINERS have been used to compare the oxygen reduction reactions (ORR) with and without the presence of lithium on a variety of polycrystalline electrodes. The behaviour of superoxide ($\text{O}_2^{\cdot-}$) without the presence of lithium was shown to be highly dependent on the electrode surface. The ORR in the presence of lithium was demonstrated to be both surface and solvent dependent on a range of carbon electrodes.

SHINERS were also used to study more practical battery electrodes, with the detection of lithium oxides and side products on the electrode surface after discharge and charge.

The use of single crystal electrode surfaces were also studied, in order to provide an ideal surface to understand the reaction mechanisms. The effect of moving from an aqueous to a non-aqueous electrolyte on a gold (111) surface was studied using voltammetry and SHINERS. The inhibition of the electrode surface with trace amounts of MeCN was detected. The degradation of MeCN was also observed with trace amounts of water.

Finally the behaviour of the sodium-oxygen system was studied on the three low index basal planes of platinum (111), (110) and (100). The electrochemical behaviour was shown to be facet dependent, with the addition of a supporting salt also affecting the reaction mechanism taking place.

Acknowledgments

I would like to thank **Prof. Laurence Hardwick** for his continual support and guidance throughout my thesis. I would also like to thank all the members of the **Hardwick group** both past and present for all their help throughout my PhD.

Special thanks to the following people:

Prof. Jian Feng Li and **Jin-Chao Dong** and **Xiamen University** for their help and guidance learning the SHINERS technique.

Dr Laura Cabo-Fernandez for help and discussion regarding all things SHINERS

Dr Iain Aldous for all his help across the whole of my PhD

To **Prof. Nichols** and the **ELECTRONANOMAT** grant for the opportunity to go to China to learn the SHINERS technique.

To **Johnson Matthey** and **the EPSRC** for funding my project

My family for the support and help along the way

And finally a huge thank you to **Marisha Cysewski** for always being there to cheer me up when I need it.

Contents

Abstract	ii
Acknowledgment	iv
List of figures	xii
List of tables	xx
List of abbreviations	xxii

1. Introduction

(Part A) The Metal–oxygen battery

1.1 Energy	1
1.2 Demand for higher energy batteries	3
1.3 Metal-oxygen batteries	4
1.4 The lithium-oxygen battery	5
1.4.1 Electrolyte	7
1.4.2 Solvent	7
1.4.3 Solution vs. surface mechanism	9
1.4.3.1 Guttmann donor number	10
1.4.4 Impurities and additives	11
1.4.5 Salt	11
1.4.6 Redox mediator	12
1.4.7 Cathode	13
1.4.8 Anode	14
1.5 The sodium-oxygen battery	14

(Part B) The importance of fundamental studies

1.6 Fundamental studies	17
1.7 Raman spectroscopy	18
1.7.1 Surface enhance Raman spectroscopy	20
1.7.2 Developments in enhanced Raman spectroscopy	22
1.7.3 Tip enhanced Raman spectroscopy	24
1.7.4 SHINERS	25

1.7.5 SHINERS applications	26
1.8 Application of enhanced Raman spectroscopy for battery research	27
1.9 Single crystals	27
1.9.1 Miller indices	28
1.9.2 Electrochemical identification of the low index basal planes on Pt	31
1.10 Summary and outlooks for thesis	33
1.11 References	34

2. Experimental and Theory

2.1 Glove box setup	49
2.2 Drying of gases	49
2.3 Purification and drying of solvents and chemicals	50
2.4 Karl fischer measurements	50
2.5 Cleaning of glassware	51
2.6 Cyclic voltammetry	52
2.6.1 iR drop	54
2.6.2 Potentiostat	54
2.6.3 Electrochemical cell	54
2.6.4 Reference electrodes	55
2.6.4.1 Aqueous electrolytes	55
2.6.4.2 Non-aqueous electrolytes	56
2.6.5 Working electrodes	58
2.6.5.1 Polycrystalline electrodes	58
2.6.5.2 Composite electrodes	58
2.6.5.3 Single crystal electrodes	59
2.6.5.3.1 Forming a full bead single crystal	59
2.6.5.3.2 Selecting a crystal facet	60
2.6.5.3.3 Grinding the single crystal bead	62
2.6.5.3.4 Polishing the half bead single crystal	63
2.6.5.3.5 Annealing	66
2.6.5.3.6 Hanging meniscus	67
2.6.5.3.7 Removal of SHINs from single crystal surfaces	68
2.6.5.3.8 Calculating surface area and surface coverages	68
2.7 Raman spectroscopy	69

2.7.1 Spectrometer	69
2.7.2 Raman cells	69
2.8 Surface enhanced Raman spectroscopy (SERS)	72
2.9 Other techniques presented in thesis	74
2.10 Useful equations	75
2.11 References	76

3. Shell isolated nanoparticles for enhanced Raman spectroscopy (SHINERS)

3.1 Abstract	79
3.2 Introduction	80
3.3 Synthesis of shell-isolated nanoparticles (SHINs)	82
3.3.1 Au nanoparticle synthesis (55 nm diameter spheres)	82
3.3.2 Coating of Au nanoparticles with a silica shell	84
3.4 Characterisation of SHINs	86
3.4.1 UV/Vis spectroscopy	86
3.4.2 TEM	87
3.4.3 Cyclic voltammetry	89
3.4.4 Raman spectroscopy	90
3.4.5 Calculating the enhancement factor (EF)	91
3.4.6 Electrode preparation and particle distribution	93
3.4.7 Casting of SHINs	95
3.4.8 Cleaning the nanoparticles	97
3.5 Conclusions and future work	103
3.6 References	104

4. Utilising *in situ* enhanced Raman spectroscopy to study the oxygen reduction reaction in aprotic electrolytes

4.1 Abstract	109
4.2 Introduction	110
4.3 ORR electrochemistry on a variety of electrode surfaces without the presence of lithium	112
4.4 Comparison of SERS, SHINERS and smooth surfaces in non-aqueous electrolytes	117

4.5 Behaviour of the ORR on different electrode surface without the presence of lithium_____	122
4.6 Studying the ORR in the lithium-oxygen battery: A surface and solvent dependent reaction_____	129
4.7 Conclusions and future work_____	135
4.8 References_____	138

5. SHINERS on carbon surfaces and composite electrodes

5.1 Abstract_____	143
5.2 Introduction_____	144
5.3 How the surface morphology affects the enhancement from the SHINs_____	145
5.4 How the substrate composition affects the distribution of particles_____	153
5.5 <i>In situ</i> electrochemical SHINERS studies of oxygen reduction of graphitic carbons_____	154
5.6 <i>In situ</i> electrochemical SHINERS studies of oxygen reduction on a composite carbon black electrode_____	162
5.7 Conclusions and future work_____	164
5.8 References_____	166

6. A fundamental study on the effect of moving from an aqueous to a non-aqueous electrolyte

6.1 Abstract_____	171
6.2 Introduction_____	172
6.3 Characterising the Au(111) surface_____	173
6.4 Understanding the ORR in an aqueous electrolyte_____	174
6.5 The electrochemical response of moving from an aqueous to a non-aqueous electrolyte_____	180
6.6 Using SHINERS to understand the electrochemical response of moving from an aqueous to a non-aqueous electrolyte_____	183
6.7 Understanding the ORR in a non-aqueous electrolyte_____	188
6.8 Solvent decomposition on the Au(111) surface_____	194
6.9 Conclusions and future work_____	196
6.10 References_____	197

7. Electrochemical behaviour of Na, Li and TBA on different platinum single crystal facets

7.1 Abstract	201
7.2 Introduction	202
7.3 Preparation of the platinum single crystal facets	202
7.4 Behaviour of NaClO ₄ on different platinum single crystal facets	203
7.5 Effect of the tetrabutylammonium cation on the reaction mechanism on different Pt single crystal facets without sodium	215
7.6 Effect of the tetrabutylammonium cation on the reaction mechanism on different Pt single crystal facets with sodium	218
7.7 Concentration effects on the reaction mechanisms in the presence of TBA ⁺ and Na ⁺ cations	222
7.8 Comparing the behaviour of LiClO ₄ and NaClO ₄ on different platinum single crystal facets	225
7.9 Conclusions and future work	229
7.10 References	231

8. Conclusions and future work

8.1 Conclusions	235
8.2 Future work	237

Summary of research papers and conference presentations	239
--	------------

List of figures

Figure 1.1 Power supplies in terms of their power rating and discharge time.

Figure 1.2 Past, present and future battery technology specific energies and cell voltages.

Figure 1.3 Schematic of the non-aqueous metal-oxygen battery showing the movement of ions upon discharge and the overall reversible chemical reaction taking place during discharge/charge.

Figure 1.4 Schematic of the surface vs. solution mechanism.

Figure 1.5 Structure of (a) MeCN, (b) DMSO demonstrating position of lone pairs.

Figure 1.6 SEM, (b) TEM of Toroidal Li_2O_2 . Taken from Shao Horn.

Figure 1.7 Energy level diagram of Raman scattering.

Figure 1.8 Chemical enhancement involves a charge transfer.

Figure 1.9 Interaction of electron field with electrons in nanoparticle.

Figure 1.10 Schematic demonstrating electromagnetic field enhancements of gold nanoparticles on SERS inactive substrate.

Figure 1.11 Schematic of Au nanostructured surface with ultra-thin transition metal coating.

Figure 1.12 Diagram demonstrating TERS near field enhancement.

Figure 1.13 Schematic of SHIN's on substrate surface demonstrating the enhancement distribution.

Figure 1.14 Schematic of the plane intercepting the basis vectors forming the unit cell.

Figure 1.15 (100), (111) and (110) Miller index planes for a face centered cubic crystal (nb. Face centered atoms removed from (111), (110) and (100) schematics for clarity). Surface structures relating to each facet below, with coordination number (C.N.) to neighbouring atoms at the surface.

Figure 1.16 Reconstruction of a (110) surface between the (1x1) and (1x2) arrangements.

Figure 1.17 Cyclic voltammograms of 0.1 M H_2SO_4 on Pt(111) (cooled in Ar), Pt(100) and Pt(110) (cooled in CO) Sweep rate 10 mV/s. Central schematic demonstrating how facets relate to beads bulk structure.

Figure 2.1 (a) Potential response in relation to time for a cyclic voltammogram, (b) Current response in relation to potential for a cyclic voltammogram.

Figure 2.2 Schematic of the electrode-electrolyte interface, demonstrating the double layer.

Figure 2.3 Schematic of a 3 electrode glass cell used for the voltammetry experiments in this thesis.

Figure 2.4 Cyclic voltammogram of the O_2/O_2^- and Fc/Fc^+ redox couples in 0.1 M TBAOTF/DMSO.

Figure 2.5 Solid/liquid boundary when synthesising a single crystal.

Figure 2.6 Picture of Single crystal alignment and polishing set up.

Figure 2.7 Schemes demonstrating angles required to identify single crystal facets, (a) cube showing the (111) green, (110) blue, (100) red facets. (b) plane cut to show angle between (111) and (100) facets. (c) cube cut along plane to show angle between (111) and (100) facets. (d) summation of angles between the (111), (100) and (110) planes, recreated from Hazzazi.

Figure 2.8 Picture of single crystal on the goniometer being ground down to a half bead crystal.

Figure 2.9 (a) CV's of Au(100) with impurities coming out the bulk with increasing cycling, (b) CV of Au(100) after being etched in HF.

Figure 2.10 Schematic of (a) no hanging meniscus, the electrode is submerged in electrolyte, therefore the sides and back of the crystal will contribute to the electrochemistry, which are not of the desired facet. (b) poor hanging meniscus, electrolyte touching the sides of the crystal. (c) an ideal hanging meniscus, electrolyte is only in contact with the desired facet.

Figure 2.11 a) Schematic of composite and polycrystalline working electrode Raman cell, b) bottom up view of polycrystalline Raman cell through the sapphire window .

Figure 2.12 Schematic of the single crystal Raman cell.

Figure 2.13 Schematic of the composite electrode cell.

Figure 2.14 Cyclic voltammogram of the oxygen reduction cycle in 0.1 M KCl used to roughen the gold electrodes.

Figure 2.15 Images of a polycrystalline gold electrode (a) before roughening, (b) after roughening.

Figure 3.1 Schematic representation of the different steps associated with the synthesis of shell isolated nanoparticles. (a) Au salt and reducing agent (trisodium

citrate), **(b)** reduction of Au salt to form nanoparticles, **(c)** APTMS exchange with citrate ligand, **(d)** growth of SiO₂ shell.

Figure 3.2 UV-Vis spectra of citrate-Au (black line) and SHINs (red line). (Spectra taken by Laura Cabo-Fernandez).

Figure 3.3 TEM images of shell isolated nanoparticles **(a)** low magnification image showing SHINs size distribution, **(b)** SHINs nanoparticles with 2-3 nm shells, **(c)** EDX image of SHINs showing elemental distribution, **(d + e)** 55 nm SHIN particle with 2-3 nm shell, **(f)** High magnification image of 2-3 nm silica shell on Au NPs, **(g)** SHINs with large pinholes, **(h)** SHIN with non-uniform silica shell and pinholes, **(i)** dark field image of SHINs with 5 nm silica shell, **(j)** SHINs with 4-5 nm silica shell, **(k)** nanocubes with 2-3 nm shell, and **(l)** nanorods.

Figure 3.4 Cyclic voltammograms of SHINERS (red) and citrate Au nanoparticles (black) on a glassy carbon electrode in 0.1 M H₂SO₄. Sweep rate 10 mv s⁻¹.

Figure 3.5 Raman spectra of pyridine on **(a)** Si/ SHINERS with pinholes **(b)** Si/ SHINERS without pinholes **(c)** Au/ SHINERS (2nm shell) **(d)** Au/SHINERS (4nm shell).

Fig. 3.6 (a) Optical image of SHINs drop casted on Au showing uneven SHINERS dispersion on the surface and ring effect. Arrows point to region 1 (edge) and region 2 (centre); **(b)** SEM images of SHINs drop cast onto Au **(c)** AFM images and height profiles of the region marked with a green line; **1**) image at the edge and **2**) at the centre of the drop. (SEM images taken by Filipe Braga, AFM images by Iain Aldous).

Fig. 3.7 (Left) Optical image of SHINs drop on a gold electrode, **(right)** Raman map of the intensity of the pyridine peak at 1010 cm⁻¹ in relation to nanoparticle distribution.

Figure 3.8 Microscope images taken with an in via optical microscope of SHINs drop casted onto a gold electrode surface. a) Particles dried in air b) dried under vacuum. Bright patches indicate gold electrode with no SHINERS particles, dark patches indicate presence of nanoparticles upon the surface.

Figure 3.9 AFM images of SHINs **(a)** drop coated edge of spot, **(b)** drop cast centre of spot, **(c)** spray coated edge of spot, and **(d)** spray coated centre of spot onto a gold substrate. (AFM images taken by Iain Aldous).

Figure 3.10. Raman spectrum of pyridine adsorbed onto an Au wafer (grey shaded region) drop cast with SHINs and the standard Raman spectra of some of the possible impurities from nanoparticle preparation.

Figure 3.11 (a) TEM image of SHINs particles connected via a silica network, **(b)** Raman spectra of pyridine on a silica wafer at different spots on the substrate.

Figure 3.12 (a) TEM image of SHINs after treatment with dilute Aqua Regia, yellow circles denote thinning of silica shell, **(b1)** Image of SHINs with pinholes after treatment with dilute Aqua Regia, SHINs have collapsed, **(b2)** Image of stable SHINs after treatment with dilute Aqua Regia, **(c)** Raman spectra of SHINs before and after acid treatment, pinholes visible after acid treatment.

Figure 3.13 Raman spectra of pyridine on Au drop casted with SHINs cleaned with a variety of techniques, using a special centrifuge tube, centrifuging with excess water, hydrogen evolution, sonication in Milli-Q water then re-dispersed in Milli-Q water. Red shade highlights pyridine peaks.

Figure 4.1 (a) Cyclic voltammogram showing argon (red dotted line) and oxygen (black) electrochemistry in 0.1 M TBAClO₄/DMSO on a glassy carbon disc electrode, sweep rate 10 mV / s **(b)** Randles Sevcik plot of 0.1 M TBAClO₄/DMSO demonstrating a 1 e⁻ transfer

Figure 4.2. Cyclic voltammograms of 0.1 M TBAClO₄ in DMSO (saturated with O₂) on a variety of polycrystalline electrode surfaces. Sweep rate 10 mV / s.

Figure 4.3 Raman spectra of 0.1 M TBAClO₄ in DMSO (saturated with O₂) on a gold polycrystalline disc electrode with accompanying diagrams comparing the differing effects of **(a)** smooth **(b)** roughened **(c)** SHIN enhanced electrode surfaces.

Figure 4.4 Raman spectra of 0.1 M TBAClO₄/ DMSO purged with argon (i.e. no oxygen) on SERS active gold.

Figure 4.5 Raman spectra of 0.1 M TBAClO₄/ DMSO purged with argon (i.e. no oxygen) on SHIN enhanced gold electrode surfaces.

Figure 4.6 Cyclic voltammograms comparing the electrochemical changes between smooth, roughened and SHIN enhanced gold surfaces. Sweep rate 50 mV /s in 0.1 M TBAClO₄/DMSO (saturated with O₂).

Figure 4.7 Raman spectra of 0.1 M TBAClO₄/DMSO on SHIN enhanced **(a)** Pd **(b)** Pt electrode surfaces.

Figure 4.8 Schematic of active Raman vibrational modes in relation to oxygen adsorbed on a platinum surface.

Figure 4.9 (a) Gaussian peak fitting of Raman bands of oxygen saturated 0.1 M TBAClO₄ in DMSO on Au, Pd and Pd electrode surfaces. **(b)** Intergrated areas from peak fitting in Fig 4.9a.

Figure 4.10 Raman spectra of 0.1 M TBAClO₄/DMSO (saturated with O₂) on SHIN enhanced glassy carbon disc electrode.

Figure 4.11 Raman spectra of 0.1 M TBAClO₄/DMSO (saturated with O₂) with a wider spectral range (200-1700 cm⁻¹) demonstrating peak formation associated solely to glassy carbon and not a result of SHINs.

Figure 4.12 Cyclic voltammograms of 0.5 M LiClO₄ in DMSO and MeCN (saturated with O₂) on a glassy carbon disc electrode. Sweep rate 10mV/s.

Figure 4.13 *In situ* Raman spectra of (a) 0.5 M LiClO₄ in MeCN (b) 0.5 M LiClO₄ in DMSO (saturated with O₂) on smooth glassy carbon disc electrodes with SHIN's drop cast. All potentials vs. Li/Li⁺.

Figure 4.14 Schematic of the how the oxygen reduction reaction mechanisms taking place in a li-oxygen system change depending on solvent and surface.

Figure 4.15 Raman spectra of solvents, salts and products associated with the oxygen reduction reactions taking place in the lithium oxygen battery

Figure 5.1 Raman spectrum of 10 mM pyridine adsorbed on a gold wafer with drop casted SHINs (55nm Au NP, 2 nm shell).

Figure 5.2 Raman spectra of **(a)** 0.1 mM rhodamine-6G in ethanol on BPPG with SHINs (red), without SHINs (black); **(b)** 0.1 mM malachite green in water on GC with SHINs (red), without SHINs (black). Shaded areas indicate the peaks analysed for EF calculations.

Figure 5.3 SEM images of **(a)** SHINs drop casted onto a ZnFe₂O₄/C composite electrode, **(b)** ZnFe₂O₄/C surface without any SHINs cast, **(c)** centre of spot where SHINs drop casted on the surface (low magnification), **(d)** edge of spot where SHINs drop casted on the surface (low magnification), **(e)** centre of spot where SHINs drop casted on the surface (high magnification), **(f)** edge of spot where SHINs drop casted on the surface (high magnification). (SEM images taken by Filipe Braga).

Figure 5.4 Comparison of the enhancement (intensity of malachite green peak at 1177 cm⁻¹) in relation to the roughness factor (calculated from voltammetry) across different electrode surfaces, including metals, planar carbon electrodes (i.e., edge-plane pyrolytic graphite (EPPG), base-plane pyrolytic graphite (BPPG), and glassy carbon (GC) and Li₄Ti₅O₁₂ and carbon black composite electrodes.

Figure 5.5 Images of a composite (Super C(70%)/ CMC (30%)) electrode cast onto aluminium foil (a) without SHINs drop casted, (b) with SHINs drop casted.

Figure 5.6 Cyclic voltammograms of 0.5 M LiClO₄ / DMSO on basal plane pyrolytic graphite (black) and edge plane pyrolytic graphite (red). Sweep rate was 100 mV/s.

Figure 5.7 *In situ* SHINERS spectra of 0.5 M LiClO₄ / DMSO (saturated with O₂) on (a) edge plane pyrolytic graphite (BPPG) without SHINs, (b) basal plane pyrolytic graphite (BPPG), and (c) edge plane pyrolytic graphite (EPPG).

Figure 5.8 *In situ* electrochemical SHINERS spectra of O₂ saturated 0.5 M LiClO₄ / DMSO on carbon black (Super C/ PTFE) composite electrode. The carbon G-band and position of LiO₂ band are highlighted in grey scale.

Figure 6.1 Cyclic voltammogram of 0.1 M H₂SO₄ in H₂O on Au(111), insert (top left) zoomed in look at double layer region. Sweep rate 50 mV/s.

Figure 6.2 CV and Raman data for 0.1 M NaClO₄ in H₂O (purged with Ar) on a Au(111) half bead single crystal (a) Cyclic voltammogram (sweep rate 10 mV s⁻¹) with integrated intensities of Raman peaks at corresponding oxidation potentials. (b) *In situ* SHINs spectra in the same electrolyte system. Potentials vs. Pd/H.

Figure 6.3 (a) Adsorption of ClO₄⁻, (b) adsorption of OH⁻, (c) simultaneous oxide formation and desorption of ClO₄⁻, (d) oxidation on terraces.

Figure 6.4 CV and Raman data for 0.1 M NaClO₄ in H₂O (purged with Ar) on a Au(111) half bead single crystal (a) Cyclic voltammogram (sweep rate 10 mV s⁻¹) with integrated intensities of Raman peaks at corresponding reduction potentials. (b) *In situ* SHINs spectra in the same electrolyte system. Potentials vs. Pd/H.

Figure 6.5 (a) Partial reduction of place exchanged O, (b) reduction of O and OH⁻, (c) complete reduction of O and adsorption of ClO₄⁻.

Figure 6.6 CV data for 0.1 M NaClO₄ in H₂O (purged with Ar) on Au(111) half bead single crystal with increasing concentration of MeCN. Sweep rate 10 mV/s.

Figure 6.7 CV data for 0.1 M NaClO₄ in H₂O (saturated with oxygen after electrolyte purged, pH 9) on Au(111) half bead single crystal with no MeCN (black), 100 mM MeCN (green). Sweep rate 10 mV/s.

Figure 6.8 *In situ* SHINs spectra for the oxidation sweep of 0.1 M NaClO₄ in H₂O (purged with Ar) on Au(111) half bead single crystal with (a) 1 mM, (b) 10 mM, (c) 100 mM MeCN. Potentials vs. Pd/H.

Figure 6.9 *In situ* SHINs spectra for the reduction sweep of 0.1 M NaClO₄ in H₂O (purged with Ar) on Au(111) half bead single crystal with (a) 1 mM, (b) 10 mM, (c) 100 mM MeCN. Potentials vs. Pd/H.

Figure 6.10 Raman spectra of 0.1 M NaClO₄ in water/acetonitrile (50:50) on Au(111) with SHINs. Potentials vs Ag/Ag⁺.

Figure 6.11 CV data for 0.1 M NaClO₄ in MeCN (saturated with oxygen after electrolyte purged, H₂O < 20 ppm) on Au(111) half bead single crystal. Sweep rate 10 mV/s.

Figure 6.12 *In situ* SHINs spectra for the reduction sweep of 0.1 M NaClO₄ in MeCN (saturated with O₂, H₂O < 20 ppm) on an Au(111) half bead single crystal. Lower wavenumbers (200 – 1200 cm⁻¹).

Figure 6.13 CV data for 0.1 M NaClO₄ in MeCN (saturated with oxygen after electrolyte purged on Au(111) half bead single crystal, with increasing H₂O concentrations. Sweep rate 10 mV/s.

Figure 6.14 *In situ* SHINs spectra for the reduction sweep of 0.1 M NaClO₄ in MeCN (saturated with O₂, H₂O ~ 120 ppm) on an Au(111) half bead single crystal. Lower wavenumbers (200 – 1200 cm⁻¹).

Figure 6.15 *In situ* SHINs spectra for the reduction sweep of 0.1 M NaClO₄ in MeCN (saturated with O₂, H₂O < 20 ppm) on an Au(111) half bead single crystal. Higher wavenumbers (2000 – 2400 cm⁻¹).

Figure 6.16 *In situ* SHINs spectra for the reduction sweep of 0.1 M NaClO₄ in MeCN (saturated with O₂, H₂O ~120 ppm) on an Au(111) half bead single crystal. Higher wavenumbers (2000 – 2400 cm⁻¹).

Figure 7.1 (a) 0.1 M NaClO₄ in DMSO (no TBA, saturated with O₂) on different platinum single crystal facets and polycrystalline platinum, (b) Pt(poly), (c) Pt(111), (d) Pt(110), (e) Pt(100). Sweep rate 50 mV/s.

Figure 7.2 0.1 M NaClO₄ in DMSO (no TBA, saturated with O₂) on Pt(111) driven to different potentials. Sweep rate 50 mV/s.

Figure 7.3 CV's of 0.1 M NaClO₄ in DMSO (saturated with O₂) on Au(100) (green), Pt(100) (blue). Sweep rate 50 mV/s.

Figure 7.4 CV's of different NaClO₄ concentrations in DMSO (saturated with O₂) on (a) Pt(111), (b) Pt(110), (c) Pt(100). Sweep rate 50 mV/s.

Figure 7.5 0.1 M NaClO₄ in DMSO (saturated with O₂) on Pt(111) 10 cycles. Sweep rate 50 mV/s.

Figure 7.6 0.1 M TBAClO₄ in DMSO (no Na, saturated with O₂) on different Pt single crystal facets. Sweep rate 50 mV/s.

Figure 7.7 Schematic of the potential dependent rearrangement of TBA cation on the electrode. Recreated from Aldous.

Figure 7.8 50mM NaClO₄ in 0.1 M TBAClO₄ in DMSO (saturated with O₂) on different Pt single crystal facets. Sweep rate 50 mV/s.

Figure 7.9 0.1 M NaClO₄ in 0.1 M TBAClO₄ in DMSO (saturated with O₂) on Pt(111) driven to different potentials. Sweep rate 50 mV/s.

Figure 7.10 100 mM NaClO₄ in 0.1 M TBAClO₄ in DMSO on Pt(111) cycled 10 times. Sweep rate 50 mV/s.

Figure 7.11 CV's of different NaClO₄ concentrations in 0.1 M / DMSO (saturated with O₂) on (a) Pt(111), (b) Pt(110), (c) Pt(100). Sweep rate 50 mV/s.

Figure 7.12 CV's of (a) 0.1 M LiClO₄ (red) and 0.1 M NaClO₄ (black) in DMSO (no TBA, saturated with O₂) on Pt(111). Sweep rate 50 mV/s, (b) 0.05 M LiClO₄ in DMSO (no TBA, saturated with O₂) on Pt (111). Sweep to different potentials to determine peak relationships. Sweep rate 50 mV/s.

Figure 7.13 0.1 M LiClO₄ in DMSO (no TBA, saturated with O₂) on different Pt single crystal facets. Sweep rate 50 mV/s.

List of Tables

Table 2.1 Standard reference potentials vs. SHE (standard hydrogen electrode)

Table 4.1 Data from cyclic voltammograms of 0.1 M TBAClO₄ in DMSO on various polycrystalline electrodes in **Fig. 4.2**.

Table 4.2 Raman band positions of surface species on various polycrystalline electrodes

Table 4.3 Peak positions and full width half maximum (FWHM) Data for peak fitting of Raman bands in **Fig. 4.7**.

Table 4.4 Peak assignments from cyclic voltammogram data in **Fig. 4.11**.

Table 4.5 Raman peak positions (cm⁻¹) of spectra in figure 4.12 and corresponding positions of products on gold surface (*Peak positions taken from Bruce et al)

Table 4.6 Standard Raman peak positions and assignments for solvents, salts, products and possible decomposition products associated with the oxygen reduction reaction mechanism taking place in the lithium oxygen battery. Peaks assigned in agreement with the literature (Li₂CO₃, MeCN, DMSO, LiOH, Li₂O₂, LiClO₄)

Table 5.1 Enhancement intensities of the 1175 cm⁻¹ band of malachite green on different substrates in arbitrary units (a.u.) (not normalised into enhancement factor). Abbreviations; edge plane pyrolytic graphite (EPPG), basal plane pyrolytic graphite (BPPG), boron doped diamond (BDD), carbon doped zinc iron oxide (ZnFe₂O₄/C, lithium titanate (Li₄Ti₅O₁₂), SGL graphitic carbon (graphite)

Table 5.2 Peak assignments from cyclic voltammogram data in **Fig. 5.6**, all peaks referenced against Li/Li⁺

Table 5.3 Raman peak positions (cm⁻¹) of spectra in **Fig. 5.7**.

Table 5.4 Raman peak positions (cm⁻¹) of spectra from 0.5 M LiClO₄/DMSO on a composite carbon cathode (Super C(70%:30%)PTFE). (**Fig. 5.8**)

Table 6.1 Peak position and assignment of cyclic voltammetry data from **Fig. 6.3 and 6.4 (a)** oxidation peaks **(b)** reduction peaks

Table 6.2 Raman peak positions from **Fig. 6.3b and 6.4b**.

Table 6.3 Peak position and assignment of cyclic voltammetry data from **Fig. 6.6**.

Table 6.4 Peak positions from CV in **Fig. 6.11**.

Table 7.1 Oxidation and reduction peak positions from cyclic voltammetry data 0.1 M NaClO₄ in DMSO from **Fig. 7.2**

Table 7.2 Charge and surface coverage of oxidation species from cyclic voltammetry data of NaClO₄ concentrations in DMSO calculated for the Pt(111) facet

List of Abbreviations

AgCl – silver chloride

BPPG – basal plane pyrolytic graphite

CV – cyclic voltammetry

D.N. – donor number

DMSO –dimethyl sulphoxide

E – potential

EPPG – edge plane pyrolytic graphite

Fc – ferrocene

Fc⁺ - ferrocenium

GC- glassy carbon

H₂O₂ – hydrogen peroxide

H₂SO₄ – sulfuric acid

HF – hydrofluoric acid

HUPD – hydrogen underpotential deposition

IHP – inner helmholzt plane

iR drop – ohmic drop

KMNO₄ – potassium permanganate

MeCN – acetonitrile

M-O₂ – metal-oxygen battery

nm – nanometer

O₂⁻ - superoxide

OCP – open circuit potential

OHP – outer helmholzt plane

P₂O₅ – phosphorus pentoxide

PEEK – polyether ether ketone

ppm – parts per million

PTFE – polytetrafluoroethylene

SERS – surface enhanced Raman spectroscopy

SHIN –shell isolated nanoparticle

SHINERS – shell isolated nanoparticles for enhanced Raman spectroscopy

μC – micro coulombs

μm – micrometer

Chapter 1

Introduction

Part A - The Metal-Oxygen Battery

1.1 Energy

Over the past couple of decades there has been a noticeable increase in the demand for energy and energy storage due to ever-increasing technological advancements and the continual growth of the global population. In order to sustain such demand, cleaner renewable and sustainable energy technologies need to be developed, to move away from current fossil fuel technologies.

The storage and delivery of energy is of particular importance, especially in areas of intermittent renewables, such as wind and solar, where maintaining a constant supply of energy can be difficult. A variety of storage techniques are being implemented and developed around the world, encompassing a range of forms from electrochemical and chemical, to mechanical and thermal. The storage techniques can be broken down related to their power rating and discharge time (**Fig. 1.1**). Pumped-storage hydroelectricity (PSH) and compressed air energy storage (CAES) can provide large power outputs for long periods of time (10 – 1000 MW for multiple hours).¹ These systems are only applicable in certain geographical locations, e.g. PSH commonly used in mountain terrain.²

Electrochemical energy storage is very adaptable to a range of systems, as it is able to deliver an array of discharge times and power outputs, i.e. batteries and supercapacitors.³ Supercapacitors have rapid charge and discharge rates, making them

suitable to supply short term power bursts, e.g. to provide rapid acceleration in cars and buses.⁴

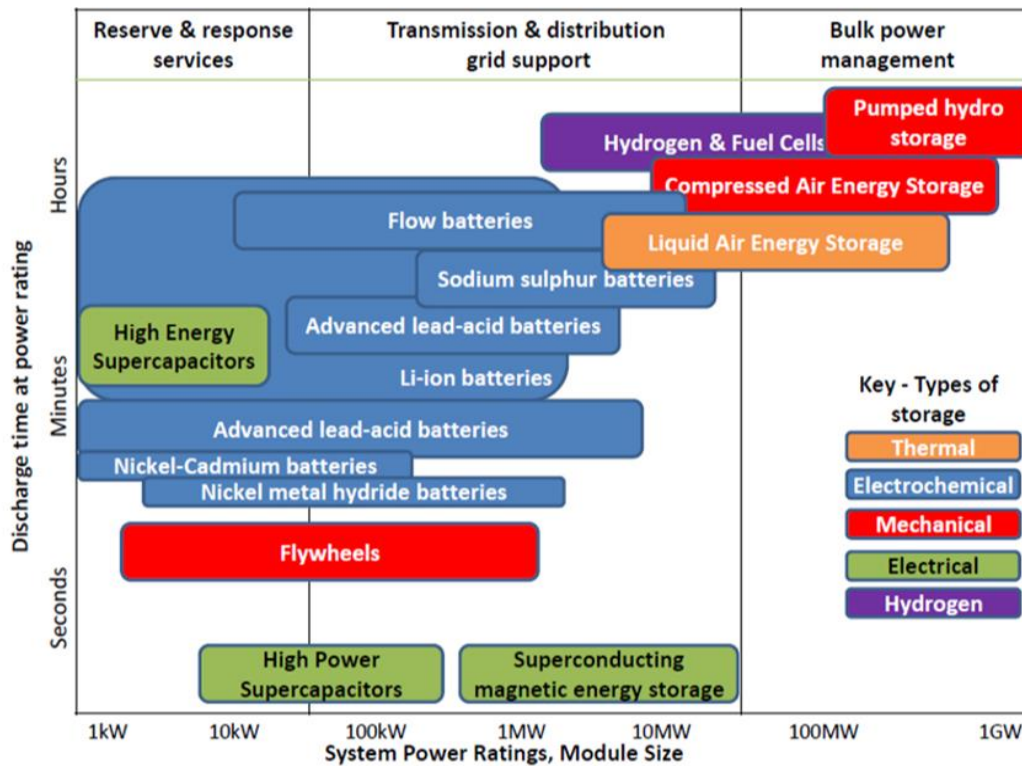


Figure 1.1 Power supplies in terms of their power rating and discharge time,⁵ for a variety of energy storage systems.

Batteries provide power in the kW – MW range over a prolonged period of time, being utilised in portable devices, electric vehicles and grid storage.⁶ A battery consists of a series of electrochemical cells aligned in a linear or parallel format. Each individual cell consists of a positive (cathode) and negative (anode) electrode. In a rechargeable battery the positive and negative electrodes swap upon charge and discharge, however for the purposes of this thesis, the negative and positive electrodes on discharge are referred to as the anode and cathode respectfully. The two electrodes are separated by a conducting electrolyte and connected via an external circuit, upon discharge and charge, ions migrate between the two electrodes through the electrolyte, whilst electrons move round the external circuit.⁷

1.2. Demand for higher energy batteries

The development of battery technologies has observed a significant increase in terms of specific energy (Wh kg^{-1}) and energy density (Wh dm^{-3}) since Alessandro Volta's initial battery (**Fig 1.2**).⁸ At present the Li-ion battery is at the forefront of battery technologies, since its commercialisation in 1990. The Li-ion battery is a vast improvement on Plante's lead-acid battery system,⁹ which has a specific energy of 171 Wh kg^{-1} . A steady increase in the specific energy has been observed since commercialisation;¹⁰ however practical Li-ion batteries are fast approaching their optimal energy storage limits ($387 \text{ Wh kg}^{-1} - \text{Li/LiCoO}_2$),¹¹⁻¹³ which is still below the target of 400 Wh g^{-1} , set by the US by the end of 2017.¹⁴ The Li-ion battery still has an important role to play in the current and short term future, but will not be able to sustain the rapid growth required to power the technological advancements in electric devices and vehicles in the long term.^{15, 16}

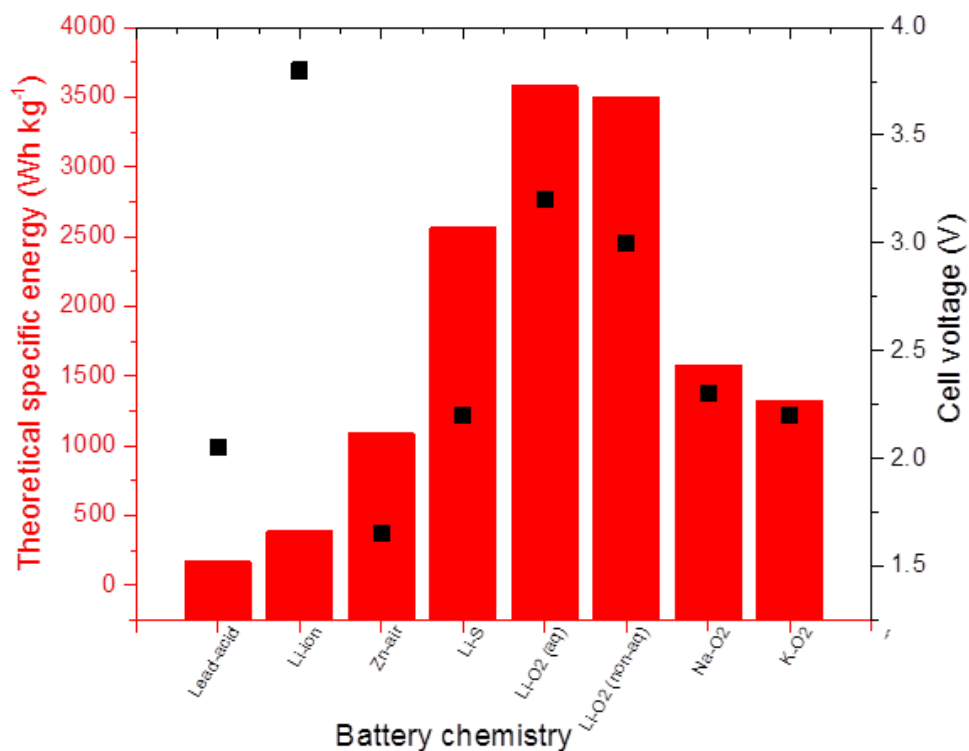


Figure 1.2 – A summary of the past, present and future battery technology specific energies and cell voltages.

A broad range of new battery technologies are being developed to succeed the Li-ion battery in terms of higher energy densities and prolonged cycle life. Lithium-sulphur (Li-S) is a prominent choice,¹⁷⁻²⁰ having a high theoretical specific energy (2566 Wh kg⁻¹).²¹ However, problems associated with the formation of soluble polysulphide species upon cycling, cause capacity fading, shortening battery life.²²

The metal-oxygen battery, in particular the Li-O₂ chemistry has been a prominent alternative to Li-S as a successor to the Li-ion battery. The Li-O₂ system has a high theoretical energy density 3505 Wh kg⁻¹ for the non-aqueous system. The aqueous system has an even higher energy density, however the complexity of the reaction mechanisms in an aqueous media due to the highly reactive nature of the lithium species in the presence of water, has led to a larger focus being placed on the non-aqueous Li-O₂ battery.

1.3. The metal-oxygen battery

The non-aqueous metal-oxygen battery differs from the lithium ion battery, which requires the intercalation of lithium in the electrodes. The M-O₂ system relies upon the reversible formation of peroxide or superoxide products (depending on the metal cation).²³ The non-aqueous Li-O₂ battery consists of a solid metal anode, a conducting electrolyte, a composite porous cathode and a catalyst or redox mediator to lower the voltage gap between charge and discharge (**Fig. 1.3**).²⁴

On discharge, metal cations move from the lithium anode through the electrolyte to the composite carbon cathode. At the cathode, the cations are reduced in the presence of oxygen to form the peroxide (Li and Na) or superoxide species (Na and K). The oxygen is sourced from the environment through a permeable membrane to prevent any impurities and moisture contaminating the reaction mechanism. The benefit of sourcing oxygen from the environment, allows the battery to be much

lighter as oxygen is not stored within the cell. The reversible formation of the M_xO_2 (peroxide or superoxide) species upon charge and discharge,²⁵ forms the basic principle for the metal-oxygen chemistry.

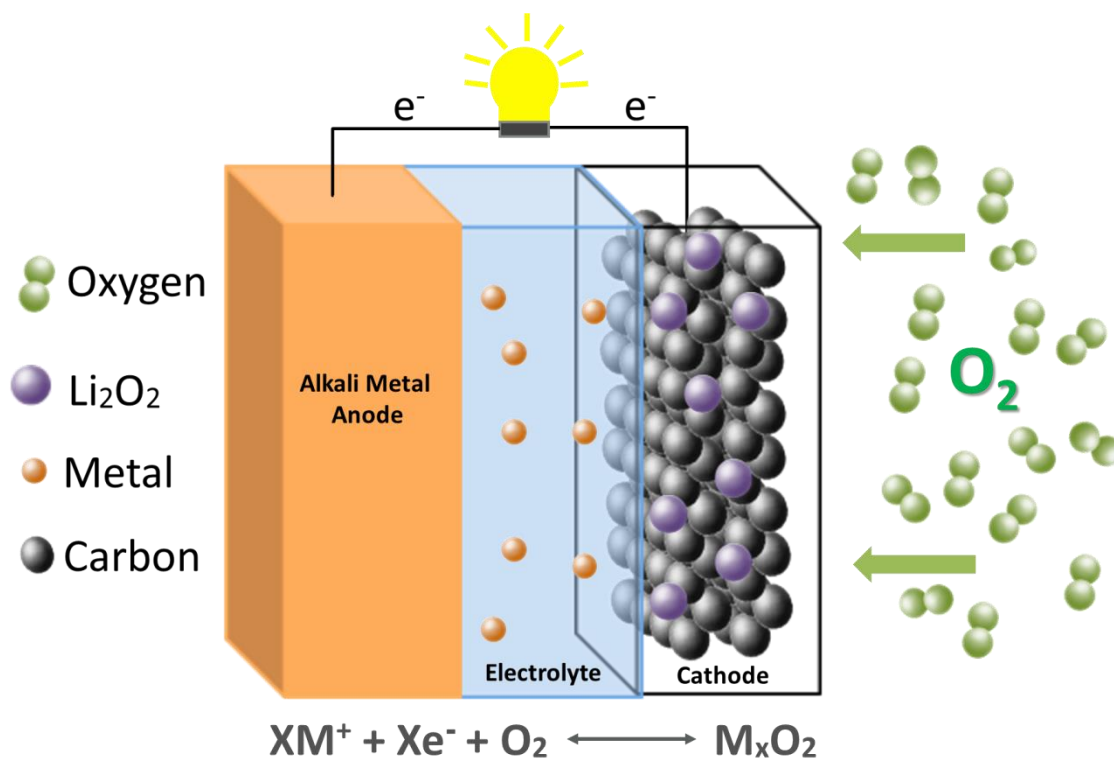


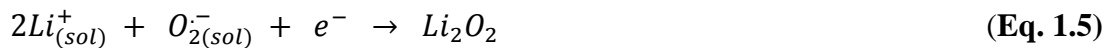
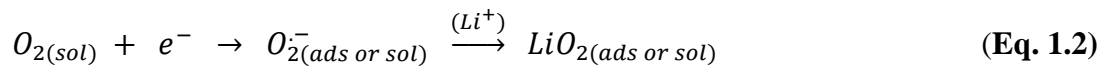
Figure 1.3 Schematic of the non-aqueous metal-oxygen battery showing the movement of ions upon charge and discharge and the overall reversible chemical reaction taking place during discharge/charge.

1.4 The lithium-oxygen battery

The first rechargeable non-aqueous Li-O₂ cell was proposed by Abraham et al²⁹ in 1996. Since the proposal of the initial Li-O₂ cell there have been a number of factors limiting the development of this chemistry that are still to be resolved. The stability of the electrolyte, anode and cathode are major problems,^{30,31} as well as the large voltage gap between charge and discharge.³²



The reversible formation and breakdown of Li_2O_2 on discharge is the basis of the Li- O_2 battery (**Eq. 1.1**), however the reaction mechanism is much more complex than this simple equation. Previous oxygen reduction and evolution reaction (OER/ORR) mechanistic studies have depicted two possible mechanisms.³³⁻³⁵ A 1 e^- reduction of O_2 in the presence of Li^+ , to form lithium superoxide (LiO_2) (**Eq. 1.2**) proceeded by a second e^- reduction to form lithium peroxide (Li_2O_2) (**Eq. 1.3**) or disproportionation of the LiO_2 species (**Eq. 1.4**). Alternatively the direct reduction of O_2^- and Li to form Li_2O_2 has also been suggested (**Eq. 1.5**).



The reduction mechanism theoretically produces various oxygen species O^{2-} , O_2^- , O_2^{2-} , as well as the different lithium superoxide and peroxide species. All of these species readily undergo nucleophilic attack on the porous carbon cathode and some electrolyte species.³⁶ The unwanted and irreversible side reactions in the electrolyte prove extremely detrimental to the Li- O_2 battery, reducing cycle life and causing cell death.

The oxidation mechanism involved in the Li- O_2 system is complex and not completely understood; it appears to be dependent on the surface and electrolyte properties. However, it is known that high over-potentials ($> 4\text{ V}$) are required to completely oxidise Li_2O_2 from the electrode surface²³ without the presence of a catalyst or redox mediator.³⁷ The high potential is often outside most organic

solvents electrochemical window (i.e. they decompose at potentials > 4 V). This has produced problems when cycling.^{38, 39}

1.4.1. Electrolyte

A key issue is finding an electrochemically and chemically stable electrolyte. This can be achieved by elucidating the electrochemical oxidation and reduction reaction mechanisms in the Li-O₂ system.

The electrolyte in the Li-O₂ cell is an ion conducting media, which allows the movement of lithium ions from the solid lithium anode to the composite porous cathode, it is important to minimise and ideally eliminate any unwanted side reactions that may occur upon the discharge/charge cycles to optimise the batteries efficiency and lifetime. An ideal electrolyte will have a large electrochemical window between 2.5 and 4.5 V.⁴⁰ It must be stable in the presence of the extremely reactive oxygen and lithium species produced during charge and discharge. The electrolyte has to have good oxygen solubility and diffusivity, mixed with lithium ion conductivity. Other important characteristics include; low volatility to avoid evaporation at the cathode,⁴¹ be able to wet the electrode surface and most importantly be safe.

1.4.2 Solvent

In order to achieve a stable electrolyte media a variety of non-aqueous solvents have been tested. Early studies focused on organic carbonates,⁴² as they have been widely used in lithium-ion batteries. Organic carbonates (e.g. propylene carbonate (PC)) were chosen because of their low volatility and oxidation stability.⁴³ Studies have shown that an organic carbonate electrolyte cannot sustain the reversible chemical reaction taking place in the Li-O₂ battery.⁴⁴ The organic carbonates are seen to decompose to lithium carbonate and alkyl carbonates in the presence of

superoxide, which forms an insulating layer on the electrode and cannot be oxidised at sufficiently low potentials $< 4.6 \text{ V}$ ³⁰ causing a decrease in capacity.

More recent studies have focused on ethers (such as tetraethyleneglycol dimethylether (TEGDME) and diethylene glycol dimethylether (DIGLYME)). Ethers are a prominent choice, due to their stability in the presence of the superoxide species. Li_2O_2 was identified as the main discharge product, but the electrolyte showed limited reversibility. Investigations using DME demonstrated decomposition of the electrolyte does occur forming lithium carbonate in the presence of the superoxide and peroxide species,⁴⁵ with only 60 % of the oxygen consumed in reduction being released upon oxidation.⁴⁶

Ionic liquids (e.g. $\text{Pyr}_{14}\text{TFSI}$) have been of considerable interest for the electrolyte as they can possess hydrophobic properties, a large electrochemical window, up to 5.5 V and are relatively stable to decomposition in the presence of superoxide species but have low Li solubility.⁴⁷⁻⁴⁹ They have a much greater stability than organic carbonates to nucleophilic superoxide species, yet electrolyte degradation is witnessed after multiple cycles.⁵⁰ Ionic liquid blends can be tailored to form a stable conducting electrolyte.⁵¹ These promising characteristics made ionic liquids a prominent area of research for use in the Li- O_2 battery.

Other non-aqueous solvents that have been studied include amides⁵² (e.g. dimethylformamide, DMF) because of their stability in the presence of the highly nucleophilic reaction species such as superoxide. Sulphones as they can have an electrochemical window stable up to 5 V⁵³ but the majority of sulphones are solid at room temperature, making them unsuitable for use. Sulphoxides, especially DMSO have been used to study the reaction mechanisms in the Li- O_2 battery^{40, 43, 48, 54, 55}. DMSO has shown reasonable stability towards the superoxide species,⁵⁶ with the

reversible formation of lithium peroxide on charge/discharge as the main product with some capacity fading overtime. IR, SERS, differential electrochemical mass spectrometry (DEMS) and NMR experiments show some decomposition products, indicating that DMSO does undergo degradation with methylsulphone and other side products being detected.^{57, 58} However, these products do not increase on cycling, as they are dissolved into solution, and do not build up on the electrode surface, making DMSO a good solvent for understanding the electrochemistry at the oxygen cathode interface.

1.4.3 Solution vs. surface mechanism

The choice of electrolyte solvent has a direct impact on the reaction mechanism that takes place in the Li-O₂ battery; this phenomenon has been experimentally demonstrated to be related to the Guttmann donor number⁵⁹ of the solvent (**Fig. 1.4**).

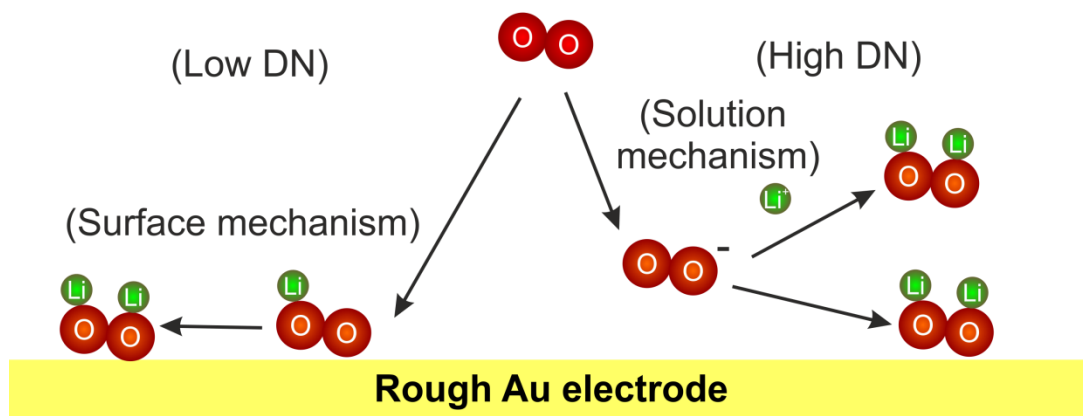


Figure 1.4 Schematic demonstrating the surface vs. solution mechanism. Redrawn from Johnson et al.⁶⁰

The Guttmann donor number is a numerical way of quantifying how well a solvent can solvate cations into solution.⁵⁹ A large Guttmann donor number, e.g. DMSO (29.8) would likely solvate cations into solution. In the Li-O₂ cell chemistry, this equates to Li-O₂ being solvated into solution.⁶¹ This allows second e⁻ transfer or

disproportion to occur in solution, which causes large toroids to form on the electrode surface.^{62 63}

Alternatively low donor number solvents, e.g. MeCN (14.1) weakly solvate the cations in solution, allowing the Li-O₂ to remain on the electrode surface, promoting the growth of thin Li₂O₂ films through second electron transfer or disproportionation, which can lead to passivation of the electrode surface.⁶¹

1.4.3.1 Guttmann donor number

The Guttmann donor number as described above is a measure of how well a solvent can solvate a cation into solution, i.e. the strength of the solvent as a lewis base (the ability to donate a pair of electrons). DMSO has been previously described as a high donor number, this is due to DMSO possessing two acceptor sites where it can donate a lone pair (S and O), O has a very high electron density, so can be described as a hard atom, whereas S still has nucleophilic characteristics due to the presence of the lone pair.⁶⁴ The lone pair on the sulphur can also be delocalized over the oxygen allowing for easier donation of the lone pair. MeCN is described as a low donor number as it cannot as readily donate an electron pair.

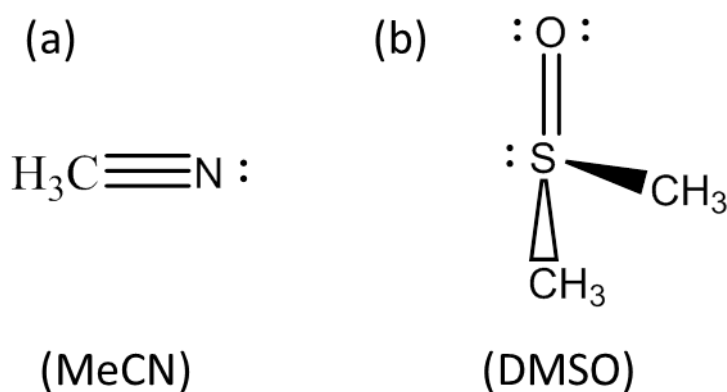


Figure 1.5 Structure of (a) MeCN, (b) DMSO demonstrating position of lone pairs.

1.4.4 Impurities and additives

Impurities and additives can have a varied effect on the mechanism and longevity of the cell life. The behaviour of these impurities is of particular importance, due to the extremely sensitive nature of the intermediate and product species involved in metal-oxygen chemistries.^{64, 65}

The addition of controlled amounts of water to the electrolyte, can promote the growth of solution based Li_2O_2 .⁶⁶ The preferential growth of solution based peroxide is a result of the water molecules acting as a mediator for charge transfer due its high acceptor number (54.8). This promotes the formation of large Li_2O_2 toroids on the electrode surface, which has been shown to increase the capacity upon discharge.^{67,}
⁶⁸ However, the addition of water has an adverse effect on the intermediates and products, forming hydroxide side products. This can cause passivation of the electrode surface after multiple cycles and ultimately cell death, although it may be overcome with the presence of a redox mediator.⁶⁵ The presence of water, with an alkyl metal anode is also not practical, due to the highly reactive nature of the two species.

Carbon dioxide would be a common contaminant from the environment and would have to be removed when extracting oxygen for the operation of the metal-oxygen cell. Addition of CO_2 into the electrolyte has been shown to have an increase in the discharge capacity.⁶⁹ However, reaction of CO_2 with the reduced oxygen species can yield carbonates,^{70, 71} which require a large overpotential to oxidise them on charge ($> 4.5 \text{ V}$).⁷²

1.4.5 Salt

A lot of focus has been placed on finding a suitable solvent with much less interest being placed on the lithium salt and understanding its role in the mechanism.

The salt is of key importance for conductivity in the electrolyte and the stability of the surface electrolyte interphase.⁷³ The small ionic radius of the lithium ion means the choice of lithium salt is limited as the salt will have low solubility, therefore may not completely dissolve in the solvent. Other requirements of the lithium salt are; thermal stability; stability towards any reactants, intermediates or products formed during charge/discharge, and the anion must be stable to decomposition at the cathode. Possible candidates for lithium salts include LiClO₄ (perchlorate), LiOTf (triflate) and LiTFSI (imide). All have reasonable conductivity with the triflate and imide salts having greater thermal stability compared to the perchlorate.⁵² The triflate salt is becoming a popular choice as it has a negative charge on the anion which can cause increased conductivity in solvents with less polarity.⁷⁴

1.4.6 Redox mediator

The growth of large toroidal shaped Li₂O₂ on reduction at the electrode surface (**Fig. 1.6**), requires a large overpotential on charge to oxidise the Li₂O₂ from the surface making the reaction kinetics sluggish.⁶¹

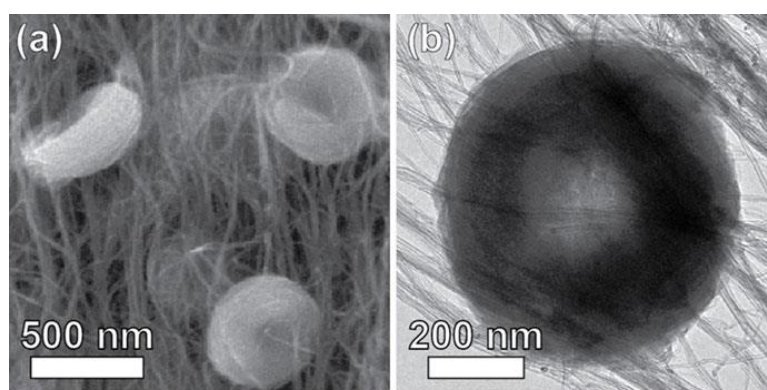


Figure 1.6 (a) SEM, (b) TEM of Toroidal Li₂O₂. Taken from Shao Horn.³⁰

A method to overcome this positive over-potential and improve the rate of charge, is to incorporate a redox mediator into the electrolyte. A redox mediator can also be deployed to aid in the discharge mechanism and improve cycle life.⁷⁵⁻⁸⁰

The redox mediator is a molecule that is dissolved in the electrolyte, upon charge, the mediator is oxidised (e.g. tetrathiafulvalene (TTF) to TTF^+) at a potential greater than the formation of Li_2O_2 .²³ The oxidised redox mediator can migrate to the toroids and oxidise the Li_2O_2 , in turn regenerating the mediator via reduction.^{76, 81}

A number of redox mediators have been investigated, to aid in the charging and other aspects of the Li-O₂ chemistry. Particular interest has focused on decreasing the over-potential for charge. TTF being a prominent option, however a lower potential of oxidation is required. Alternative options include 2,2,6,6-tetramethylpiperidinyloxy (TEMPO),⁸² tris(2,4,6-trichlorophenyl)methyl (TTM).⁸³

1.4.7 Cathode

The cathode used in the Li-O₂ cell, usually consists of a porous composite carbon and a binder. The porosity and morphology of the cathode is required to maximise the surface area available for the reaction intermediates and products to react or precipitate onto the electrode surface.⁸⁴ The stability of the cathode in the presence of the reaction species upon charge and discharge is important. Carbon electrodes have been observed to decompose in the presence of peroxide on charge, at potentials > 3 V.⁸⁵⁻⁸⁷ The stability of the binder has also been a topic of interest, recently, polyvinylidene fluoride (PVDF) has been shown to decompose upon discharge, this has promoted polytetrafluorethylene (PTFE) as the prominent choice for the binder.⁸⁸

The choice of electrode material is important; nanoporous gold has been shown to have reasonable charge and discharge properties. However, the weight and cost of this material make it impractical for practical application. Alternative cathode materials of interest, other than carbon, include metal carbides.³¹ Titanium – carbide

(Ti-C) has been shown to reduce the side reactions occurring as a result of electrode decomposition, whilst retaining 98 % capacity.³¹

1.4.8 Anode

The maximum energy density for the metal-oxygen battery is achieved when an alkali metal is used as the anode, i.e. Li. The use of Li or Na as the anode brings a multitude of problems. The highly reactive nature of alkali metals in the presence of water, plating of alkali cations, inhibition of dendrites and a stable solid electrolyte interphase (SEI) layer are all factors which need to be addressed for the safe use of lithium or sodium as the anode.⁸⁹⁻⁹² Alternative anode materials include silicon and antimony structures. These structures can be loaded with lithium or sodium ions, and upon discharge the cations de-intercalate. This method would mitigate the problems associated with the solid alkali metal anode, albeit at the expense of energy density.

1.5 The sodium-oxygen battery

The last few years has seen an increase in the study of alternative alkali metals, in place of lithium, for the metal-oxygen battery. Potassium and magnesium have been investigated as viable alternatives⁶¹; however attention has predominantly been directed towards sodium.⁹³⁻⁹⁵ The main drawbacks inhibiting the initial study of the Na-O₂ battery, was the reduced specific energy,^{96,97} the lower cell voltage and higher reactivity of sodium, relative to lithium. However upon investigation, it was determined that the reaction mechanisms with sodium were more simplistic, with possibly fewer detrimental side reactions.^{93, 98-103}

The main reaction product in the Li-O₂ battery is generally assumed to be Li₂O₂. However, in the Na-O₂ system, the major discharge product has not been conclusively assigned. A number of contributing factors have been shown to affect the final discharge product, with Na₂O₂, NaO₂ and Na₂O₂·2H₂O all suggested in the

literature.⁹⁹ Thermodynamically, Na_2O_2 and NaO_2 are both possible products, Na_2O_2 is thermodynamically slightly more favourable than NaO_2 .^{93, 99, 104} However, the margin of error between the free energies is minimal, therefore either could be formed.

The inconsistent use of solvent, salt and experimental setup across the literature inhibits the conclusive assignment of reaction products. It is also possible that the variation in electrolyte may be a substantial factor in the formation of the discharge product. This was apparent in the Li-O_2 system where donor number had a significant impact on the reaction pathway, although this effect is minimised with sodium.²³

The identification of $\text{Na}_2\text{O}_2 \cdot 2\text{H}_2\text{O}$ has been thermodynamically proven in the presence of large volumes of water; it is extremely unlikely trace water in the electrolyte can drive the formation of the hydrated species.¹⁰⁵ In dry electrolytes the presence of NaO_2 has been conclusively assigned, however the reaction pathway is still not fully understood. The growth of NaO_2 cubes has been observed via TEM, however the growth of Na_2O_2 has not been unequivocally assigned. It is believed that the size of the NaO_2 cube has an effect on the thermodynamic stability of the discharge product; the growth of crystallite structures < 10 nm thermodynamically favour NaO_2 , structures larger than 10 nm favour the growth of Na_2O_2 .^{100, 103}

The discharge and charge reactions involved in the Na-O_2 battery are still not fully understood. It is important to understand the fundamental steps that are taking place during the reaction and the effect of solvent and salt on these pathways, in order to progress the development of this chemistry.

Part B – Fundamental Studies

1.6 The importance of fundamental studies for the metal-oxygen battery

The reaction mechanisms taking place in the metal-oxygen batteries are very complex and dependent on numerous factors, such as electrolyte composition, anode/cathode type and morphology, temperature, humidity, water content, impurities and additives. All these factors can have a drastic effect on the reaction pathway and overall charge and discharge products. In order to develop a greater understanding of the reaction mechanisms, it is important to study the fundamental processes that are occurring before applying the technology to a more practical scale.

Fundamental studies using a variety of electrochemical and spectroscopic techniques have already helped elucidate different aspects of the Li-O₂ and Na-O₂ batteries. Solid state nuclear magnetic resonance spectroscopy (NMR) has helped to detect discharge products in the Li-O₂ battery.¹⁰⁶ Differential electrochemical mass spectroscopy (DEMS),³⁴ surface enhanced infrared adsorption spectroscopy,¹⁰⁷ various voltammetry techniques including cyclic voltammetry,^{108, 109} rotating disc,¹¹⁰ impedance spectroscopy^{111, 112} and atomic force microscopy (AFM)^{40, 113} have all assisted to gain insights into the reaction mechanisms, pathways and solvent stability. Raman spectroscopy^{100, 114-117} is another valuable technique that has already provided a strong insight into the chemistry taking place within the metal-oxygen batteries.

1.7 Raman Spectroscopy

Raman spectroscopy is a type of optical vibration spectroscopy. The Raman signal is produced by photons being inelastically scattered after colliding with molecules in the gas phase, solution or on a substrate surface. Elastic scattering (Rayleigh) occurs at the same time as the inelastic scattering. Rayleigh scattering is where photons are scattered with the same frequency at which they collide with the surface (i.e. no change in energy, therefore light of the same wavelength). This accounts for the majority of light scattered from the surface.¹²¹

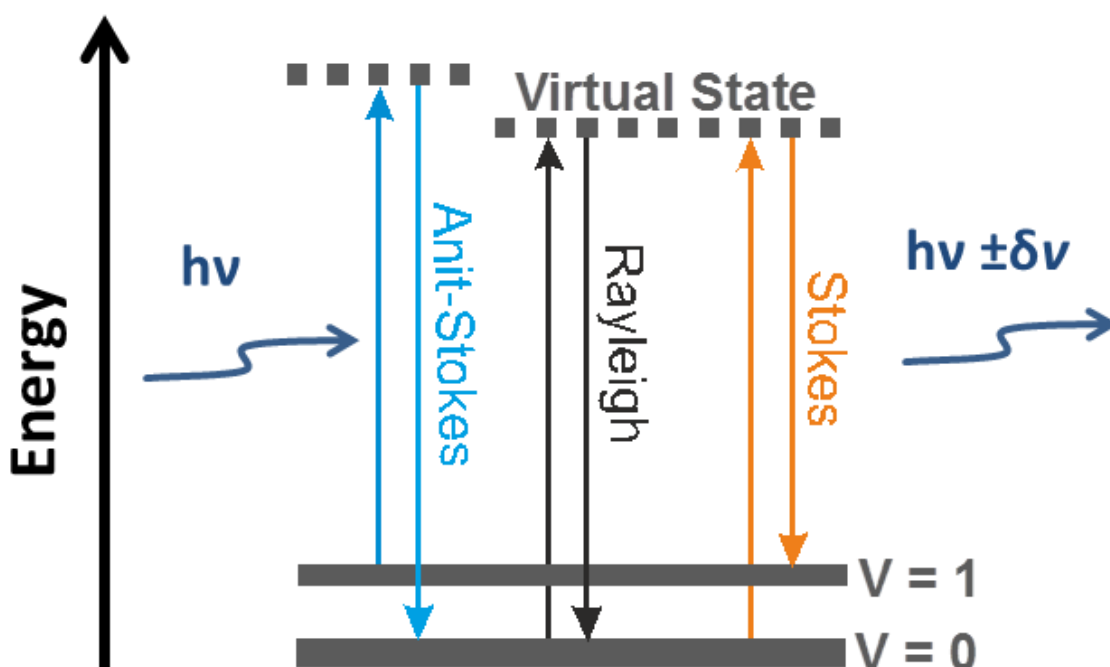


Figure 1.7 Energy level diagram of Raman scattering adapted from Larkin.¹²⁰

Raman scattering can be broken up into higher and lower wavelengths (Stokes and anti-Stokes scattering) (Fig.1.7). Upon collision, if energy is transferred from photon to molecule, then Stokes scattering occurs, (i.e. $h\nu - \delta\nu$), the reverse happens if energy is transferred from a vibrationally excited state to the ground state (antistokes, $h\nu + \delta\nu$). The Stokes scattering is usually only measured because as in agreement with the Boltzmann law, a molecule prefers to be in its vibrational ground

state rather than its excited state.¹²² Therefore it is much more common for a molecule to gain energy than to lose it.

For a vibrational mode of a molecule to be Raman active, a change in the polarisability of the molecule must occur. Polarisation and a dipole moment are created when the molecule is present in an electric field, pushing the electrons in the molecule away from the nuclei. The Raman signal is produced by focusing the light source (electromagnetic radiation beam) on the sample and measuring the intensity of scattered radiation (Raman counts (photons)) in relation to the Raman wavenumber (ω). The magnitude of polarisation is directly related to the strength of the electric field.^{118, 119}

The Raman band position is dependent on the difference in energy between the photons initial state and its excited state. Therefore the band position is dependent on the force constant of the bond (κ) and the reduced mass (μ) (**Eq. 1.6**).¹¹⁸ In general smaller μ will have higher wavenumbers and a larger force constant (usually associated with stronger bonds) will give bands at higher wavenumbers. It can also be noted the type of vibrational mode will affect the position of the Raman mode, i.e. stretching modes (ν) occur at higher wavenumbers than bending modes (δ). This is a result of the increase energy required in (ν) modes as the bond length is altered, whereas (δ) only affect the angle of bonding.

$$\nu_{\nu} = \frac{1}{2 \cdot \pi} \cdot \sqrt{\frac{\kappa}{\mu}} \quad \text{(Eq. 1.6)}$$

1.7.1 Surface Enhance Raman Spectroscopy

Raman spectroscopy is based on a scattering processes that is intrinsically weak when compared to optical processes like absorption and fluorescence;¹²³ therefore, it requires an amplification of the signal.¹²³ Over the past couple of decades promising developments have been achieved in surface enhanced Raman spectroscopy (SERS) since its first observation in 1973 by Fleischmann and subsequent description by Van Duyne.¹²⁴⁻¹²⁷ The Raman signal can be enhanced by electrochemically roughening the surface,^{128, 129} which creates a nanostructured surface, this gives a signal enhancement of $\sim 10^{11}$ times.¹³⁰

This effect is most pronounced on precious metals (e.g. Au, Ag and Cu). Roughening the surface creates a signal enhancement because;

1. Electric field enhancement at the surface – using nanoparticles or electrochemically roughening the surface forms nanoparticles which when excited by photons allows for a redistribution of charge,¹³³ this creates an enhancement of the local electric field as described below.

The presence of nanoparticles or a nanostructured layer on the surface creates localised surface plasmons (LSP) if the frequency of the incident light (laser beam) excites the electrons in the structure. A plasmon is a wave of ordered electrons which can oscillate across the surface, forcing a charge separation within the structure (**Fig. 1.8**). Roughening re-orientates the plasmon perpendicular to the planar surface and allows the plasmons to be localised in the vicinity of the nanostructure or particle. Energy from the localised plasmon is temporally transferred to the nearby molecule (within 10 nm of the nanoparticle, as the field gradient decays the further away from the nanoparticle), this causes a change in polarisation within the molecule. The energy is then transferred back

to the plasmon where it is scattered. The degree of polarisation is dependent on the size of the electromagnetic field, i.e. the closer to the nanoparticle, the greater the field gradient, therefore the greater the degree of polarisation. This coincides with the probability of scattering, i.e. the greater the electromagnetic field, the greater the probability of inelastic scattering.

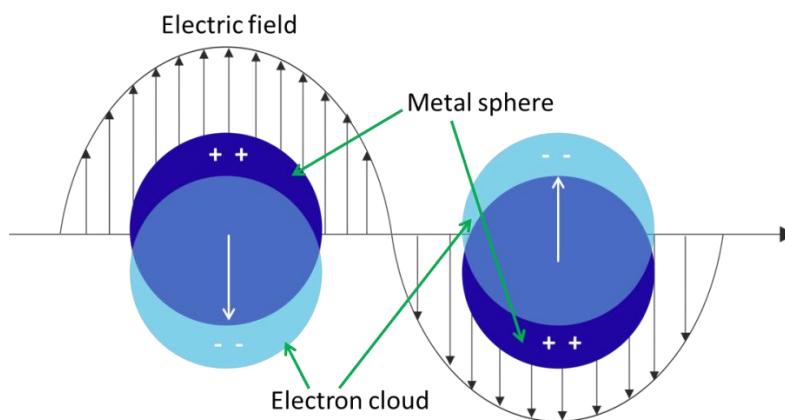


Figure 1.8 Interaction of electron field with electrons in nanoparticle. Recreated from Van Duyne.¹³⁴

2. Chemical enhancement (**Fig. 1.9**) - molecules adsorbed onto the surface can undergo charge transfer with the surface which can in turn increase the polarisability¹³¹

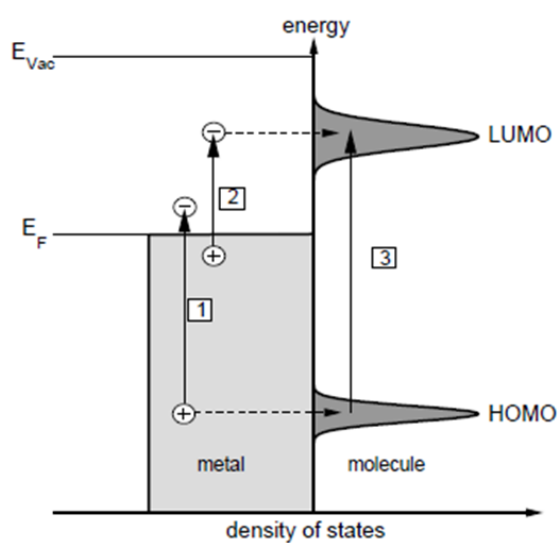


Figure 1.9 Chemical enhancement involves a charge transfer. Figure from Arnolds¹³² and Aroca.¹³¹

Raman spectroscopy is a non-invasive and non-destructive technique, making it a valuable technique for studying the interactions of species at the electrode surface during charge and discharge in battery systems¹³⁵

1.7.2 Developments in enhanced Raman spectroscopy

It is well known that Raman scattering is an intrinsically weak process¹³⁶ due to a limited number of inelastically scattered photons. As mentioned previously to overcome this various surface enhanced techniques have been employed to increase the Raman signal. However, surface enhanced Raman spectroscopy (SERS) is generally restricted to metal surfaces that can form a nanostructured surface.¹³⁷ The enhancement produced by this rough layer is highly dependent on the size and morphology of the layer, with only precious metals such as Au or Ag producing a viable surface enhancement due to their electronic structure.¹³⁶ This has inhibited surface enhanced Raman spectroscopy from being employed in biological, medical and many more practical and industrial applications.

In 1983, Van Duyne¹³⁸ developed a method to bypass the surface limiting aspect of SERS. This technique used a donating effect from an external source on the surface to create a localised enhancement.¹³⁹⁻¹⁴¹ This effect utilised the electromagnetic field emitted from either an Ag or Au nanostructured or nanoparticle surface in order to enhance the vibrational effect of nearby molecules (**Fig. 1.10**). Ag and Au are highly SERS active due to the large electromagnetic field enabling a localised plasmon to be formed. The size¹⁴² and shape¹⁴³ of the nanoparticle or nanostructured surface also has an unprecedented effect on the enhancement of the substrate.^{144, 145} The electromagnetic field produced from the enhanced layer has a penetrating depth between 1-10 nm, therefore only molecular vibrations within this

distance will be enhanced. This requires an ultra-thin layer of nanoparticles or nanostructure in order to prevent passivation of the enhancement on the surface.¹⁴⁶

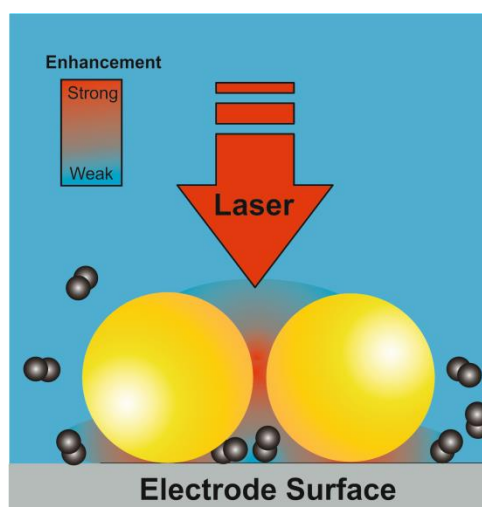


Figure 1.10 Schematic demonstrating electromagnetic field enhancement of gold nanoparticles on a SERS inactive substrate.

The deposited Ag or Au SERS layers produced reasonable enhancement factors however there were problems associated with limiting the adsorption of molecules on the nanoparticle surface in addition to the substrate surface. In some cases adsorption on the Ag or Au was more favourable than the substrate surface. A method of overcoming this for transition metal surfaces was developed by coating the Ag or Au nanostructure¹¹⁸ (**Fig. 1.11**) or nanoparticles¹⁴⁷ with a thin layer of transition metal.¹⁴⁸ This produced large enhancements across a range of metal surfaces,^{141, 149, 150} whilst limiting any effect from the Ag or Au.

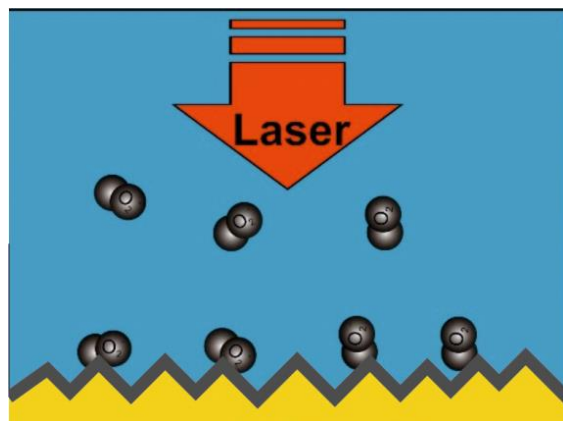


Figure 1.11 Schematic of Au nanostructured surface with ultra-thin transition metal coating.

1.7.3 Tip enhanced Raman spectroscopy

Tip enhanced Raman spectroscopy (TERS) results were first published in 1999 by Kawata et al,¹⁵¹ this built on work a number of years earlier by Kawata and Inouye.¹⁵² TERS mixes the benefits of enhanced Raman spectroscopy with the atomic resolution of atomic force microscopy.

The basic principle of TERS, involves a SERS active AFM tip, achieved by using a tip coated with a metal, e.g. Au, which is SERS active.¹⁵³ The area of surface enhanced Raman effect is therefore limited to the end of the AFM tip (roughly 100 nm, depending on the tip).¹⁵³ The AFM tip is brought in contact with the surface and the laser is then focused on the end of the tip and the surface (**Fig. 1.12**). TERS is experimentally challenging but can provide substantial enhancement on the electrode surface, being used for a number of studies and allows the detection of single molecules.^{154, 155}

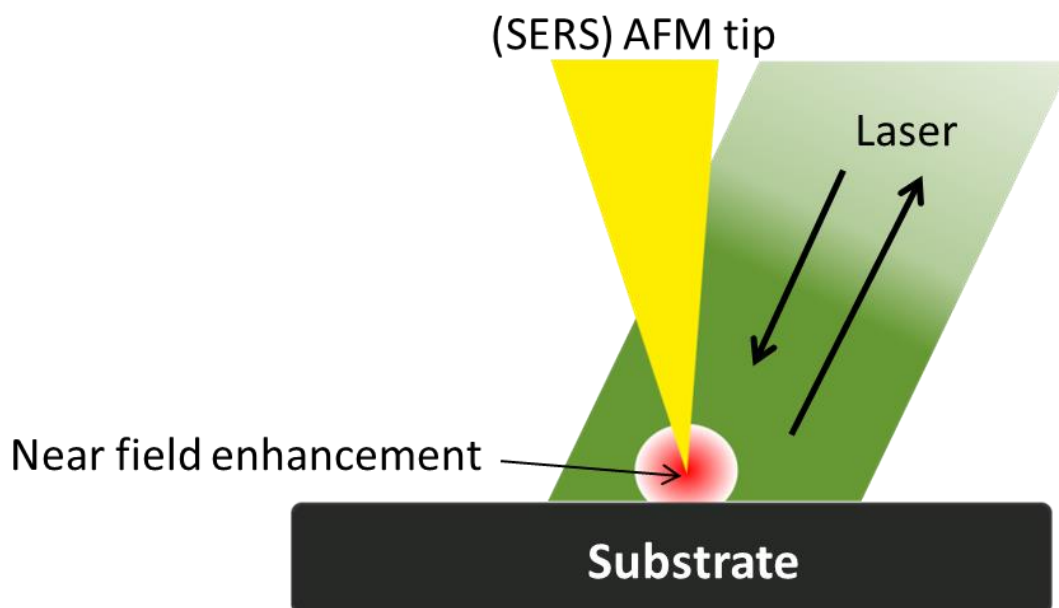


Figure 1.12 Diagram demonstrating TERS near field enhancement. Recreated from the TERS company UNISOKU¹⁵⁶

1.7.4 SHINERS

Shell isolated nanoparticles for enhanced Raman spectroscopy (SHINERS) were developed by the Tian group in 2010.¹⁵⁷ They employed the basic principle of TERS¹⁵⁸ by effectively creating a surface covered with a monolayer of TERS tips. These TERS tips are Au or Ag nanoparticles encapsulated in an ultra-thin (2-3nm) optically inert silica dioxide shell (**Fig. 1.13**). The shell has to be ultrathin in order for the nanoparticles to provide an electromagnetic enhancement to the vibrational modes of nearby molecules and to inhibit any catalytic effect from the gold surface.¹⁵⁹ The accumulated enhancement across the nanoparticles can provide enhancements up to 10^5 on substrate surfaces.¹⁵⁷ SHINERS negates the limitations of SERS to precious metal surfaces, being able to enhance most substrate surfaces without any risk of the Ag or Au core having an effect on the system being investigated due to the silica shell.

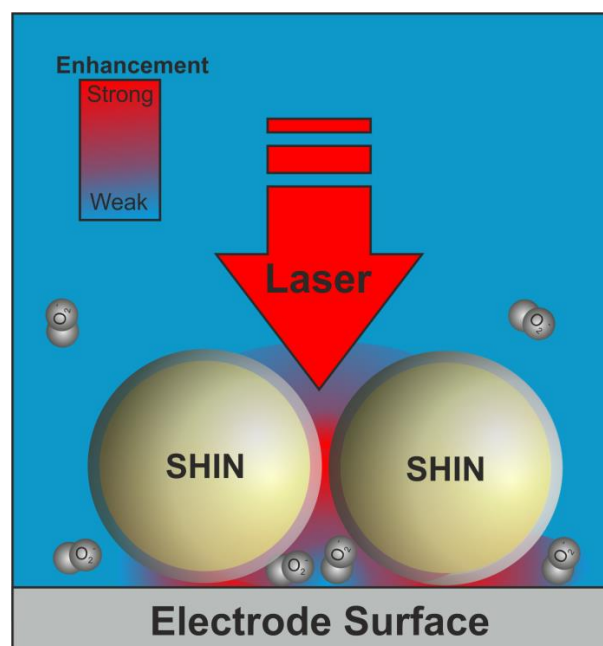


Figure 1.14 Schematic of SHIN's on substrate surface demonstrating the enhancement distribution.

1.7.4.1 SHINERS applications

The diversity of SHINERS to be used as an analytical tool across a range of different research areas has previously been demonstrated. Many SHINERS studies have focused on the enhancement of single crystal surfaces which are SERS inactive due to the flat nature of their morphologies inhibiting any surface plasmon character. SHINERS have been able to enlighten surface interactions, with studies showing the structure sensitivity in catalytic hydrogenation,¹⁶⁰ *in situ* electro-oxidation of Au(111),¹⁶¹ and the detection of different DNA base nucleotides.¹⁶²

Further studies have shown SHINERS to be able to detect the presence of pesticides on orange skins, and have even been used in medical sensing.^{163, 164} Overall they have been shown to enhance a variety of different substrate surfaces both metallic and non-metallic, with applications both *in situ* and *ex situ* for electrochemical applications. Few studies have been carried out in non-aqueous media, with only a handful of these being conducted in relation to battery

materials.^{165, 166} Understanding the interactions occurring at electrode interfaces upon charge and discharge would be very beneficial for developing battery technologies.

1.8 Application of enhanced RAMAN spectroscopy for battery research

The main benefit of this technique is that it permits the user to take advantage of the SERS phenomenon, via the utilisation of localised plasmon enhancement,¹⁶⁷ upon a broader range of substrates, and interrogate electrode-electrolyte interfaces under potential control. Significantly this opens up the possibility of using SHINERS to study practical battery electrodes that consist of a porous matrix of complex interfaces such as conductive carbons, semiconducting transition metal oxides and ‘inert’ polymeric binders. SHINERS can also be applied to studying ideal electrodes, such as single crystals, in order to ascertain important fundamental information about the reaction mechanisms and interactions at the electrode interface for metal-oxygen batteries.

1.9 Single crystals

Understanding the electrochemical behaviour at the solid electrolyte interphase is of particular interest, especially in battery applications. The complicated nature of products and intermediates involved, mixed with the effect of surface variations provides a large degree of uncertainty in ascertaining the reaction pathways and any related surface effects. The use of ideal, well ordered surfaces, i.e. single crystals can help to negate this uncertainty.

A single crystal surface, is a surface which is specifically ordered in relation to its bulk crystallographic orientation.¹⁶⁸ Since the development of the half bead single crystal surface by Clavilier,¹⁶⁹ these highly ordered surfaces have been employed for a variety of electrochemical systems.^{110, 161, 170, 171} The ideal nature of these surfaces allows the electrochemical interactions (e.g. adsorption) at the surface to be

understood and controlled in relation to the surface orientation.¹⁷² The use of single crystal surfaces can aid in identifying the electrochemical behaviour occurring on polycrystalline surfaces of the same material.¹⁷³⁻¹⁷⁵

1.9.1 Miller indices

Single crystal surfaces or facets are assigned in relation to their bulk structure. Common bulk structures are hexagonal close packed and body centered cubic. The gold and platinum crystals used in this thesis have a face-centered cubic (f.c.c.) structure (**Fig. 1.15**).¹⁷⁶ In order to achieve a desired surface orientation or facet, the single crystal is cut along a specific plane, using a calculated angle (**see experimental**). The plane at which the bulk structure has been cut along, is described by its miller indices.¹⁷⁷

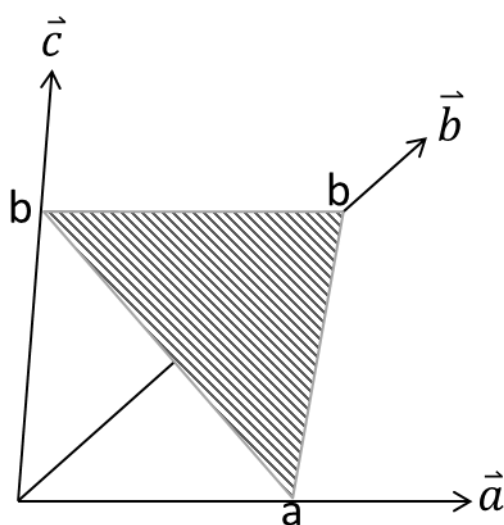


Figure 1.14 Schematic of the plane intercepting the basis vectors forming the unit cell. Recreated from Hazzazi.¹⁷⁸

The miller indices are defined as the reciprocals of the intercepts of the plane on the x, y and z axis. Miller indices are defined by 3 lattice points, usually given as (h,k,l).¹⁷⁹ These lattice points can be calculated by the distance at which the plane

intercepts the coordinate axis (**Fig. 1.14**), forming the unit cell, described by the basis vectors $\vec{a}, \vec{b}, \vec{c}$. The reciprocal of these values are then taken (**Eq. 1.7**).

$$h' = \frac{1}{a}, \quad k' = \frac{1}{b}, \quad l' = \frac{1}{c} \quad (\text{Eq. 1.7})$$

The values are then scaled accordingly to produce a set of integer values, denoted by the lattice points (h,k,l), i.e. if reciprocals = $(\frac{1}{2}, \frac{1}{2}, 1)$ then scaled by a common factor to produce (1,1,2).

The three low miller index planes are the (111), (110) and (100), their surface structures have been demonstrated in **Fig. 1.15**. These planes have been investigated in this thesis. The low index miller indices are of particular interest, as they are relatively stable and make up the majority of the different aspects of polycrystalline surfaces.¹⁸⁰ The facets all exhibit different surface properties and reactivity's, due to the arrangement of the atoms and the availability of adsorption sites.¹⁸¹

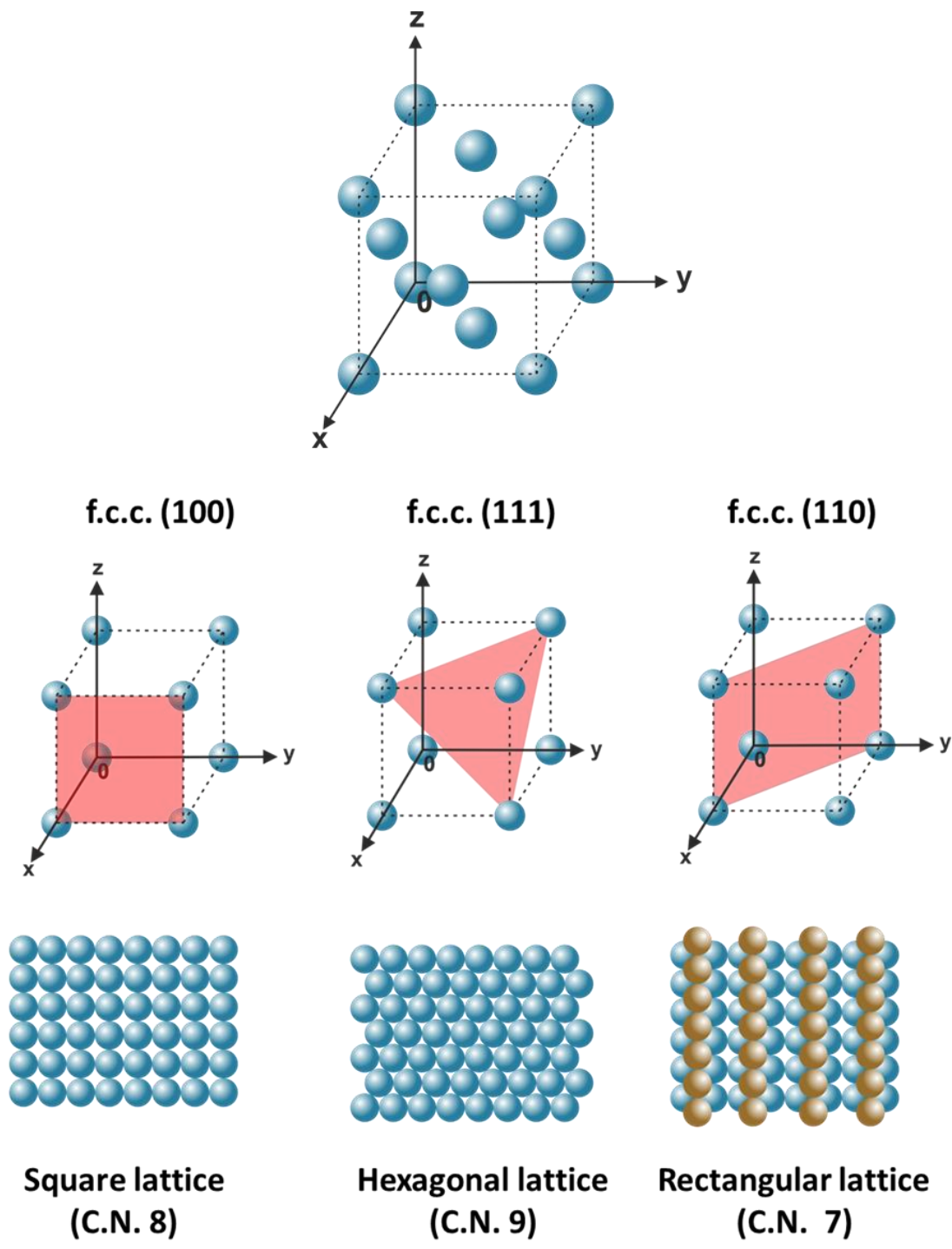


Figure 1.15 (100), (111) and (110) miller index planes for a face centered cubic crystal (nb. Face centered atoms removed from (111), (110) and (100) schematics for clarity). Surface structures relating to each facet below, with coordination number (C.N.) to neighbouring atoms at the surface.

1.9.2 Electrochemical identification of the low index basal planes on Pt

The voltammetric response of each of the (111), (110) and (100) platinum facets display different characteristics indicative of that crystal plane (**Fig. 1.17**). Thus cyclic voltammetry is a very useful characterisation tool to obtain information regarding the quality of the crystal surface, i.e terrace sizes, defects.^{182, 183}

The Pt(100) was cooled in CO after annealing (**Fig1.17b**) and protected with a droplet of water prior to being transferred to the electrochemical cell for experiments. The CV of Pt(10) in 0.1 M H₂SO₄ showed two peaks were observed in the CV, a redox pair at 0.23 V, followed by a more intense couple at 0.35 V. The peaks at 0.23 V are associated with the adsorption of hydrogen at step sites. The peaks at 0.35 V haven been assigned to the adsorption of hydrogen on (100) terraces.^{184, 185}

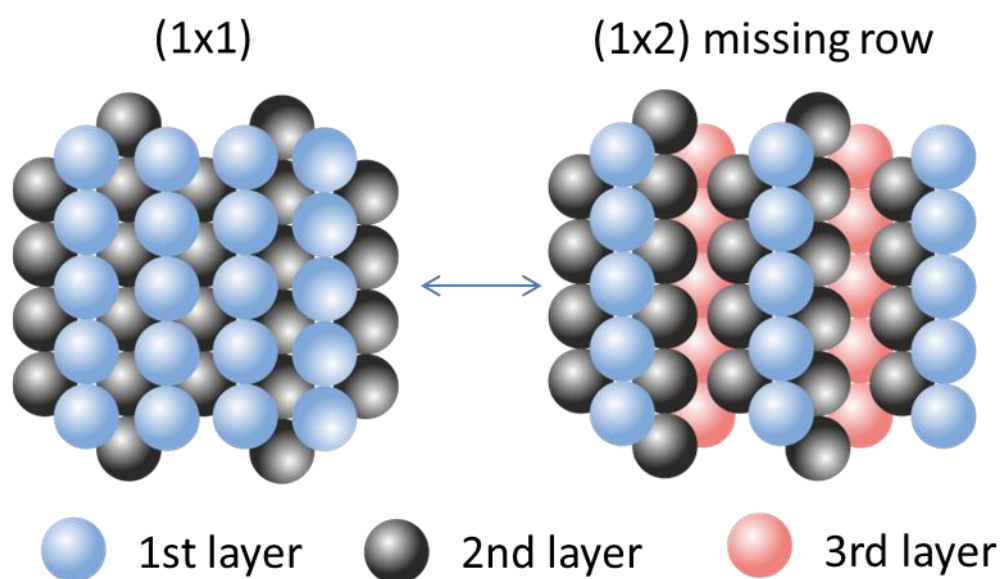


Figure 1.16 Reconstruction of a (110) surface between the (1x1) and (1x2) arrangements. From Attard.¹⁷⁹

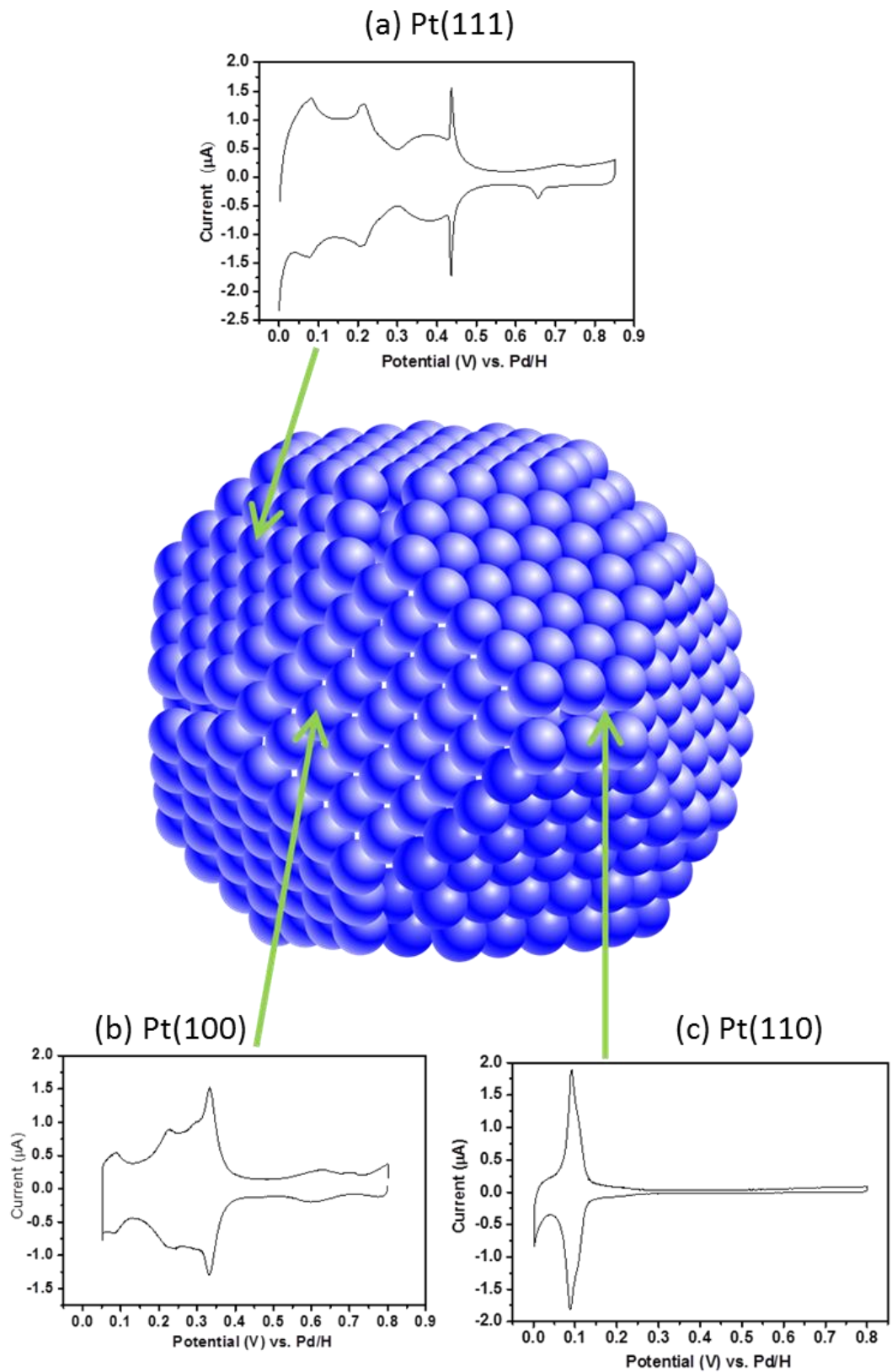


Figure 1.17 Cyclic voltammograms of 0.1 M H_2SO_4 on Pt(111) (cooled in Ar), Pt(100) and Pt(110) (cooled in CO) Sweep rate 10 mV/s. Central schematic demonstrating how facets relate to beads bulk structure.

The Pt(110) was cooled in CO after annealing (**Fig1.16b**) and protected with a droplet of water prior to being transferred to the electrochemical cell for experiments. The CV of Pt(110) in 0.1 M H₂SO₄ observed a strong peak at 0.09 V for the adsorption of hydrogen on (110) terraces (**Fig. 1.17c**). Cooling in CO causes the reconstruction of the (2x1) (missing row) surface structure after annealing to be lifted, forming the (1x1) structure (**Fig. 1.16**).^{186, 187}

The CV of Pt(111) in 0.1 M H₂SO₄ (**Fig. 1.16**), has a strong spike at 0.45 V, this spike is intrinsically linked with a phase transition of the adsorbed sulphate to form an ordered anion structure.^{176, 188} The size of this spike is associated with the quality of the surface.¹⁸⁹

1.10 Summary and outlook for thesis

The utilisation of fundamental techniques such as voltammetry and Raman spectroscopy accompanied by ideal single crystal electrodes will give valuable insight into the complex reaction pathways and mechanisms taking place in the metal-oxygen batteries. The inclusion of SHINERS as a spectro-electrochemical technique will provide information that was previously inaccessible due to the limitations of SERS on more practical battery electrodes.

1.11 References

1. P. G. Taylor, R. Bolton, D. Stone and P. Upham, *Energy Policy*, 2013, **63**, 230-243.
2. D. S. Waghmode, G. P. Umbare, P. C. Mandage and G. F. Aher, *IRJET Int. J. Eng. Technol.*, 2017, **4**, 3212-3215.
3. M. Winter and R. J. Brodd, *Chem. Rev.*, 2004, **104**, 4245-4270.
4. C. Zhu, R. Lu, L. Tian and Q. Wang, 2006.
5. P. Taylor, R. Bolton, D. Stone, X. P. Zhang, C. Martin and P. Upham, *Pathways for Energy Storage in the UK*, University of Birmingham UK, 2012.
6. C. Packham and J. Regan, Tesla to install world's largest grid-scale battery in South Australia).
7. J. R. Owen, *Chem. Soc. Rev.*, 1997, **26**, 259-267.
8. E. Tretkoff, March 20, 1800: Volta describes the Electric Battery).
9. R. R. Dell and *Understanding batteries*, Royal Society of Chemistry, Cambridge, 2001.
10. G. Crabtree, E. Kócs and L. Trahey, *MRS Bull.*, 2015, **40**, 1067-1078.
11. P. G. Bruce, L. J. Hardwick and K. M. Abraham, *MRS Bull.*, 2011, **36**, 506-512.
12. R. C. Armstrong, W. Wolfram, K. P. De Jong, R. Gross, N. S. Lewis, B. Boardman, A. J. Ragauskas, K. Ehrhardt-Martinez, G. Crabtree and M. V. Ramana, *Nat. Energy*, 2016, **1**, 15020.
13. Panasonic, *Lithium Ion NCR18650B specifications*(Panasonic, 2012), <http://go.nature.com/2b1p3ss>, 2012, 11/08/2017.
14. Editorial, *Nat. Energy*, 2016, **1**, 16147.

15. P. He, Y. Wang and H. Zhou, *Electrochem. Commun.*, 2010, **12**, 1686-1689.
16. R. van Noorden, *Nature*, 2014, **507**, 26-28.
17. P. G. Bruce, S. A. Freunberger, L. J. Hardwick and J.-M. Tarascon, *Nat. Mater.*, 2012, **11**, 19-29.
18. L. Ma, K. E. Hendrickson, S. Wei and L. A. Archer, *Nano Today*, 2015, DOI: 10.1016/j.nantod.2015.04.011, 315.
19. S. Wei, S. Xu, A. Agrawal, S. Choudhury, Y. Lu, Z. Tu, L. Ma and L. A. Archer, *Nat. Commun.*, 2016, **7**, 11722.
20. Q. Pang, X. Liang, C. Y. Kwok and L. F. Nazar, *J. Electrochem. Soc.*, 2015, **162**, A2567-A2576.
21. Y.-X. Yin, S. Xin, Y.-G. Guo and L.-J. Wan, *Angew. Chem.-Int. Edit.*, 2013, **52**, 13186-13200.
22. Q. Pang, X. Liang, C. Y. Kwok and L. F. Nazar, *Nat. Energy*, 2016, **1**, 16132.
23. D. Sharon, D. Hirshberg, M. Afri, A. A. Frimer, M. Noked and D. Aurbach, *J. Solid State Electrochem.*, 2017, **21**, 1861-1878.
24. R. Cao, J. S. Lee, M. L. Liu and J. Cho, *Adv. Energy Mater.*, 2012, **2**, 816-829.
25. B. D. McCloskey, R. Scheffler, A. Speidel, G. Girishkumar and A. C. Luntz, *J. Phys. Chem. C*, 2012, **116**, 23897-23905.
26. G. N. Lewis and F. G. Keyes, *J. Am. Chem. Soc.*, 1913, **35**, 340-344.
27. G. N. Lewis, *J. Am. Chem. Soc.*, 1906, **28**, 158-171.
28. G. N. Lewis and C. A. Kraus, *J. Am. Chem. Soc.*, 1910, **32**, 1459-1468.
29. K. M. Abraham and Z. Jiang, *J. Electrochem. Soc.*, 1996, **143**, 1-5.

30. N. Imanishi, A. C. Luntz and P. G. Bruce, *The Lithium Air Battery: Fundamentals*, Springer, 2014.
31. M. M. Ottakam Thotiyl, S. A. Freunberger, Z. Peng, Y. Chen, Z. Liu and P. G. Bruce, *Nat. Mater.*, 2013, **12**, 1050-1056.
32. H.-G. Jung, J. Hassoun, J.-B. Park, Y.-K. Sun and B. Scrosati, *Nat. Chem.*, 2012, **4**, 579-585.
33. I. Gunasekara, S. Mukerjee, E. J. Plichta, M. A. Hendrickson and K. M. Abraham, *J. Electrochem. Soc.*, 2014, **161**, A381-A392.
34. C. Li, O. Fontaine, S. A. Freunberger, L. Johnson, S. Grugeon, S. Laruelle, P. G. Bruce and M. Armand, *J. Phys. Chem. C*, 2014.
35. N. Mahne, O. Fontaine, M. M. Ottakam Thotiyl, M. Wilkening and S. A. Freunberger, *Chem. Sci.*, 2017.
36. V. S. Bryantsev, V. Giordani, W. Walker, M. Blanco, S. Zecevic, K. Sasaki, J. Uddin, D. Addison and G. V. Chase, *J. Phys. Chem. A*, 2011, **115**, 12399-12409.
37. Y. Chen, S. A. Freunberger, Z. Peng, O. Fontaine and P. G. Bruce, *Nat. Chem.*, 2013, **5**, 489-494.
38. A. Khetan, H. Pitsch and V. Viswanathan, *J. Phys. Chem. Lett.*, 2014, 1318-1323.
39. K. U. Schwenke, S. Meini, X. Wu, H. A. Gasteiger and M. Piana, *Phys. Chem. Chem. Phys.*, 2013, **15**, 11830-11839.
40. S. E. Herrera, A. Y. Tesio, R. Clarenc and E. J. Calvo, *Phys. Chem. Chem. Phys.*, 2014.
41. L. J. Hardwick and P. G. Bruce, *Curr. Opin. Solid State Mater. Sci.*, 2012, **16**, 178-185.

42. F. Mizuno, S. Nakanishi, Y. Kotani, S. Yokoishi and H. Iba, *Electrochemistry*, 2010, **78**, 403-405.
43. D. Sharon, M. Afri, M. Noked, A. Garsuch, A. A. Frimer and D. Aurbach, *J. Phys. Chem. Lett.*, 2013, **4**, 3115-3119.
44. W. Xu, K. Xu, V. V. Viswanathan, S. A. Towne, J. S. Hardy, J. Xiao, D. Hu, D. Wang and J.-G. Zhang, *J. Power Sources*, 2011, **196**, 9631-9639.
45. S. A. Freunberger, Y. Chen, N. E. Drewett, L. J. Hardwick, F. Barde and P. G. Bruce, *Angew. Chem.-Int. Edit.*, 2011, **50**, 8609-8613.
46. B. D. McCloskey, D. S. Bethune, R. M. Shelby, G. Girishkumar and A. C. Luntz, *J. Phys. Chem. Lett.*, 2011, **2**, 1161-1166.
47. F. Soavi, S. Monaco, C. Arbizzani and M. Mastragostino, *Meeting Abstracts*, 2014, 1061.
48. M. J. Trahan, S. Mukerjee, E. J. Plichta, M. A. Hendrickson and K. M. Abraham, *J. Electrochem. Soc.*, 2013, **160**, A259-A267.
49. M. Hayyan, F. S. Mjalli, I. M. AlNashef and M. A. Hashim, *Int. J. Electrochem. Sci.*, 2012, **7**, 9658-9667.
50. J. Herranz, A. Garsuch and H. A. Gasteiger, *J. Phys. Chem. C*, 2012, **116**, 19084-19094.
51. P. Radjenovic and L. Hardwick, *Faraday Discuss.*, 2017, DOI: 10.1039/C7FD00170C.
52. Y. Chen, S. A. Freunberger, Z. Peng, F. Barde and P. G. Bruce, *J. Am. Chem. Soc.*, 2012, **134**, 7952-7957.
53. D. Xu, Z. L. Wang, J. J. Xu, L. L. Zhang, L. M. Wang and X. B. Zhang, *Chem. Commun.*, 2012, **48**, 11674-11676.
54. D. T. Sawyer and J. L. Roberts Jr, *J. Electroan. Chem.*, 1966, **12**, 90-101.

55. P. Krtil, L. Kavan, I. Hoskovcová and K. Kratochvilová, *J. Appl. Electrochem.*, 1996, **26**, 523-527.
56. A. D. Goolsby and D. T. Sawyer, *Anal. Chem.*, 1968, **40**, 83-86.
57. N. Mozhzhukhina, L. P. Méndez De Leo and E. J. Calvo, *J. Phys. Chem. C*, 2013, **117**, 18375-18380.
58. M. A. Schroeder, N. Kumar, A. J. Pearse, C. Liu, S. B. Lee, G. W. Rubloff, K. Leung and M. Noked, *ACS Appl. Mater. Interfaces*, 2015, **7**, 11402-11411.
59. V. Gutmann, *Coord. Chem. Rev.*, 1976, **18**, 225-255.
60. L. Johnson, C. M. Li, Z. Liu, Y. H. Chen, S. A. Freunberger, P. C. Ashok, B. B. Praveen, K. Dholakia, J. M. Tarascon and P. G. Bruce, *Nat. Chem.*, 2014, **6**, 1091.
61. D. Aurbach, B. D. McCloskey, L. F. Nazar and P. G. Bruce, *Nat. Energy*, 2016, **1**, 16128.
62. N. B. Aetukuri, B. D. McCloskey, J. M. García, L. E. Krupp, V. Viswanathan and A. C. Luntz, *Nat. Chem.*, 2015, **7**, 50-56.
63. F. Li, S. Wu, D. Li, T. Zhang, P. He, A. Yamada and H. Zhou, *Nat. Commun.*, 2015, **6**, 7843.
64. D. Martin, A. Weise and H. J. Niclas, *Angew. Chem-Int. Edit.*, 1967, **6**(4), 318-334
65. T. Liu, M. Leskes, W. Yu, A. J. Moore, L. Zhou, P. M. Bayley, G. Kim and C. P. Grey, *Science*, 2015, **350**, 530-533.
66. K. U. Schwenke, M. Metzger, T. Restle, M. Piana and H. A. Gasteiger, *J. Electrochem. Soc.*, 2015, **162**, A573-A584.

67. S. Meini, M. Piana, N. Tsiouvaras, A. Garsuch and H. A. Gasteiger, *Electrochem. Solid-State Lett.*, 2012, **15**, A45-A48.
68. X. Yao, Q. Dong, Q. Cheng and D. Wang, *Angew. Chem.-Int. Edit.*, 2016, **55**, 11344-11353.
69. S. Xu, S. Lau and L. A. Archer, *Inorg. Chem. Front.*, 2015, **2**, 1070-1079.
70. S. Zhang, M. J. Nava, G. K. Chow, N. Lopez, G. Wu, D. R. Britt, D. G. Nocera and C. C. Cummins, *Chem. Sci.*, 2017, **8**, 6117-5122
71. W. I. Al Sadat and L. A. Archer, *Sci. Adv.*, 2016, **2**, e1600968
72. W. Xu, V. V. Viswanathan, D. Wang, S. A. Towne, J. Xiao, Z. Nie, D. Hu and J.-G. Zhang, *J. Power Sources*, 2011, **196**, 3894-3899.
73. D. V. Tripkovic, D. Strmcnik, D. van der Vliet, V. Stamenkovic and N. M. Markovic, *Faraday Discuss.*, 2009, **140**, 25-40.
74. K. Xu, *Chem. Rev.*, 2004, **104**, 4303-4417.
75. X. Gao, Z. P. Jovanov, Y. Chen, L. R. Johnson and P. G. Bruce, *Angew. Chem.-Int. Edit.*, 2017, **56**, 6539-6543.
76. X. Gao, Y. Chen, L. Johnson and P. G. Bruce, *Nat. Mater.*, 2016, **15**, 882-888.
77. M. J. Lacey, J. T. Frith and J. R. Owen, *Electrochem. Commun.*, 2013, **26**, 74-76.
78. L. Yang, J. T. Frith, N. Garcia-Araez and J. R. Owen, *Chem. Commun.*, 2015, **51**, 1705-1708.
79. D. Sun, Y. Shen, W. Zhang, L. Yu, Z. Yi, W. Yin, D. Wang, Y. Huang, J. Wang, D. Wang and J. B. Goodenough, *J. Am. Chem. Soc.*, 2014, **136**, 8941-8946.

80. H.-D. Lim, B. Lee, Y. Zheng, J. Hong, J. Kim, H. Gwon, Y. Ko, M. Lee, K. Cho and K. Kang, *Nat. Energy*, 2016, **1**, 16066.
81. S. A. Freunberger, *Nat. Energy*, 2016, **1**, 16074.
82. B. J. Bergner, A. Schürmann, K. Peppler, A. Garsuch and J. Janek, *J. Am. Chem. Soc.*, 2014, **136**, 15054-15064.
83. A. Y. Tesio, D. Blasi, M. Olivares-Marin, I. Ratera, D. Tonti and J. Veciana, *Chem. Commun.*, 2015, **51**, 17623-17626.
84. J. Lu, Y. Lei, K. C. Lau, X. Luo, P. Du, J. Wen, R. S. Assary, U. Das, D. J. Miller, J. W. Elam, H. M. Albishri, D. A. El-Hady, Y.-K. Sun, L. A. Curtiss and K. Amine, *Nat. Commun.*, 2013, **4**, 2383.
85. B. D. McCloskey, A. Speidel, R. Scheffler, D. C. Miller, V. Viswanathan, J. S. Hummelshøj, J. K. Nørskov and A. C. Luntz, *J. Phys. Chem. Lett.*, 2012, **3**, 997-1001.
86. B. M. Gallant, R. R. Mitchell, D. G. Kwabi, J. Zhou, L. Zuin, C. V. Thompson and Y. Shao-Horn, *J. Phys. Chem. C*, 2012, **116**, 20800-20805.
87. M. M. Ottakam Thotiyl, S. A. Freunberger, Z. Peng and P. G. Bruce, *J. Am. Chem. Soc.*, 2013, **135**, 494-500.
88. J. K. Papp, J. D. Forster, C. M. Burke, H. W. Kim, A. C. Luntz, R. M. Shelby, J. J. Urban and B. D. McCloskey, *J. Phys. Chem. Lett.*, 2017, **8**, 1169-1174.
89. K. J. Harry, D. T. Hallinan, D. Y. Parkinson, A. A. MacDowell and N. P. Balsara, *Nat. Mater.*, 2014, **13**, 69-73.
90. E. Eweka, J. R. Owen and A. Ritchie, *J. Power Sources*, 1997, **65**, 247-251.
91. N. Togasaki, T. Momma and T. Osaka, *J. Power Sources*, 2016, **307**, 98-104.
92. Z. W. Seh, J. Sun, Y. Sun and Y. Cui, *ACS Cent. Sci.*, 2015, **1**, 449-455.

93. H. Yadegari, Q. Sun and X. Sun, *Adv. Mater.*, 2016, **28**, 7065 -7093.
94. I. Landa-Medrano, C. Li, N. Ortiz-Vitoriano, I. Ruiz de Larramendi, J. Carrasco and T. Rojo, *J. Phys. Chem. Lett.*, 2016, **7**, 1161-1166.
95. P. Hartmann, C. L. Bender, M. Vračar, A. K. Dürr, A. Garsuch, J. Janek and P. Adelhelm, *Nat. Mater.* , 2013, **12**, 228-232.
96. H. Yadegari, Y. Li, M. N. Banis, X. Li, B. Wang, Q. Sun, R. Li, T.-K. Sham, X. Cui and X. Sun, *Energy & Environ. Sci.*, 2014, **7**, 3747-3757.
97. P. Hartmann, C. L. Bender, M. Vračar, A. K. Dürr, A. Garsuch, J. Janek and P. Adelhelm, *Phys. Chem. Chem. Phys.*, 2013, **15**, 11661-11672.
98. S. Y. Sayed, K. P. C. Yao, D. G. Kwabi, T. P. Batcho, C. V. Amanchukwu, S. Feng, C. V. Thompson and Y. Shao-Horn, *Chem. Commun.*, 2016, **52**, 9691-9694.
99. C. L. Bender, D. Schroder, R. Pinedo, P. Adelhelm and J. Janek, *Angew. Chem.-Int. Edit.*, 2016, **55**, 4640-4649.
100. I. M. Aldous and L. J. Hardwick, *Angew. Chem.-Int. Edit.*, 2016, **55**, 8254-8257.
101. C. Xia, R. Black, R. Fernandes, B. Adams and L. F. Nazar, *Nat. Chem.*, 2015, **7**, 496-501.
102. P. Hartmann, M. Heinemann, C. L. Bender, K. Graf, R.-P. Baumann, P. Adelhelm, C. Heiliger and J. Janek, *J. Phys. Chem. C.*, 2015, **119**, 22778-22786.
103. S. Kang, Y. Mo, S. P. Ong and G. Ceder, *Nano Lett.*, 2014, **14**, 1016-1020.
104. C. L. Bender, P. Hartmann, M. Vračar, P. Adelhelm and J. Janek, *Adv. Energy Mater.*, 2014, **4**, 1301863.

105. R. Pinedo, D. A. Weber, B. Bergner, D. Schröder, P. Adelhelm and J. Janek, *J. Phys. Chem. C*, 2016, **120**, 8472-8481.
106. M. Leskes, N. E. Drewett, L. J. Hardwick, P. G. Bruce, G. R. Goward and C. P. Grey, *Angew. Chem.-Int. Edit.*, 2012, **51**, 8560-8563.
107. J. P. Vivek, N. Berry, G. Papageorgiou, R. J. Nichols and L. J. Hardwick, *J. Am. Chem. Soc.*, 2016, **138**, 3745-3751.
108. C. Ó'Laoire, Northeastern University, 2010.
109. C. O. Laoire, S. Mukerjee, K. M. Abraham, E. J. Plichta and M. A. Hendrickson, *J. Phys. Chem. C.*, 2009, **113**, 20127-20134.
110. J. Staszak-Jirkovský, R. Subbaraman, D. Strmcnik, K. L. Harrison, C. E. Diesendruck, R. Assary, O. Frank, L. Kobr, G. K. H. Wiberg, B. Genorio, J. G. Connell, P. P. Lopes, V. R. Stamenkovic, L. Curtiss, J. S. Moore, K. R. Zavadil and N. M. Markovic, *ACS Catal.*, 2015, **5**, 6600-6607.
111. K. B. Knudsen, J. E. Nichols, T. Vegge, A. C. Luntz, B. D. McCloskey and J. Hjelm, *J. Phys. Chem. C*, 2016, **120**, 10799-10805.
112. I. Landa-Medrano, J. T. Frith, I. Ruiz de Larramendi, I. Lozano, N. Ortiz-Vitoriano, N. Garcia-Araez and T. Rojo, *J. Power Sources*, 2017, **345**, 237-246.
113. C. Liu and S. Ye, *J. Phys. Chem. C*, 2016, **120**, 25246-25255.
114. F. S. Gittleson, K. P. C. Yao, D. G. Kwabi, S. Y. Sayed, W.-H. Ryu, Y. Shao-Horn and A. D. Taylor, *ChemElectroChem*, 2015, **2**, 1446-1457.
115. D. Zhai, H.-H. Wang, K. C. Lau, J. Gao, P. C. Redfern, F. Kang, B. Li, E. Indacochea, U. Das, H. Sun, H. H. Sun, K. Amine and L. A. Curtiss, *J. Phys. Chem. C.*, 2014, DOI: 10.1021/jz501323n.
116. A. I. and H. L., *J. Phys. Chem. Lett.*, 2014, **5**, 3924-3930.

117. J. T. Frith, A. E. Russell, N. Garcia-Araez and J. R. Owen, *Electrochem. Commun.*, 2014, **46**, 33-35.
118. B. Schrader, in *Infrared and Raman Spectroscopy*, Wiley-VCH Verlag GmbH, 2007, pp. 1-5.
119. A. Wokaun, *Berichte der Bunsengesellschaft für physikalische Chemie*, 1996, **100**, 1268-1268.
120. P. Larkin, *Infrared and raman spectroscopy : principles and spectral interpretation*, Amsterdam ; Boston : Elsevier, 2011.
121. M. Baia, S. Astilean and T. Iliescu, in *Raman and SERS Investigations of Pharmaceuticals*, Springer Berlin Heidelberg, Berlin, Heidelberg, 2008, pp. 9-35.
122. P. Vandenaabeele, in *Practical Raman Spectroscopy – An Introduction*, John Wiley & Sons, Ltd, 2013, pp. 1-38.
123. E. C. Le Ru and P. G. Etchegoin, *Principles of Surface Enhanced Raman Spectroscopy and Related Plasmonic Effects*, Elsevier, 2009.
124. M. Fleischmann, P. J. Hendra and A. J. McQuillan, *Chem. Phys. Lett.* , 1974, **26**, 163-166.
125. D. L. Jeanmaire and R. P. Van Duyne, *J. Electroan. Chem. Interfacial Electrochem.* , 1977, **84**, 1-20.
126. S.-Y. Ding, J. Yi, J.-F. Li, B. Ren, D.-Y. Wu, R. Panneerselvam and Z.-Q. Tian, *Nat. Rev. Mater.*, 2016, **1**, 1-16.
127. A. Otto, I. Mrozek, H. Grabhorn and W. Akemann, *J. Phys. Condens. Matter*, 1992, **4**, 1143-1212.
128. U. Oesch and J. Janata, *Electrochim. Acta*, 1983, **28**, 1247-1253.
129. U. Oesch and J. Janata, *Electrochim. Acta*, 1983, **28**, 1237-1246.

130. V. Stancovski and S. Badilescu, *J. Appl. Electrochem.* , 2014, **44**, 23-43.
131. R. Aroca, *Surface-Enhanced Vibrational Spectroscopy*, Wiley, 2006.
132. H. Arnolds, unpublished work.
133. K. Kneipp, M. Moskovits and H. Kneipp, *Surface-Enhanced Raman Scattering: Physics and Applications*, Physica-Verlag, 2006.
134. K. A. Willets and R. P. Van Duyne, in *Annu. Rev. Phys. Chem.* , Annual Reviews, Palo Alto, 2007, vol. 58, pp. 267-297.
135. S. F. Amalraj and D. Aurbach, *J. Solid State Electrochem.*, 2011, **15**, 877-890.
136. A. Otto, I. Mrozek, H. Grabhorn and W. Akemann, *J Phys. Cond. Matt.* , 1992, **4**, 1143-1212.
137. Z.-Q. Tian, B. Ren and D.-Y. Wu, *J. Phys. Chem. B*, 2002, **106**, 9463-9483.
138. R. P. Vanduyne and J. P. Haushalter, *J. Phys. Chem.*, 1983, **87**, 2999-3003.
139. M. Fleischmann, Z. Q. Tian and L. J. Li, *J. Electroan. Chem.*, 1987, **217**, 397-410.
140. M. Fleischmann and Z. Q. Tian, *J. Electroan. Chem.*, 1987, **217**, 411-416.
141. L. W. H. Leung and M. J. Weaver, *J. Electroan. Chem.*, 1987, **217**, 367-384.
142. J. Gersten and A. Nitzan, *J. Chem. Phys.*, 1980, **73**, 3023-3037.
143. P. K. Aravind, A. Nitzan and H. Metiu, *Surf. Sci.* , 1981, **110**, 189-204.
144. A. Nitzan and L. E. Brus, *J. Chem. Phys.*, 1981, **75**, 2205-2214.
145. M. G. Albrecht and J. A. Creighton, *J. Am. Chem. Soc.*, 1977, **99**, 5215-5217.
146. K. Kneipp, Y. Wang, H. Kneipp, L. T. Perelman, I. Itzkan, R. Dasari and M. S. Feld, *Phys. Rev. Lett.*, 1997, **78**, 1667-1670.
147. S. Park, P. X. Yang, P. Corredor and M. J. Weaver, *J. Am. Chem. Soc.*, 2002, **124**, 2428-2429.

148. S. Z. Zou and M. J. Weaver, *Anal. Chem.*, 1998, **70**, 2387-2395.
149. D.-Y. Wu, J.-F. Li, B. Ren and Z.-Q. Tian, *Chem. Soc. Rev.*, 2008, **37**, 1025-1041.
150. L. W. H. Leung and M. J. Weaver, *Abstracts of Papers: Am. Chem. Soc.*, 1987, **194**, 51-COLL.
151. R. M. Stöckle, Y. D. Suh, V. Deckert and R. Zenobi, *Chem. Phys. Lett.*, 2000, **318**, 131-136.
152. Y. Inouye and S. Kawata, *Opt. Lett.*, 1994, **19**, 159-161.
153. N. Kumar, S. Mignuzzi, W. Su and D. Roy, *EPJ Techniques and Instrumentation*, 2015, **2**, 9.
154. D. Kurouski, S. Zaleski, F. Casadio, R. P. Van Duyne and N. C. Shah, *J. Am. Chem. Soc.*, 2014, **136**, 8677-8684.
155. N. Martín Sabanés, T. Ohto, D. Andrienko, Y. Nagata and K. F. Domke, *Angew. Chem.-Int. Edit.*, 2017, **56**, 9796-9801.
156. http://www.unisoku.com/products/usm1400_It_ters.html), 10/08/2017.
157. J. F. Li, Y. F. Huang, Y. Ding, Z. L. Yang, S. B. Li, X. S. Zhou, F. R. Fan, W. Zhang, Z. Y. Zhou, D. Y. Wu, B. Ren, Z. L. Wang and Z. Q. Tian, *Nature*, 2010, **464**, 392-395.
158. R. M. Stockle, Y. D. Suh, V. Deckert and R. Zenobi, *Chem. Phys. Lett.*, 2000, **318**, 131-136.
159. C. Y. Li, J. C. Dong, X. Jin, S. Chen, R. Panneerselvam, A. V. Rudnev, Z. L. Yang, J. F. Li, T. Wandlowski and Z. Q. Tian, *J. Am. Chem. Soc.*, 2015, **137**, 7648-7651.
160. S. Guan, O. Donovan-Sheppard, C. Reece, D. J. Willock, A. J. Wain and G. A. Attard, *ACS Catal.*, 2016, **6**, 1822-1832.

161. U. Zhurav, A. V. Rudnev, J.-F. Li, A. Kuzume, T.-H. Vu and T. Wandlowski, *Electrochim. Acta*, 2013, **112**, 853-863.
162. B.-Y. Wen, X. Jin, Y. Li, Y.-H. Wang, C.-Y. Li, M.-M. Liang, R. Panneerselvam, Q.-C. Xu, D.-Y. Wu, Z.-L. Yang, J.-F. Li and Z.-Q. Tian, *Analyst*, 2016, **141**, 3731-3736.
163. C. Zheng, W. Shao, S. K. Paidi, B. Han, T. Fu, D. Wu, L. Bi, W. Xu, Z. Fan and I. Barman, *Nanoscale*, 2015, **7**, 16960-16968.
164. J.-F. Li, A. Rudnev, Y. Fu, N. Bodappa and T. Wandlowski, *ACS Nano*, 2013, **7**, 8940-8952.
165. S. Hy, F. Felix, J. Rick, W.-N. Su and B. J. Hwang, *J. Am. Chem. Soc.*, 2014, **136**, 999-1007.
166. S. Hy, Felix, Y.-H. Chen, J.-y. Liu, J. Rick and B.-J. Hwang, *J. Power Sources*, 2014, **256**, 324-328.
167. S. L. Guan, O. Donovan-Sheppard, C. Reece, D. J. Willock, A. J. Wain and G. A. Attard, *ACS Catal.*, 2016, **6**, 1822-1832.
168. J. O. M. Bockris and S. U. M. Khan, *Surface Electrochemistry: A Molecular Level Approach*, Springer US, 2013.
169. J. Clavilier, A. Rodes, K. Elachi and M. A. Zamakhchari, *J. Chim. Phys. Phys.-Chim. Biol.*, 1991, **88**, 1291-1337.
170. G. A. Attard, A. Brew, K. Hunter, J. Sharman and E. Wright, *Phys. Chem. Chem. Phys.*, 2014, **16**, 13689-13698.
171. O. A. Hazzazi, G. A. Attard, P. B. Wells, F. J. Vidal-Iglesias and M. Casadesus, *J. Electroan. Chem.*, 2009, **625**, 123-130.
172. G. Tremiliosi-Filho, H. Kim, W. Chrzanowski, A. Wieckowski, B. Grzybowska and P. Kulesza, *J. Electroan. Chem.*, 1999, **467**, 143-156.

173. J. A. Schoeffel and A. T. Hubbard, *Anal. Chem.*, 1977, **49**, 2330-2336.
174. J. Clavilier, R. Faure, G. Guinet and R. Durand, *J. Electroan. Chem.*, 1980, **107**, 205-209.
175. Hamelin, *Modern Aspects of Electrochemistry*, Plenum Press, New York 1985.
176. L. A. Kibler, University of Ulm, 2003. PhD Thesis.
177. M. J. Buerger, 1963. PhD Thesis.
178. O. Hazzazi, PhD, University of Cardiff, 2003. PhD Thesis.
179. G. Attard and C. Barnes, *Surfaces* Oxford University Press, 1998.
180. G. A. Somorjai and Y. Li, *Introduction to Surface Chemistry and Catalysis*, John Wiley & Sons, 2010.
181. P. Atkins and J. De Paula, *Atkins' Physical Chemistry*, Oxford University Press, Oxford, 10th edn., 2014.
182. J. Clavilier, D. Armand, S. G. Sun and M. Petit, *J. Electroan. Chem. Interfacial Electrochem.*, 1986, **205**, 267-277.
183. J. Clavilier, D. Armand and B. L. Wu, *J. Electroan. Chem. Interfacial Electrochem.*, 1982, **135**, 159-166.
184. M. P. Sumino and S. Shibata, *J. Electroan. Chem.*, 1992, **322**, 391-397.
185. J. Clavilier, R. Durand, G. Guinet and R. Faure, *J. Electroan. Chem. Interfacial Electrochem.*, 1981, **127**, 281-287.
186. J. Clavilier, R. Faure, G. Guinet and R. Durand, *J. Electroan. Chem. Interfacial Electrochem.*, 1980, **107**, 205-209.
187. J. Clavilier, *J. Electroan. Chem. Interfacial Electrochem.*, 1980, **107**, 211-216.

188. J. A. Santana, C. R. Cabrera and Y. Ishikawa, *Phys. Chem. Chem. Phys.*, 2010, **12**, 9526-9534.
189. D. A. Scherson and D. M. Kolb, *J. Electroan. Chem. Interfacial Electrochem.*, 1984, **176**, 353-357.

Chapter 2

Experimental and Theory

2.1 Glove box setup

A large part of this thesis focuses on non-aqueous electrolyte systems for M-O₂ batteries. This implies very dry and inert conditions were required for experimental setup. In order to achieve these stringent conditions, an argon filled glove box with water content < 0.1 ppm and O₂ < 0.1 ppm was used. All chemicals and electrolytes were stored and prepared inside the glove box. Voltammetry experiments were also carried out inside the glove box to prevent moisture or contamination from the atmosphere.

The glovebox was equipped with both oxygen and argon gas lines for purging and bubbling of the electrolytes through specifically designed electrochemical cells whilst not contaminating the glove box atmosphere.

2.2 Drying of gases

Argon and oxygen gas bottles were purchased from BOC gases up to N5 purity (99.999% purity). However, the gas lines were naturally still wet in electrochemical terms, leading to solvents with 50-100 ppm H₂O content after gas purging. In order to overcome this, a drying system was created, which used phosphorous pentoxide (P₂O₅) as a drying agent. P₂O₅ was particularly useful as an increase in H₂O content could be visually observed by a colour change in the P₂O₅ powder. After bubbling of argon and oxygen through electrolytes the H₂O content could be controlled to < 20 ppm, measured using a Karl Fischer coulombic titrator.

2.3 Purification and drying of solvents and chemicals

The water content and purity of the solvents, salts, and other reagents involved in this thesis was of primary concern. The reaction mechanisms are very sensitive to any form of contaminant, creating side reactions and unwanted degradation products. To overcome this, all salts were dried overnight under vacuum before being stored in an argon filled glove box.

The majority of solvents used in this thesis were dried and purified by distillation,¹ they were then stored in the glove box over molecular sieves. This allowed for H₂O contents down to < 20 ppm.

2.4. Karl Fischer measurements

A Karl Fischer coulometric titrator was used to measure the H₂O content of electrolyte samples with accuracy down to < 10 ppm. The apparatus used hydranal AD as the titrating reagent. The titrator was calibrated monthly to maintain accurate readings.

The Karl Fischer titrator calculates the H₂O content by measuring the simultaneous stoichiometric reaction of H₂O and I₂, as well as SO₃ and AOH (**Eq. 2.1 and 2.2**). The I₂ is produced by electrolysis, therefore the amount of electricity needed to produce enough I₂ to consume the H₂O, quantitatively determines the H₂O content in the electrolyte.²



Karl Fischer measurements were carried out using a 1 ml sample with a corresponding density. This was appropriate for most samples, as the density of the

solvent could be used, taking into account that the addition of a salt has a very minor influence on the density of the sample. Any samples where a known density was not available were tested by weight/volume.

2.5. Cleaning of glassware

Most of the experiments carried out in this thesis required ultra-clean conditions; any slight contaminant will interfere with the experimental results. This is particularly important in SHIN's synthesis, where impurities will inhibit uniform shell growth or aid aggregation of nanoparticles. Contaminants will also affect electrochemical measurements, in particular single crystal surfaces.

All glassware and PTFE cells, including new apparatus were soaked in fresh piranha solution (volume ratio, 5H₂SO₄: 1H₂O₂) overnight prior to use. Care must be taken when handling this solution as it heats up very quickly. The glassware was then rinsed thoroughly in Milli-Q water and boiled 3 times in Milli-Q water to remove any excess sulphate groups. After boiling, the glassware was rinsed multiple times (Milli-Q water) and stored in Milli-Q water prior to use.

Glassware involved in SHINs synthesis will develop silica contaminants after multiple uses, the silica can be removed by soaking in HF for 5-10 minutes but care must be taken as glassware can become weak after multiple HF washes. Changing glassware every 6 months is recommended to allow reproducible SHIN production.

2.6. Cyclic voltammetry

Cyclic voltammetry (CV) is a technique used for studying the electrochemistry of a system. CV measures the changes in current of a system in relation to potential, controlled via a potentiostat (**Fig. 2.1b**). A potential is applied and swept to a maximum voltage and reversed back to the initial voltage (**Fig. 2.1a**). The rate at which the potential is swept between the initial and final potentials is known as the sweep rate (**Eq. 2.3**).³

$$v = \frac{\Delta E}{t} \quad (\text{Eq. 2.3})$$

v = sweep rate (V s^{-1}), t = time (s), ΔE = potential step size (V)

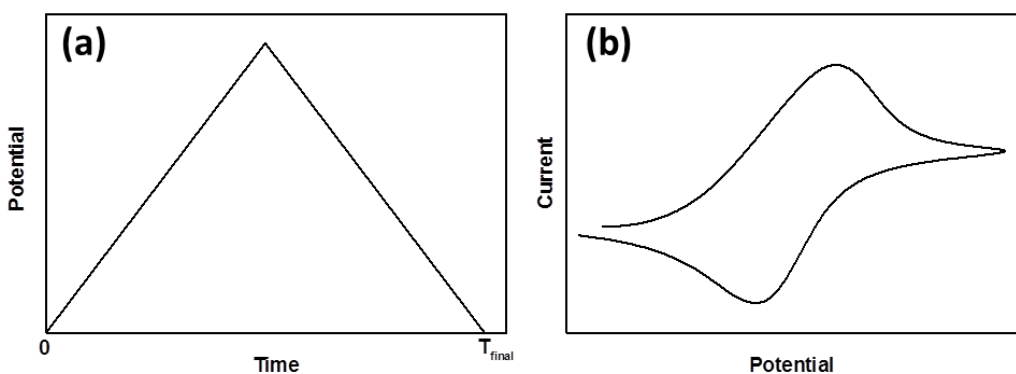


Figure 2.1 (a) Potential response in relation to time for a cyclic voltammogram, (b) current response in relation to potential for a cyclic voltammogram.

The notable current responses indicate the potentials at which electrochemical reactions are taking place, i.e. when a large enough overpotential is applied from the open circuit potential (OCP), the electrochemical oxidation, or reduction of a species via charge transfer at the electrode interface will occur (**Eq. 2.4**).⁴



O is the oxidised species, R is the reduced species.

Electron transfer within the double layer region occurs via either an outer sphere, or inner sphere mechanism (**Fig. 2.2**).⁵ In an outer sphere mechanism the coordination/solvation shell is intact, therefore transfer of electrons occurs via tunnelling in solution.⁶ Inner sphere electron transfer occurs directly at the electrode interface, within the inner Helmholtz layer (**Fig. 2.2**).

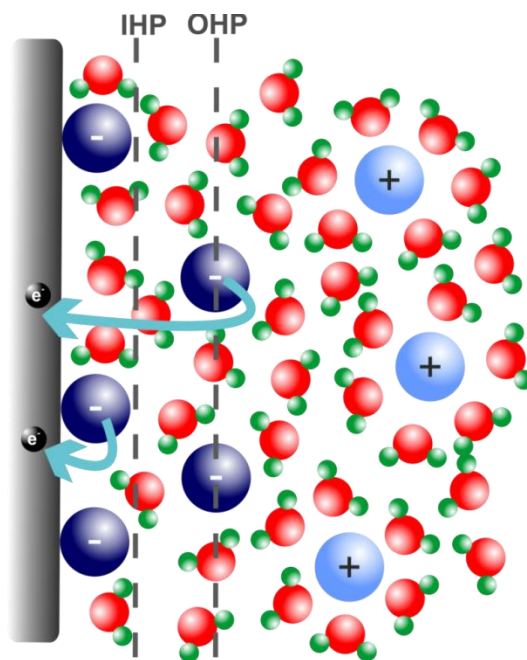


Figure 2.2 Schematic of the electrode-electrolyte interface, demonstrating the double layer and outer and inner sphere electron transfer.

The practical, simplistic nature of this technique promotes it as a popular initial tool to investigate unknown electrochemical properties at the interface. Cyclic voltammetry can provide information on the reversibility of the redox species, as well as kinetic and thermodynamic properties, as the electrochemical response is sensitive to the concentration of reactants, electrode composition and sweep rate.

2.6.1 iR drop

The ohmic drop (iR drop) is a drop in potential between working and reference electrodes.⁷ This potential drop is a result of increased resistance from poor electrolyte conductivity, large currents and the separation of electrodes. The ohmic drop can be calculated from **Eq. 2.5**. It is important to check the ohmic drop and compensate for the increased resistance, as this may have an effect on the voltammetric response.

$$\Delta E_{ohmic} = iR_{\Omega} \quad (\text{Eq. 2.5})$$

2.6.2 Potentiostat

The Electrochemical experiments conducted in this thesis were done using a Biologic (VSP100 or VMP) potentiostat.

2.6.3 Electrochemical cell

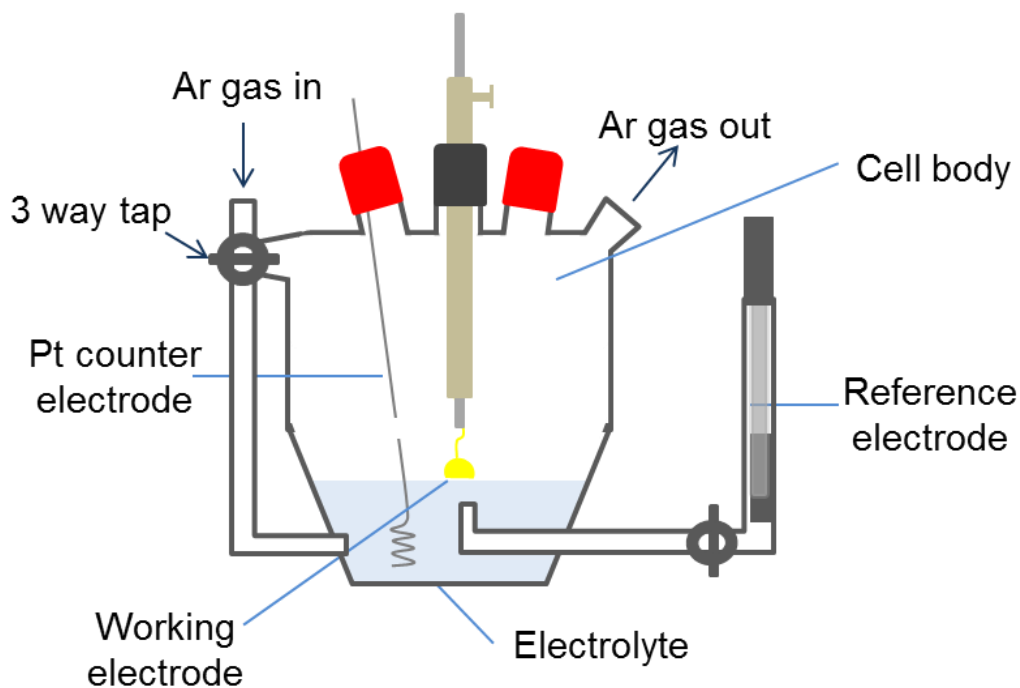


Figure 2.3 Schematic of a 3-electrode glass cell used for the voltammetry experiments in this thesis.

Specifically designed 3 electrode glass cells were used for both polycrystalline and single crystal electrochemical measurements (**Fig. 2.3**). These cells consisted of a gas inlet and outlet for bubbling and purging of electrolyte solutions. The single crystal cell included an extra gas inlet, connected via a three-way tap. This allowed for purging of the electrolyte and for a continuous stream of gas across the electrolyte surface. An adjustable single crystal holder allowed easy translation of the single crystal up and down in the cell, for making a hanging meniscus (**see section 2.6.5.3.6**).

The electrode cell had a luggin style capillary to limit contamination from the reference electrode, and to provide a constant distance between reference and working electrodes to minimise the ohmic drop.³

2.6.4 Reference electrode

The choice of reference electrode can vary depending on a number of factors, i.e. aqueous or non-aqueous media. A good reference electrode must have a stable potential with varying current in order to accurately regulate the potential at the working electrode.⁴

2.6.4.1 Aqueous electrolytes

A Pd/H electrode was used for the majority of aqueous experiments conducted in this thesis. The reference electrode was composed of a platinum wire sealed in a glass tube and a Pd wire welded to the Pt just below the glass tube. The electrode was cleaned using acidified potassium permanganate (KMNO_4), followed by annealing to an orange colour to remove any impurities.⁸ The electrode was charged either by bubbling hydrogen over the wire or placing in a dilute solution of H_2SO_4 and electrochemically

evolving hydrogen. Both procedures were carried out for 40 minutes to produce a β -hydride phase that was stable for \sim 4-5 hours.⁸

The palladium hydride was chosen as it is relatively easy to maintain and does not add any unwanted contaminants to the electrolyte solution, which may occur from alternative reference electrodes e.g. Ag/AgCl.

2.6.4.2 Non-aqueous electrolytes

It is important that the composition of the reference electrode must not have an impact on the electrochemistry. Therefore, for non-aqueous systems it is not suitable to use a common aqueous reference electrode, e.g. Ag/AgCl as it contains an aqueous filling solution, which will contaminate the electrolyte. Other options for non-aqueous systems include the palladium hydride electrolyte. This is also not feasible as hydrogen contamination will poison the aprotic reaction systems that are being studied.

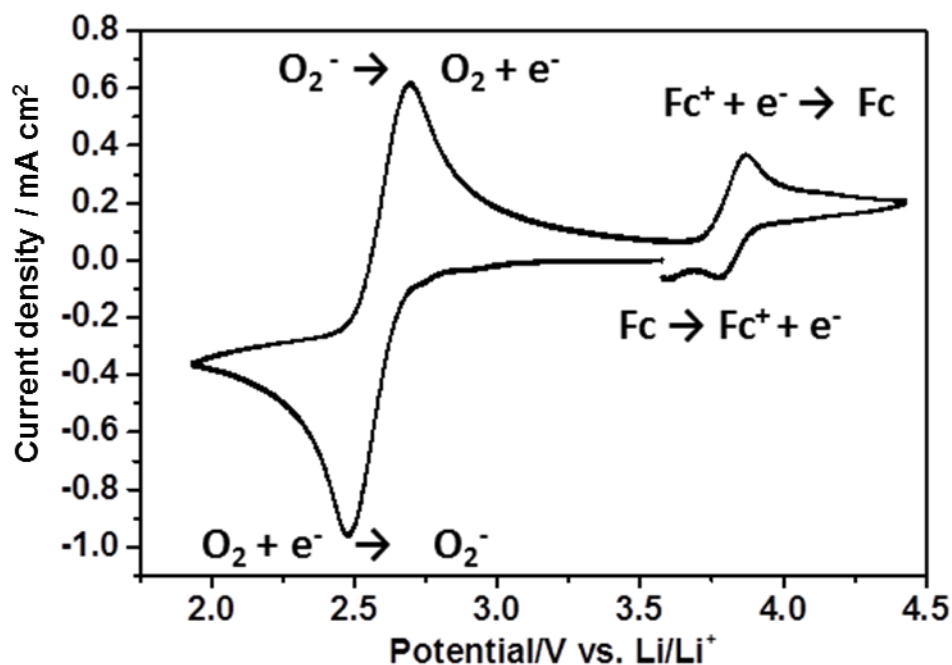


Figure 2.4 Cyclic voltammogram of the O₂/O₂⁻ and Fc/Fc⁺ redox couples in 0.1 M TBAOTF/DMSO

A silver wire was used as a pseudo reference electrode for the non-aqueous experiments. The Ag/Ag⁺ couple is an effective reference electrode, however from solvent to solvent and between experiments the reference potential can shift. A known redox couple, such as ferrocene/ferrocenium (Fc/Fc⁺) is required as an internal standard to calibrate the reference potential to enable accurate comparisons between experiments (**Fig. 2.4**). The potentials can then be calibrated against the Na or Li couple using the standard reduction potentials (**Table 2.1**).³

Table 2.1 Standard reference potentials vs. SHE (standard hydrogen electrode).³

Reaction	Standard electrode Potential (E ⁰) / V vs. SHE	Solvent
Li ⁺ + e ⁻ ↔ Li	-3.045	N/A
Na ⁺ + e ⁻ ↔ Na	-2.971	N/A
K ⁺ + e ⁻ ↔ K	-2.931	N/A
AgCl + e ⁻ ↔ Ag + Cl ⁻	+ 0.222	N/A
Pd/H	+ 0.05	N/A
Fc ⁺ + e ⁻ ↔ Fc	+ 0.69	MeCN
Fc ⁺ + e ⁻ ↔ Fc	+ 0.68	DMSO
Fc ⁺ + e ⁻ ↔ Fc	+ 0.40	H ₂ O

2.6.5 Working electrode

The working electrodes used in this thesis were either polycrystalline disc electrodes, single crystals or composite electrodes, the synthesis and cleaning procedures for which have been described below.

2.6.5.1 Polycrystalline electrodes

Polycrystalline electrodes were purchased from BASI, with either a 3 mm diameter or 1.6 mm diameter. Prior to experiments the electrodes were washed in acetone and Milli-Q water and sonicated before drying in a vacuum oven overnight. A similar procedure was followed after experiments. The electrodes were washed and sonicated; the electrodes were also polished with varying degrees of alumina suspension down to 0.05 mm to provide a smooth surface.

2.6.5.2 Composite electrodes

Arrays of composite electrodes, with varying compositions and characteristics have been used in this thesis. The majority of cathodes consisted of a free-standing film of carbon black (Super C65, IMERYS) prepared by mixing the powder with PTFE binder (polytetrafluoroethylene, Sigma Aldrich) in a 70:30 weight ratio in ethanol (stated if different). The resulting 'putty' mixture after ethanol evaporation was passed through a calendaring machine to obtain a thin, free-standing film and then cut into 8 mm diameter electrodes. Similarly, cathodes were synthesised from a slurry consisting of active carbon material, Kynar, carboxymethyl cellulose (CMC) or polytetrafluoroethylene (PTFE) and n-methyl-2-pyrrolidone (NMP). The slurry was sonicated and then cast onto aluminium or copper foil and cut into electrodes.

2.6.5.3 Single crystal electrodes

In this thesis, single crystals of varying materials and facets have been used. Unless otherwise stated the crystals used were synthesised using the Clavilier half bead method,⁹ as described below.

2.6.5.3.1 Forming a full bead single crystal

To synthesise a half bead single crystal a 0.5-1 mm diameter wire of the required metal with purity (99.999%) was carefully melted at one end using a propane/ oxygen flame. Melting the wire at one end produces a small bead, which will grow in size upon further melting. Care must be taken to grow this bead slowly. Between each growth in bead size, aqua regia and water can be used to remove impurities from the single crystal by etching. When the bead is around 2-3 mm in diameter (any bigger and the bead will likely be too heavy and drop off), carefully anneal the crystal bead, maintaining a solid-liquid interface in the bead (a visible line should be observed, **Fig. 2.5**). This should be held for at least 2 minutes. If the bead cools from liquid to solid in a smooth symmetric fashion from top to bottom this is a good indication of single crystal production. Once cooled upon close inspection of the bead, facets should be visible to eye (or under a magnifying glass). These facets correspond to (111) and (100) planes on all metals (some metals need to be prepared under argon to avoid oxidation), which using the goniometer and a laser source can be aligned to produce single crystals of the desired planes.

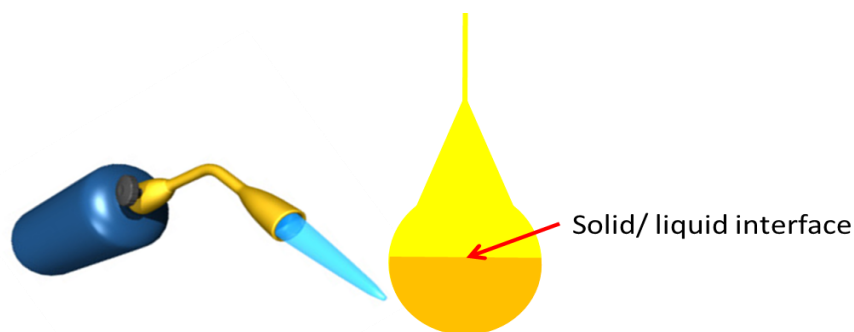


Figure 2.5 Solid/liquid boundary when synthesising a single crystal.

It is quite common for the wire to contain impurities within it, which can translate to contaminants in the crystal bead. At this point it is possible to chemically etch the bead in order to remove/reduce the levels of impurities. The bead can be etched by undergoing cycles of annealing, dipping in HF followed by water. This is repeated around 20 times. This procedure can be applied again once the half bead is formed if impurities are visible in the electrochemistry.

2.6.5.3.2 Selecting a crystal facet

Prior to selecting the single crystal facet, the crystal needs to be mounted onto the goniometer (**Fig. 2.6**), this is achieved by melting paraffin wax in the single crystal holder and allowing it to solidify, securing the single crystal in place.

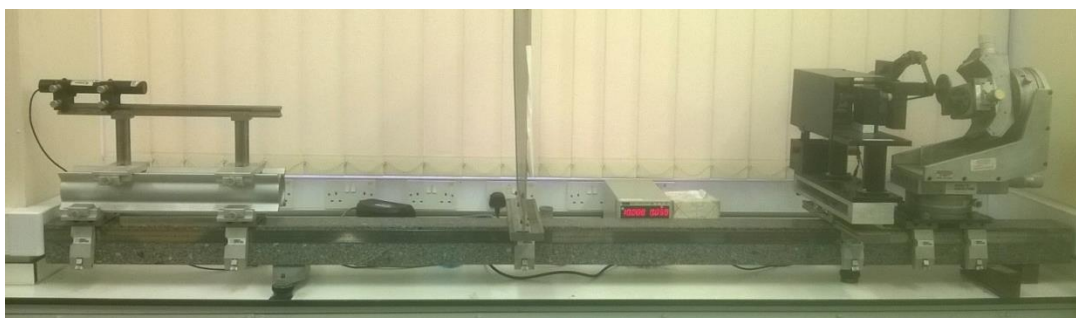


Figure 2.6 Picture of Single crystal alignment and polishing set up.

Selecting the desired crystal facet is achieved using a He-Ne laser, which is aligned onto the single crystal bead. The bead has (111) and (100) facets visible. The (111) planes are portrayed by much brighter and circular reflection spots, compared to the (100) spots, which are fainter and more rectangular in nature. To check the quality of the single crystal the angle between the (111) and (100) facets in the same plane should be 54.45° . Calculating the angles relative to these planes using the goniometer allows for cutting of the crystal to the desired facet of choice (**Fig. 2.7**).⁸

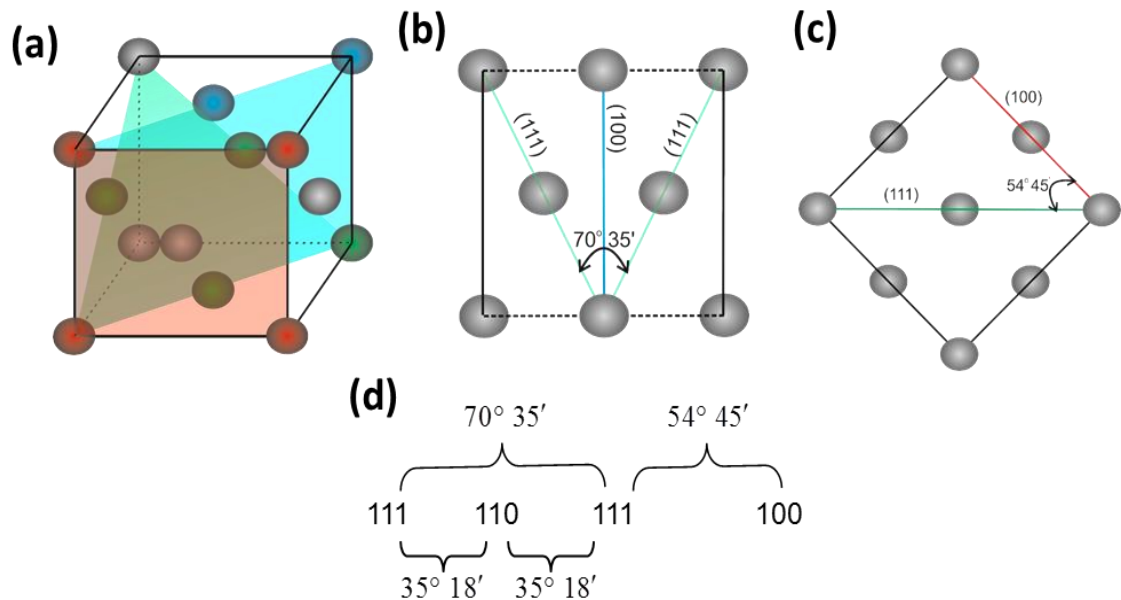


Figure 2.7 Schemes demonstrating angles required to identify single crystal facets, (a) cube showing the (111) green, (110) blue, (100) red facets. (b) plane cut to show angle between (111) and (100) facets. (c) cube cut along plane to show angle between (111) and (100) facets. (d) summation of angles between the (111), (100) and (110) planes, recreated from Hazzazi.⁸

2.6.5.3.3 Grinding the single crystal bead

Once the crystal has been correctly aligned using the laser and goniometer as described previously, the full bead crystal needs to be ground down to form a half bead. The crystal was held in place using quick drying epoxy resin. First epoxy resin is placed around the back of the crystal and left to dry to hold it in place. The alignment of the crystal is checked again before a further coating of epoxy is placed over the front of the crystal to secure the desired facet in the correct orientation (**Fig. 2.8**) (It is important to measure the diameter of the crystal bead prior to grinding).

An “800 grit” carborundum (Buehler) pad was attached to the grinding wheel. Grinding was carried out on the bead for around 30 minutes, whilst constantly being lubricated with distilled water. The crystal will be ground down quite quickly with this level of grinding pad, therefore care must be taken to avoid over grinding the crystal. Checking the crystal diameter every 5-10 minutes is recommended. Continue grinding until the epoxy is completely removed and the single crystal surface is exposed. At this point swap to a “1200 grit” carborundum pad and continue grinding, again keep lubricated with distilled water. Check the grinding every 15 minutes, continue to grind until the crystal diameter starts to decrease. The length of time for this step varies depending on the bead material, so regular checks are required to prevent grinding the whole crystal away. At this point the crystal will look rough with lots of visible scratches and scuffs; polishing is required to produce a mirror finish.

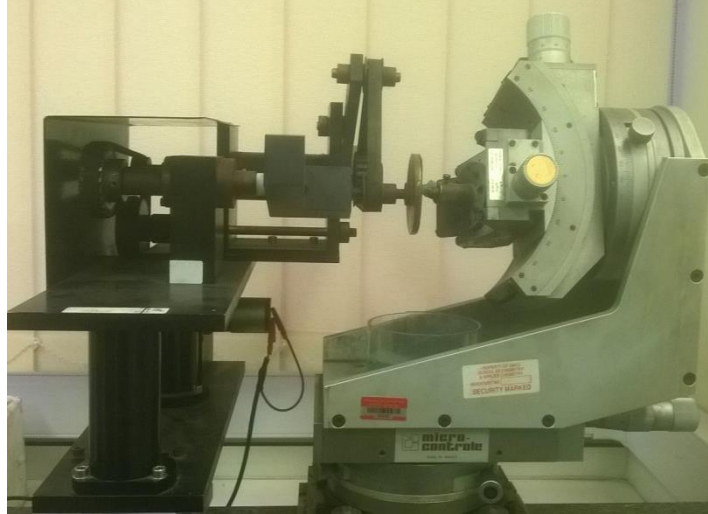


Figure 2.8 Picture of single crystal on the goniometer being ground down to a half bead crystal.

2.6.5.3.4 Polishing the half bead crystal

Polishing the single crystal applies the same principle as grinding, however the grit of the pad is less severe, so decrease in the size of the crystal diameter will be negligible. Place a “2400 grit” pad on the polishing wheel and polish for approx. 2 hours, lubricating with distilled water every 5-10 minutes. Repeat the procedure again with a “4000 grit” pad. Most large scratches should be removed from the crystal surface; small scratches may still be visible but should be of reasonably equal roughness. If this is not the case continue to polish with “4000 grit” until this is achieved.

The next step is to switch to a textmet polishing pad (Buehler); this multistep procedure with different polishing pastes produces a mirror finish on the crystal face. Firstly use a 3 μm diamond spray with blue lubricant for around 2 hours. This is followed by a new pad with 1 μm diamond spray with blue lubricant once again. Finally, use a $\frac{1}{4}$ mm diamond spray with red lubricant. These steps are done for roughly an hour each. The quality of the mirror finish can be checked with a magnifying glass or

more precisely with the He-Ne laser. The smoother the surface the sharper the reflection spots will be. This should be apparent if checked between each step.

Once a mirror finish is achieved the crystal holder can be removed from the goniometer and left in dichloromethane (DCM) overnight, this should dissolve the epoxy resin and paraffin wax, allowing the crystal to be removed from the holder.

The crystal can then be rinsed and annealed multiple times, or for a prolonged time depending on the surface, forming an ordered surface. The quality of the crystal can be checked by its electrochemistry (**Fig. 2.9**). In some cases, impurities may be present; impurities can diffuse from the bulk to the surface upon cycling. This was the case, in **Fig 2.9a** where a surface bound redox couple (0.2-0.5 V) was present on the Au(100) surface. Repeating the etching procedure described above in HF should remove any impurities (e.g. silicates) coming out of the bulk (**Fig. 2.9**).

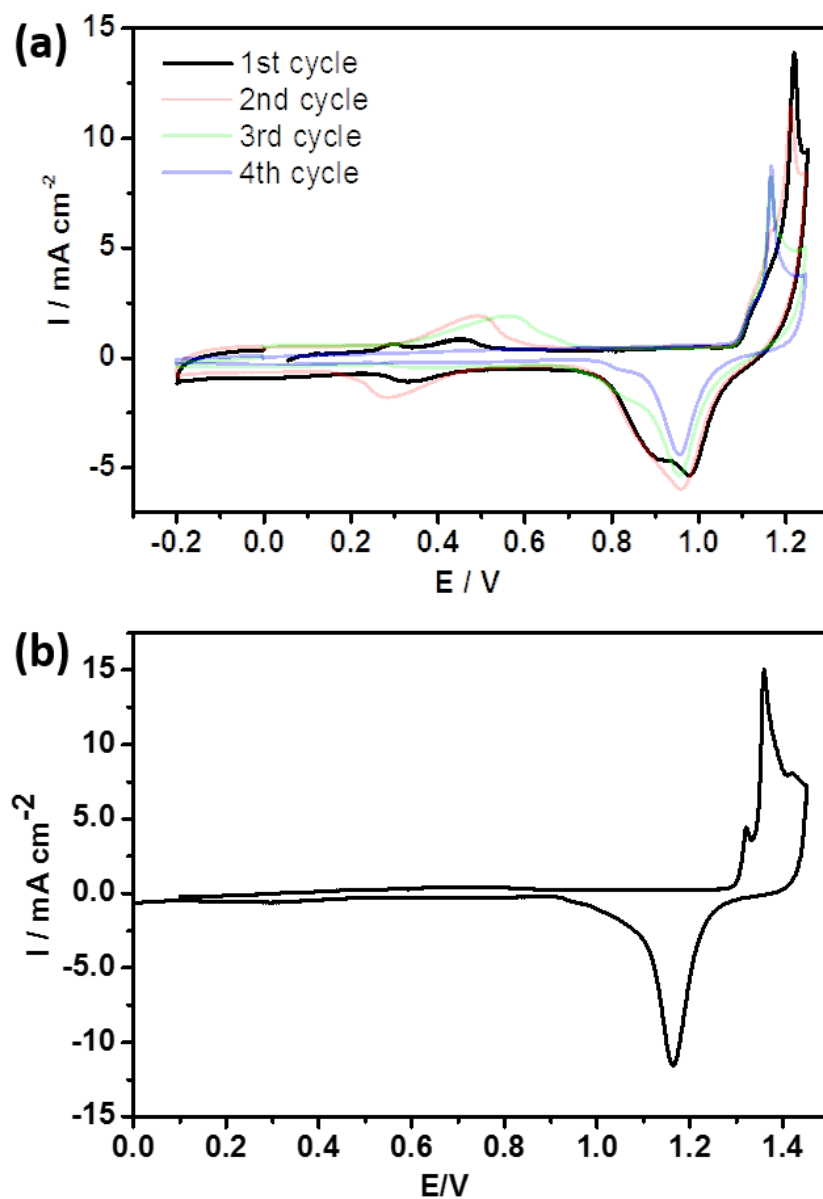


Figure 2.9 (a) CV's of Au(100) in 0.1 M H₂SO₄ with impurities coming out the bulk with increasing cycling, (b) CV of Au(100) after being etched in HF, showing impurity free CV, with the oxidation of gold surface around 1.3 V and the reduction of gold oxide at 1.2 V.

2.6.5.3.5 Annealing

In order to produce a well ordered clean single crystal facet, the crystals were heated to a yellow/orange colour in a butane flame which removed the majority of organic impurities from the electrode surface. Au crystals can be cooled in air or an argon environment. Other crystals such as Pt required cooling in CO and hydrogen to produce a clean ordered surface. The crystal must be allowed to cool before making contact with the electrolyte or water. If the crystal is too hot when contact is made, quenching of the crystal will occur. This causes bulk deformation of the crystal, causing the crystal to become polycrystalline in nature.¹⁰

Many single crystal experiments were conducted inside a glove box to prevent contamination from air and moisture. The normal annealing procedure cannot however be conducted inside the glove box; annealing outside, and then transferring into the glove box negates the initial annealing procedure as the surface becomes contaminated. A water droplet could not be used to protect the surface either, as it contaminated the dry electrolyte. The solution was to anneal outside the glove box and cool in a sealable vessel containing argon. The crystal was enclosed in the sealed argon cell and then transferred into the glove box minimising contamination. This was sufficient for gold surfaces; however, a more complex procedure was employed for platinum and other more sensitive metal surfaces.

Platinum surfaces were prepared using a multistep procedure; the crystal was annealed in a butane flame and cooled in CO. Once cool, the crystal was protected with a droplet of water. The crystal was then dipped in a 1 mM solution of sodium bromide (NaBr), to protect the crystal surface. The crystal was then dried in the glove box

chamber before use. This produced well-ordered dry platinum surfaces. **2.6.5.3.6**

2.6.5.3.6 Hanging meniscus (single crystal)

To perform accurate electrochemistry with a single crystal electrode, a hanging meniscus needs to be formed (**Fig. 2.10**), this prevents any signal being taken from the sides or the back of the crystal. This is important as only the face of the crystal has the desired facet. The experiments are carried out in a flow of argon to dry the sides of the crystal after the meniscus has been formed.

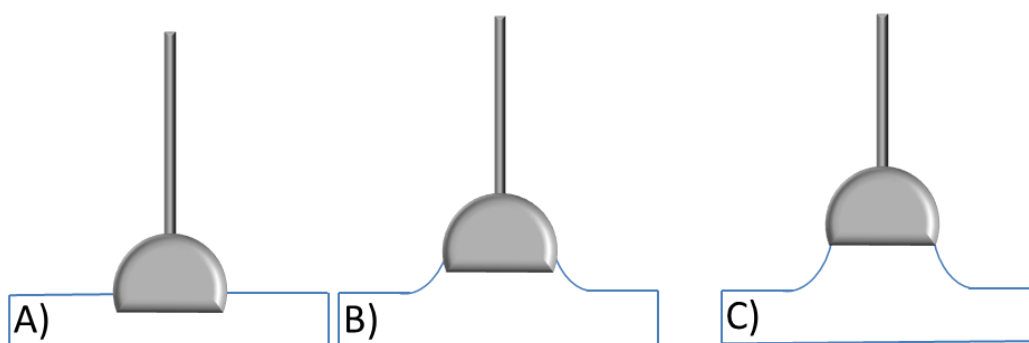


Figure 2.10 Schematic of (a) no hanging meniscus, the electrode is submerged in electrolyte, therefore the sides and back of the crystal will contribute to the electrochemistry, which are not of the desired facet. (b) poor hanging meniscus, electrolyte touching the sides of the crystal. (c) an ideal hanging meniscus, electrolyte is only in contact with the desired facet.

2.6.5.3.7 Removal of SHINs from single crystals surfaces

The synthesis and use of SHINs on electrode surfaces will be discussed in the next chapter. In relation to single crystal surfaces if SHINs are deposited onto the electrode surface it is imperative that they are removed before the crystal is annealed. If a crystal is annealed with SHINs on the surface, it will cause the SHINs to be embedded into the crystal bulk during reconstruction. This causes serious problems within the crystal bulk and requires extensive grinding and polishing to recover the desired facet.

Electrochemical etching can be used to remove the SHINs from the electrode surface. This requires the use of 0.1 M H₂SO₄ and 1 M HCl at 5 V and - 0.2 V followed by electrochemical polishing to remove the SHINs and recover the electrode surface.

2.6.5.3.8 Calculating surface area and surface coverages

The electrochemical surface area of the single crystal electrodes were calculated using the CVs of 0.1 M H₂SO₄ on the different facets. The area can then be calculated by subtracting the double layer charge and integrating the hydrogen underpotential deposition (HUPD) region.^{11, 12}

The fractional surface coverage for a 1 e⁻ transfer mechanism can be calculated from the charge (area under peak, in microcoulombs per cm²) of the peak of interest. The charge is then divided by the charge for a monolayer coverage (~ 240 μC cm⁻² for Pt(111), 210 μC cm⁻² for Pt(100) and 150 μC cm⁻² for Pt(110)).^{13, 14}

2.7 Raman spectroscopy

Raman spectroscopy is a type of optical vibration spectroscopy, for a vibrational mode of a molecule to be Raman active, a change in the polarisability of the molecule must occur. Polarisation and a dipole moment are created when the molecule is present in an electric field, pushing the electrons in the molecule away from the nuclei. The polarisation is directly related to the strength of the electric field.¹⁵

2.7.1 Spectrometer

Raman experiments were carried out on Renishaw In-Via Raman spectrometers with either an inverted or normal confocal microscope. Either a 633 nm or 785 nm wavelength laser was used for the majority of the experiments.

2.7.2 Raman Cells

Raman experiments were conducted in a variety of specifically designed glass and PTFE cells with either a sapphire window on the top or bottom of the cell to accommodate for a normal or inverted laser alignment. Only sapphire or quartz can be used as the optical window, as they have no optical effect on the Raman bands, unlike normal glass, which can be seen to have a large band around 1500 cm^{-1} .

The polycrystalline cell consisted of a three-electrode design with gas inlet and outlet, to allow purging and bubbling of the electrolyte (**Fig. 2.11a**). The cell could then be sealed and transferred to the Raman spectrometer. A sapphire window was screwed onto the bottom of the cell (**Fig. 2.11b**) to allow the sample to be exposed to the inverted laser.

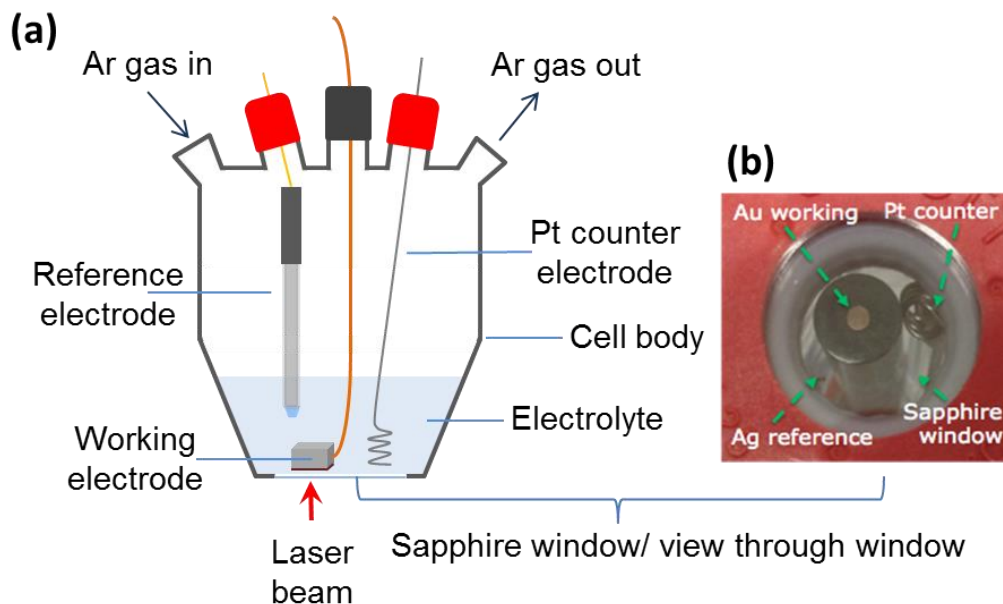


Figure 2.11 (a) Schematic of composite and polycrystalline working electrode Raman cell, (b) bottom up view of polycrystalline Raman cell through the sapphire window.

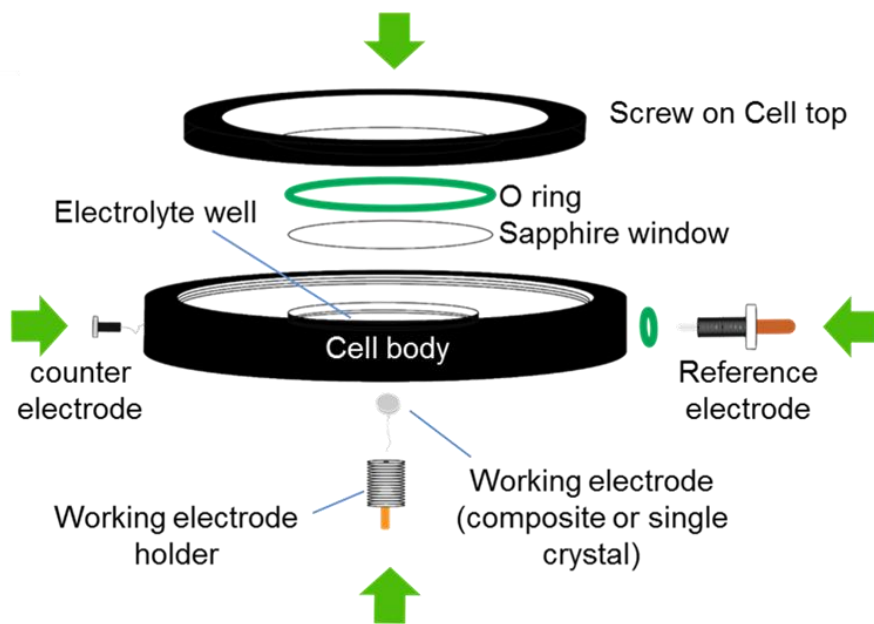


Figure 2.12 Schematic of the single crystal Raman cell.

The single crystal cell was supplied by the Li group in Xiamen. It consisted of a PTFE upper and lower section, which can be screwed into the top section. It has a three-electrode design and inlets and outlets for filling with electrolyte (**Fig. 2.12**). The single crystal was inserted from the bottom and can be adjusted to a fixed height below the window, by measuring the distance between window and surface focal points.

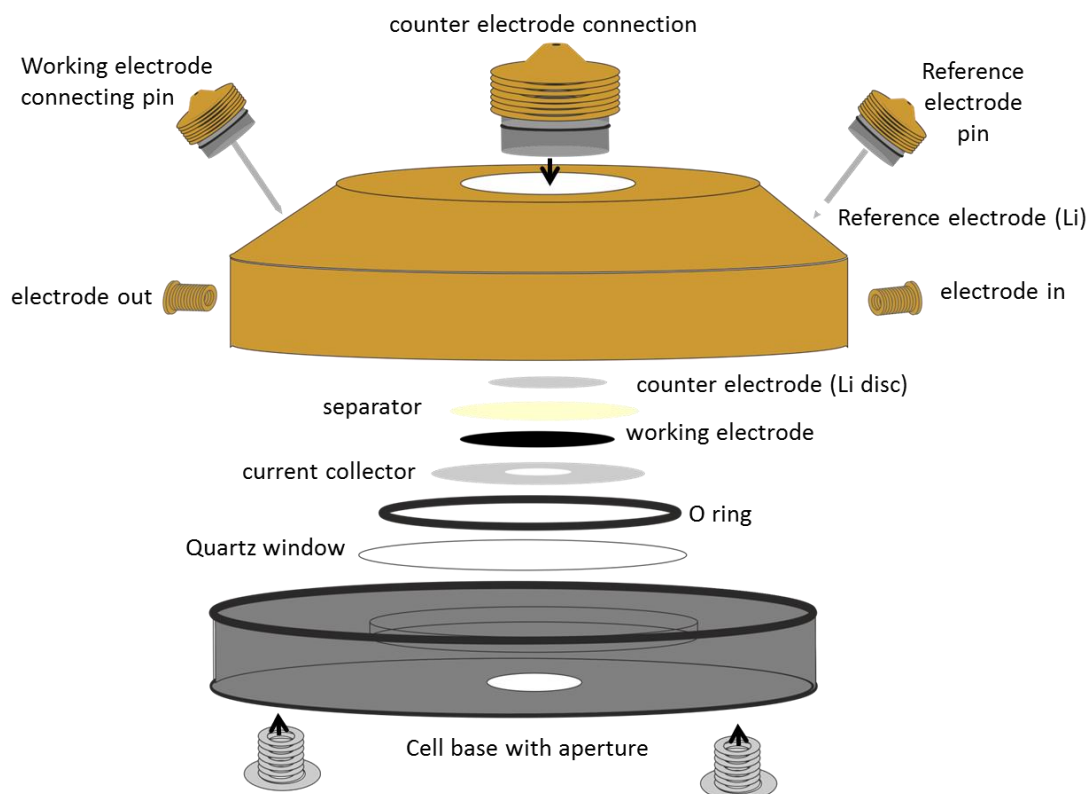


Figure 2.13 Schematic of the composite electrode cell.

The composite electrode cell (**Fig. 2.13**), consisted of a PEEK (Polyether ether ketone) upper section and stainless steel bottom which could be screwed together to encompass the working and counter electrodes. This cell setup could be modified depending on the purpose. The arrangement of the electrodes could be varied with a two

or 3 electrode setup possible. This cell could not be cleaned in acid prior to use, instead multiple sonications in ethanol and water was used.

2.7 Surface enhanced Raman spectroscopy (SERS)

SERS active gold surfaces were prepared by roughening polycrystalline gold electrodes to produce a uniform nanostructured surface. The electrodes were roughened using methods previously described by the Gewirth^{16, 17} and Tian groups.¹⁸ Multiple oxidation reduction cycles in 0.1 M KCl (**Fig. 2.14**) were used to roughen the surface.^{19, 20} The following steps described below highlight the phenomenon observed voltametrically in **Fig. 2.14**. The initial negative reduction potential strips the surface of Au and forms $[\text{AuCl}_4]^-$ complexes under extreme conditions ensuring roughening across the surface.^{19,20} By then applying 25 oxidation-reduction cycles between + 4.6 V and 3.2 V vs. Li/Li^+ it strips and deposits Au onto the surface sequentially. Aldous conducted a study, determining the optimum cycle number to be 25.²¹ This is due to the uneven roughening of the surface, 25 cycles produces the most uniform distribution of enhancement across the surface. At lower potentials Cl^- is desorbed before being absorbed between 3.5 and 4.1 V vs. Li/Li^+ . At this stage you form AuCl_4^- and AuCl_2^- . As the potential further increases Au is oxidised to Au^{3+} . Upon the reverse sweep the stripped gold complexes are plated back onto the surface as shown by the CV in **Fig. 2.14** as a broad reduction feature at 3.8 V vs. Li/Li^+ . The cycle completes at 3.2 V vs. Li/Li^+ where any Cl^- is desorbed from the surface. This roughens and nanostructures the Au electrode in a non-uniform way creating the SERS active surface. The inhomogeneous roughening by this method means cycling is crucial to produce as even a nanostructure as possible, thus providing a greater average enhancement as opposed to

small ‘hotspot’ areas. Sequentially applying a negative step at the end of the cycle decreases the amount of adsorbed gold chloride at the interface, which may change and interfere with SERS measurements or in this case possibly take part in the reaction.

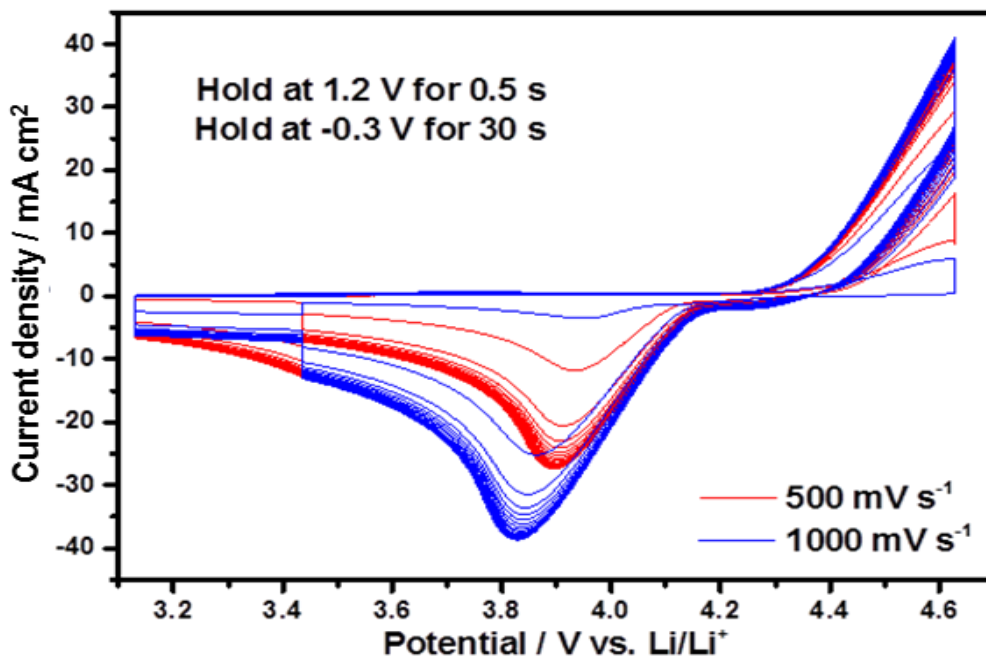


Figure 2.14 Cyclic voltammogram of the oxygen reduction cycle in 0.1 M KCl used to roughen the gold electrodes.

After the oxidation reduction cycle, a visibly rough surface can be observed, with a slight reddish tint (**Fig. 2.15**). The electrode was then rinsed gently with Milli-Q water taking care not to remove the roughened surface layer. The electrode was then dried under vacuum prior to use.

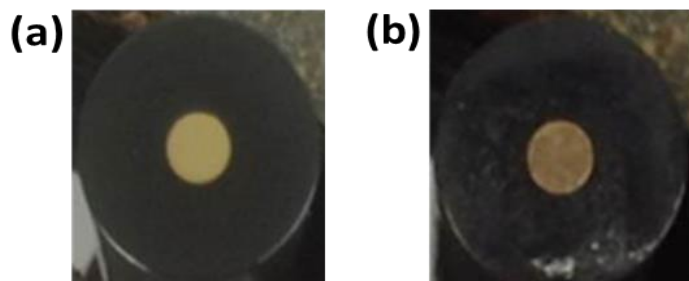


Figure 2.15 Images of a polycrystalline gold electrode **(a)** before roughening, **(b)** after roughening.

2.9 Other techniques used in thesis

TEM – Transmission electron microscope measurements were conducted using a JEOL 3010 microscope.

SEM – All scanning electron microscopy measurements in this thesis were conducted on a JEOL, JSM 7001F microscope, by Filipe Braga.

AFM – All Atomic force microscopy measurements in this thesis were conducted on a Bruker, multimode 8, by Iain Aldous.

UV/Vis – Measurements were conducted on a Shimadzu 2600 spectrometer, by Laura Cabofernandez.

2.10 Useful equations

Stoke Einstein equation

The Stokes Einstein equation (**Eq. 2.6**) can be used to theoretically determine the diffusion constant.²²

$$D = \frac{kT}{6\pi\eta R} \quad (\text{Eq. 2.6})$$

k is the Boltzman constant ($1.38 \times 10^{-23} \text{ J K}^{-1}$), **T** is the temperature (K), **η** is the viscosity of the solvent, **R** is the hydrodynamic radius (i.e. the hypothetical hard sphere radius, this is dependent on the solvent properties, such as solvent size, polarity)

Theoretical specific energy

The specific energy i.e. the energy per unit mass, it can be calculated from the cell voltage (E) and the electrochemical equivalent (Z) (**Eq. 2.7**).

$$\begin{array}{lll} \textit{Specific energy} = \textit{cell voltage} \cdot \textit{electrochemical equivalent} & & (\text{Eq. 2.7}) \\ (Wh kg^{-1}) & (V) & (Ah kg^{-1}) \end{array}$$

The theoretical cell voltage (E) can be calculated from the number of electrons transferred (n) and free enthalpy of formation (ΔG_f) (**Eq. 2.8**).

$$E = \Delta G_f / -nF \quad (\text{Eq. 2.8})$$

The electrochemical equivalent (Z) is the molecular mass (Mr) of material deposited when 1 C (A . s) is passed.²³ Therefore Z can be calculated from the number of electrons transferred (n), faradays constant (the amount of charge (C) carried per 1 mole)²³ and the mass of the materials (molecular mass, Mr) (**Eq. 2.9**). Z can then be converted from (C g⁻¹) to (Ah kg⁻¹).

$$Z = (nF) / M_r \quad (\text{Eq. 2.9})$$

2.11 References

1. W. L. F. Armarego, *Purification of Laboratory Chemicals*, Elsevier Science, 2017.
2. E. Scholz, *Karl Fischer titration: determination of water*, Springer, 1984.
3. C. G. Zoski, *Handbook of Electrochemistry*, Elsevier, 2007.
4. A. J. Bard and L. R. Faulkner, *Electrochemical Methods: Fundamentals and Applications*, 1980.
5. N. M. Markovic, *Nat. Mater.*, 2013, **12**, 101-102.
6. R. Compton and C. Banks, *Understanding Voltammetry*, Imperial College Press, 2nd edn., 2011.
7. W. Oelßner, F. Berthold and U. Guth, *Mater. Corros.*, 2006, **57**, 455-466.
8. O. Hazzazi, PhD, University of Cardiff, 2003.
9. J. Clavilier, R. Faure, G. Guinet and R. Durand, *J. Electroan. Chem.*, 1980, **107**, 205-209.
10. L. A. Kibler, University of Ulm, 2003.
11. D. Chen, Q. Tao, L. W. Liao, S. X. Liu, Y. X. Chen and S. Ye, *Electrocatalysis*, 2011, **2**, 207.
12. G. G. Barna, S. N. Frank and T. H. Teherani, *J. Electrochem. Soc.*, 1982, **129**, 746-749.
13. B. E. Conway and H. Angerstein-Kozłowska, *Acc. Chem. Res.*, 1981, **14**, 49-56.
14. V. Climent and J. M. Feliu, in *Adv. Electrochem. Sci. Eng.*, Wiley-VCH Verlag GmbH & Co. KGaA, 2017, DOI: 10.1002/9783527340934.ch1, pp. 1-57.

15. B. Schrader, in *Infrared and Raman Spectroscopy*, Wiley-VCH Verlag GmbH, 2007, DOI: 10.1002/9783527615438.ch01, pp. 1-5.
16. X. Li, D. Heryadi and A. A. Gewirth, *Langmuir*, 2005, **21**, 9251-9259.
17. X. Li and A. A. Gewirth, *J. Raman. Spec.*, 2005, **36**, 715-724.
18. Z.-Q. Tian, B. Ren and D.-Y. Wu, *J. Phys. Chem. B*, 2002, **106**, 9463-9483.
19. U. Oesch and J. Janata, *Electrochim. Acta*, 1983, **28**, 1247-1253.
20. U. Oesch and J. Janata, *Electrochim. Acta*, 1983, **28**, 1237-1246.
21. I. M. Aldous, PhD Thesis, University of Liverpool, 2016.
22. C. O. Laoire, E. Plichta, M. Hendrickson, S. Mukerjee and K. M. Abraham, *Electrochim. Acta*, 2009, **54**, 6560-6564.
23. R. G. Ehl and A. J. Ihde, *J. Chem. Educ.*, 1954, **31**, 226.

Chapter 3

Shell Isolated Nanoparticles for Enhanced Raman Spectroscopy (SHINERS)

3.1 Abstract

The results and experimental procedures presented in this chapter provide an in depth method for synthesising pinhole free shell isolated nanoparticles with substantial enhancement factors, without contamination.

A detailed set of characterisation tools have also been studied and described to ascertain the quality, i.e size, shape, shell thickness, pinholes, contaminants and enhancement factors of the synthesised nanoparticles.

A study on the distribution of the nanoparticles on the Au surface has also been portrayed, to understand and optimise the distribution of the shell isolated nanoparticles on the electrode surface, in order to provide the maximum enhancement.

3.2 Introduction

Since the discovery of the Raman effect by C. V. Raman in 1928¹, Raman spectroscopy has been an invaluable characterisation technique. However, the Raman signal is inherently weak, with only 1 in 10^7 photons being inelastically scattered (as explained in chapter 1), and this has been a limiting factor in the use of Raman spectroscopy as a technique to study phenomena at substrate surfaces. Since the discovery of surface enhanced Raman spectroscopy (SERS) by Fleischmann and then further work by Van Duyne², there has been a substantial development in enhanced Raman spectroscopy³⁻⁷ with a range of Raman active surfaces (e.g., electrochemically roughened gold and silver surfaces)⁸⁻¹⁰ and techniques (e.g. tip enhanced Raman spectroscopy (TERS)¹¹) having been developed. Until the discovery of SHINERS by Tian¹² this was limited to coinage metals.

SHINs are a type of core shell nanoparticles, consisting of an inner core (gold or silver) surrounded by an ultra-thin, optically transparent outer shell (SiO_2 or Al_2O_3). SHINERS have been a popular choice for enhancing Raman spectroscopy due to a number of factors such as:

- **Synthesis** – Quick procedure for synthesising the particles. They can be synthesised in a fume cupboard and can be easily applied to a surface. However, synthesis is sensitive to glassware contamination and other contaminants.
- **Cost** – Relatively cheap due to low production cost and materials.
- **Stability**¹³ – Addition of silica shell can prolong lifetime of the nanoparticles by preventing aggregation.
- **Tuneable and versatile**¹⁴ – In principle, it can be used on any substrate. In addition, the shape, size, morphology, and material of the particles can be

controlled to optimise the particles for specific requirements (i.e. laser wavelength, surface morphology).

SHINERS has been used for a wide variety of applications since its discovery in 2010¹⁵. They have been used to investigate electrochemical interactions on a multitude of single crystal surfaces, looking at the oxidation of Na₂SO₄ on gold via the hydroxyl intermediate¹⁶. Studies have also been conducted looking at the catalytic hydrogenation on platinum surfaces¹⁷. Recently SHINERS has been used to study the formation of the solid electrolyte interphase (SEI) in anode materials¹⁸, and Li₂O evolution on Li-rich cathodes in lithium-ion batteries¹⁹. The technique has also been applied to fundamental studies for the lithium oxygen battery.²⁰ This array of applications demonstrates the capabilities of SHINERS as well as the possible areas it can be applied to; in particular with regards to studying the reaction mechanisms taking place at the electrode surface in battery systems. However, before SHINs can be used they must first be synthesised and accurately characterised in order to ascertain the quality and purity of the particles.

3.3 Synthesis of shell-isolated nanoparticles (SHINs)

SHINs were synthesised in a similar method to the Tian group¹², with a few modifications to the original synthesis. Before synthesis of SHINs and Au nanoparticles all glassware and other apparatus (i.e. water bottle, stirrer bars) were thoroughly cleaned with piranha solution and boiled to remove any impurities. Ultra-pure Milli-Q water was used for all parts of the synthesis and experiments. The synthesis is broken down into two parts, the initial synthesis of the gold nanoparticles, followed by the coating of the particles with a SiO₂ shell.

3.3.1 Au nanoparticle synthesis (55 nm diameter spheres)

Gold nanoparticles were synthesised using the standard sodium citrate reduction method²¹. A 200ml solution of 0.291 mM HAuClO₄·3H₂O was brought to reflux with vigorous stirring. Once the solution was boiling, 1.4 ml of a 1% trisodium citrate trihydrate solution was added and left to reflux for 40 minutes with vigorous stirring (**Fig. 3.1a-b**). The citrate has a dual function, one is to reduce Au(III) to Au(0)²²⁻²³, and the second as a capping agent to prevent nanoparticle aggregation²⁴. A colour change can be observed from pale yellow to dark blue/purple after approximately 1 minute of citrate solution addition, indicating the start of nucleation and formation of nanoparticles. After 5 minutes the solution should have turned a reddish brown upon complete formation of the nanoparticles. The colour of the nanoparticle solution is an indication of the nanoparticle size and is highly dependent on the ratio of citrate to gold salt²⁵. The dimensions of the gold nanoparticles were verified with TEM (**Fig. 3.3**).

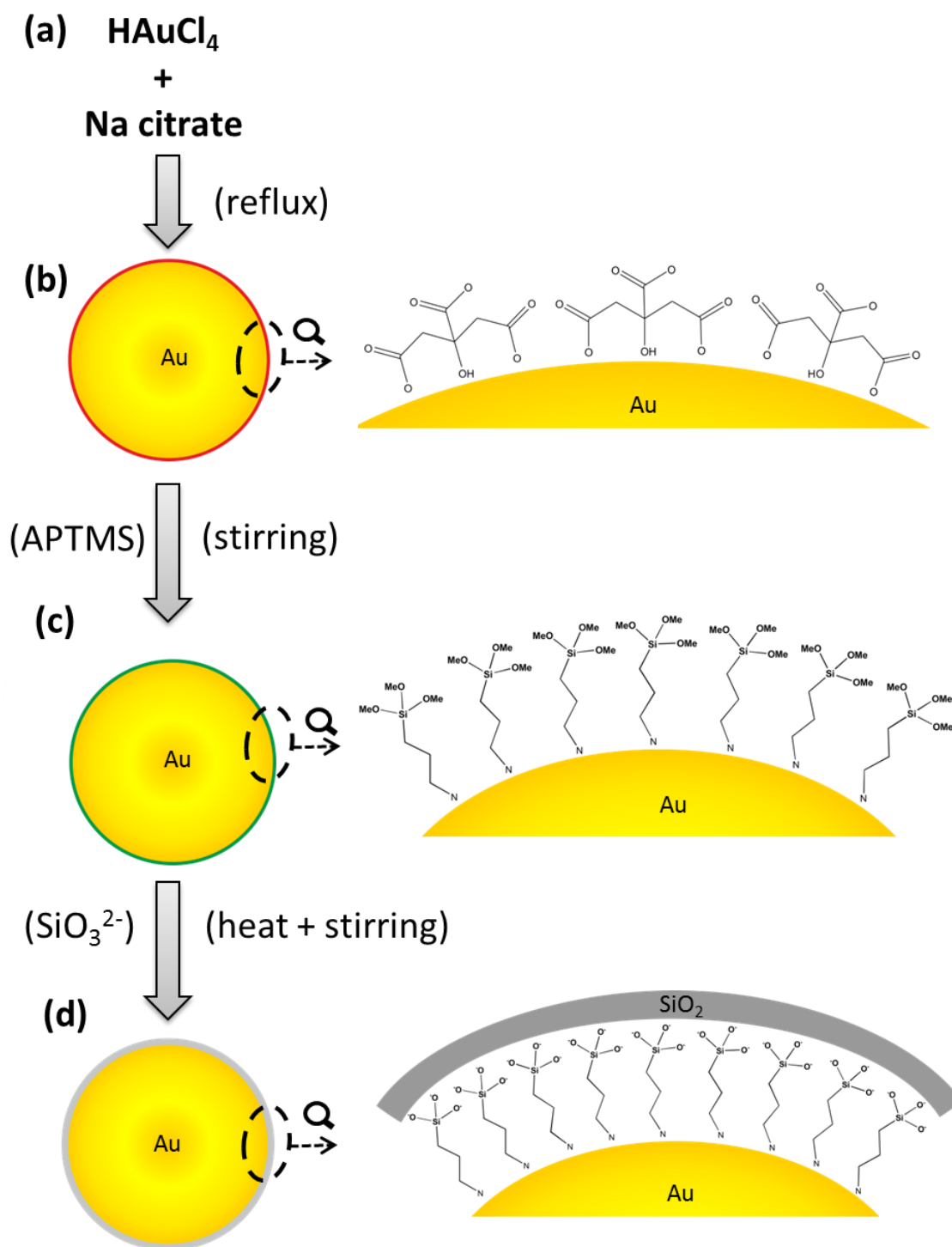


Figure 3.1 Schematic representation of the different steps associated with the synthesis of shell isolated nanoparticles. (a) Au salt and reducing agent (trisodium citrate), (b) reduction of Au salt to form nanoparticles, (c) APTMS exchange with citrate ligand, (d) growth of SiO_2 shell.

3.3.2 Coating of Au nanoparticles with a silica shell

In order to coat the 55 nm gold nanoparticles with a 2-3 nm silica shell, 0.4 ml of ((3-Aminopropyl)trimethoxysilane, 97%) APTMS solution (1 mM) was added to 30 ml Au nanoparticles solution with vigorous stirring (**Fig 3.1b-c**). This allowed the APTMS ligand to exchange with the citrate ligand. The APTMS forms a uniform layer around the gold nanoparticles and prevents aggregation and increases the vitrophilic character of gold for the incorporation of silicon dioxide.²⁶

A 3.2 ml sodium silicate solution (pH 10.3) was freshly made in a volumetric flask. The pH of the solution was controlled with 1 M HCl in order for uniform shell growth to occur. A solution with a high pH (> 11) will inhibit growth of the silica shell due to the presence of NaOH, thus an extremely thin shell and pinholes will form (**Fig. 3.3g**)²⁷. On the other hand if the pH is too low (< 9) rapid, uncontrolled shell growth occurs. This can result in an uneven shell and large pinholes (**Fig. 3.3h**). The flask should be shaken vigorously prior to addition to allow hydrolysis of the sodium silicate. After shaking, the solution was added (quickly, in one go) to the round bottom flask, whilst stirring rapidly (the stirrer bar should be visible at the bottom of the vortex, ~1200 rpm). The solution was stirred for 10 minutes at room temperature to initiate shell growth; the flask was then transferred to a preheated water bath (94°C) (**Fig 3.2c-d**). This temperature allows a rapid, and controlled shell growth²⁸. In previous reports, the reaction was done at room temperature, with growth times of ~2 days for a 2 nm shell²⁶. The elevated temperature allows a 2-3 nm shell to be grown in 30 minutes (**Fig 3.3d-f**) or a 4 nm shell in 60 minutes (**Fig 3.3i-j**).

After heating, the nanoparticle suspension was immediately transferred into an ice bath to stop shell growth. The solution was then washed multiple times via centrifugation at 5500 rpm and left in a concentrated water suspension (0.1 ml).

Different size and shape nanoparticles can also be synthesised (**Fig 3.3k and l**).^{27, 29-}

³¹ The advantage of alternative shaped particles, i.e. nanorods and nanocubes, allows for the wavelength at which the maximum surface plasmon resonance (SPR) occurs. The SPR can be shifted towards a desired laser wavelength, depending on the size of the rods and cubes. This allows utilisation of wavelengths closer to the infrared region.²⁷ Bigger particles generally produce a greater enhancement due to the larger electromagnetic field, this may also be beneficial for more porous substrate morphologies.

The APTMS is not removed from the gold surface, when the silica shell is added, it is therefore expected that APTMS might have a contribution to the Raman signal, as APTMS is Raman active. However this is not the case, principally due to the fixed order structure of the silica shell and the gold core, as the APTMS vibrational modes become Raman inactive.

3.4 Characterisation of SHINs

Shell isolated nanoparticles are a good tool for enhanced Raman spectroscopy; however, before use it is imperative to check the quality of the particles, in order to validate the accuracy of the results. The particles need to be checked for

- 1) **Pinholes** – any exposed gold surface may have a catalytic effect on the reaction under investigation.
- 2) **Enhancement** – if the electromagnetic field from the gold core is blocked they will not enhance the nearby molecules.
- 3) **Contaminants** – unwanted species may add additional peaks to the Raman spectra interfering in the spectroscopic analysis.

3.4.1 UV/Vis spectroscopy

UV/Vis can be used to check the maximum absorbance of light by the nanoparticles. The localised surface plasmon resonance (LSPR) of the nanoparticles, i.e. when the oscillation of the electrons in the nanoparticles, coincide with that of the incident light¹⁵ is dependent on the frequency of the incident light. The frequency range to excite a plasmon in a gold nanoparticle occurs from 500 nm to the near red infra-red region (850 nm).³² However, the maximum absorbance (λ_{max}) in the UV/Vis spectra for 55 nm Au particles is 531 nm (**Fig 3.2**). The λ_{max} is a strong indication of where adsorption will occur, this in turn results in weak scattering. Therefore the use of a 532 nm laser is not suitable as absorption of light will occur, limiting the scattering of photons. Laser wavelengths of 633 or 785 nm will provide optimum enhancement as adsorption is minimised, whilst still within the frequency range where a plasmon can be excited³³. It was noted that the size and shape of the nanoparticles can be tuned to different wavelengths³⁴⁻³⁵. The addition of a uniform SiO₂ shell is also established by the shift in the absorption maximum of

the surface plasmon band (SPB) shown in **Fig. 3.2**. The shift is not only due to the increase in the nanoparticle size, but also by the change in the dielectric constant induced by the silica coating.³⁶

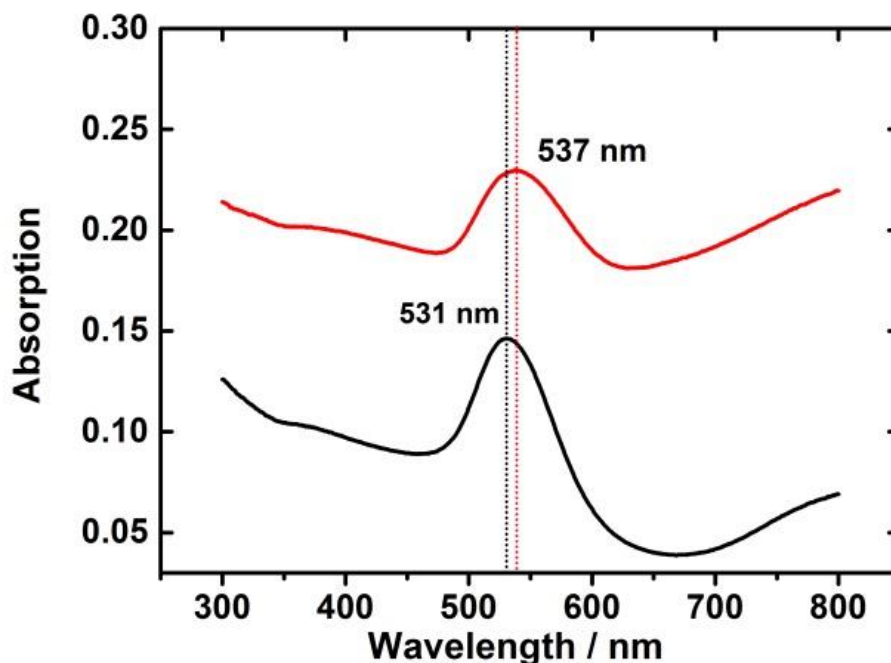


Figure 3.2 UV-Vis spectra of citrate-Au (black line) and SHINs (red line). (Spectra taken by Laura Cabo-Fernandez).

3.4.2 TEM

TEM (Transmission electron microscopy) can be used in order to characterise the SHINs. Initially TEM can be a useful visual aid in order to determine whether large pinholes are present in the silica shell (**Fig. 3.3g and h**). However, if pinholes are very small they may not be detectable and another technique would be required to determine if pinholes are present. TEM is key in determining the nanoparticle size (**Fig. 3.3a-c**) and an accurate method of measuring shell thickness (**Fig. 3.3d-f, h-j**). It can also be used to confirm shell composition (**Fig. 3.3c**).

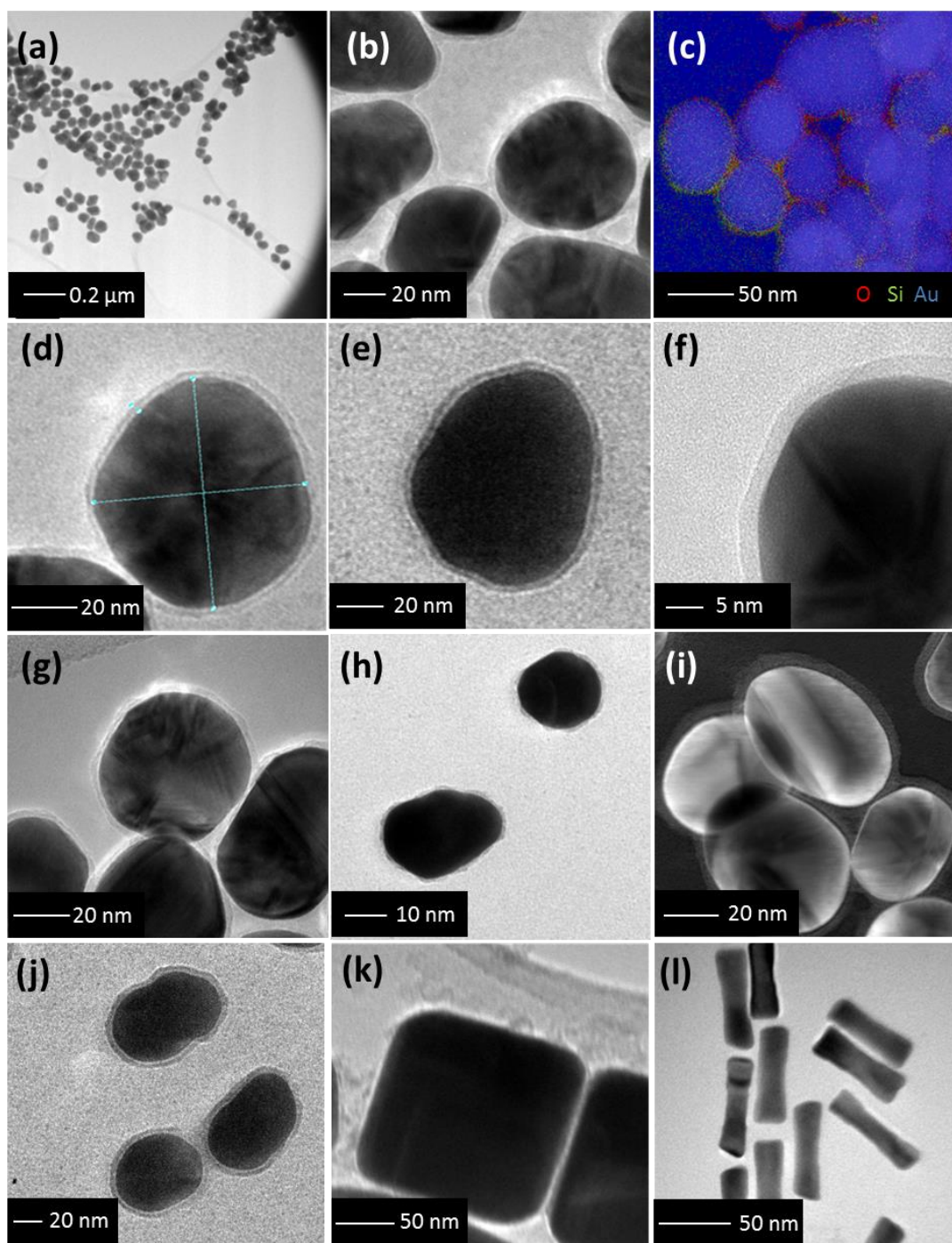


Figure 3.3 TEM images of shell isolated nanoparticles **(a)** low magnification image showing SHINs size distribution, **(b)** SHINs nanoparticles with 2-3 nm shells, **(c)** EDX image of SHINs showing elemental distribution, **(d + e)** 55 nm SHIN particle with 2-3 nm shell, **(f)** High magnification image of 2-3 nm silica shell on Au NPs, **(g)** SHINs with large pinholes in the silica shell, **(h)** SHIN with non-uniform silica shell and pinholes, **(i)** dark field image of SHINs with 5 nm silica shell, **(j)** SHINs with 4-5 nm silica shell, **(k)** nanocubes with 2-3 nm shell, and **(l)** nanorods

3.4.3 Cyclic voltammetry

Cyclic voltammetry is a quick and easy method of determining whether or not pinholes are present in the silica shell. For this purpose, 2 μl of SHIN's solution is deposited on a glassy carbon electrode and left to dry in the atmosphere. Once dry a cyclic voltammogram was run in a 0.1 M H_2SO_4 electrolyte (**Fig. 3.4**). Another CV was run as a comparison with citrate-capped gold nanoparticles on the carbon electrode surface in the same electrolyte.

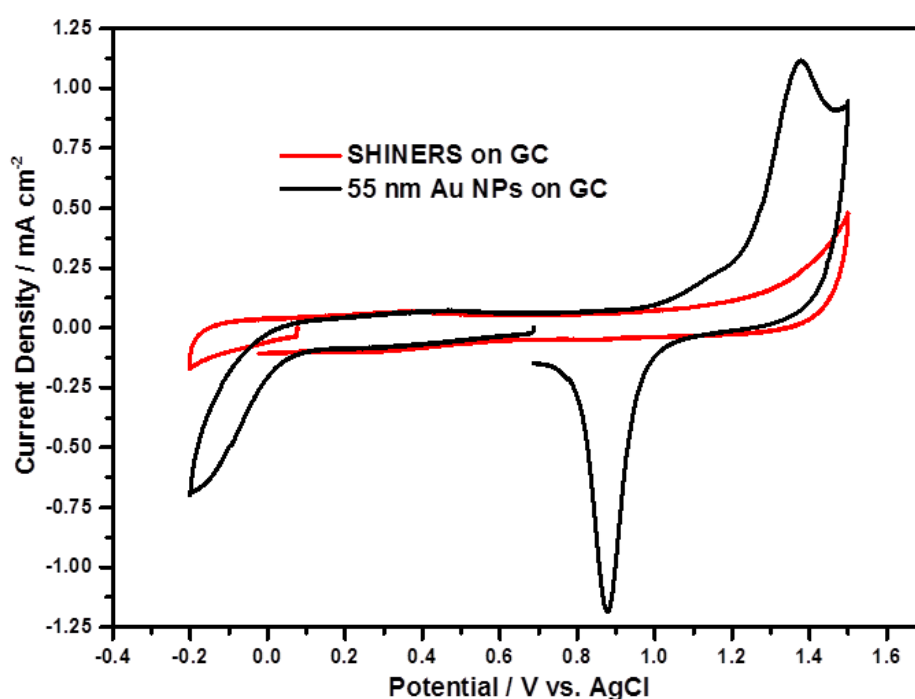


Figure 3.4 Cyclic voltammograms of SHINERS (red) and citrate Au nanoparticles (black) on a glassy carbon electrode in 0.1 M H_2SO_4 . Sweep rate 10 mv s^{-1} .

If pinholes are present in the silica shell a peak at 1.2 V in the oxidation scan and at 0.9V in the reverse scan related to the oxidation and reduction of gold, respectively. This was demonstrated in the CV with citrate gold nanoparticles on the electrode surface. The absence of these redox peaks is an indication of a completely inert silica shell. This technique is a good method for determining whether or not

pinholes are present, but will not differentiate between shell thicknesses, which have an influence on the nanoparticle enhancement factor.

3.4.4 Raman Spectroscopy

Raman spectroscopy can be used to check whether pinholes are present in the silica shell, it can also determine the enhancement factor of the SHINs as well as the presence of any contaminants.

To test for pinholes in the SHINs, 2 μl of the particles are deposited onto a silica substrate and left to dry. Pyridine (3 μl , 10 mM) is then dropped onto the silica substrate and left to adsorb for a couple of minutes. If pinholes are present 2 peaks will be visible in the Raman spectra at 1010 and 1030 cm^{-1} (**Fig. 3.5b**) for the ν_1 ring breathing mode and the symmetric triangular ring deformation mode ν_{12} of pyridine adsorbed on gold³⁷. If no peaks are present in this region, then there is no pyridine adsorption on gold, therefore there is no gold surface exposed i.e. there are no pinholes (**Fig. 3.5a**).

The enhancement factor from SHINERS is dependent on the shell thickness, if the silica shell is too thick then the penetration distance of the gold core's electromagnetic field will be blocked. This is around 10 nm for 55nm particles; larger particles will have a larger penetration depth. Raman spectroscopy can be used to calculate the enhancement factor. SHINs are deposited on an Au surface and pyridine is dropped onto the surface and left to adsorb for a couple of minutes. The intensity of the pyridine-gold adsorption bands at 1010 cm^{-1} and 1030 cm^{-1} are related to the shell thickness and in turn the enhancement factor (calculated below). SHINs with a shell thickness of 4 nm will have weak Raman bands between 1000-1030 cm^{-1} (**Fig 3.5c**). Comparatively, SHINs with a 2-3 nm shell will exhibit intense

bands at 1010 and 1030 cm^{-1} (**Fig 3.5d.**), as a result of the greater electromagnetic field around the particles.

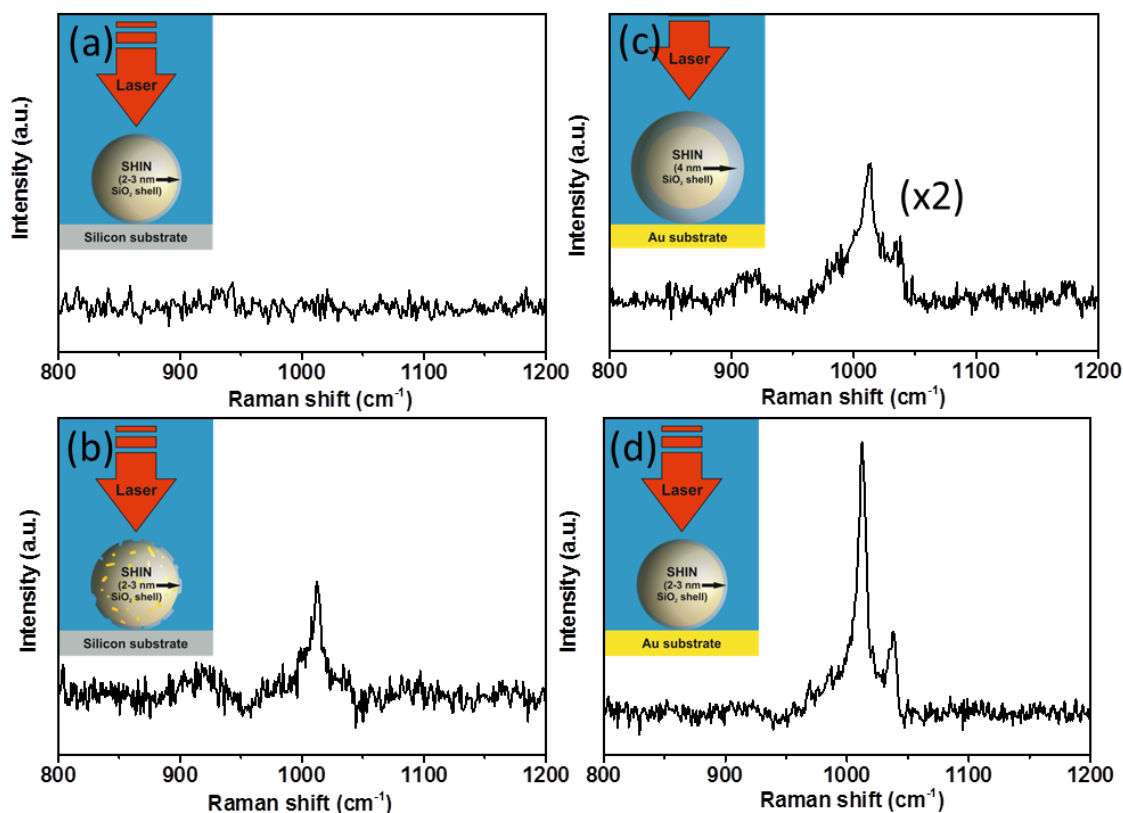


Figure 3.5 Raman spectra of pyridine on (a) Si/SHINERS without pinholes (b) Si/SHINERS with pinholes (c) Au/SHINERS (4 nm shell) (d) Au/SHINERS (2 nm shell).

3.4.5 Calculating the enhancement factor (EF)

The enhancement factor (**EF**) is important and is not just from the intensity of the Raman bands as it encompasses a multitude of contributing factors which can affect the behaviour of the nanoparticles between experiments³⁸. In order to have a uniform value for enhancement, pyridine was used on gold or platinum substrates³⁹⁻⁴¹. This allowed the comparison of intensity between pyridine surface and solution species whilst normalising laser setup and surface morphology (**Eq. 3.1-3.4**)⁴².

$$EF = \frac{(I_{\text{surface}}/N_{\text{surface}})}{(I_{\text{solution}}/N_{\text{solution}})} \quad (\text{Eq. 3.1})$$

I_{surface} - Integrated intensity of the pyridine (ν_{1a}) ring breathing mode for surface species

I_{bulk} - Integrated intensity of the pyridine (ν_{1a}) ring breathing mode for solution species

N_{solution} - The number of solution molecules present in the laser beam

N_{surface} - The number of surface molecules present in the laser beam

$$N_{\text{surface}} = \frac{R A}{\sigma} \quad (\text{assuming monolayer adsorption}) \quad (\text{Eq. 3.2})$$

R - Roughness factor

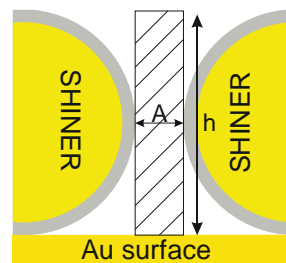
A - Area of focal spot of the Raman laser

σ - Area of 1 adsorbed pyridine molecule

$$N_{\text{surface}} = A h c N_a \quad (\text{Eq. 3.3})$$

h - Focal depth of the laser

c - Concentration of pyridine



The enhancement factor can then be calculated from combining equations 1, 2 and 3

$$G = \frac{I_{\text{surface}} c N_a \sigma h}{I_{\text{solution}} R} \quad (\text{Eq. 3.4})$$

Typical enhancement factors of up to 1.5×10^5 can be achieved for SHINERS on Au(111) surfaces⁷. Polycrystalline gold was shown to have an enhancement factor of 2.9×10^5 . This was calculated with the above equation using the pyridine adsorption

on gold with SHINERS from **Fig. 3.5d**. The enhancement was not as strong as SERS, but was suitable to detect products on the electrode surface.

3.4.6 Electrode preparation and particle distribution

The preparation of the substrate material with SHINs is an important step, and to gain maximum enhancement a uniform monolayer of SHINs is required. This means there will be an even enhancement of the Raman signal across the whole area illuminated by the laser. Production of a uniform layer is notoriously difficult due to a culmination of factors. A major problem is related to the cohesive nature of water, the solvent in which SHINs are suspended, as, when drops were cast onto the electrode surface and left to dry, a thick ring formed (**Fig. 3.6a**).

Scanning electron microscopy (SEM) and atomic force microscopy (AFM) images of SHINs on an Au wafer demonstrate the variant coverage of the particles. At the edge of the ring, SEM (**Fig. 3.6b1**) displays a concentrated group of particles, with clear clumps of particles stacked on each other. Height profiles from AFM images suggest that the nanoparticles at the edge of the drop are grouped into larger islands with typical clusters ranging from 2 up to 11 nanoparticles. Up to three layers of particles on top of each another can be found (**Fig 3.6c1**), reducing or completely blocking the amplification of the signal; however, monolayers are still observed in some areas. At the edge of the drop a single layer with 3 or 4 clusters per island are observed (**Fig 3.6c2**), in agreement with previous results from Li *et al.*⁴³. This also correlates with the SEM image at the centre of the drop (**Fig 3.6b2**).

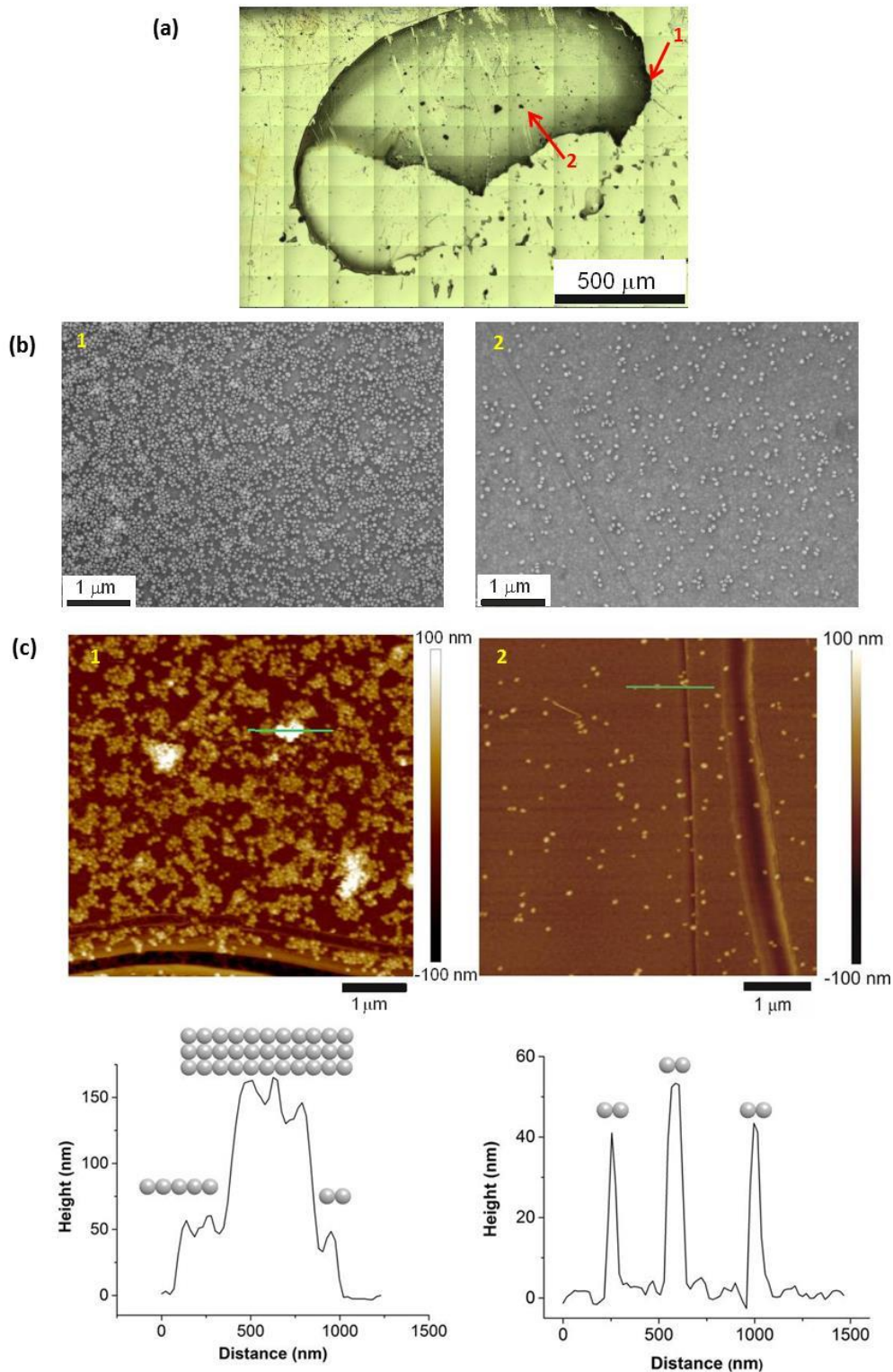


Figure 3.6 (a) Optical image of SHINs drop casted on Au showing uneven NP dispersion on the surface and ring effect. Arrows point to region 1 (edge) and region 2 (centre); (b) SEM images of SHINs drop cast onto Au (c) AFM images and height profiles of the region marked with a green line; **1**) image at the edge and **2**) at the centre of the drop. (SEM images taken by Filipe Braga, AFM images by Iain Aldous).

The effect on the variation in enhancement of the Raman signal due to the distribution of nanoparticles has been observed by the mapping of the pyridine peak intensity on the gold surface with Raman spectroscopy, shown in **Fig. 3.7**. Here a Raman map of the intensity of the pyridine peak at 1010 cm^{-1} is shown to correlate in relation to nanoparticle distribution observed from the optical microscope image, where some areas display significant enhancements (shown in red).

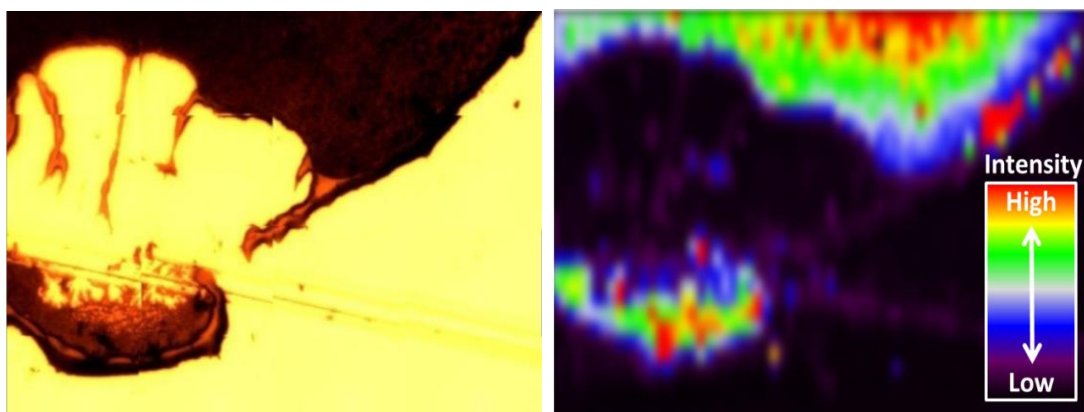


Fig. 3.7 (Left) optical image of SHINs drop on a gold electrode, (right) Raman map of the intensity of the pyridine peak at 1010 cm^{-1} in relation to nanoparticle distribution.

3.4.7 Casting of SHINs

As mentioned above, the formation of a uniform layer of particles is important in maximising the enhancement from the SHINs. Previously SHINs have been deposited onto a substrate via a drop casting method and left to dry in air, this produced a thick ring (**Fig. 3.8a**). To overcome this problem, initially changing the solvent the nanoparticles were suspended in was tried. Ethanol and isopropanol were both attempted, however, did not prove successful as the particles are susceptible to aggregation after 3 or more washes.

Instead of air drying the substrate after drop casting, vacuum drying was used. This produced a better distribution of particles across the substrate surface, with no thick ring being observed optically (**Fig. 3.8b**).

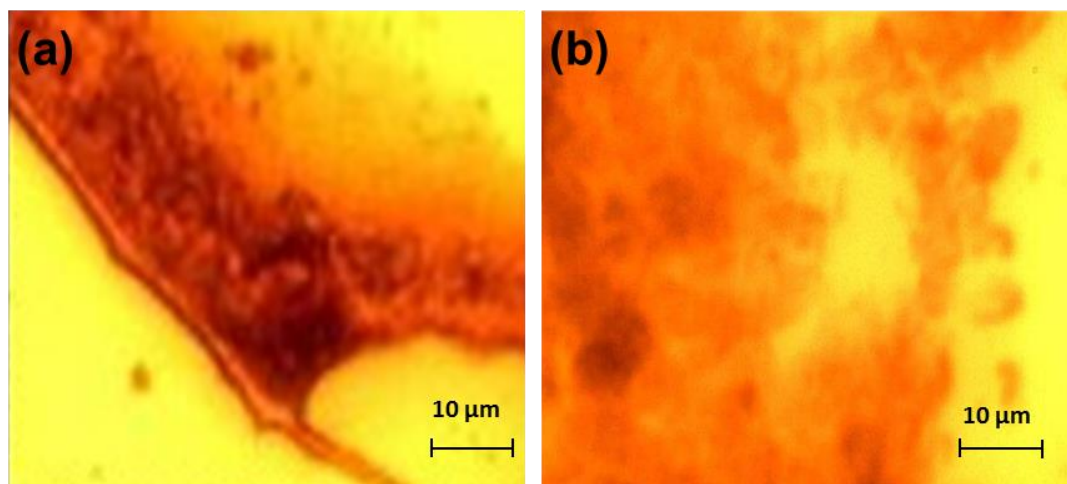


Figure 3.8 Microscope images taken with an in via optical microscope of SHINS drop casted onto a gold electrode surface. a) Particles dried in air b) dried under vacuum. Bright patches indicate gold electrode with no SHINERS particles, dark patches indicate presence of nanoparticles upon the surface.

In addition to drop casting, SHINs were deposited onto an electrode using a spray casting technique. The spray casting set up was quite rudimentary, it involved using a perfume bottle with a fine hose, to deliver the particles. AFM was used to compare the particle distribution between spray and drop casting (**Fig. 3.9**). The spray coating delivered a series of small spots across the surface compared to the one large spot observed with drop casting. Both spray and drop casting showed a similar trend between the centre and edge of the spots (**Fig. 3.9a and b**). The centre being sparsely covered relative to the edge. It can be noted that the spray coating coverage, produced larger clumps of particle relative to the drop casting technique.

These results suggest that at present drop casting of the nanoparticles and drying under vacuum is the most efficient method of distributing the nanoparticles. Spray

coating needs to be refined in order to optimise the particle distribution. This encompasses future work to be conducted with the aid of Johnson Matthey, to test a new spray coating technique under heat and vacuum to disperse the particles in a more uniform and reproducible method.

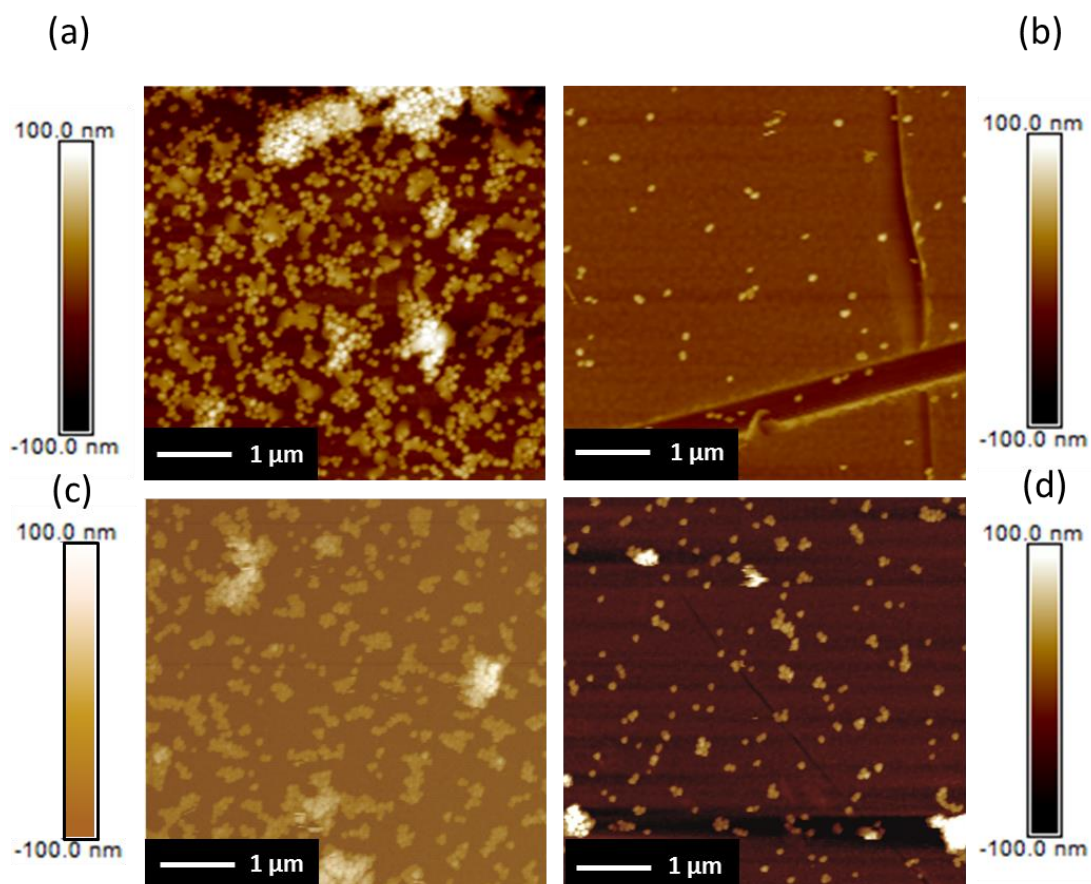


Figure 3.9 AFM images of SHINs (a) drop coated edge of spot, (b) drop cast centre of spot, (c) spray coated edge of spot, and (d) spray coated centre of spot onto a gold substrate. (AFM images taken by Iain Aldous).

3.4.8 Cleaning the nanoparticles

The presence of several peaks between 1000 and 1700 cm^{-1} and in the region corresponding to C-H stretching vibrations (2700 - 3000 cm^{-1}) have been observed in the Raman spectra collected during EF tests on gold substrates. These peaks are related to reaction compounds that remained in the nanoparticle solution despite the washing steps carried out during the coating step. **Fig. 3.10** compares the spectrum

of the SHINs with pyridine drop cast on gold with that of the reactants used during the synthesis. Sodium citrate is clearly observed as the major contaminant in the SHINs spectrum, probably due to an excess in solution. Sodium silicate also has a small contribution with minimal APTMS observed as a contaminant.

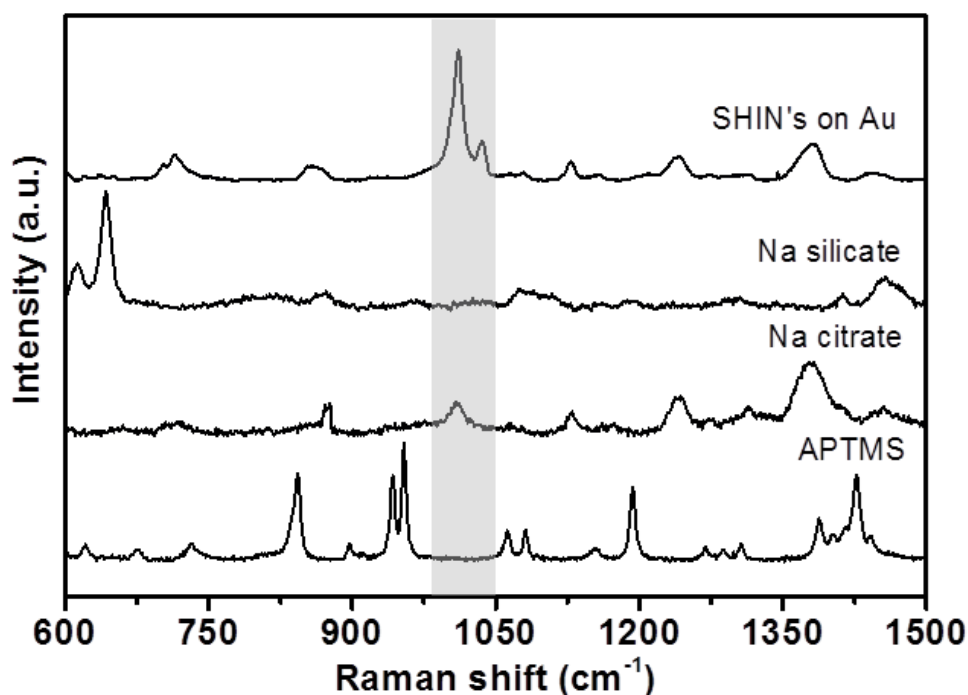


Figure 3.10. Raman spectrum of pyridine adsorbed onto an Au wafer (grey shaded region) drop cast with SHINs and the standard Raman spectra of some of the possible impurities from nanoparticle preparation.

The presence of impurities from organic species in the SHIN solution has previously been reported.⁴³⁻⁴⁴ Li *et al.* described a successful method to remove the contaminants from single crystals by hydrogen evolution reaction (HER) in aqueous media.⁴³ However, HER on battery electrode materials in aqueous media is not feasible; therefore, an alternative method is required.

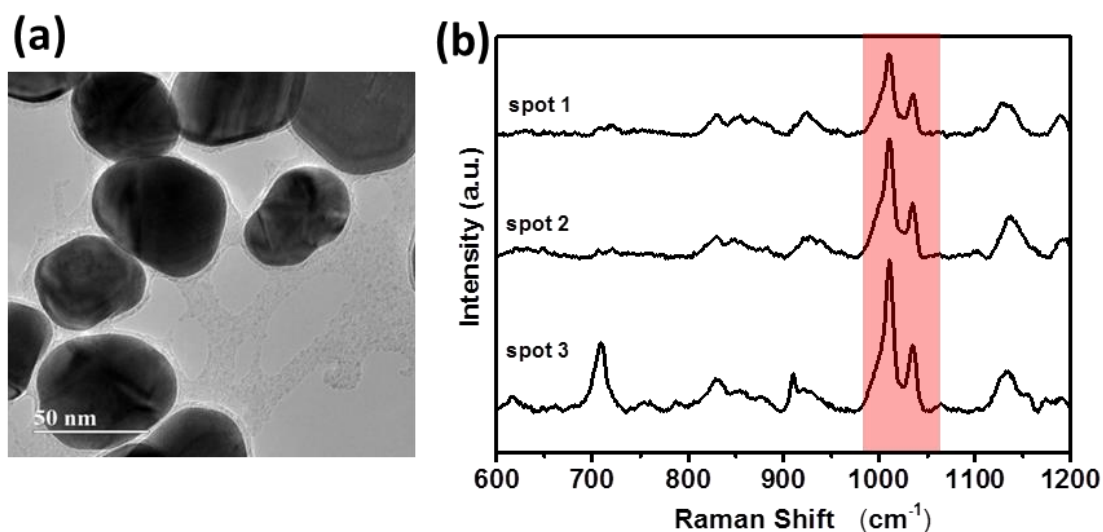


Figure 3.11 (a) TEM image of SHINs particles connected via a silica network, (b) Raman spectra of pyridine on a silica wafer at different spots on the substrate.

Fig. 3.10 demonstrated sodium citrate was the main contaminant in the SHINs spectra. The sodium citrate is exchanged with APTMS in the synthesis of the silica shell, an excess of citrate may be present prior to this step. To overcome this before addition of APTMS, the Au nanoparticles were centrifuged at 4500 rpm to remove excess citrate. This proved unsuccessful; TEM observed a network of SHINs connected through a silica framework (**Fig. 3.11a**) and Raman spectroscopy detected the presence of pinholes and contaminants (**Fig. 3.11b**). This result suggested that washing the particles prior to shell coating may have partially removed the citrate capping ligands, leading to partial exchange with the APTMS.

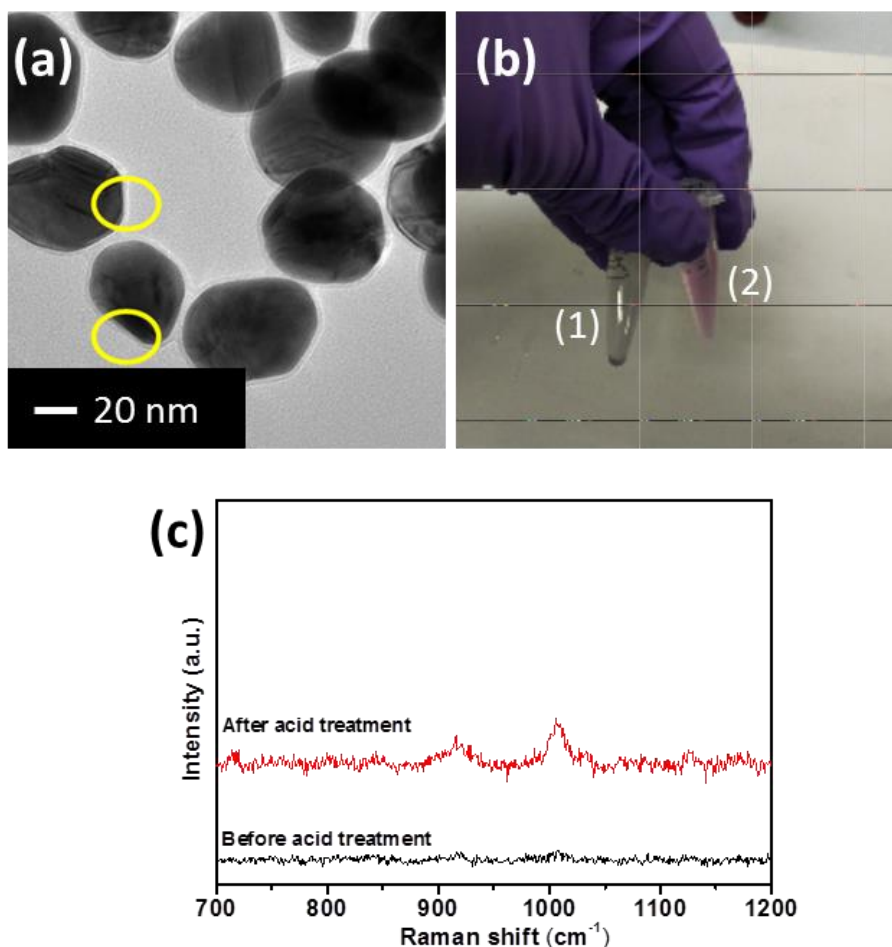


Figure 3.12 (a) TEM image of SHINs after treatment with dilute Aqua Regia, yellow circles denote thinning of silica shell. (b1) Image of SHINs with pinholes after treatment with dilute Aqua Regia, SHINs have collapsed. (b2) Image of stable SHINs after treatment with dilute Aqua Regia. (c) Raman spectra of SHINs before and after acid treatment, pinholes visible after acid treatment.

Chemical methods have also been investigated to remove the contaminants, such as washing the SHINs with diluted Aqua Regia. After several washes with Milli-Q water during the coating process of the gold seeds, the concentrated SHIN solution was washed with Aqua Regia (0.2 % v/v) followed by washing with Milli-Q water until the solution had a neutral pH. This procedure has been reported to check the chemical stability of Ag-SiO₂ core-shell nanoparticles (Fig. 3.12b1).⁴⁵ The nanoparticles collected at the end were stable (Fig. 3.12b2) with no aggregation but

pinholes have been detected during Raman investigation, as seen in **Fig. 3.12c**. The reason for this could be a thinning of the shell in some regions of the nanoparticles (< 2 nm) due to the acid wash (**Fig. 3.12a**), and therefore, the pyridine peaks are observed in the spectra.

A range of techniques to remove contaminants in the SHINs have been summarised below and investigated spectroscopically for contaminants (**Fig. 3.13**).

- **Centrifugation using centrifuge tubes with a permeable membrane** – the particles were centrifuged in a special centrifuge tube, with a permeable membrane to collect the nanoparticles and remove contaminants. This proved unsuccessful as contaminants were still present in the Raman spectra. The tubes are also single use and expensive increasing the cost of nanoparticle preparation, making this method impractical.
- **Wash particles deposited on a substrate followed by sonication** – SHINs tend to collapse when increasing the number of centrifugation steps; therefore, they were drop casted onto a gold or silicon wafer and washed several times with excess Milli-Q water to avoid aggregation. Afterwards, the wafer was sonicated in Milli-Q water to remove the particles from the surface. They were then centrifuged and drop casted onto another gold wafer for Raman characterisation. This also failed to remove the contaminants. However, the particles remained pinhole free and did not aggregate. Similarly, particles deposited on Si wafer were washed with diluted Aqua Regia (0.2 % v/v) and Milli-Q water but it was not possible to remove the particles from the wafer by sonication.
- **Washed in excess H₂O** – After synthesis the SHINs particles were collected in a large centrifuge tube (1.5 ml in 50 mL instead of a 1.5 ml tube). The particles were cooled under ice. Once cooled the particles were diluted up to 50 ml,

centrifuged twice then concentrated. The particles remained pinhole free, but contaminants were still observed.

- **Hydrogen evolution reaction (HER)** - Particles were deposited on a gold electrode and then electrochemically cleaned by forcing hydrogen evolution in 0.1 M Na₂SO₄ /H₂O⁴³. The contaminants were successfully removed from the electrode surface as previously reported⁴³.

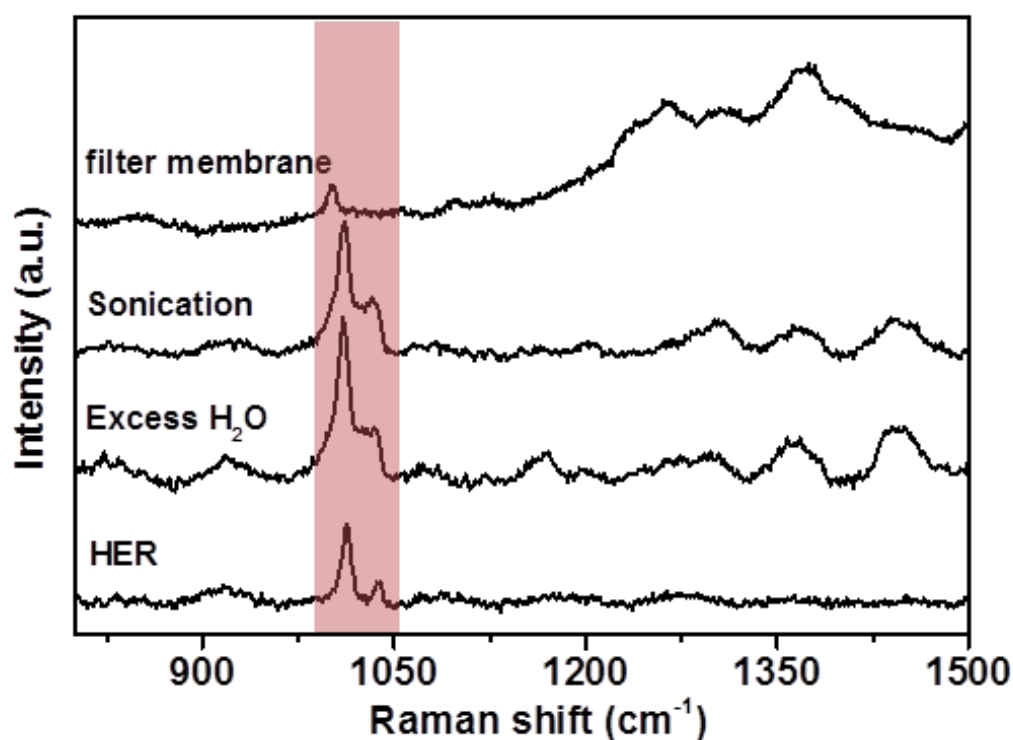


Figure 3.13 Raman spectra of pyridine on Au drop casted with SHINs cleaned with a variety of techniques, using a special centrifuge tube, centrifuging with excess water, hydrogen evolution (HER), sonication in Milli-Q water then re-dispersed in Milli-Q water. Red shade highlights pyridine peaks.

As mentioned previously hydrogen evolution is only applicable in aqueous media, it is not suitable for non-aqueous systems. In some non-aqueous media this is not a problem, such as DMSO, as it dissolves the contaminants from the electrode surface, due to its high donor number.

3.5 Conclusions and Future work

The next step to overcome the contaminants in other non-aqueous media is to combine both sonication and hydrogen evolution steps. Initial attempts failed as aggregation of the particles occurred after sonication. Future work should be focused at overcoming this.

Overall this chapter demonstrates the successful synthesis of pinhole free SHINs, with good enhancement. A clear detailed method for characterising and synthesising these particles has been laid out in this chapter.

The results showed SHINERS can provide a substantial enhancement of the Raman signal, however understanding the distribution of the particles on the electrode surface is invaluable to develop this technique. This provides a good platform for the utilisation of SHINERS in battery systems.

3.6 References

1. Raman, C. V.; Krishnan, K. S., *Nature* 1928, **121**, 501-502.
2. Jeanmaire, D. L.; Van Duyne, R. P., *J. Electroanal. Chem.* 1977, **84** (1), 1-20.
3. Albrecht, M. G.; Creighton, J. A., *J. Am. Chem. Soc.* 1977, **99** (15), 5215-5217.
4. Moskovits, M., *Rev. Mod. Phys.* 1985, **57** (3), 783-826.
5. Otto, A.; Mrozek, I.; Grabhorn, H.; Akemann, W., *J. Phys.: Condens. Matter* 1992, **4** (5), 1143-1212.
6. Tian, Z. Q., *J. Raman Spectrosc.* 2005, **36** (6-7), 466-470.
7. Tian, Z. Q.; Ren, B.; Mao, B. W., *J. Phys. Chem. B* 1997, **101** (8), 1338-1346.
8. Zou, S.; Weaver, M. J.; Li, X. Q.; Ren, B.; Tian, Z. Q., *J. Phys. Chem. B* 1999, **103** (21), 4218-4222.
9. Ren, B.; Lin, X.-F.; Yan, J.-W.; Mao, B.-W.; Tian, Z.-Q., *J. Phys. Chem. B* 2003, **107** (4), 899-902.
10. Moskovits, M., *J. Chem. Phys.* 1978, **69** (9), 4159-4161.
11. Wessel, J., *J. Opt. Soc. Am. B* 1985, **2** (9), 1538-1541.
12. Li, J. F.; Huang, Y. F.; Ding, Y.; Yang, Z. L.; Li, S. B.; Zhou, X. S.; Fan, F. R.; Zhang, W.; Zhou, Z. Y.; Wu, D. Y.; Ren, B.; Wang, Z. L.; Tian, Z. Q., *Nature* 2010, **464** (7287), 392-395.
13. Hartman, T.; Wondergem, C. S.; Kumar, N.; van den Berg, A.; Weckhuysen, B. M., *J. Phys. Chem. Lett.* 2016, **7** (8), 1570-1584.
14. Ghosh Chaudhuri, R.; Paria, S., *Chem. Rev.* 2012, **112** (4), 2373-2433.
15. Li, J.-F.; Zhang, Y.-J.; Ding, S.-Y.; Panneerselvam, R.; Tian, Z.-Q., *Chem. Rev.* 2017, **117** (7), 5002-5069.
16. Zhumaev, U.; Rudnev, A. V.; Li, J.-F.; Kuzume, A.; Vu, T.-H.; Wandlowski, T., *Electrochim. Acta* 2013, **112** (0), 853-863.

17. Guan, S.; Donovan-Sheppard, O.; Reece, C.; Willock, D. J.; Wain, A. J.; Attard, G. A., *ACS Catal.* 2016, **6** (3), 1822-1832.
18. Hy, S.; Felix; Chen, Y.-H.; Liu, J.-y.; Rick, J.; Hwang, B.-J., *J. Power Sources* 2014, **256**, 324-328.
19. Hy, S.; Felix, F.; Rick, J.; Su, W.-N.; Hwang, B. J., *J. Am. Chem. Soc.* 2014, **136** (3), 999-1007.
20. Galloway, T. A.; Hardwick, L. J., *J. Phys. Chem. Lett.* 2016, **7** (11), 2119-2124.
21. Frens, G., *Nature Phy. Sci.* 1973, **241**.
22. Kimling, J.; Maier, M.; Okenve, B.; Kotaidis, V.; Ballot, H.; Plech, A., *Turkevich J. Phys. Chem. B* 2006, **110** (32), 15700-15707.
23. Turkevich, J.; Stevenson, P. C.; Hillier, J., *Discuss. Faraday Soc.* 1951, **11** (0), 55-75.
24. Bastús, N. G.; Comenge, J.; Puentes, V., *Langmuir* 2011, **27** (17), 11098-11105.
25. Turkevich, J., Colloidal Gold. Part I. *Gold Bull.* 1985, **18** (3), 86-91.
26. Liz-Marzán, L. M.; Giersig, M.; Mulvaney, P., *Langmuir* 1996, **12** (18), 4329-4335.
27. Li, J. F.; Tian, X. D.; Li, S. B.; Anema, J. R.; Yang, Z. L.; Ding, Y.; Wu, Y. F.; Zeng, Y. M.; Chen, Q. Z.; Ren, B.; Wang, Z. L.; Tian, Z. Q., *Nat. Protoc.* 2013, **8** (1), 52-65.
28. Li, J.-F.; Li, S.-B.; Anema, J. R.; Yang, Z.-L.; Huang, Y.-F.; Ding, Y.; Wu, Y.-F.; Zhou, X.-S.; Wu, D.-Y.; Ren, B.; Wang, Z.-L.; Tian, Z.-Q., *Appl. Spectrosc.* 2011, **65** (6), 620-626.
29. Perezjuste, J.; Pastorizasantos, I.; Lizmarzan, L.; Mulvaney, P., *Coord. Chem. Rev.* 2005, **249** (17-18), 1870-1901.
30. Wu, H.-L.; Tsai, H.-R.; Hung, Y.-T.; Lao, K.-U.; Liao, C.-W.; Chung, P.-J.; Huang, J.-S.; Chen, I. C.; Huang, M. H., *Inorg. Chem.* 2011, **50** (17), 8106-8111.
31. Scarabelli, L.; Sánchez-Iglesias, A.; Pérez-Juste, J.; Liz-Marzán, L. M., *A J. Phys. Chem. Lett.* 2015, **6** (21), 4270-4279.

32. Smith, W. E., *Chem. Soc. Rev.* 2008, **37**, 955-964
33. Willets, K. A.; Duynne, R. P. V., *Annu. Rev. Phys. Chem.* 2007, **58** (1), 267-297.
34. Solís, D. M.; Taboada, J. M.; Obelleiro, F.; Liz-Marzán, L. M.; García de Abajo, F. J., *ACS Photonics* 2017, **4** (2), 329-337.
35. Benz, F.; Chikkaraddy, R.; Salmon, A.; Ohadi, H.; de Nijs, B.; Mertens, J.; Carnegie, C.; Bowman, R. W.; Baumberg, J. J., *J. Phys. Chem. Lett.* 2016, **7** (12), 2264-2269.
36. Vanderkooy, A.; Chen, Y.; Gonzaga, F.; Brook, M. A., *ACS Appl. Mater. Interfaces* 2011, **3** (10), 3942-3947.
37. Tian, X.-D.; Liu, B.-J.; Li, J.-F.; Yang, Z.-L.; Ren, B.; Tian, Z.-Q., *J. Raman Spectrosc.* 2013, **44** (7), 994-998.
38. Liu, B.; Blaszczyk, A.; Mayor, M.; Wandlowski, T., *ACS Nano* 2011, **5** (7), 5662-5672.
39. Li, J.-F.; Ding, S.-Y.; Yang, Z.-L.; Bai, M.-L.; Anema, J. R.; Wang, X.; Wang, A.; Wu, D.-Y.; Ren, B.; Hou, S.-M.; Wandlowski, T.; Tian, Z.-Q., *J. Am. Chem. Soc.* 2011, **133** (40), 15922-15925.
40. Li, J.-F.; Zhang, Y.-J.; Rudnev, A. V.; Anema, J. R.; Li, S.-B.; Hong, W.-J.; Rajapandiyam, P.; Lipkowski, J.; Wandlowski, T.; Tian, Z.-Q., *J. Am. Chem. Soc.* 2015, **137** (6), 2400-2408.
41. Ding, S.-Y.; Yi, J.; Li, J.-F.; Tian, Z.-Q., *Surf. Sci.* 2015, **631**, 73-80.
42. Huang, Y.-F.; Li, C.-Y.; Broadwell, I.; Li, J.-F.; Wu, D.-Y.; Ren, B.; Tian, Z.-Q., *Electrochim. Acta* 2011, **56** (28), 10652-10657.
43. Li, J.-F.; Rudnev, A.; Fu, Y.; Bodappa, N.; Wandlowski, T., *ACS Nano* 2013, **7** (10), 8940-8952.
44. Smith, S. R.; Leitch, J. J.; Zhou, C.; Mirza, J.; Li, S. B.; Tian, X. D.; Huang, Y. F.; Tian, Z. Q.; Baron, J. Y.; Choi, Y.; Lipkowski, J., *Anal. Chem.* 2015, **87**, 3791-3799.

45. Li, C. Y.; Chen, S. Y.; Zheng, Y. L.; Chen, S. P.; Panneerselvam, R.; Chen, S.; Xu, Q. C.; Chen, Y. X.; Yang, Z. L.; Wu, D. Y.; Li, J. F.; Tian, Z. Q., *Electrochim. Acta* 2016, **199**, 388-393.

Chapter 4

Utilising *in situ* Enhanced Raman Spectroscopy to Study the Oxygen Reduction Reaction in Aprotic Electrolytes

4.1 Abstract

The results presented in this chapter demonstrate the effectiveness of SHINERS to enhance the Raman signal of surface species on previously inaccessible substrate electrode materials. Initial findings verified that SHINERS can accurately reproduce results obtained using *in situ* SERS, without having any additional or adverse effects on the reaction mechanism.

A simple study of the reduction mechanisms taking place in a non-aqueous solvent and supporting salt on a selection of electrode materials allowed subtle differences to be detected between the materials, notably the strong interaction between platinum and oxygen affecting the potential dependent orientation of the superoxide molecule on the surface.

The effect of changing the solvent donor number was also carried out on a glassy carbon surface in the presence of lithium. Both a solution and surface mechanism was detected, however it can be noted the reaction mechanism is both surface and solvent dependent.

4.2 Introduction

Oxygen is a very important element; it is a necessity for maintaining life through aerobic respiration. Dioxygen can be harnessed for many industrial processes, such as ore refinement, rocket fuel¹ and drug synthesis. The use of dioxygen plays a vital role in energy conversion for fuel cells² and recent development in battery technologies have started to utilise the reduction of oxygen with alkali metals (metal-oxygen batteries)³.

The electrochemical reduction and oxidation of dioxygen can be affected by a number of factors, pH, solvent and electrode material. These factors promote a variety of reaction pathways, through various intermediary species culminating in differing final products.⁴ The oxygen reduction reaction (ORR) mechanism in aqueous environments proceeds predominantly via a 2 or 4 electron reduction pathway. These pathways are affected by the pH, with acidic electrolytes promoting the production of H₂O or H₂O₂ (Eq. 4.1-4.3), comparatively basic media produce OH⁻ and HO₂⁻ products (Eq. 4.4-4.6).

- **Oxygen reduction reactions in Acidic media**⁵



- **Oxidation reduction reaction in Alkaline media**⁶



- **Oxidation reduction reactions in non-aqueous solvents (aprotic)**⁷



In aprotic systems a 1 electron reduction of oxygen to superoxide (O_2^-) (Eq. 4.7) is generally preferred but this can be influenced by the solvent and other species⁷⁻⁹, due to the highly nucleophilic nature of the superoxide radical¹⁰. The superoxide radical can be stabilised in solution with the addition of an alkyl ammonium salt.¹¹ The second electron reduction of superoxide to a free standing uncoordinated peroxide ion (O_2^{2-}) (Eq. 4.8) is thermodynamically unstable.¹² However in the presence of metal ions and protons, peroxide can be stabilised.¹³ This is of particular interest with the alkali metals, especially Li. The reversible formation of lithium peroxide (Li_2O_2) provides the basic, simplified reaction for the lithium-oxygen (Li- O_2) cell.¹⁴

The highly sensitive nature of the ORR is of key interest for non-aqueous systems, especially in relation to the metal-oxygen cell, where the ORR can be very complex involving multiple intermediate species. Therefore, developing a greater knowledge of the fundamental mechanisms taking place at the electrode surfaces can aid in the production of more stable electrolytes and cathode (positive electrode) materials.

4.3 ORR electrochemistry on a variety of electrode surfaces without the presence of lithium.

To fully elucidate the oxygen evolution and reduction reactions (OER and ORR) taking place in the Li-O₂ cell, a range of non-aqueous solvents have been tested to provide a suitable electrolyte.¹⁵ DMSO (dimethyl sulfoxide) is a possible candidate^{16, 17} as it is a polar aprotic solvent with a high Guttmann donor number indicating good Lewis basicity. The solvent has good salt solubility mixed with a large electrochemical window (**Fig. 4.1a dashed line**), which provides a stable media to understand the oxygen reduction and evolution reactions¹⁶.

The potential separation (ΔE) between the reduction peak potential (E_{pc}) and oxidation peak potential (E_{pa}) is 0.11 V for the reaction of oxygen enriched 0.1 M TBAClO₄ in DMSO on glassy carbon (**Fig. 4.1a**). The potential separation between E_{pa} and E_{pc} for an ideal 1 e⁻ reversible reaction (ΔE_{ideal}) is 59/n mV¹⁸. The peak separation ΔE_p for the TBAClO₄/DMSO electrolyte on the glassy carbon surface is greater than 59/n mV, implying it is not an ideal reversible 1 e⁻ reaction. The reaction can be described as a pseudo 1 e⁻ transfer reaction, demonstrated by a Randles-Sevcik plot¹⁹ (**Fig. 4.1b**). A correlation between the experimental and theoretical calculations from the Randles-Sevcik equation (**Eq. 4.9**) for a 1 e⁻ reduction is observed, which agrees with previous results²⁰.

$$I_p = (2.69 \times 10^5)n^{3/2}AD^{1/2}\nu^{1/2}C \quad \text{(Eq. 4.9)}$$

I_p – peak current (A)

A – area of the electrode (cm⁻²)

D – diffusion coefficient (9.75 x 10⁻⁶ cm²s⁻¹)²¹

C – concentration (mol cm⁻³)

ν – sweep rate

n – number of electrons transferred

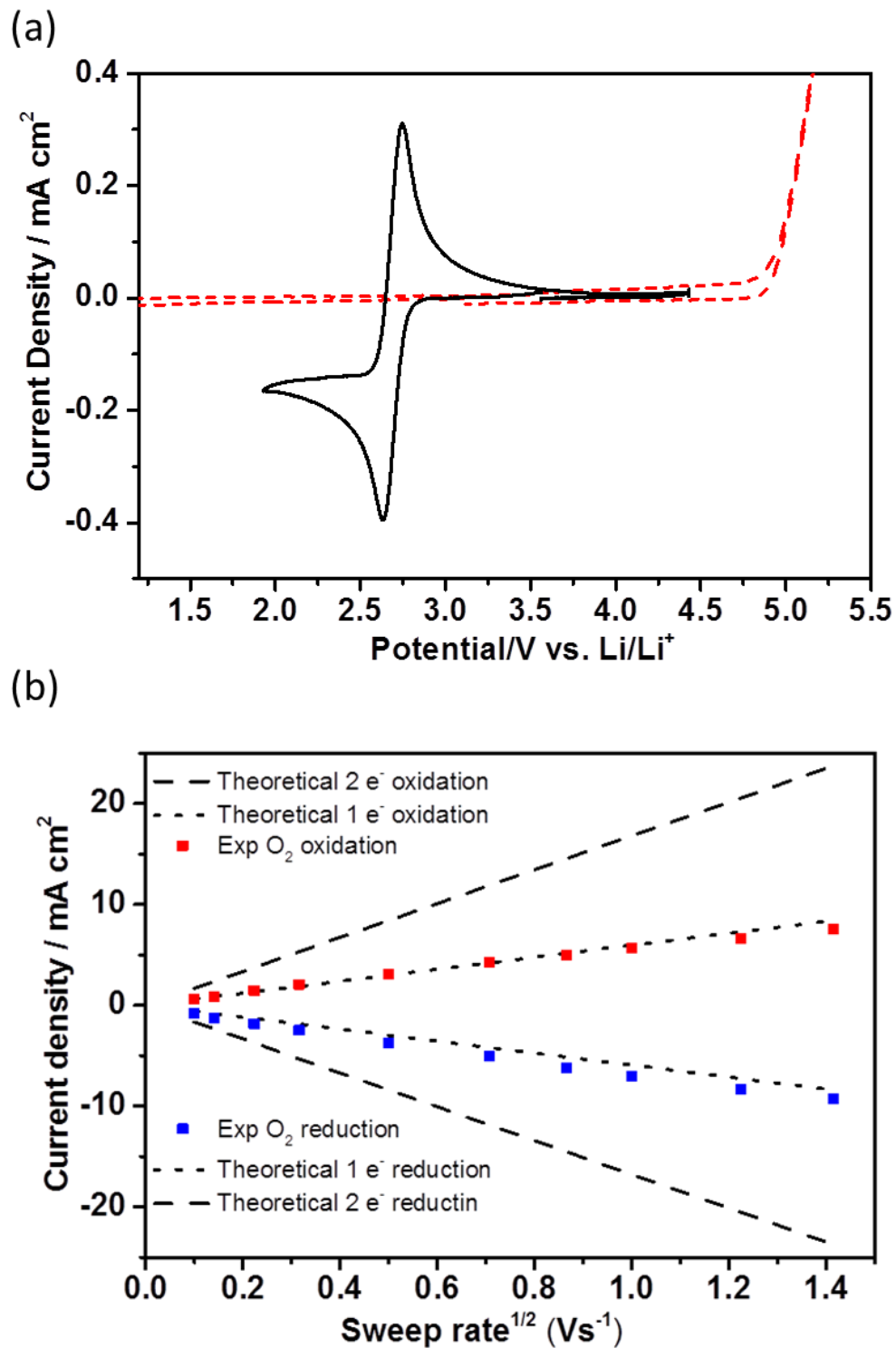


Figure 4.1 (a) Cyclic voltammogram in 0.1 M TBAClO₄/DMSO on a glassy carbon disc electrode, sweep rate 10 mV / s. Showing argon (red dotted line) and oxygen saturated solution (black) electrochemistry (b) Randles Sevcik plot of 0.1 M TBAClO₄/DMSO demonstrating a 1 e⁻ transfer.

The reversible behaviour of the superoxide redox couple O_2/O_2^- in the $TBA^+/DMSO$ media is a result of the stable solution species, in agreement with the HSAB (Hard/soft Lewis acid/base) theory²¹. Hard acids (small radius/ high positive charge) coordinate strongly to hard bases and the same for soft acids/bases. The TBA^+ is a soft acid due to its large radius and is weakly solvated in DMSO, therefore interactions between solvent and TBA^+ are weak, allowing the TBA^+ ions to move freely in the electrolyte²². TBA^+ is stabilised by the O_2^- (soft base - large radius, small charge density). Strong coordination between TBA^+ and O_2^- inhibits additional reduction to form peroxide²⁰. The change in ΔE for the reaction could be a result of the high viscosity of the solvent, this causes a slower rate of diffusion of the TBA^+ ion in the electrolyte, which coincides with the low charge passed ($Q_a/Q_c = 0.70$) in the electrolyte.

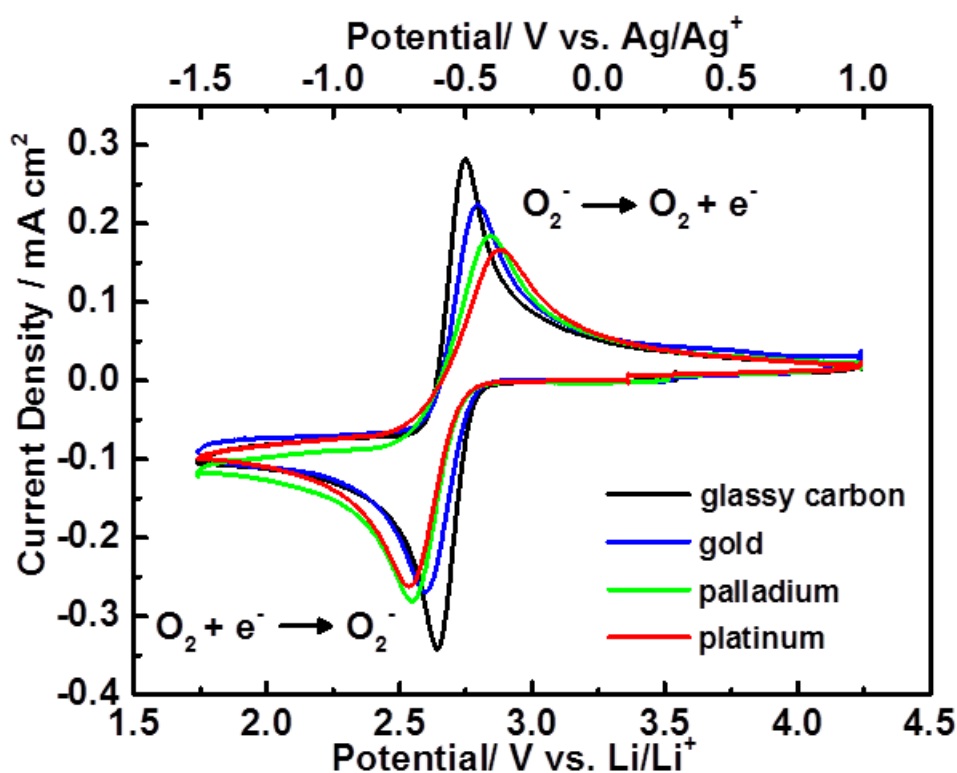


Figure 4.2. Cyclic voltammograms of 0.1 M $TBAClO_4$ in DMSO (saturated with O_2) on a variety of polycrystalline electrode surfaces. Sweep rate 10 mV / s.

Table 4.1 Data from cyclic voltammograms of 0.1 M TBAClO₄ in DMSO on various polycrystalline electrodes in Figure 4.2

	E_p^c (V) vs. Li/Li ⁺	E_p^a (V) vs. Li/Li ⁺	I_p^c (mA cm ⁻²)	I_p^a (mA cm ⁻²)	ΔE_p (V) vs. Li/Li ⁺	I_p^a/I_p^c	Q_a/Q_c
GC	2.64	2.75	0.35	0.35	0.11	0.89	0.70
Au	2.60	2.79	0.29	0.27	0.19	0.93	0.79
Pd	2.55	2.84	0.32	0.25	0.29	0.78	0.90
Pt	2.53	2.88	0.28	0.22	0.35	0.79	0.95

The electrochemistry of 0.1 M TBAClO₄ in DMSO saturated with oxygen varies between different electrode surfaces (**Fig. 4.2**). The reversibility of the O₂⁻ couple is affected when the electrode surface is changed.²³ Glassy carbon (GC) is the most reversible ($\Delta E = 110$ mV), whereas platinum is the least reversible ($\Delta E = 350$ mV) (**Table 4.1**). The change in reversibility is accounted for by the interactions of O₂⁻ with the surface, whereby Pt has the slowest reaction kinetics of the three surfaces (Pt < Pd < Au), with O₂⁻ being the most strongly chemisorbed, which is in agreement with density function theory calculations, where O₂⁻ is energetically favourable to chemisorb to the Pt surface.²⁴ There is little interaction with the surface on the GC electrode, unlike Au, Pd and Pt, where dioxygen can chemisorb.^{25, 26} Pt has the strongest interaction with O₂⁻ due to the bonding of the 5d_{xy} and O₂⁻ 2π* orbitals, giving a higher adsorption energy and shorter metal-oxygen bond length than with Au. Au has a filled d orbital so O₂⁻ is not chemisorbed like Pt; a weaker interaction still occurs due to a distortion of charge density creating an overlap of bonding

orbitals.²⁴ The same principle is applied for Pd (bonding of the $4d_{xy}$ and $O_2^- 2\pi^*$ orbitals), however Pd has a lower oxygen binding energy than Pt.²⁶ Previous studies have shown similar behaviour on GC electrodes with different solvent electrolytes such as dimethyl ether where a change in reversibility is observed due to the different solubility and kinetics, but a $1e^-$ reduction mechanism is still observed.²¹

4.4 Comparison of SERS, SHINERS and smooth surfaces in non-aqueous electrolytes

Studying the ORR using 0.1 M TBAClO₄ in dimethyl sulfoxide (DMSO) on a smooth polycrystalline gold electrode demonstrated that Raman spectroscopy on a surface without any enhancement is inherently weak (**Fig. 4.4a**). The spectrum at open circuit potential (OCP) displays DMSO solvent peaks. No spectral bands were observed for the supporting salt. The lack of peaks is likely a result of no surface plasmons to enhance the inelastically scattered photons of surface adsorbed tetrabutylammonium (TBA⁺). Raman scans were taken at decreasing potentials down to 1.84 V. There was no change observed in peak position or intensity from the OCP spectrum at any potential.

The Au surface can be electrochemically roughened prior to experiments using an oxidation-reduction cycle as mentioned earlier (**Chapter 2.7**); this created a nanostructured surface, which leads to a distribution of charge when excited by photons²⁶, enhancing the local electric field. The chemically adsorbed molecules can also undergo charge transfer with the surface that can in turn increase the polarisability²⁷. Roughening the surface displays a notable enhancement of the surface species (**Fig. 4.3b**) in the same electrochemical system as **Fig. 4.3a** compared with the smooth surface. At the open circuit potential (OCP) only peaks assigned to DMSO were visible (**Fig. 4.15 and Table 4.6**). The growth of two peaks at 1110 cm⁻¹ and 490 cm⁻¹ were observed when the potential was decreased, these peaks account for the formation of free superoxide (O₂⁻) and Au-O respectfully. The position of these peaks agree well with literature.^{19,28} The experiment was run without the presence of oxygen (cell purged with argon) (**Fig. 4.4**) no peaks grew in

either the superoxide or Au-O region, confirming these peaks are a result of the presence of oxygen.

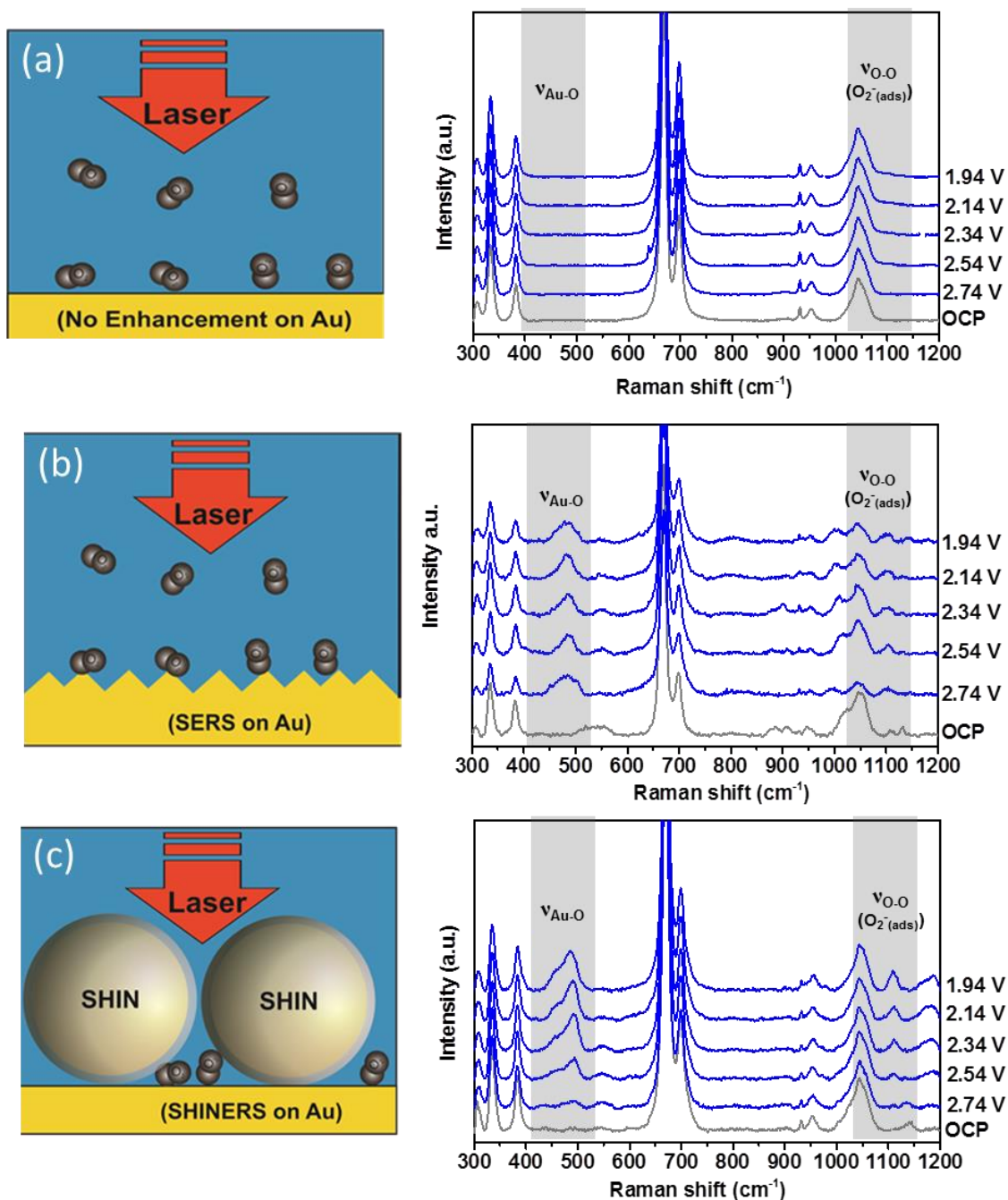


Figure 4.3 Raman spectra of 0.1 M TBAClO₄ in DMSO (saturated with O₂) on a gold polycrystalline disc electrode with accompanying diagrams comparing the differing effects of (a) smooth (b) roughened (c) SHIN enhanced electrode surfaces

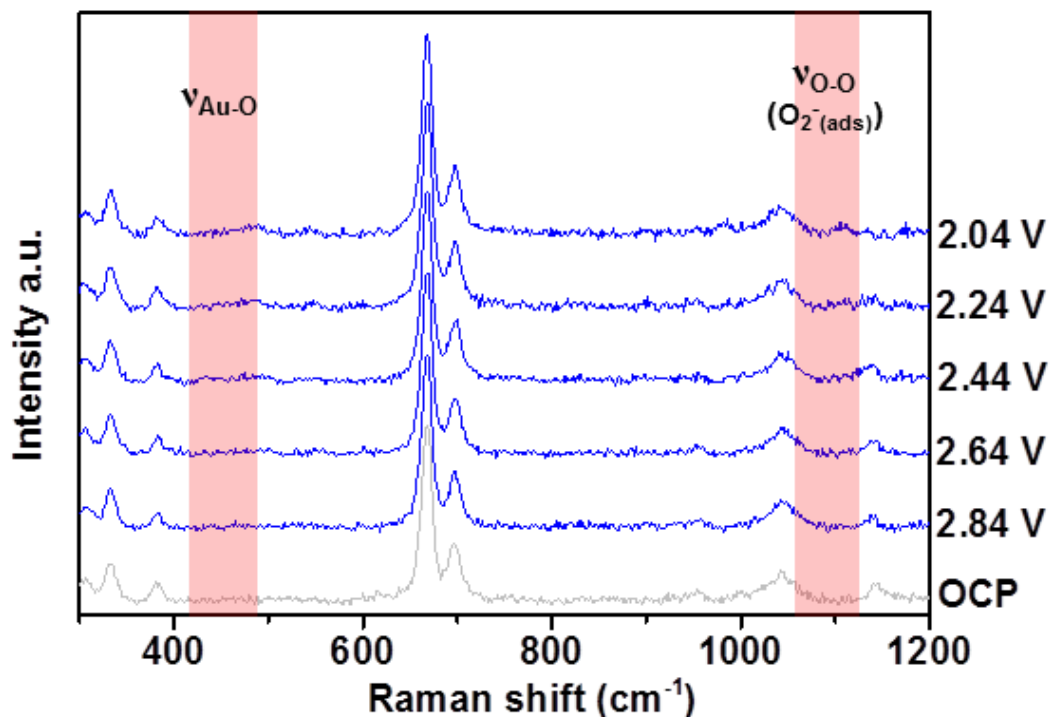


Figure 4.4 Raman spectra of 0.1 M TBAClO₄/ DMSO purged with argon (i.e. no oxygen) on SERS active gold.

SHINs are an alternative method of enhancing the Raman signal of the substrate molecules on the electrode surface. In the same 0.1 M TBAClO₄/DMSO electrolyte media as the reaction on a smooth polycrystalline gold electrode, 2 μ l of SHINs were drop cast onto the Au surface (**Fig. 4.3c**). The OCP Raman spectrum only showed DMSO solvent peaks in agreement with the polycrystalline surface with and without surface enhancement. The *in situ* Raman spectra (**Fig. 4.3c**) between 2.84 V and 1.84 V observed the growth of two peaks at 1110 cm⁻¹ and 490 cm⁻¹ for the free O₂⁻ and gold oxide peaks.²⁷ Additional peaks have also been observed to grow in both the SERS and SHINS spectra at 550 cm⁻¹ and 1020 cm⁻¹ (Fig. 4.3b and c). These peaks have previously been assigned by Aldous as a result of the reorientation of TBA⁺ at the electrode surface.²⁷

A comparison of the two sets of spectra for SERS and SHINERS demonstrated that SHINERS is a useful technique to monitor the ORR in a non-aqueous electrolyte

media, without loss of signal intensity from the different method of phonon enhancement. To confirm the origin of the observed peaks, the experiment was run without the presence of oxygen, under argon (**Fig. 4.5**). No peaks are seen to grow in either the O_2^- or Au-O spectral region, within similar potential cycling limits.

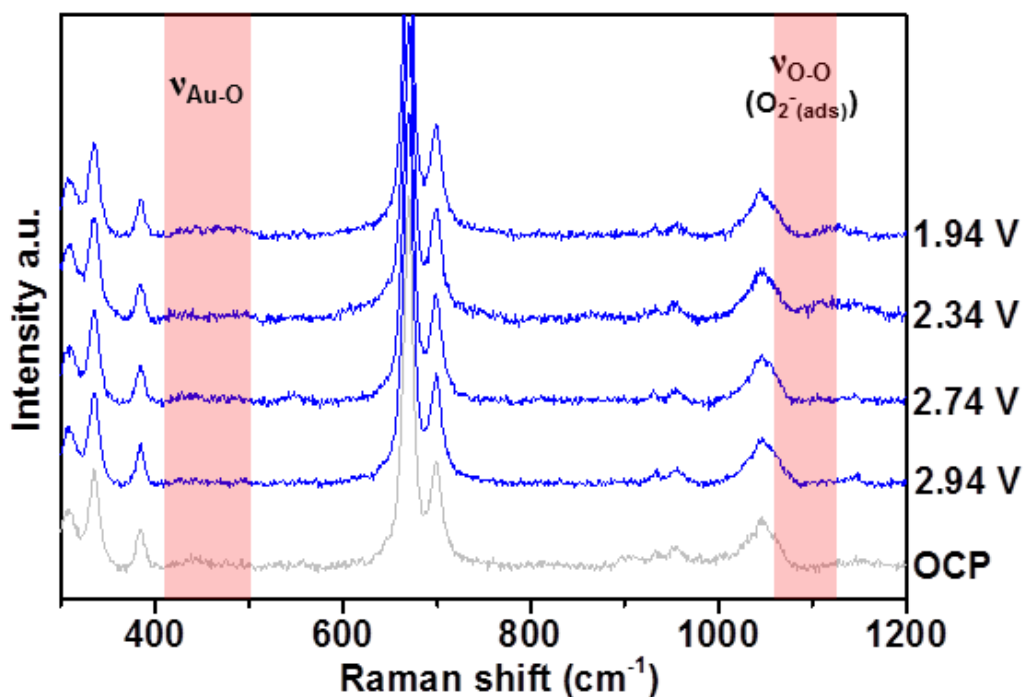


Figure 4.5 Raman spectra of 0.1 M TBAClO₄/ DMSO purged with argon (i.e. no oxygen) on SHIN enhanced gold electrode surfaces.

Furthermore **Fig. 4.6** shows that SHINs have no effect on the electrochemistry as the electrochemical response with and without SHINS is very similar after taking into account the changes in surface area between each technique.

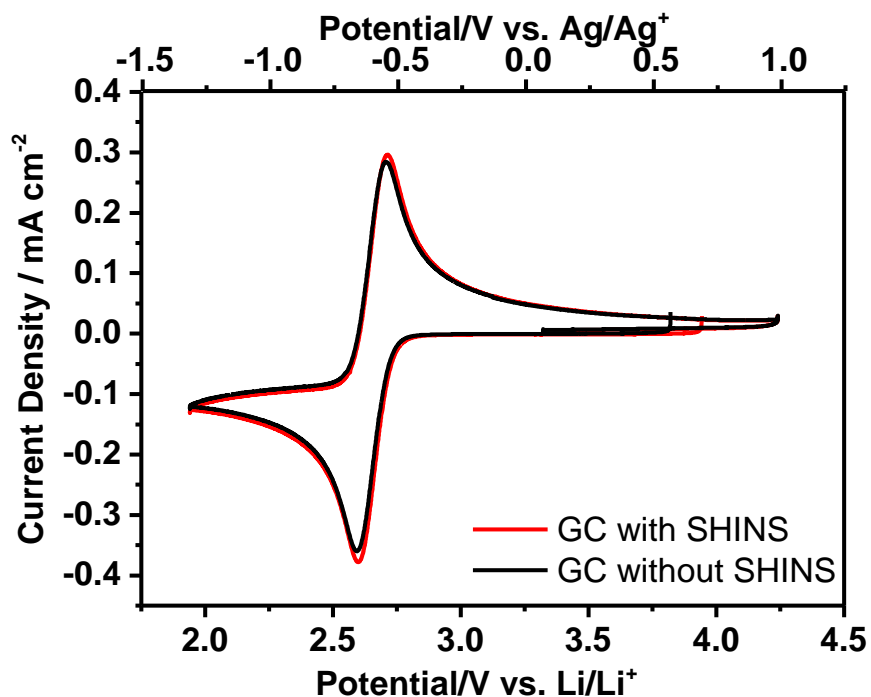


Figure 4.6 Cyclic voltammograms comparing the electrochemical changes between smooth, roughened and SHIN enhanced gold surfaces. Sweep rate 50 mV /s in 0.1 M TBAClO₄/DMSO (saturated with O₂).

4.5 Behaviour of the ORR on different electrode surfaces without the presence of lithium

The Pd surface exhibits similar behavior to the Au surface for the ORR (Fig. 4.7a). A peak at 1108 cm^{-1} for O_2^- is observed from 2.74 V and grows in intensity with decreasing potential, correlating with the cyclic voltammetry data in Fig. 4.2. A corresponding peak at 486 cm^{-1} for ($\nu_{\text{Pd-O}}$) grows proportionally to the O_2^- peak. The *in situ* Raman spectra on Pt (Fig. 4.7b) showed a variance in the spectral response in comparison to Au and Pd. At 1108 cm^{-1} a peak assigned to $\nu_{\text{O-O}}$ of O_2^- grew in intensity with increasing reduction potential, similar to that observed on Au and Pd. However, on Pt unlike Au and Pd the interaction with the Pt surface was different.

Table 4.2 Raman band positions of surface species on various polycrystalline electrodes.

Electrode Surface	Raman peak positions (cm^{-1})	
	Superoxide (O_2^-)	Metal-oxygen
GC	1107-1128	N/A
Au	1110	490
Pd	1108	486
Pt	1108	456 + 484

Initially on the Pt surface, a peak was observed at the lower wavenumber of 456 cm^{-1} and grew in intensity with decreasing potential. A second peak at 484 cm^{-1} grew at more negative potentials at the expense of the 456 cm^{-1} peak, which then decreased in intensity. The onset of the 484 cm^{-1} occurs at the same potential as superoxide is observed on the Pt surface. In both Fig. 4.4c and 4.7b, a small band at

1179 cm^{-1} is observed to appear (and diminish in the case of Pt); its assignment will be discussed later within this chapter. An additional band at 920 cm^{-1} grows with potential on the Pd and Pt surface, this is related to the O_2^- and TBA^+ interaction at the surface but cannot be conclusively assigned without further understanding.

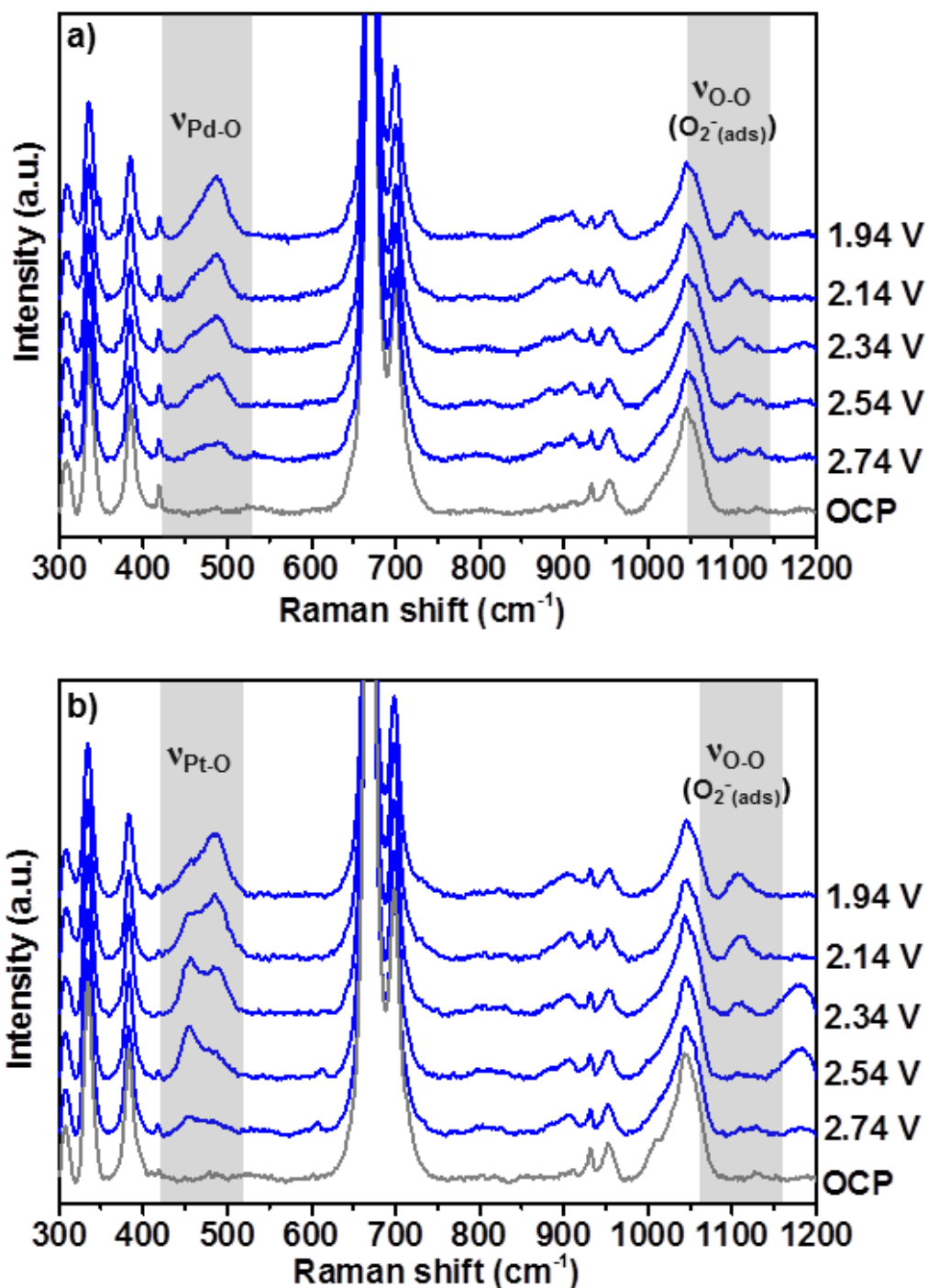


Figure 4.7 Raman spectra of 0.1 M $\text{TBAClO}_4/\text{DMSO}$ (saturated with O_2) on SHIN enhanced (a) Pd (b) Pt electrode surfaces.

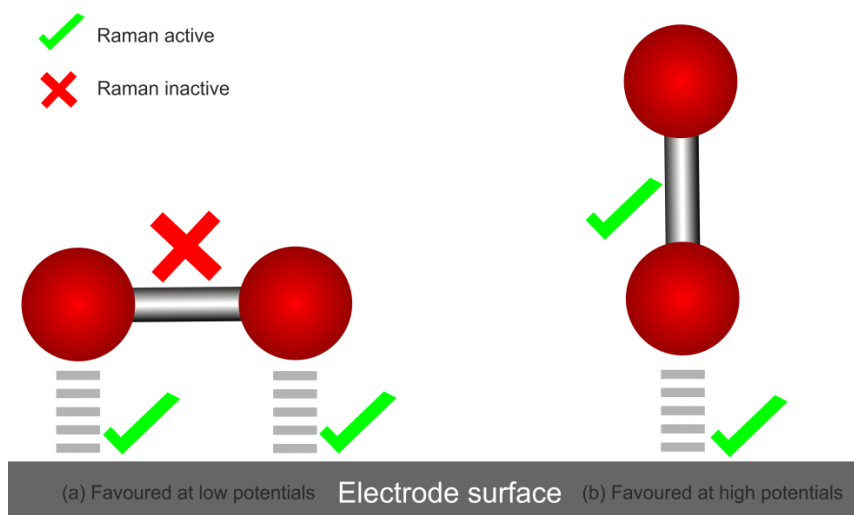


Figure 4.8 Schematic of active Raman vibrational modes in relation to oxygen adsorbed on a platinum surface.

The SHINERS data demonstrates variation of O_2^- interaction between Pt and the two other metal surfaces (**Fig. 4.9 and Table 4.3**). All three surfaces exhibit a shoulder at 456 cm^{-1} , for Au and Pd this remains a shoulder on the peak at 490 cm^{-1} . At lower reduction potentials, the peak at 456 cm^{-1} is more intense, as the potential decreases the peak at 490 cm^{-1} becomes dominant, whilst the earlier peak decreases in intensity (**Fig. 4.9b**). It is likely the two peaks originate from different vibrational stretching modes of O_2^- adsorbed on the metal surface²⁸. At lower potentials, there is a lower surface coverage of O_2^- on Pt allowing the O_2^- to have a flat orientation; with increasing negative reduction potentials, an end on orientation is favoured (**Fig. 4.8**). This could account for the flat conformation rather than the end on conformation on Pt, unlike Au and Pd, which favour the end on conformation due to a weaker interaction with the surface of the electrode²⁴. A flat O_2^- conformation would account for no superoxide band being present at more positive potentials. This is a result of the O-O stretch parallel to the surface being Raman inactive. Furthermore the interaction of the solvent with the electrode surface also needs to be taken into account; at less negative potentials DMSO may passivate the surface, preventing the

onset of dioxygen adsorption. Future studies using single crystal electrodes with SHINERS would be required to clarify the exact mechanism taking place at the platinum surface, in combination with appropriate level theory calculations.

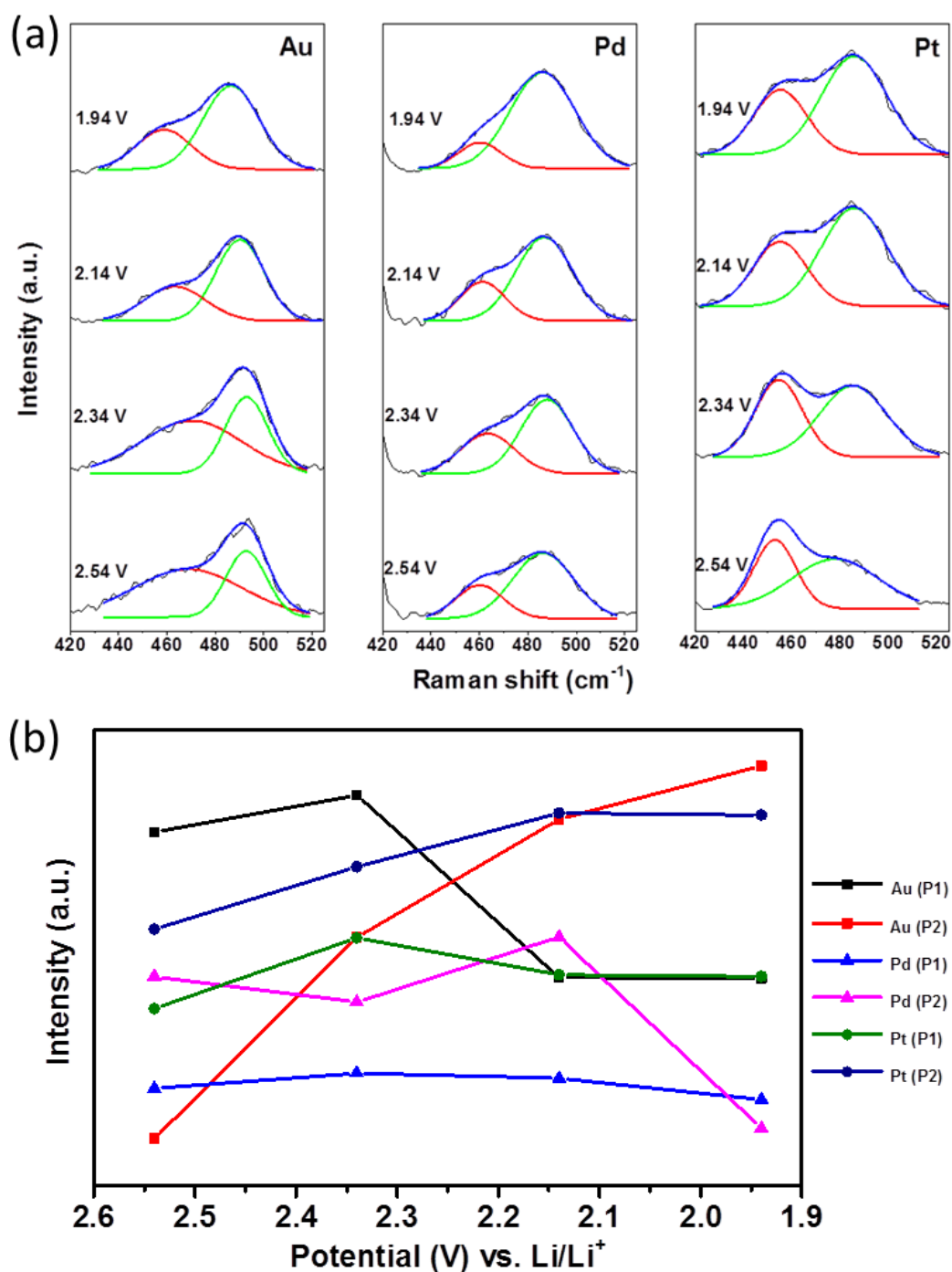


Figure 4.9 (a) Gaussian peak fitting of Raman bands of oxygen saturated 0.1 M TBAClO₄ in DMSO on Au, Pd and Pt electrode surfaces. **(b)** Integrated areas from peak fitting in Fig 4.9a.

Table 4.3 Peak positions, integrated area and full width half maximum (FWHM) data for Gaussian peak fitting of Raman bands in **Fig. 4.7**.

E	Au			Pt			Pd		
	Peak Position (cm ⁻¹)	FWHM (cm ⁻¹)	Area (a.u.)	Peak Position (cm ⁻¹)	FWHM (cm ⁻¹)	Area (a.u.)	Peak Position (cm ⁻¹)	FWHM (cm ⁻¹)	Area (a.u.)
1.94 V	458	27	81134	455	26	82001	460	21	27920
	486	27	174465	485	32	152800	486	32	15296
2.14 V	461	30	81592	455	26	82737	461	22	37314
	490	24	151055	485	32	153724	486	27	99232
2.34 V	470	48	161483	454	23	98995	463	26	39508
	492	20	99212	485	33	130042	488	26	70610
2.54 V	468	53	145317	453	20	67859	460	33	32695
	493	20	10687	477	42	102749	486	30	81913

The GC surface exhibits different behaviour to the metal surfaces analysed previously (**Fig. 4.10**). There was no Raman peak observed between 400 and 550 cm^{-1} at any potential on the GC electrode surface. Thereby there is an absence of a metal- O_2^- interaction, which indicates that the SHINs are pinhole free (#). This provides strong verification that the O_2^- peak ($\nu_{\text{O-O}}$) at $\sim 1110 \text{ cm}^{-1}$ originates solely from its interaction at the GC surface, not with the gold core of the SHIN, with it being detected solely due to the Raman enhancement from the SHIN particles.

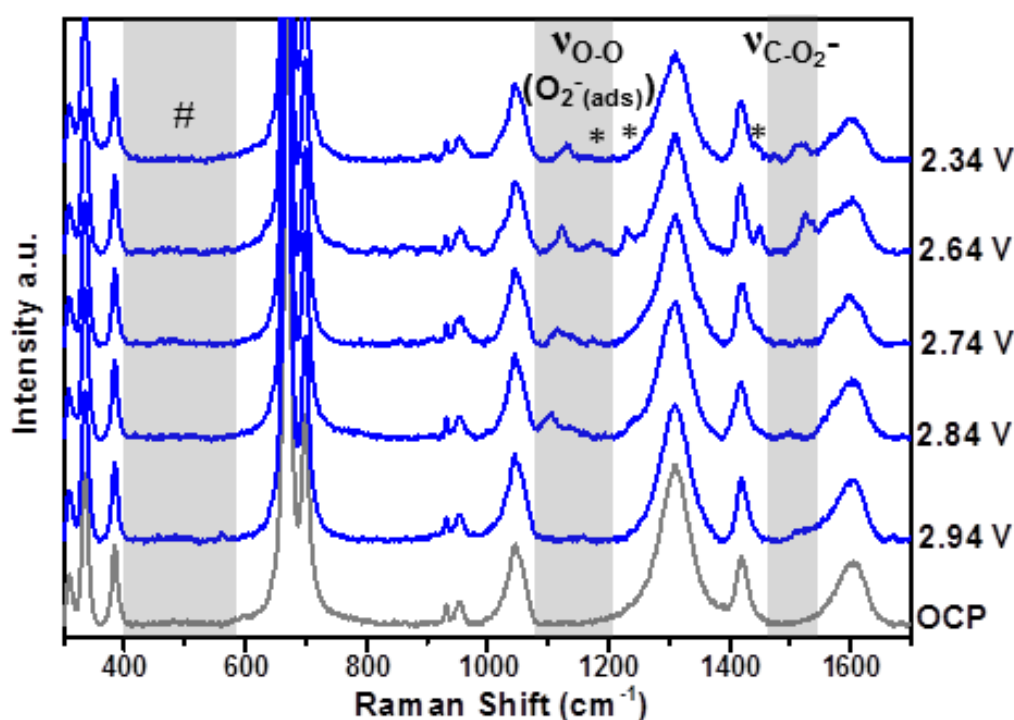


Figure 4.10 Raman spectra of 0.1 M $\text{TBAClO}_4/\text{DMSO}$ (saturated with O_2) on SHIN enhanced glassy carbon disc electrode. (# is Metal- oxygen region, * tentatively assigned bands).

The formation of O_2^- on the GC surface occurred below 2.84 V in the reduction sweep at 1107 cm^{-1} , the band has a blue shift to 1123 cm^{-1} with decreasing potential.²⁹ At lower potentials, O_2^- is bound at more favourable sites on the surface, with increasing concentration O_2^- is forced into less favourable sites, reducing the interaction with the surface causing a positive shift in the Raman band, this coincides

with a peak at 1520 cm^{-1} that could be a result of the interaction of O_2^- with the graphitic rings in the carbon.³⁰ The interaction of the O_2^- with the graphitic ring could increase with decreasing potential, creating greater distortion within the ring and accounting for the wavenumber shift of the O_2^- peak. Spectra with a larger Raman window were taken on a gold electrode (**Fig 4.11**). This data demonstrated the peaks in the 1200 cm^{-1} to the 1500 cm^{-1} region were a result of interaction with the carbon surface and not generic to any substrate surface.

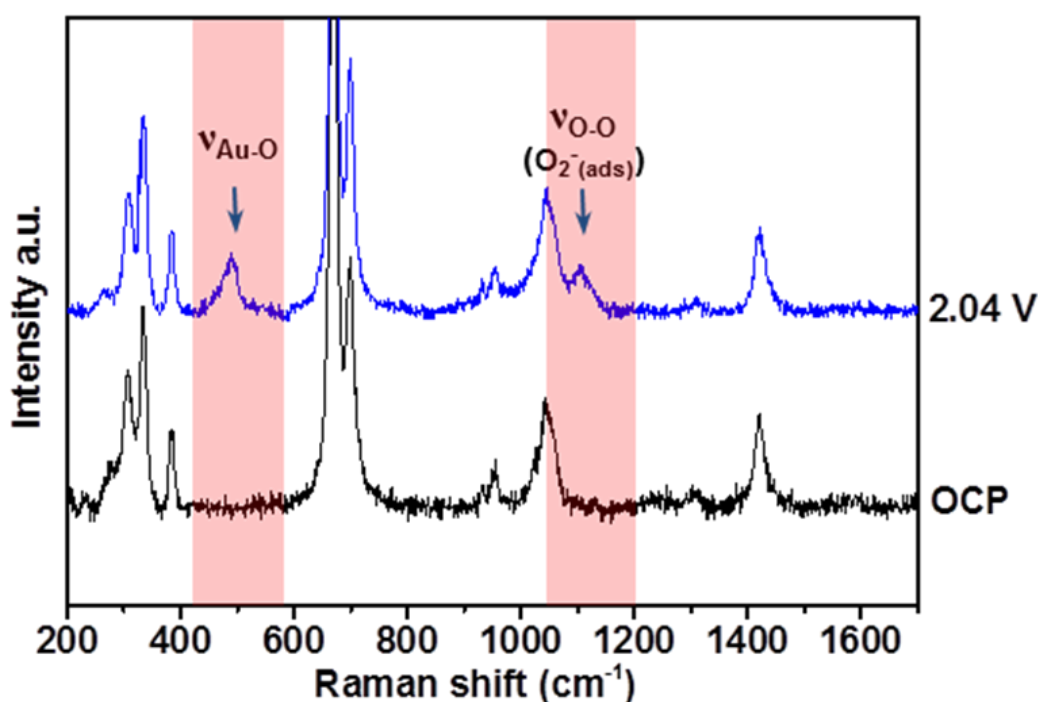


Figure 4.11 Raman spectra of 0.1 M TBAClO₄/DMSO (saturated with O₂) with a wider spectral range (200-1700 cm⁻¹) demonstrating peak formation associated solely to glassy carbon and not a result of SHINs.

SHINERS on GC also displayed bands at 1179, (as seen in **Fig. 4.4c** and **4.7b**) 1230 and 1450 cm⁻¹ that coincide with the ORR (**Fig. 4.10**). No potential dependent electrolyte bands could be assigned to these peaks, nor known reduced oxygen salts (**Fig. 4.15** and **Table 4.6**).²⁷ We speculate that the band at 1179 cm⁻¹ could be assigned to HO₂, as its position is close to the band at 1165 cm⁻¹ identified by the group of Gewirth for HO₂ adsorbed onto Au in perchloric acid (HClO₄) solution.³¹

Concurrently the band at 1450 cm^{-1} can be then tentatively assigned as $\nu\text{HO}_2\text{-C}$, with the band at 1230 cm^{-1} remaining as yet unassigned. Strict drying protocol ensured that all measurements took place in H_2O content below 20 ppm, as determined by Karl Fisher titration. Thereby we believe the nature of the measurements is sensitive to trace water contamination. Certainly further investigations using SHINERS to understand the effect of water concentration on these bands, with the use of isotopic labelling to strengthen band assignments is warranted.

4.6 Studying ORR in the lithium-oxygen battery: A surface and solvent dependant reaction

A comparison of the cyclic voltammetry data of 0.5 M LiClO_4 in DMSO and MeCN solvents (**Fig. 4.12**) displays a notable difference in the electrochemical behaviour of the reduction and oxidation species between the two solvents on glassy carbon (**Table 4.4**). Acetonitrile exhibits a single very wide reduction peak at 2.46 V. It is hypothesised that this peak is a result of a 1 e^- reduction of oxygen in the presence of lithium to form lithium superoxide. This also accounts for the loss of current as LiO_2 can lead to electrode passivation.³² In comparison DMSO has a much stronger reduction peak. This reduction peak has a shoulder around 2.5 V, indicating a second process. At lower concentrations there is a clear separation of these two peaks, which has been regularly observed in the literature.³² In DMSO the first peak is likely a result of a one electron reduction of O_2 to O_2^- followed by ion coupling with Li^+ to form LiO_2 ³². This is followed by the second electron transfer or disproportionation of LiO_2 to form Li_2O_2 (**see introduction, Eq. 1.1-1.5**).

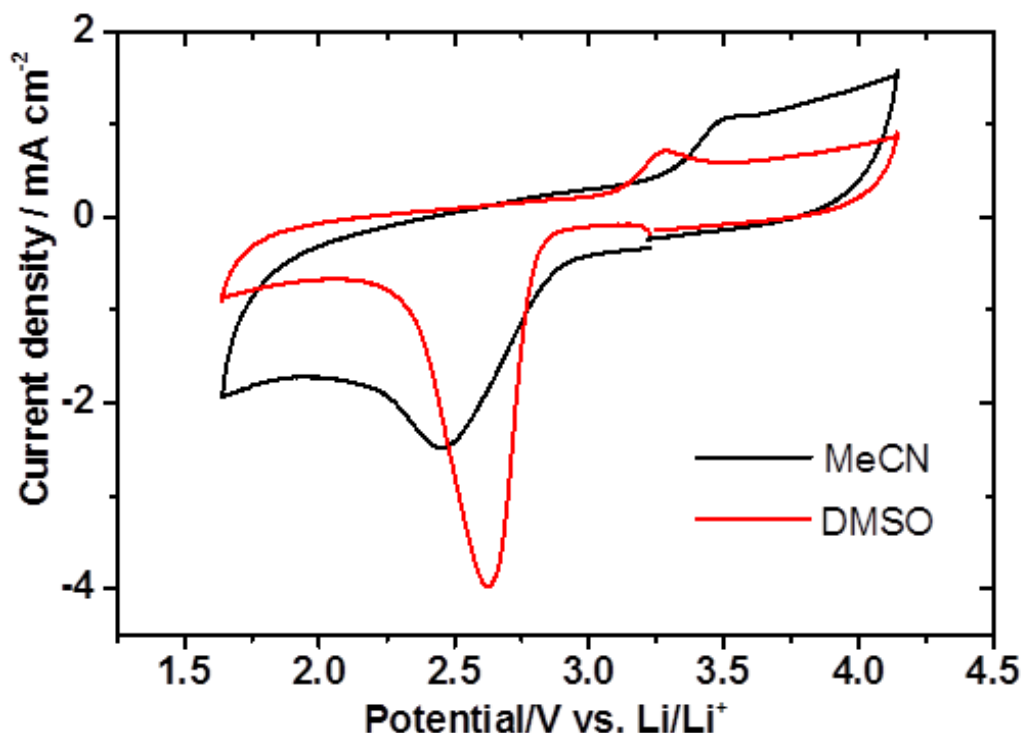


Figure 4.12 Cyclic voltammograms of 0.5 M LiClO₄ in DMSO and MeCN (saturated with O₂) on a glassy carbon disc electrode. Sweep rate 10mV/s.

Table 4.4 Peak assignments from cyclic voltammogram data in **Fig. 4.12**.

	E_p^c (V) vs. Li/Li ⁺	E_p^a (V) vs. Li/Li ⁺	I_p^c (mA cm ⁻²)	I_p^a (mA cm ⁻²)
DMSO	2.62	3.28	3.97	0.72
MeCN	2.46	3.51	2.51	1.10

SHINERS were employed to investigate the ORR in the presence of Li⁺ in low (MeCN, 14.1) and high (DMSO, 29.8) donor number solvents. In 0.5 M LiClO₄/MeCN (**Fig. 4.13a**), SHINERS detected the growth of LiO₂ at 1129 cm⁻¹ on GC below 2.84 V, with Li₂O₂ not detected, due to the absence of the main peroxide band at 790 cm⁻¹. In addition, a peak at 1500 cm⁻¹ was observed in the MeCN Raman

spectra at lower reduction potentials. This peak is likely the result of LiO_2 interacting with a vibrational mode of the graphitic ring³⁰ (**Table 4.5**). Additional peaks (*) were observed in the spectra however they have not been conclusively assigned. SHINERS on GC in 0.5 M $\text{LiClO}_4/\text{DMSO}$ (**Fig. 4.13b**) showed the appearance of Li_2O_2 at 789 cm^{-1} from 2.74 V, which remained as the potential decreased further to 1.74 V. At 2.74 V bands pertaining to LiO_2 at 1130 cm^{-1} and $\text{LiO}_2\text{-C}$ at 1500 cm^{-1} were also detected on the GC electrode. The appearance of LiO_2 is indicative of a mechanism where both Li_2O_2 and LiO_2 are formed as stable products on the GC surface. A small peak at 1105 cm^{-1} was observed at 1.94 V possible due to O_2^- on the electrode surface. The proposed decomposition reaction of DMSO to dimethyl sulphone (DMSO_2) was unable to be established in our measurements, due to the absence of a peak around 1142 cm^{-1} .^{25, 33}

Table 4.5 Raman peak positions (cm^{-1}) of spectra in **Fig. 4.13** and corresponding positions of products on gold surface (*Peak positions taken from Bruce et al³⁴).

Assignment	GC		Au	
	MeCN	DMSO	MeCN*	DMSO
Li_2O_2	-	789	790	789
LiO_2	1129	1130	1132	-
$\text{C-O}_2\text{Li}$	1450	1500	-	-
HO_2	1179	-	-	-
D band	1310	1309	N/A	N/A
G band	1600	1600	N/A	N/A

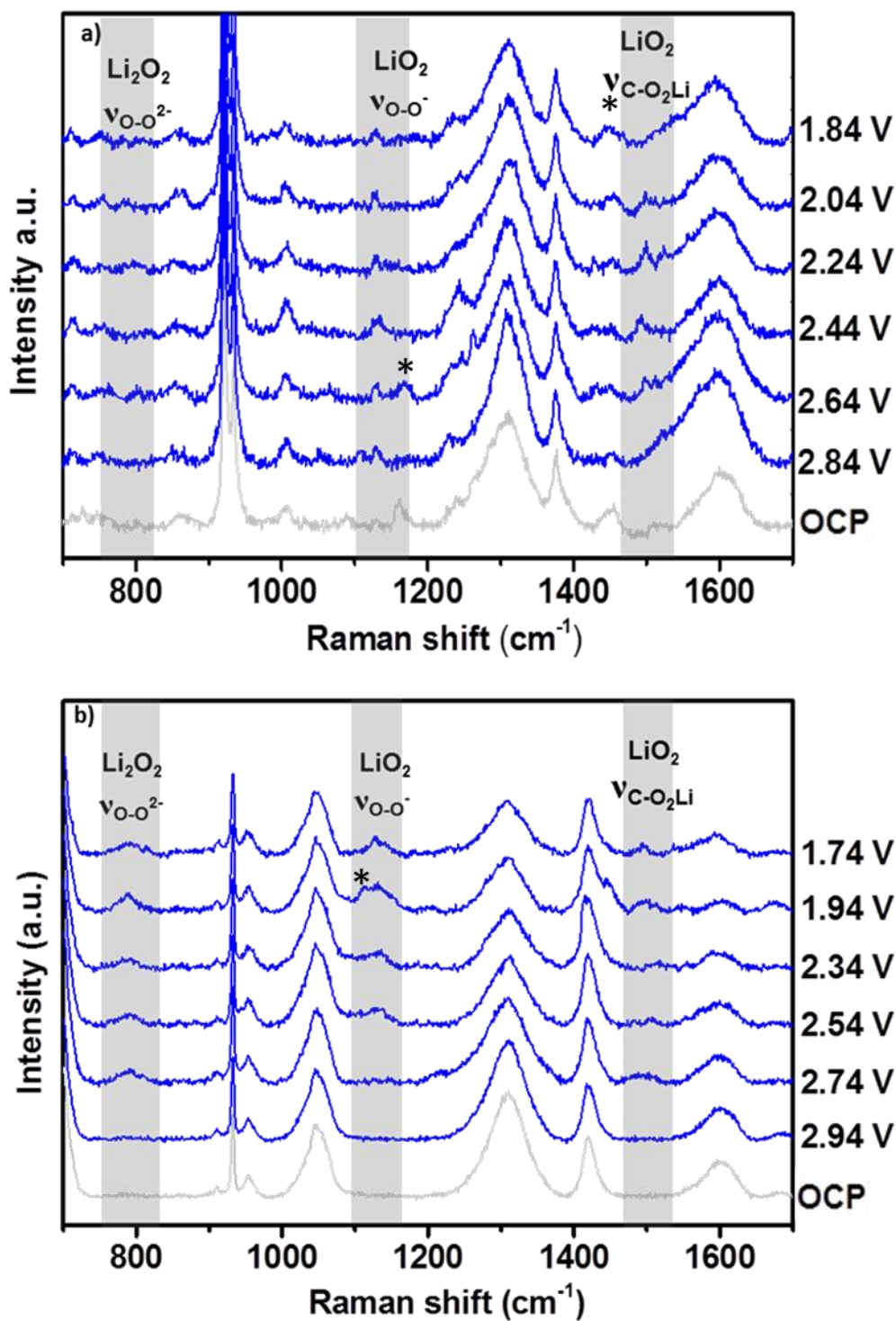
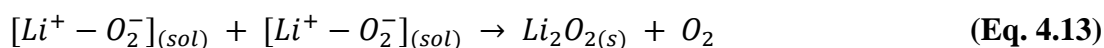
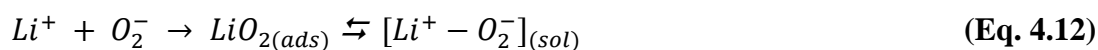


Figure 4.13 *In situ* Raman spectra of (a) 0.5 M LiClO_4 in MeCN (b) 0.5 M LiClO_4 in DMSO (saturated with O_2) on smooth glassy carbon disc electrodes with SHIN's drop cast. All potentials vs. Li/Li^+ .

The data reported herein on GC is suggestive of a reaction mechanism that is both surface and solvent dependent. The solvation of the Li^+ cation in MeCN is lower due to a positive Gibbs free energy, therefore the ORR occurs on the surface and LiO_2 will be observed on the electrode³⁵ (**Eq. 4.10 and 4.11**). The interaction of LiO_2 with the carbon surface appears to stabilise the adsorbed LiO_2 species and within the experiment, no Li_2O_2 formation is observed to occur from a second electron transfer or via disproportionation. This observation agrees with work of Lu et al.³⁵ that shows the stable cycling of LiO_2 . This differs from behaviour on Au where a second electron reduction or disproportion occurs to form Li_2O_2 .³⁴ In DMSO (**Eq. 4.10, 4.11 and 4.13**), a partial surface/solution mechanism occurs, whereby both Li_2O_2 and LiO_2 are formed as the major reduction products, which is contrary to what has been reported on Au electrode substrates³⁵ (**Fig. 4.14**). LiO_2 is also bound to the carbon surface in DMSO (1500 cm^{-1}). LiO_2 can then desorb and diffuse into the bulk electrolyte, where it can disproportionate to give Li_2O_2 in agreement with data published by Ye et al.³⁶ Li_2CO_3 was not detected during ORR on GC (**Fig 4.15 and Table 4.6**), implying the decomposition of the carbon electrode was negligible during the time frame of the measurement.



The comparative differences between the reaction mechanisms on the carbon surface and that of the gold (Fig. 4.14), imply that the ORR in the presence of lithium is not solely solvent dependent. It is also dependant on substrate surface. The glassy carbon surface has a stabilising effect on LiO_2 .³² This is hypothesised to be a result of defects on the carbon surface inhibiting second electron reduction to Li_2O_2 on the surface^{32,36}.

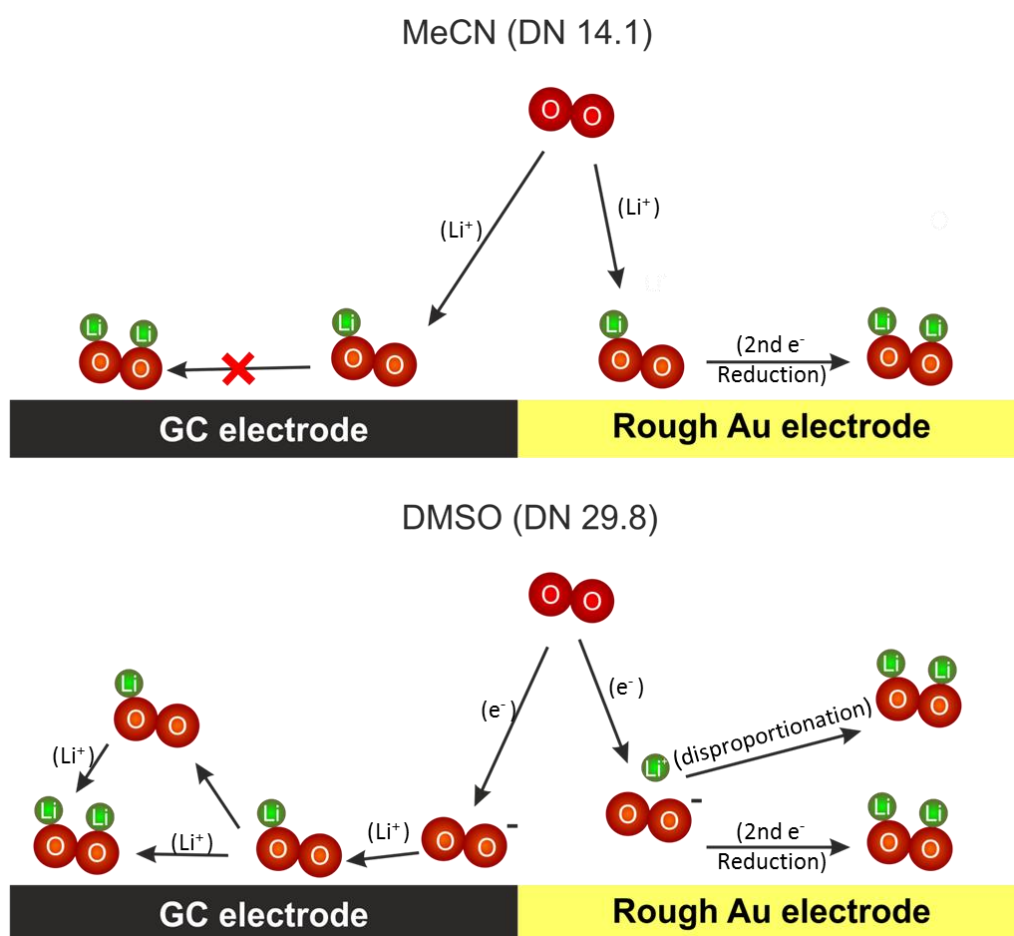


Figure 4.14 Schematic of the how the oxygen reduction reaction mechanisms taking place in a non-aqueous electrolyte in the presence of the dissolved O_2 and Li^+ .

4.7 Conclusions and future work

SHINERS has been demonstrated as an effective method of detecting intermediate species and ORR products on an array of electrode substrates, including Pt, Pd and GC, which previously SERS has been unable to access. The consistency of SHINERS has been validated by its ability to reproduce data gathered using SERS in the same electrolyte media on Au electrode surfaces. Notably the metal-superoxide band shape varies between the noble metals depending on superoxide interaction at the surface. The use of SHINERS in the presence of Li^+ has shown that both surface and solvent can be harnessed to influence ORR pathways, which may be critical in designing electrode/electrolyte interfaces that can minimise side reactions within Li-O_2 cells. This work provides a strong platform to study more complex electrolyte and electrode systems with the SHINERS technique.

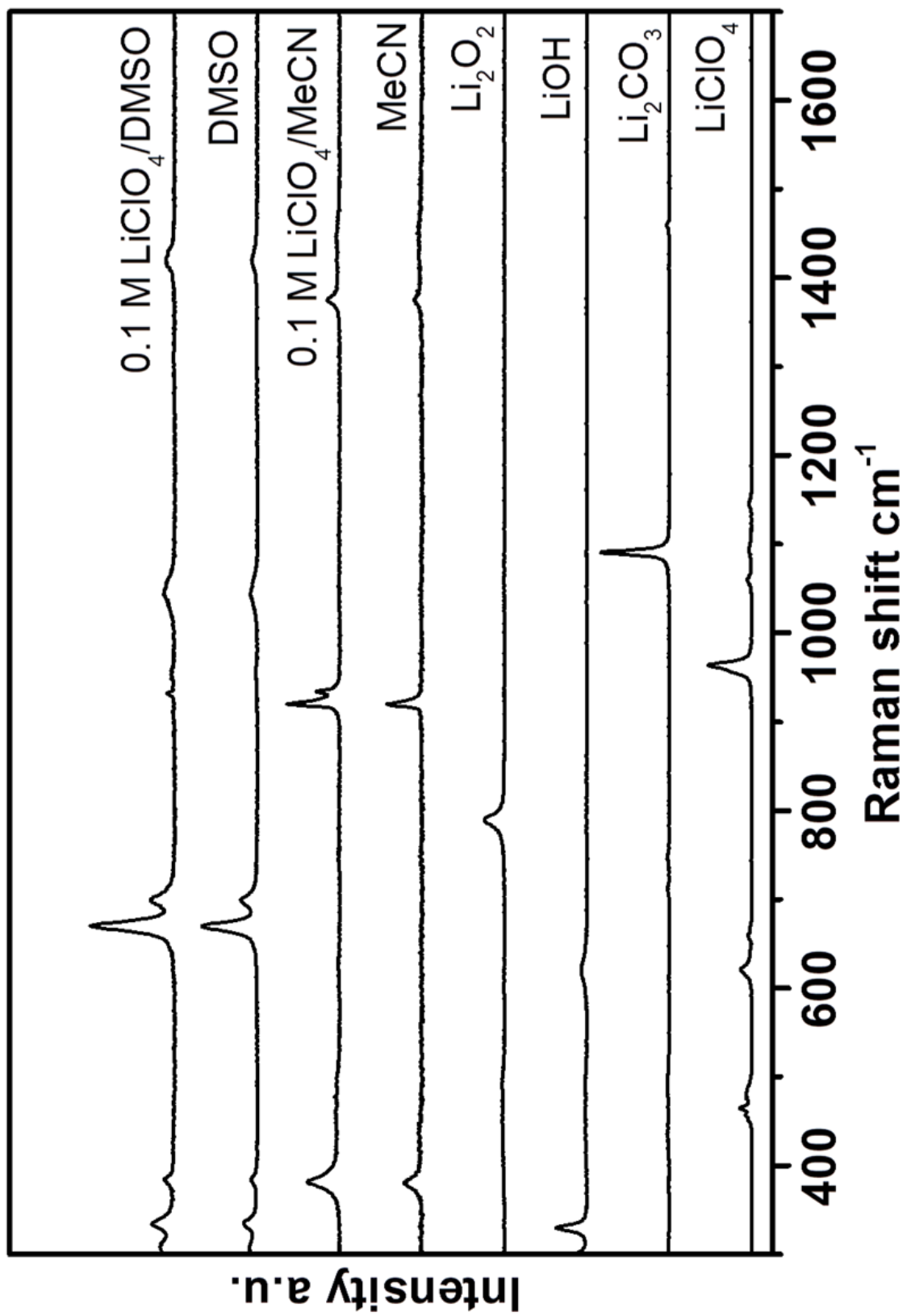


Figure 4.15 Raman spectra of solvents, salts and products associated with the oxygen reduction reactions taking place in the lithium oxygen battery.

Table 4.6 Standard Raman peak positions and assignments for solvents, salts, products and possible decomposition products associated with the oxygen reduction reaction mechanism taking place in the lithium oxygen battery. Peaks assigned in agreement with the literature (Li_2CO_3 ³⁷, MeCN ³⁸, DMSO ³⁹, LiOH ^{40, 41}, Li_2O_2 ⁴², LiClO_4 ^{43, 44})

DMSO	MeCN	LiClO ₄	Li ₂ O ₂	Li ₂ CO ₃	LiOH
334 v _{as} (C-S-O) bend	379 (CCN) _{bend}	464 (ClO ₄ ⁻)	257 (O-O) _{stretch}	274 (CO ₃ ²⁻)	288 (OH) _{lib}
382 v _s (C-S-O) bend	919 (CC) _{stretch}	483 s(ClO ₄ ⁻) _{stretch}	787 (O-O) _{stretch}	710 (A _g or B _g)	299 (OH) _{lib}
669 v _s (C-S) _{stretch}	1375 (CH ₃) _{bend}	621 (ClO ₄ ⁻)		746 (A _g or B _g)	330 (LiO)
698 v _{as} (C-S) stretch		659 (Cl-OLi)		1091 (A _g , v ₁)	620 (Li-O)
955 v _(CH3) rocking		964 v _s (Cl-O) _{stretch}		1461 (A _g or B _g , v ₃)	
1044 v _(S=O) stretch		1060 v _s (ClO ₄ ⁻) _{stretch}			
1418 v _(CH3) degen def		1095			
		1145 as(ClO ₄ ⁻) _{stretch}			
		1190 as(ClO ₄ ⁻) _{stretch}			

4.8 References

1. T. Edwards, *J. Propul. Power*, 2003, **19**, 1089-1107.
2. A. S. Arico, P. Bruce, B. Scrosati, J. M. Tarascon and W. Van Schalkwijk, *Nat. Mater.*, 2005, **4**, 366-377.
3. P. G. Bruce, S. A. Freunberger, L. J. Hardwick and J.-M. Tarascon, *Nat. Mater.*, 2012, **11**, 19-29.
4. D. T. Sawyer and R. J. P. Williams, *Oxygen Chemistry*, Oxford University Press, 1991.
5. C. Song and J. Zhang, in *PEM Fuel Cell Electrocatalysts and Catalyst Layers: Fundamentals and Applications*, ed. J. Zhang, Springer London, London, 2008, DOI: 10.1007/978-1-84800-936-3_2, pp. 89-134.
6. N. Ramaswamy and S. Mukerjee, *Adv. Phys. Chem.* , 2012, **2012**, 17.
7. D. Vasudevan and H. Wendt, *J. Electroan. Chem.*, 1995, **392**, 69-74.
8. D. H. Chin, G. Chiericato, E. J. Nanni and D. T. Sawyer, *J. Am. Chem. Soc.*, 1982, **104**, 1296-1299.
9. K. A. Radyushkina, E. O. Zonina and M. R. Tarasevich, *Soviet Electrochem.*, 1992, **28**, 736-744.
10. D. T. Sawyer and J. S. Valentine, *Acc. Chem. Res.* , 1981, **14**, 393-400.
11. K. M. Abraham, *J. Electrochem. Soc.*, 2015, **162**, 3021-3031.
12. D. T. Sawyer, M. J. Gibian, M. M. Morrison and E. T. Seo, *J. Am. Chem. Soc.*, 1978, **100**, 627-628.
13. A. W. Lodge, M. J. Lacey, M. Fitt, N. Garcia-Araez and J. R. Owen, *Electrochim. Acta*, 2014, **140**, 168-173.
14. B. Scrosati, P. Bruce, A. C. Luntz and N. Imanishi, 2015, **54**.

15. V. S. Bryantsev, J. Uddin, V. Giordani, W. Walker, D. Addison and G. V. Chase, *J. Electrochem. Soc.*, 2013, **160**, A160-A171.
16. D. Xu, Z.-l. Wang, J.-j. Xu, L.-l. Zhang and X.-b. Zhang, *Chem Commun*, 2012, **48**, 6948-6950.
17. R. Younesi, P. Norby and T. Vegge, *ECS Electrochemistry Letters*, 2014, **3**, A15-A18.
18. R. Compton and C. Banks, *Understanding Voltammetry*, Imperial College Press, 2nd edn., 2011.
19. A. J. Bard and L. R. Faulkner, *Electrochemical Methods: Fundamentals and Applications*, 1980.
20. C. Ó'Laoire, Northeastern University, 2010. PhD Thesis
21. C. O'Laoire, S. Mukerjee, K. M. Abraham, E. J. Plichta and M. A. Hendrickson, *J. Phys. Chem. C.*, 2010, **114**, 9178-9186.
22. C. O'Laoire, S. Mukerjee, K. M. Abraham, E. J. Plichta and M. A. Hendrickson, *J. Phys. Chem. C.*, 2009, **113**, 20127-20134.
23. D. T. Sawyer and J. L. Roberts Jr, *J. Electroan. Chem.*, 1966, **12**, 90-101.
24. R. G. Jungst and E. S. Meeting, *Power Source Modeling: Proceedings of the International Symposium*, Electrochemical Society, 2002.
25. M. A. Schroeder, N. Kumar, A. J. Pearse, C. Liu, S. B. Lee, G. W. Rubloff, K. Leung and M. Noked, *ACS Appl. Mater. Interfaces*, 2015, **7**, 11402-11411.
26. J. K. Nørskov, J. Rossmeisl, A. Logadottir, L. Lindqvist, J. R. Kitchin, T. Bligaard and H. Jónsson, *J. Phys. Chem. B*, 2004, **108**, 17886-17892.
27. I. M. Aldous and L. J. Hardwick, *J. Phys. Chem. Lett.*, 2014, **5**, 3924-3930.

28. J. R. McBride, G. W. Graham, C. R. Peters and W. H. Weber, *J. Appl. Phys.* , 1991, **69**, 1596-1604.
29. H. H. Yang and R. L. McCreery, *J. Electrochem.Soc.* , 2000, **147**, 3420-3428.
30. D. Zhai, H.-H. Wang, K. C. Lau, J. Gao, P. C. Redfern, F. Kang, B. Li, E. Indacochea, U. Das, H. Sun, H. H. Sun, K. Amine and L. A. Curtiss, *J. Phys. Chem. C.*, 2014,
31. X. Li and A. A. Gewirth, *J. Am. Chem. Soc.*, 2005, **127**, 5252-5260.
32. A. I. Belova, D. G. Kwabi, L. V. Yashina, Y. Shao-Horn and D. M. Itkis, *J. Phys. Chem. C*, 2017, **121**, 1569-1577.
33. N. Mozhzhukhina, L. P. Méndez De Leo and E. J. Calvo, *J Phys Chem C*, 2013, **117**, 18375-18380.
34. L. Johnson, C. Li, Z. Liu, Y. Chen, S. A. Freunberger, P. C. Ashok, B. B. Praveen, K. Dholakia, J.-M. Tarascon and P. G. Bruce, *Nat. Chem.*, 2014, **6**, 1091-1099.
35. J. Lu, Y. Jung Lee, X. Luo, K. Chun Lau, M. Asadi, H.-H. Wang, S. Brombosz, J. Wen, D. Zhai, Z. Chen, D. J. Miller, Y. Sub Jeong, J.-B. Park, Z. Zak Fang, B. Kumar, A. Salehi-Khojin, Y.-K. Sun, L. A. Curtiss and K. Amine, *Nature*, 2016, **529**, 377-382.
36. Y. Qiao and S. Ye, *J. Phys. Chem. C*, 2016, **120**, 8033-8047.
37. M. H. Brooker and J. Wang, *Spectrochim. Acta, Part A*, 1992, **48**, 999-1008.
38. Y. Sun, B. C. Pein and D. D. Dlott, *J. Phys. Chem. B*, 2013, **117**, 15444-15451.
39. W. N. Martens, R. L. Frost, J. Kristof and J. Theo Klopogge, *J. Raman Spectrosc.*, 2002, **33**, 84-91.

40. S. F. Parker, K. Refson, R. I. Bewley and G. Dent, *J. Chem. Phys.*, 2011, **134**, 084503.
41. F. Harbach and F. Fischer, *J. Phys. Chem. Solids*, 1975, **36**, 601-603.
42. T. K. Zakharchenko, A. Y. Kozmenkova, D. M. Itkis and E. A. Goodilin, *Beilstein J. Nanotechnol.* , 2013, **4**, 758-762.
43. M. Chabanel, D. Legoff and K. Touaj, *J. Chem. Soc., Faraday Trans.*, 1996, **92**, 4199-4205.
44. M. I. S. Sastry and S. Singh, *Can. J. Chem.* , 1985, **63**, 1351-1356.

Chapter 5

SHINERS on Carbon Surfaces and Composite

Electrodes

5.1 Abstract

The work presented in this chapter shows the effect of varying the substrate surface on the intensity of the signal produced from SHINERS. This has been shown by a comparative study calculating the enhancement factors on several electrode substrates and how the enhancement varies from spot to spot due to various surface factors, such as porosity.

The application of the SHINERS technique has also been used to study the mechanistic difference between edge plane and pyrolytic graphite electrodes. The detection of various reaction intermediates, products and decomposition products has helped elucidate the electrochemical pathways on the different carbon planes.

The use of SHINERS on a more practical battery electrode has also been demonstrated, with initial *in situ* spectroscopic studies for the OER within the lithium-oxygen system.

5.2 Introduction

Improvements in the lifetime and safety of lithium metal anodes and the development of stable cathodes within Li-O₂ batteries requires an understanding and control of electrode interfaces. Surface layers form at electrode interfaces either through spontaneous chemical reactions or during electrochemical cycling. This can be advantageous, providing stabilisation, but it can also hinder activity by inhibiting the kinetics and hence the rate of charge/discharge. The solid electrolyte interphase (SEI) is a passivation layer formed on the lithium metal negative electrode in non-aqueous electrolytes that allows the diffusion of lithium cations, but it is an electron insulator. It influences not only the stability and conductivity, but also the irreversible charge loss, power capability, cycle life and safety.^{1, 2} Surface layer formation is also important in Li-O₂ batteries since the formation of the reduction products can cause degradation or passivation of the electrode surface, limiting their performance and cyclability.³

Raman spectroscopy is an attractive spectroscopic technique for *in situ* investigation of lithium battery materials,⁴⁻⁷ and surface reactions in M-O₂ batteries.⁸⁻¹¹ However, the need for a surface plasmon that would be excited by the laser is limited by the structure and morphology of the surface (i.e. only roughened coinage metals).¹²⁻¹⁴ In 2010 Li *et al.*^{15, 16} developed shell isolated nanoparticles for enhanced Raman spectroscopy (SHINERS). This technique employs gold nanoparticles as portable plasmons to enhance the local vibrational modes of nearby molecules when deposited on the electrode surface (see **chapter 1**).¹⁷

SHINERS has been applied in multiple fields.¹⁸ It has been used to study an array of electrode surfaces, predominantly flat in nature, i.e. single crystals.^{19, 20} However, it is known that the roughness of the surface has a direct impact on the

enhancement factor of the SHINS, since a change in magnitude can be observed between single crystal facets of the same metal.²¹ There are only a few studies on surfaces with more porous morphologies.²² It is therefore, important to understand the varying enhancement among different surfaces in order to optimise the Raman technique for battery investigations.

5.3 How the surface morphology affects the enhancement from the SHINs

SHINERS have been used as a successful method to enhance a variety of different substrates.^{10,15} Understanding the enhancement across different substrates is of particular importance to determine whether SHINs can be utilised in different environments or whether some surfaces are SHINERS inactive. However, a quantifiable enhancement factor has only been determined on gold surfaces.^{16,21,23} Li *et al.*²¹ noted that even between different gold single crystal facets a notable change in enhancement can be observed. Such a variance in enhancement from facet to facet indicates the enhancement from substrate to substrate may change drastically.

The enhancement on gold has been determined by measuring the adsorption of pyridine on the surface. Pyridine is used as it adsorbs strongly onto the gold surface (**Fig. 5.1**), and exhibits two bands at 1010 cm^{-1} and 1036 cm^{-1} that can be assigned to the ring bending modes of the pyridine skeleton.²¹ Measuring the intensity of these bands allow the determination of the enhancement factor. However, the adsorption of pyridine is limited to gold and platinum surfaces, as pyridine does not adsorb on non-metallic substrates²⁴ such as carbon or more practical battery materials (i.e., carbon black, graphitic carbon or lithium titanate ($\text{Li}_4\text{Ti}_5\text{O}_{12}$) particles). An alternative probe molecule is required to determine the enhancement of these electrode surfaces, in order to demonstrate whether SHINERS is a viable technique to study battery mechanisms.

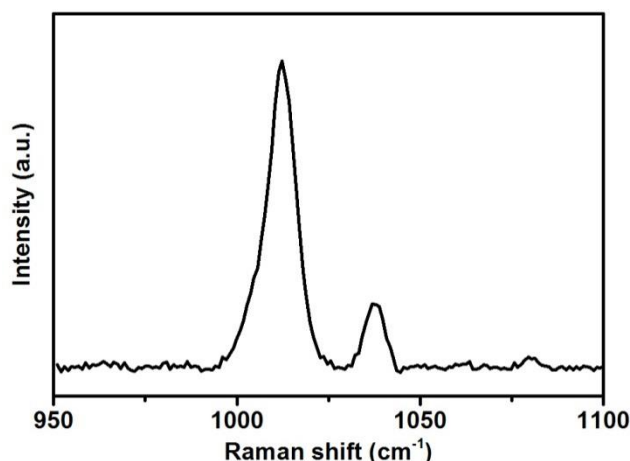


Figure 5.1 Raman spectrum of 10 mM pyridine adsorbed on a gold wafer with drop casted SHINs (55 nm Au NP, 2 nm shell).

A range of dyes have been investigated as possible candidates to study the varying enhancements between substrate surfaces. Malachite green (MG), rhodamine-6G (R-6G) and crystal violet (CryV) have all been observed to adsorb on both metallic and non-metallic substrates. Chen *et al.*²⁵ used R-6G and CryV organic dyes to investigate the SERS enhancement on substrates containing graphene oxide shell-isolated silver particles. These dyes have also been used by Zhang *et al.*²⁶ to determine EF from SHINs synthesised by atomic layer deposition (ADL) method. MG is another organic dye with characteristic Raman signal used in EF studies of starch-coated Ag nanoparticles,²⁷ and as a standard in tip-enhanced Raman spectroscopy (TERS) measurements.²⁸ Raman spectra for all the dyes show pronounced bands due to adsorption on the different surfaces, which can be clearly enhanced by the SHINs (**Fig. 5.2**). The Rhodamine 6-G (**Fig. 5.2a**) Raman spectrum has multiple absorption bands; the band at 774 cm^{-1} due to C-H out of plane bending vibration of the Xanthene skeleton was used to analyse the enhancements across different surfaces. A second band at 1180 cm^{-1} band resulting from the ring deformation was also analysed to verify the enhancement was not band specific.^{25, 29} Likewise, the 938 cm^{-1} and 1177 cm^{-1} peaks for MG and the 911 cm^{-1} and 1175 cm^{-1}

for CryV were analysed. These bands were chosen to minimise any contribution to the peak intensity from the carbon D (ca. 1330 cm⁻¹) and G (ca. 1590 cm⁻¹) bands.

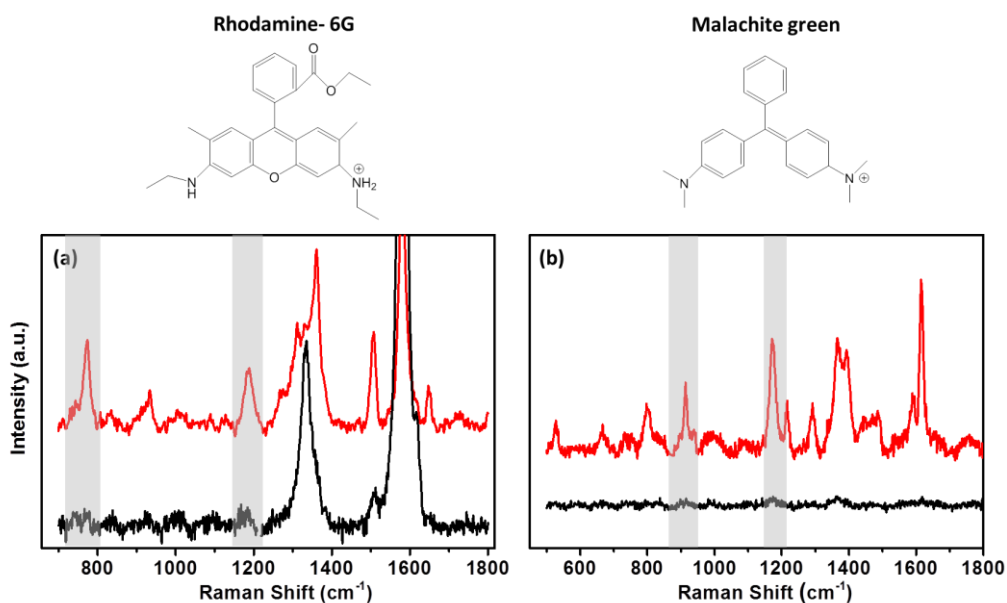


Figure 5.2 Raman spectra of (a) 0.1 mM rhodamine-6G in ethanol on BPPG with SHINs (red), without SHINs (black); (b) 0.1 mM malachite green in water on GC with SHINs (red), without SHINs (black). Shaded areas indicate the peaks analysed for EF calculations.

The intensity of the bands change from one surface to another following the trend **Au > Cu > Pt > Si > GC > carbon black** (Table 5.1), indicating the enhancement from the SHINs is directly affected by the surface nature and morphology. The enhancement is also dependent on the surface coverage of nanoparticles; therefore the peak intensity changes from spot to spot. Au displays the strongest enhancement across all of the substrates tested, with other precious metals also displaying strong enhancement (e.g. Cu and Pt). Au has been proven as a highly SERS active surface, due to the conductive nature of the surface and the dampening of the imaginary part of the dielectric function (ϵ) when roughened (Eq. 5.1).²⁴

$$\frac{E}{E_0} = \frac{6}{Im(\epsilon)} \quad (\text{Eq. 5.1})$$

The imaginary part of the dielectric function is a measure of the absorption energy of the molecule or surface, therefore minimising the energy of absorption as a result of photon excitations (ideally $\text{Im}(\epsilon) \approx 0$), will maximise the plasmon enhancement. The surface can contribute to the localised surface plasmon of the SHINs on the surface. A surface contribution is maximised on Au, then decreasing through the less SERS active materials such as Pt and Cu, followed by other transition metals having little surface contribution.³⁰

Table 5.1 Enhancement intensities of the 1175 cm^{-1} band of malachite green on different substrates in arbitrary units (a.u.) (laser power, exposure time normalised for each surface). Abbreviations; edge plane pyrolytic graphite (EPPG), basal plane pyrolytic graphite (BPPG), boron doped diamond (BDD), carbon doped zinc iron oxide ($\text{ZnFe}_2\text{O}_4/\text{C}$), lithium titanate ($\text{Li}_4\text{Ti}_5\text{O}_{12}$), SGL graphitic carbon (graphite).

Electrode Surface	Gold	Copper	Platinum	Silicon	Nickel	EPPG
Intensity (a.u.)	65700	29000	22350	19983	18600	14240

Electrode Surface	BPPG	BDD	Glassy carbon	$\text{ZnFe}_2\text{O}_4/\text{C}$	$\text{Li}_4\text{Ti}_5\text{O}_{12}$	Graphite
Intensity (a.u.)	13260	12130	10030	2920	1766	809

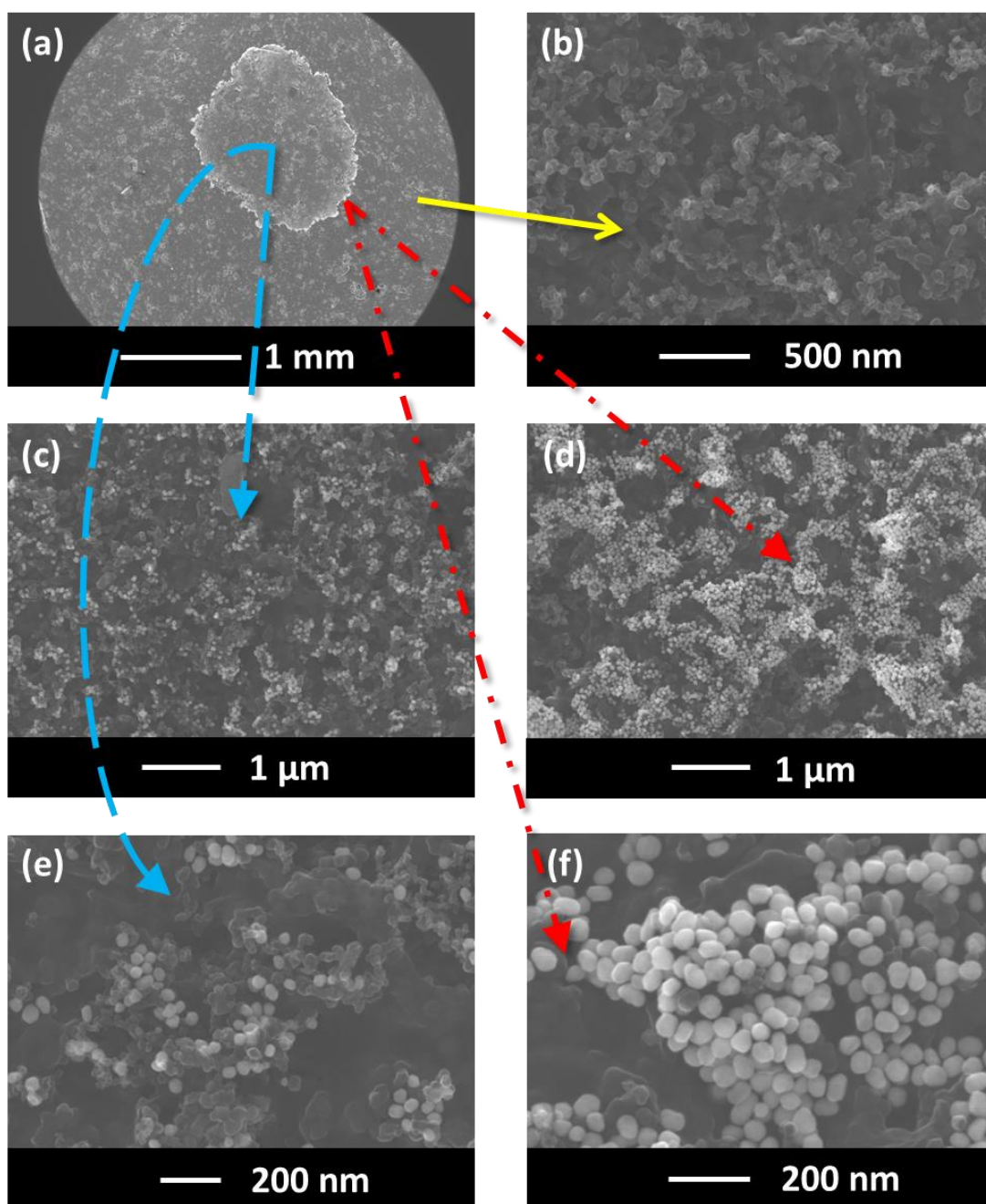


Figure 5.3 SEM images of (a) SHINs drop casted onto a $\text{ZnFe}_2\text{O}_4/\text{C}$ composite electrode, (b) $\text{ZnFe}_2\text{O}_4/\text{C}$ surface without any SHINs cast, (c) centre of spot where SHINs drop casted on the surface (low magnification), (d) edge of spot where SHINs drop casted on the surface (low magnification), (e) centre of spot where SHINs drop casted on the surface (high magnification), (f) edge of spot where SHINs drop casted on the surface (high magnification). (SEM images taken by Filipe Braga).

Alternative non-metallic surfaces, such as carbon, rely solely on the surface plasmon resonance (SPR) from the SHINs generating hot spots on the substrate.³⁰ The morphology of the surface has a direct impact on the enhancement, where optimal enhancement from the SHINs occurs on a flat surface, as a uniform monolayer of SHINs can be achieved. This uniform layer is difficult to achieve, as air or vacuum drying of the drop cast nanoparticle solution leads to the formation of a thick ring at the edge of the drop, due to the cohesive nature of water (as explained in chapter 3).

Polycrystalline Au is relatively flat in nature compared with graphitic carbons, which have varying degrees of roughness and porosity, as demonstrated by **Fig. 5.3b**. The SEM image ZnFe₂O₄/C surface demonstrates the rough nature of the composite surface, thus when the nanoparticles are cast onto the surface spaces exist in-between deposited particles (**Fig. 5.3c-d**), this is most apparent in the centre of the drop where the particles are sparsely distributed. Therefore, rough surfaces make it more challenging to form a consistent uniform layer of nanoparticles, in turn affecting the SPR intensity. This acts as a limiting factor in the calculation of an enhancement factor. In order to determine a quantifiable value for the enhancement factors, it is necessary to include a value for the roughness factor (**R**) (**Eq. 5.2**).

$$EF = \frac{I_{surface}CN_a\sigma h}{I_{sol}R} \quad (\text{Eq. 5.2})$$

Where $I_{surface}$ and I_{sol} are the integrated peak intensity of the probe molecule for surface and solution species, respectively. C is the concentration of probe molecule; N_a is Avogadro's number ($6.02 \times 10^{23} \text{ mol}^{-1}$), σ is the area of 1 adsorbed probe molecule ($0.21 \times 10^{-18} \text{ m}^2$ for pyridine) and h (m) focal depth of the laser.¹⁰ In this case the probe molecules are R-6G, CryV and MG. The molecule area used for the

different dyes in the calculation are $1.24 \times 10^{-18} \text{ m}^2$ for R-6G, $2.24 \times 10^{-18} \text{ m}^2$ for CryV, and $1.81 \times 10^{-18} \text{ m}^2$ for MG.³¹

The roughness factor can be calculated from the relation between the electrode real and geometrical areas (**Eq. 5.3**). The actual electrode area (A) was estimated using the Randles-Sevcik equation by plotting i_p vs $v^{1/2}$ (**Eq. 5.4**), from the values obtained from cyclic voltammetry of the Fc/Fc⁺ redox couple in (tetraethylammonium perchlorate) TEAClO₄ in acetonitrile electrolyte.

$$R = \frac{A_{\text{electrochemical}}}{A_{\text{geometrical}}} \quad (\text{Eq. 5.3})$$

$$i_p = 0.4463nFAC\left(\frac{nF\upsilon D}{RT}\right)^{\frac{1}{2}} \quad (\text{Eq. 5.4})$$

where n is the number of electrons involved in the redox reaction (1 e⁻ for Fc/Fc⁺ couple), F is the Faraday constant (96,485 C mol⁻¹), A the electrode area (cm²), C concentration of redox species, v the scan rate (V s⁻¹), D is the diffusion coefficient ($D = 2.11 \times 10^{-5} \text{ cm}^2 \text{ s}^{-1}$, calculated from Stokes-Einstein equation (**see experimental**),³² R the gas constant (8.31 J K⁻¹ mol⁻¹) and T the temperature (298 K).

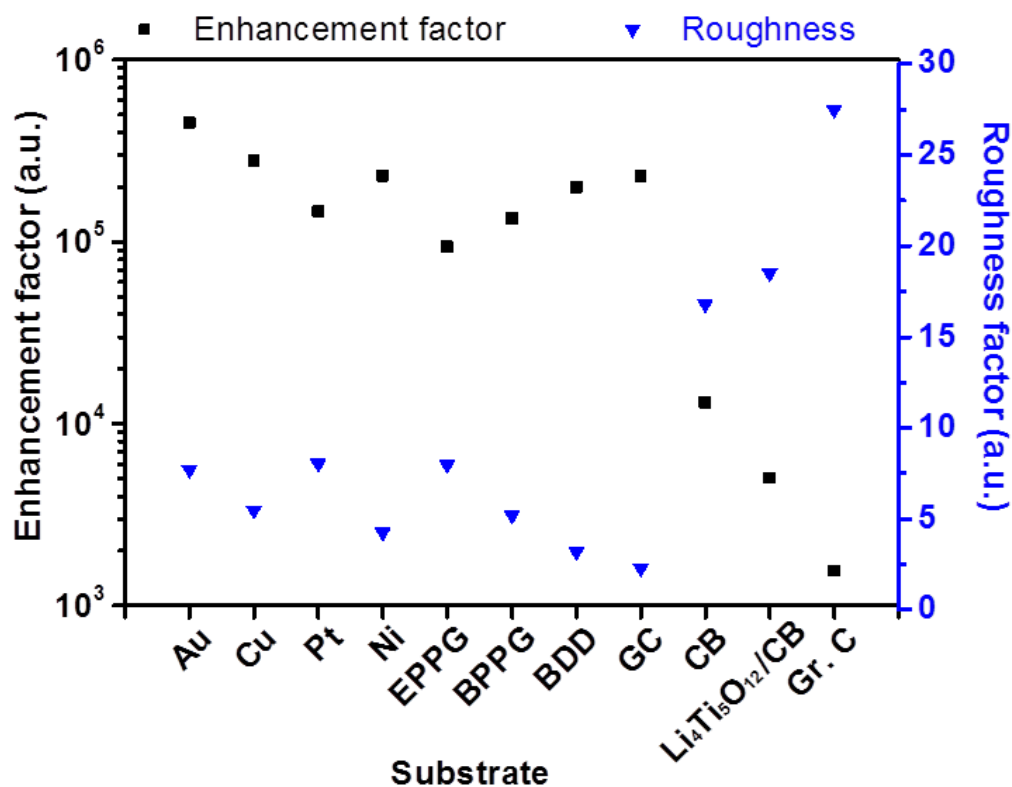


Figure 5.4 Comparison of the enhancement (intensity of malachite green peak at 1177 cm^{-1}) in relation to the roughness factor (calculated from voltammetry) across different electrode surfaces, including metals, planar carbon electrodes (i.e. edge-plane pyrolytic graphite (EPPG), basal-plane pyrolytic graphite (BPPG), and glassy carbon (GC) and $\text{Li}_4\text{Ti}_5\text{O}_{12}$ and carbon black composite electrodes.

Fig. 5.4 demonstrates a relationship between surface roughness and enhancement factor (calculated from **Eq. 5.2**) across a range of different electrode surfaces. The metallic surfaces have similar experimentally calculated roughness values; therefore, enhancement factor variation is likely a result of differing amounts of surface contribution. Graphitic carbon (Super C), Carbon black and $\text{Li}_4\text{Ti}_5\text{O}_{12}/\text{C}$ electrodes have considerably larger roughness factors, these account for the loss of enhancement, due to poor distribution of the particles on the surface as explained above. SHINERS have been shown to produce substantial enhancements on metallic substrates, with enhancement factors in excess of 4×10^5 for polycrystalline gold. From this evaluation, SHINERS can lead to enhancement factors of 2×10^3 on more

practical electrode materials, such as carbon black, thus showing that SHINERS provides sufficient signal enhancement to investigate more complex composite electrode surfaces.

5.4 How the substrate composition affects the distribution of particles

The composition of composite battery electrodes can vary depending upon the application, previously a common binder used in the synthesis of composite carbon electrodes was polyvinylidene fluoride (PVDF). However this has been reported to decompose upon charge and discharge in the presence of superoxide species.³³ In order to overcome this carboxymethyl cellulose (CMC) and polytetrafluoroethylene (PTFE) have been utilised as alternative binders.

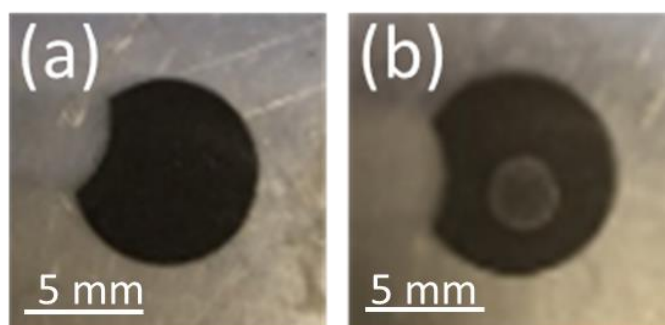


Figure 5.5 Images of a composite (Super C(70%)/ CMC (30%)) electrode cast onto aluminium foil (a) without SHINs drop casted, (b) with SHINs drop casted.

CMC is not hydrophobic in nature, this allows for a better distribution of particles on the surface when drop casted. However, upon deposition of the particles the binder is broken down. This causes a visible decomposition of the carbon surface in the presence of the drop **Fig. 5.5**, a silver ring (aluminium foil) is visible around the edge of the drop where the carbon surface has been affected.

PTFE is hydrophobic in nature, this presents a difficulty in distributing nanoparticles evenly on the surface. When SHINs are deposited on an electrode with PTFE as a binder, positioning the drop in a desired location is difficult as the

drop often migrates to the edge of the electrode. If the drop is positioned in the correct position, after drying a small very concentrated spot is left on the surface. This promotes difficulty in finding a viable enhancement, as the area of the electrode coated in SHINs is fairly small ($\sim 1 \text{ mm}^2$). However, the PTFE binder has not been shown to decompose spectroscopically.

The hydrophobicity of a substrate surface is a problem which may pose a difficulty in achieving even SHIN distribution on surfaces, not just for battery applications. In order to overcome this it may be necessary to support the particles in an alternative solvent other than water, which would be an area of future research.

5.5 *In situ* electrochemical SHINERS studies of oxygen reduction on graphitic carbons

Most *in situ* spectro-electrochemical studies have been conducted using gold electrodes.³⁴ However, minimal studies have utilised *in operando* spectroscopic techniques to probe more practical Li-O₂ cell cathode materials, such as various carbon interfaces and structures. Cyclic voltammetry on basal plane pyrolytic graphite (BPPG) and edge plane pyrolytic graphite (EPPG), in 0.5 M LiClO₄/DMSO electrolyte (saturated with O₂) display different activity in both the reduction and oxidation sweeps (**Fig. 5.6**).

Concentrating on oxygen reduction, BPPG has two distinct peaks in the CV cathodic sweep, the first one at 2.68 V followed by a second peak at 2.35 V. Comparatively, EPPG has a similar peak with greater intensity relative to the basal plane at 2.67 V. A broad shoulder at 2.32 V accompanies the peak at 2.67 V for EPPG. The reduction peaks at ca. 2.7 V and ca. 2.3 V have been previously associated with the initial electrochemical reduction of dissolved oxygen to superoxide (O₂⁻) which then leads to the formation of lithium peroxide via chemical

or electrochemical means through a surface or solution processes (Eq. 5.5-5.8).^{34, 35}

36

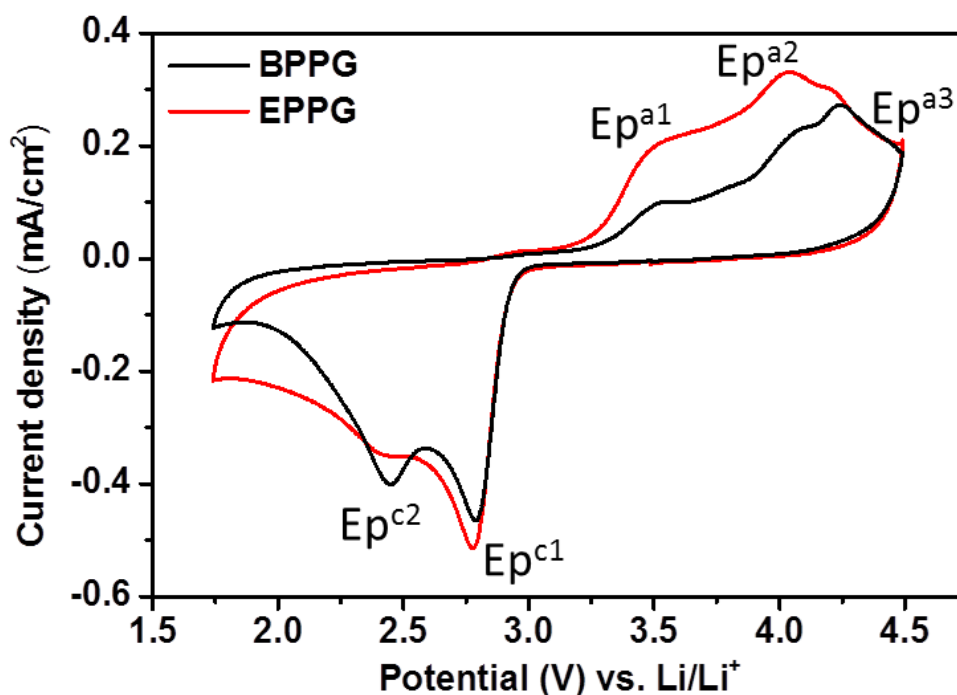
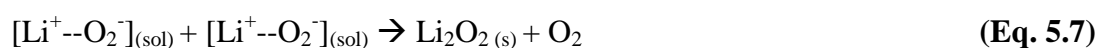


Figure 5.6 Cyclic voltammograms of 0.5 M LiClO₄ / DMSO (saturated with O₂) on basal plane pyrolytic graphite (black) and edge plane pyrolytic graphite (red). Sweep rate was 100 mV/s.

Table 5.2 Peak assignments from cyclic voltammogram data in **Fig. 5.6**, all peaks referenced against Li/Li⁺.

	E_p^{c1} (V)	E_p^{c2} (V)	E_p^{a1} (V)	E_p^{a2} (V)	E_p^{a3} (V)
BPPG	2.68	2.35	3.43	3.93	4.14
EPPG	2.67	2.32	3.42	3.90	4.12

The difference in peak intensity between the two graphites could be due to the increased activity associated with the edge plane surface (from the surface oxygen groups), compared to the basal plane.³⁷ Belova *et al.*³⁸ reported that the electrochemical formation of Li₂O₂ occurs on the nearly ideal basal plane.



In the anodic scan three peaks were observed on both graphitic electrodes at 3.43, 3.90 and 4.14 V. These peaks are associated with the partial oxidation of Li₂O₂ at 3.43 V with the surface being completely oxidised at 4.14 V as observed by Liu and Ye.³⁶ The peak at 3.9 V could be associated with the oxidation of superoxide formed in solution as the peroxide is oxidised from the electrode surface.³⁵

The intensity of these peaks is noticeably larger on the edge plane surface, this could again be linked with the increased activity of the EPPG surface due to the larger active surface area as demonstrated by the roughness calculations conducted above (**Fig. 5.4**).

SHINERS can be used to ascertain the species involved during the oxygen reduction process taking place on the different graphitic surfaces within a non-aqueous electrolyte in the presence of Li⁺. Initial studies without SHINERS of 0.5 M LiClO₄/DMSO on EPPG demonstrated that without any surface enhancement only solvent and carbon peaks can be observed in the Raman spectra, and little change can be observed with changing potential (**Fig. 5.7a**).

SHINERS measurements were conducted on both the edge and basal plane graphite electrodes in a 0.5 M LiClO₄ / DMSO electrolyte (**Fig. 5.7**). The Raman

spectrum at OCP (3.04 V) on BPPG (**Fig. 5.7b**) shows only peaks associated with the electrolyte and graphitic D and G bands.³⁹ As the potential is reduced below 2.85 V the formation of Li_2O_2 (band at 787 cm^{-1}) is observed on the electrode surface. This is the main reduction product which agrees with previous data in the literature on porous carbons.⁴⁰ At lower reduction potentials a band at 1130 cm^{-1} is observed, this has been assigned as LiO_2 . The observation of LiO_2 at reduction potentials below 2 V has not been previously reported and its detection is counterintuitive considering the detected formation of Li_2O_2 at higher potentials. The observation of LiO_2 at potentials below 2 V may result from the saturation of $[\text{Li}^+--\text{O}_2^-]_{(\text{sol})}$ at the electrode interface, and so a surface mechanism is favoured, whereby $[\text{Li}^+--\text{O}_2^-]_{(\text{ads})}$ remains adsorbed at the carbon surface rather than going into solution.

Reducing the potential below 1.70 V the LiO_2 band is no longer present, demonstrating its kinetic and thermodynamic instability with its conversion to Li_2O_2 either via a solution disproportionation or via a second electron reduction (**Eq. 5.7 and 5.8**).

At reduction potentials below 1.5 V, Raman bands at 1101 and 1470 cm^{-1} (\square) are observed. These have been tentatively assigned to the formation of Li_2CO_3 . The appearance of the bands coincides with the decrease in intensity of lithium peroxide on the electrode surface, as well as a colour change from colourless to a cloudy black in the electrolyte. Li_2CO_3 is not readily reported as a side product in DMSO based electrolytes and so it is likely to occur from reaction of the carbon surface with reduced oxygen species.⁴¹ The degradation of the carbon electrode surface via reaction with reduced oxygen species leads to its breakup and fragmentation, as well as Li_2CO_3 formation. These findings highlight the significant challenge for the use of

carbon based electrodes as cathodes within Li-O₂ cells due to the carbon surface's instability with reduced oxygen species.

Similarly to BPPG, EPPG has Li₂O₂ as the main reduction product (**Fig. 5.7c**) with a strong broad band at 787 cm⁻¹, with a FWHM of 21.5 cm⁻¹ appearing below 2.76 V. The band intensity grows until ca. 2.5 V while at lower potentials it is observed to decrease in intensity. This is either due to some of the Li₂O₂ precipitate (SEM data from the literature typically show particle sizes of 50-100 nm)⁴² moving away from the electrode (the electrode configuration could mean that Li₂O₂ could move away due to gravity). Alternatively, the growth of Li₂O₂ has inhibited the SHINERS effect due to blocking or forced separation of the SHINs particles on the surface, thus decreasing the average enhancement from the overall laser spot.

Formation of Li₂O₂ is expected due to the highly solvating nature of the electrolyte solvent DMSO due to its high donor number of 29.8, leading to a solution based mechanism. However, on EPPG, superoxide (O₂⁻) is detected at 2.80 V. The O₂⁻ band at 1108 cm⁻¹ (♦) is accompanied by a band at 1530 cm⁻¹ (♦'), which has previously been assigned to the deformation of the carbon ring stretching mode, due to its interaction with the superoxide.¹⁰ When the potential is decreased below 2.4 V a band at 1130 cm⁻¹ begins to grow due to the presence of LiO₂. This band remains visible down to 1.85 V. At lower reduction potentials a band at 1505 cm⁻¹ (*) appears which could be linked to the ring stretching mode associated with absorbed LiO₂ interacting with the carbon surface.⁴³ At lower potentials (2.4 V), the Li₂CO₃ band at 1476 cm⁻¹ (□) is observed representing the beginning of the degradation EPPG electrode interface. The accompanying band at 1101 cm⁻¹ is not as clearly visible above the signal noise for all spectra, but can just be seen for the spectrum at 2.21 V. Comparatively with the basal plane surface, the onset of degradation on

EPPG occurs at a more positive potential (2.4 V vs 1.5 V), this appears to be related to the potential at which LiO_2 is observed on the electrode surface. The variance in potential of LiO_2 formation is likely a result of the increased surface area of the edge plane surface, and thus increasing the reactivity at the surface, due to the edge groups.⁴⁰ At potentials below 2.0 V a band at 835 cm^{-1} is formed (\odot), this has been tentatively assigned to LiOOH ,⁴⁴ which may form as a result of reaction with R-OH functional groups on the carbon surface.

Overall on the two graphitic carbons it can be suggested that a partial surface/solution mechanism is taking place, with both having Li_2O_2 as the dominant reduction product, but LiO_2 forming as an intermediate (**Eq. 5.6**). This interaction occurs predominantly on the edge plane surface, which stabilises the superoxide before chemical reaction to LiO_2 , where it is then solvated by DMSO and undergoes a disproportionation reaction to form Li_2O_2 . At low reduction potentials it is also apparent that the onset of LiO_2 on the electrode surface starts to cause electrode degradation as confirmed by the peaks at 1101 cm^{-1} and 1476 cm^{-1} , which are pronounced on the edge plane surface, due to the presence of surface groups at the carbon edge.

Table 5.3 Raman peak positions (cm^{-1}) of spectra in **Fig. 5.7**.

Assignment and/or mode	Raman peak positions (cm^{-1})	
	BPPG	EPPG
Li_2O_2 ($\nu_{\text{o-o}}$)	787	787
Li_2OOH	-	835
νLiO_2 ($\nu_{\text{o-o}}$)	1130	1130
$\nu\text{LiO}_2\text{-C}$	-	1505
O_2^- ($\nu_{\text{o-o}}$)	-	1108
$\nu\text{O}_2\text{-C}_{(\text{graohitic ring})}$	-	1530
Li_2CO_3	1101	1101
Li_2CO_3 ($\nu_{\text{C-O}}$)	1470	1476
D	1419	1418
G	1583	1583

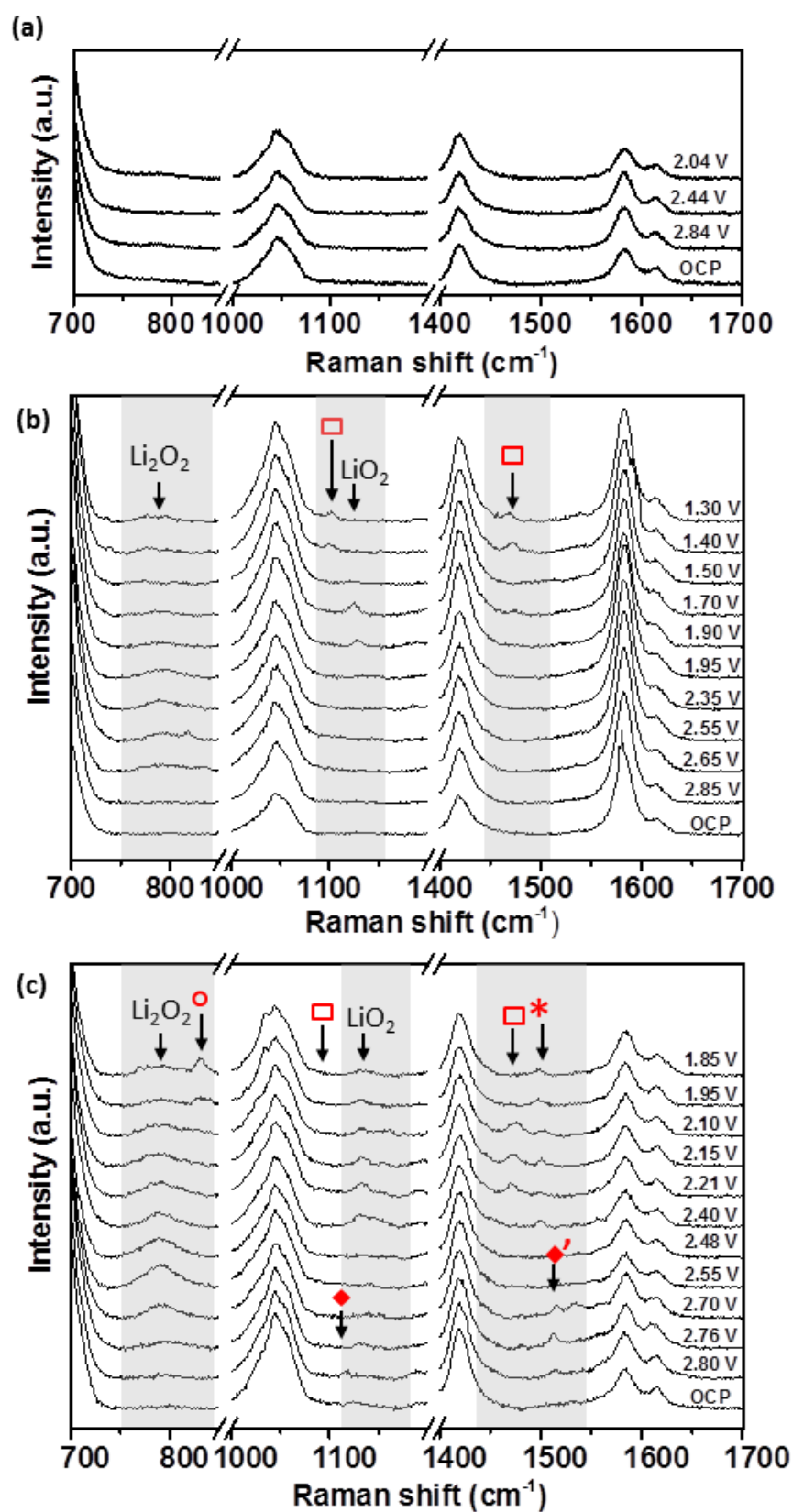


Figure 5.7 *In situ* SHINERS spectra of 0.5 M LiClO₄ / DMSO (saturated with O₂) on (a) edge plane pyrolytic graphite (BPPG) without SHINs, (b) basal plane pyrolytic graphite (BPPG), and (c) edge plane pyrolytic graphite (EPPG).

5.6 *In situ* electrochemical SHINERS studies of oxygen reduction on a composite carbon black electrode

Initial studies on a composite carbon electrode (Super C/ PTFE) in a 0.5 M LiClO₄/DMSO electrolyte demonstrated that SHINERS can be used to track reaction intermediates and products at the carbon surface (**Fig. 5.8**) of more practical electrodes. After discharge from the OCP (3.3 V) down to 1.9 V a peak at 1130 cm⁻¹ is observed, which has been assigned as LiO₂.⁴³ A significant broadening of the G band (1600 cm⁻¹) is observed due to the collective contributions of the interactions with the carbon rings and reaction intermediates of the carbon surface, oxygen reduction species formed during discharge and Li₂CO₃.^{38,45} However contribution from the carbonate species could not be conclusively assigned at this potential with peak fitting.

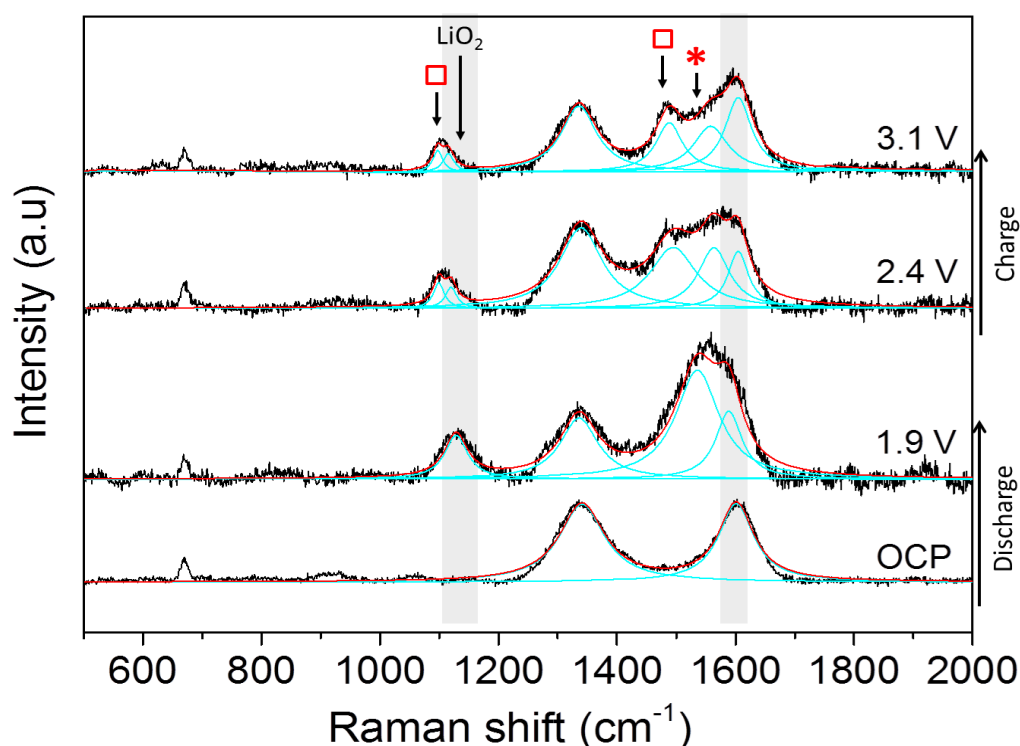


Figure 5.8 *In situ* electrochemical SHINERS spectra of O₂ saturated 0.5 M LiClO₄ / DMSO on carbon black (Super C/ PTFE) electrode. The carbon G-band and position of LiO₂ band are highlighted in grey scale. Peaks fitted with a Gaussian function.

Table 5.4 Raman peak positions (cm⁻¹) of spectra from 0.5 M LiClO₄/DMSO on a composite carbon cathode (super C(70%:30%)PTFE). (**Fig. 5.8**).

	Raman peak positions (cm ⁻¹)
Assignment	Composite electrode
Li ₂ O ₂	-
LiO ₂	1130
O ₂ ⁻	1110
LiO ₂ -C	-
Li ₂ CO ₃	1098 and 1490
D	1340
G	1600

The Gaussian peak fitting (Fig. 5.8) shows that as the potential is raised to 2.4 and 3.1 V, the intensity of the band at 1130 cm⁻¹ decreases, indicating the disappearance of LiO₂ and it shifts to lower wavenumbers (1110 cm⁻¹) that could be related to O₂⁻. This is accompanied by the growth of two peaks (□) at 1098 cm⁻¹ and 1490 cm⁻¹, which are both associated with Li₂CO₃, also observed on BPPG and EPPG electrodes during discharge, resulting from the reaction of the carbon

electrode surface with LiO_2 .^{38, 45} The result indicates that at even 2.4 V carbon surface oxidation is occurring in the presence of LiO_2 , resulting in the growth of a Li_2CO_3 layer upon the carbon surface.

In contrast to the data from BPPG and EPPG, no band from Li_2O_2 at 787 cm^{-1} is observed. This may be due to the stability of LiO_2 species on carbon surfaces containing larger number of defects, as Li_2O_2 is formed by disproportionation of LiO_2 in solution.³⁸

This initial study on a composite carbon electrode highlights how SHINERS can be effectively used to probe important electrode/electrolyte interfaces in battery related studies. Undoubtedly further work needs to be carried out in order to fully characterise the complex oxygen surface chemistry and side reactions upon carbon and other substrates, and this will be subject to further ongoing work.

5.7 Conclusions and future work

Au-SiO₂ core-shell nanoparticles have been synthesised for SHINERS studies on the carbon cathode of the Li-O₂ cell. The enhancement factor of the nanoparticles has been investigated in a range of metallic, carbon based and semiconducting electrode materials using the organic dyes rhodamine 6G, crystal violet and malachite green. A maximum signal enhancement of 4×10^5 was observed on gold. Planar carbon electrodes, such as EPPG and BPPG, also presented good enhancements of 9×10^4 and 1×10^5 , respectively, and more practical carbon black electrodes, though lower, still displayed useful enhancements of 2×10^3 .

SHINERS results have demonstrated the ability to track the reduction reaction mechanisms at carbon electrodes. EPPG and BPPG were both observed to produce Li_2O_2 as the main reduction product. Initial studies on a carbon black composite electrode tracked the oxidation of the electrode surface, with both LiO_2 and O_2^-

detected. The degradation of the electrode surface, principally forming Li_2CO_3 has also been observed on both graphitic and composite carbon substrates.

To summarise, this work has shown that Au-SiO₂ core-shell nanoparticles can be used to enhance the Raman signal not only on metallic planar electrodes, but also in non-metallic electrodes, within a certain porosity and roughness. This has been demonstrated in the initial SHINERS measurements in the Li-O₂ battery that will lead onto the continued investigation on more practical electrodes for other battery systems.

5.8 References

1. E. Peled, *J. Electrochem. Soc.*, 1979, **126**, 2047-2051.
2. P. Verma, P. Maire and P. Novák, *Electrochim. Acta*, 2010, **55**, 6332-6341.
3. Z. Peng, S. A. Freunberger, Y. Chen and P. G. Bruce, *Science*, 2012, **337**, 563-566.
4. R. Baddour-Hadjean and J.-P. Pereira-Ramos, *Chem. Rev.*, 2010, **110**, 1278-1319.
5. L. Cabo-Fernandez, F. Mueller, S. Passerini and L. J. Hardwick, *Chem. Commun.*, 2016, **52**, 3970-3973.
6. L. J. Hardwick, M. Holzapfel, P. Novák, L. Dupont and E. Baudrin, *Electrochimica Acta*, 2007, **52**, 5357-5367.
7. C. Sole, N. E. Drewett and L. J. Hardwick, *Farad. Discuss.*, 2014, **172**, 223-237.
8. I. M. Aldous and L. J. Hardwick, *J. Phys. Chem. Lett.*, 2014, **5**, 3924-3930.
9. I. M. Aldous and L. J. Hardwick, *Angew. Chem., Int. Ed.*, 2016, **55**, 8254-8257.
10. T. A. Galloway and L. J. Hardwick, *J. Phys. Chem. Lett.*, 2016, **7**, 2119-2124.
11. F. S. Gittleson, K. P. C. Yao, D. G. Kwabi, S. Y. Sayed, W.-H. Ryu, Y. Shao-Horn and A. D. Taylor, *Chem. Electro. Chem.*, 2015, **2**, 1446-1457.
12. W. E. Smith, *Chem. Soc. Rev.*, 2008, **37**, 955-964.
13. D. Y. Wu, J. F. Li, B. Ren and Z. Q. Tian, *Chem. Soc. Rev.*, 2008, **37**, 1025-1041.
14. E. C. Le Ru and P. G. Etchegoin, *Principles of Surface Enhanced Raman Spectroscopy and Related Plasmonic Effects*, Elsevier, 2009.
15. J.-F. Li, X. D. Tian, S. B. Li, J. R. Anema, Z. L. Yang, Y. Ding, Y. F. Wu, Y. M. Zeng, Q. Z. Chen, B. Ren, Z. L. Wang and Z. Q. Tian, *Nat. Protocols*, 2013, **8**, 52-65.
16. J.-F. Li, Y.-F. Huang, Y. Ding, Z.-L. Yang, S.-B. Li, X. S. Zhou, F. R. Fan, W. Zhang, Z. Y. Zhou, D.-Y. Wu, B. Ren, Z. L. Wang and Z. Q. Tian, *Nature*, 2010, **464**, 392-395.

17. X. D. Tian, B. J. Liu, J. F. Li, Z. L. Yang, B. Ren and Z. Q. Tian, *J. Raman Spectrosc.*, 2013, **44**, 994-998.
18. J.-F. Li, Y.-J. Zhang, S.-Y. Ding, R. Panneerselvam and Z.-Q. Tian, *Chem. Rev.*, 2017, **117**, 5002-5069.
19. S. Y. Ding, J. Yi, J. F. Li and Z. Q. Tian, *Surf. Sci.*, 2015, **631**, 73-80.
20. J.-F. Li, Y. J. Zhang, A. V. Rudnev, J. R. Anema, S. B. Li, W. J. Hong, P. Rajapandiyam, J. Lipkowski, T. Wandlowski and Z. Q. Tian, *J. Am. Chem. Soc.*, 2015, **137**, 2400-2408.
21. J.-F. Li, S. Y. Ding, Z. L. Yang, M. L. Bai, J. R. Anema, X. Wang, A. Wang, D. Y. Wu, B. Ren, S. M. Hou, T. Wandlowski and Z. Q. Tian, *J. Am. Chem. Soc.*, 2011, **133**, 15922-15925.
22. S. Hy, F. Felix, J. Rick, W.-N. Su and B.-J. Hwang, *J. Am. Chem. Soc.*, 2014, **136**, 999-1007.
23. J.-F. Li, A. Rudnev, Y. Fu, N. Bodappa and T. Wandlowski, *ACS Nano*, 2013, **7**, 8940-8952.
24. S. Schlücker, *Surface Enhanced Raman Spectroscopy: Analytical, Biophysical and Life Science Applications*, Wiley, 2011.
25. S. Chen, X. Li, Y. Zhao, L. Chang and J. Qi, *Carbon* 2015, **81**, 767-772.
26. W. Zhang, J.-C. Dong, C.-Y. Li, S. Chen, C. Zhan, R. Panneerselvam, Z.-L. Yang, J.-F. Li and Y.-L. Zhou, *J. Raman Spectrosc.*, 2015, **46**, 1200-1204.
27. Y. Zhao, Y. Tian, P. Ma, A. Yu, H. Zhang and Y. Chen, *Anal. Methods*, 2015, **7**, 8116-8122.
28. B. Pettinger, B. Ren, G. Picardi, R. Schuster and G. Ertl, *J. Raman Spectrosc.*, 2005, **36**, 541-550.
29. L. Jensen and G. C. Schatz, *J. Phys. Chem. A Lett.*, 2006, **110**, 5973-5977.

30. S.-Y. Ding, J. Yi, J.-F. Li, B. Ren, D.-Y. Wu, R. Panneerselvam and Z.-Q. Tian, *Nat. Rev. Mater.*, 2016, **1**, 1-16.
31. C. H. Giles and R. B. McKay, *J. Bacteriol.*, 1965, **89**, 390-397.
32. C. O. Laoire, E. J. Plichta, M. A. Hendrickson, S. Mukerjee and K. M. Abraham, *Electrochimica Acta*, 2009, **54**, 6560-6564.
33. J. K. Papp, J. D. Forster, C. M. Burke, H. W. Kim, A. C. Luntz, R. M. Shelby, J. J. Urban and B. D. McCloskey, *J. Phys. Chem. Lett.*, 2017, **8**, 1169-1174.
34. L. Johnson, C. Li, Z. Liu, Y. Chen, S. A. Freunberger, P. C. Ashok, B. B. Praveen, K. Dholakia, J. M. Tarascon and P. G. Bruce, *Nat. Chem.*, 2014, **6**, 1091-1099.
35. Q. Yu and S. Ye, *J. Phys. Chem. C*, 2015, **119**, 12236-12250.
36. C. Liu and S. Ye, *J. Phys. Chem. C*, 2016, **120**, 25246-25255.
37. R. N. Goyal, S. Chatterjee and A. R. S. Rana, *Talanta*, 2010, **83**, 149-155.
38. A. I. Belova, D. G. Kwabi, L. V. Yashina, Y. Shao-Horn and D. M. Itkis, *J. Phys. Chem. C*, 2017, **121**, 1569-1577.
39. L. Bokobza, J.-L. Bruneel and M. Couzi, *C*, 2015, **1**, 77-79.
40. Y. Qiao and S. Ye, *J. Phys. Chem. C*, 2016, **120**, 8033-8047.
41. D. G. Kwabi, T. P. Batcho, C. V. Amanchukwu, N. Ortiz-Vitoriano, P. Hammond, C. V. Thompson and Y. Shao-Horn, *J. Phys. Chem. Lett.*, 2014, **5**, 2850-2856.
42. S. Lau and L. A. Archer, *Nano Lett.*, 2015, **15**, 5995-6002.
43. D. Zhai, H.-H. Wang, K. C. Lau, J. Gao, P. C. Redfern, F. Kang, B. Li, E. Indacochea, U. Das, H.-H. Sun, H.-J. Sun, K. Amine and L. A. Curtiss, *J Phys Chem Lett*, 2014, **5**, 2705-2710.
44. H. H. Eysel and S. Thym, *Z. Anorg. Allg. Chem.*, 1975, **411**, 97-102.

45. D. M. Itkis, D. A. Semenenko, E. Y. Kataev, A. I. Belova, V. S. Neudachina, A. P. Sirotnina, M. Havecker, D. Teschner, A. Knop-Gericke, P. Dudin, A. Barinov, E. A. Goodilin, Y. Shao-Horn and L. V. Yashina, *Nano Lett.*, 2013, **13**, 4697-4701.

Chapter 6

A fundamental Study on the Effects of Moving from an Aqueous to Non-Aqueous Electrolyte

6.1 Abstract

The results presented in this chapter investigate the behaviour of electrochemical systems when moving from an aqueous to a non-aqueous electrolyte on a Au(111) single crystal electrode. In an aqueous electrolyte the detection of the hydroxide intermediate was observed in both the oxidation and reduction reactions via voltammetry and *in situ* SHINERS. The addition of small quantities of MeCN inhibited the adsorption of the hydroxide intermediate and delayed the onset potential of oxidation. MeCN was also observed to preferentially adsorb on step and defect sites over large terraces.

In the context of the Na-O₂ system with acetonitrile (MeCN), the presence of Na₂O₂ was observed as the overriding reduction product with small amounts of NaO₂ being detected simultaneously. The addition of water showed the possible formation of hydro-peroxy species and carbonates.

The decomposition of MeCN was also detected on the single crystal surface, via the presence of the cyanide band; the addition of water appears to cause an increased stark shift, related to interactions between the water and CN⁻ within the double layer region.

6.2 Introduction

The effect of water on the reaction mechanisms involved in the metal-oxygen battery has been of particular interest in recent years.¹ Initial reports suggested water has an extremely detrimental effect on the fundamental reaction mechanisms due to the highly nucleophilic nature of the reaction intermediates, causing degradation of the electrolytes and electrodes.² However, recent reports on the Li-O₂ battery have suggested reaction mechanisms, where water can influence alternative reaction pathways via a LiOH mechanism.³⁻⁵ The effect of water on the reaction mechanisms involved in the Na-O₂ cells has also been published,⁶ suggesting water can promote a catalytic reaction via a hydrated superoxide species to form a hydrated peroxide.⁷ There have also been reports that water has a detrimental effect on NaO₂; however it is believed the fundamental reaction products (NaO₂ and Na₂O₂) are more stable in the presence of trace amounts of water than LiO₂ in the lithium system.

Understanding the fundamental electrochemical behaviour on an ideal electrochemical surface when moving from a completely aqueous electrolyte to a non-aqueous system may provide valuable insight into the reaction pathways and the effects that water or organic solvents have on the intermediates and products produced.

6.3 Characterisation of the Au(111) surface

In order to assure the quality of the results, it is important to check the quality of the single crystals used in this chapter. The crystal quality was checked by cyclic voltammetry in 0.1 M H₂SO₄ (**Fig. 6.1**).

At 0.4 V in the oxidation sweep (**point 1, Fig. 6.1**) lifting of the thermally reconstructed surface occurs to form the (1x1) surface.⁸ The broad hump (**2**) is attributed to the adsorption of hydrogen and sulphate ions. The sulphate layer reorders to form a commensurate ($\sqrt{3} \times \sqrt{7}$) layer at point 3 (sharp spike).⁹ The shape and intensity of this spike are related to the degree of crystallinity and the size of the (111) terraces.⁹ The oxidation and reduction of the (111) terraces occurs at (5 + 6), oxidation of step and defect sites occurs at slightly lower potentials (**4**).

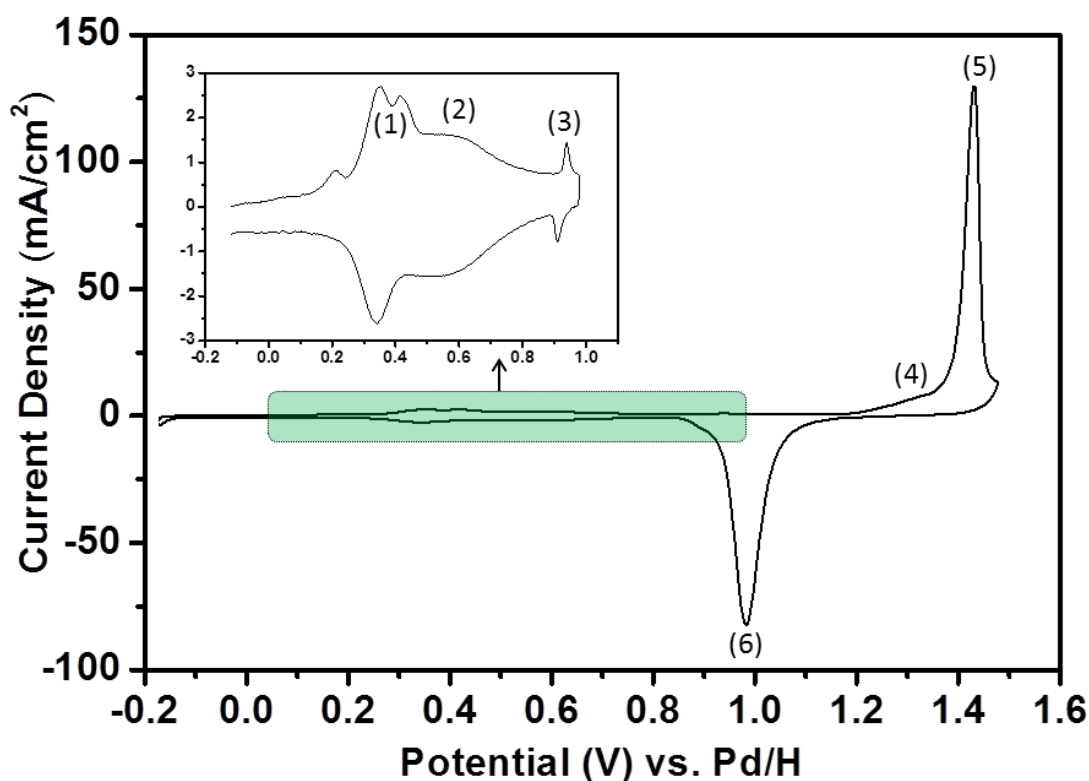


Figure 6.1 Cyclic voltammogram of 0.1 M H₂SO₄ in H₂O on Au(111), insert (top left) zoomed in look at double layer region. Sweep rate 50 mV/s.

6.4 Understanding the ORR in an aqueous electrolyte

A solution of 0.1 M NaClO₄ in H₂O was prepared with a pH of 9. This solution was used as the baseline for all subsequent experiments. The pH was kept constant for all experiments. Cyclic voltammetry was used to initially analyse the solution. The results showed three oxidation peaks and three reduction peaks (**Table 6.1 + Fig. 6.2a**). In the oxidation sweep, the first oxidation peak at ~0.3 V- 0.5 V is associated with the adsorption of ClO₄⁻ onto the Au(111) surface (**Fig. 6.3a**). This is followed by the co-adsorption of a hydroxyl intermediate (OH⁻) (**Fig 6.3b**).^{8, 10} A second oxidation band at ~1.0 V is due to the simultaneous desorption of perchlorate ions from the electrode surface and the place exchange and oxide formation on defect and step sites (**Fig 6.3c**). At potentials above 0.8 V up to 1.25 V complete desorption of perchlorate ions occurs and oxidation of the OH⁻ intermediate on terrace sites takes place (**Fig. 6.3d**).⁸

Table 6.1 Peak position and assignment of cyclic voltammetry data from **Fig. 6.3 and 6.4** (a) oxidation peaks (b) reduction peaks.

(a)	Ep ^{a1}	Ep ^{a2}	Ep ^{a3}
Peak position (V) vs. Pd/H	0.49	0.99	1.27

(b)	Ep ^{c1}	Ep ^{c2}	Ep ^{c3}
Peak position (V) vs. Pd/H	0.84	0.45	0.34

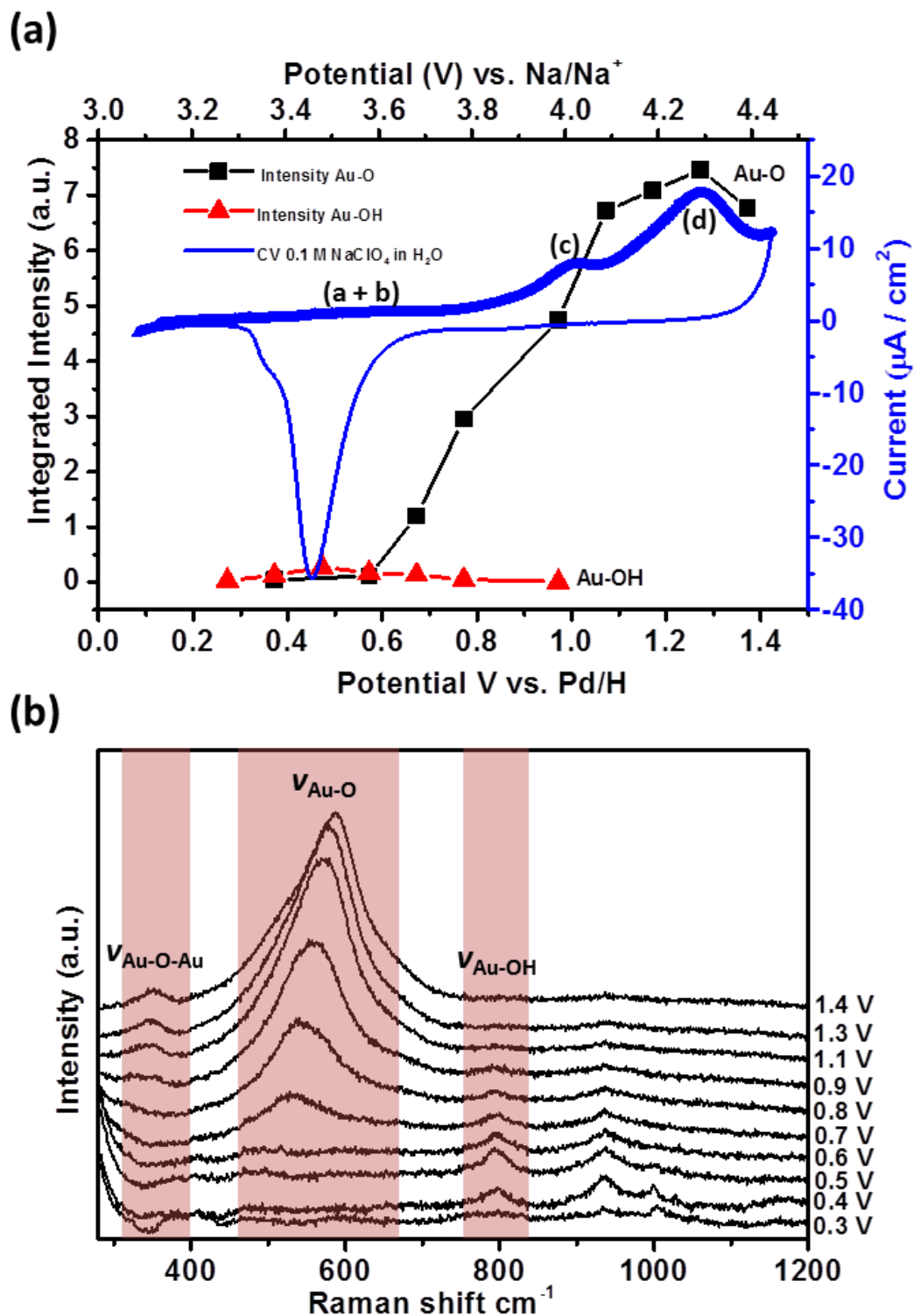


Figure 6.2 CV and Raman data for 0.1 M NaClO₄ in H₂O (purged with Ar) on a Au(111) half bead single crystal (a) Cyclic voltammogram (sweep rate 10 mV s⁻¹) with integrated intensities of Raman peaks at corresponding oxidation potentials. (b) *In situ* SHINs spectra in the same electrolyte system. Potential measured vs. Pd/H.

In situ Raman spectroscopy using shell isolated nanoparticles for enhanced Raman spectroscopy (SHINERS) allowed the reaction intermediates and species to be tracked on the Au(111) surface. The SHINERS spectra showed the adsorption of perchlorate on the Au surface, at ~ 0.4 V.¹¹ The perchlorate bands were accompanied by a small band at 800 cm^{-1} , which is indicative of the OH^- intermediate. The integrated intensity of the OH band relative to potential, demonstrates the agreement between Raman spectra and CV data (**Fig 6.2a**).

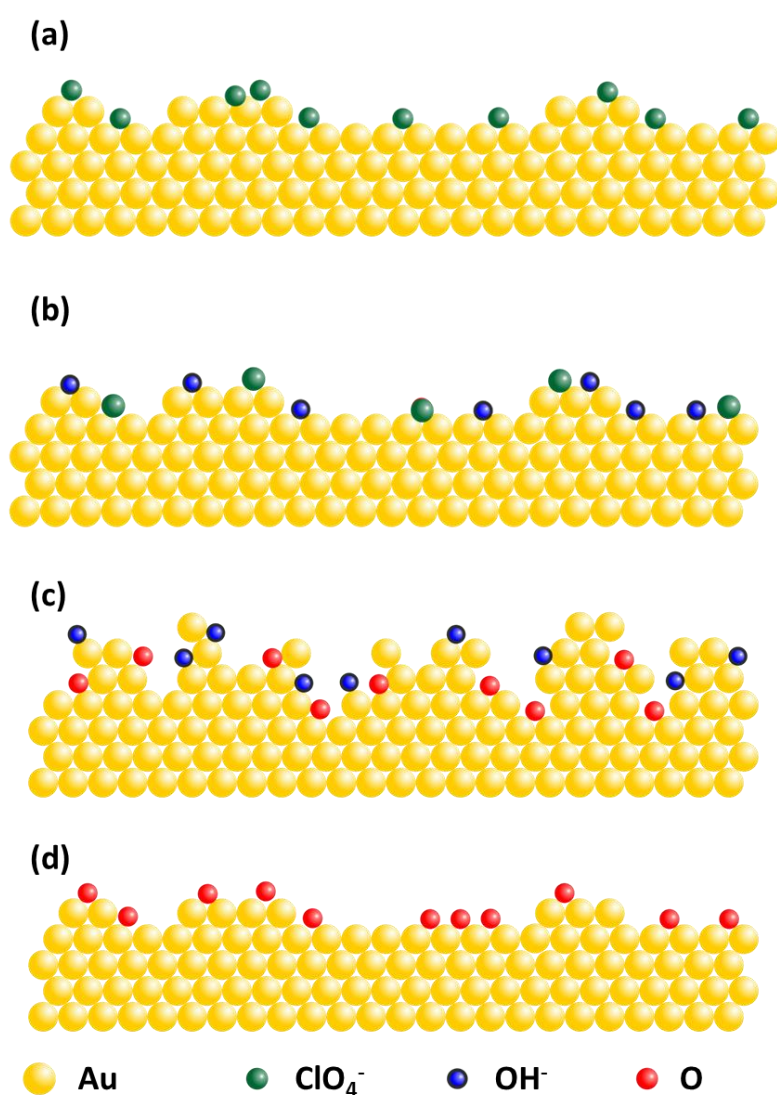


Figure 6.3 (a) adsorption of ClO_4^- , (b) adsorption of OH^- , (c) simultaneous desorption of ClO_4^- and oxide formation at step and defect sites (d) oxidation on terraces.

A band centred at 550 cm^{-1} grows as the potential is driven more positive, which coincides with the disappearance of the band at 800 cm^{-1} . This implies the OH^- is being oxidised, with the band at 550 cm^{-1} assigned to the Au-O peak.¹² The Au-O band grows in intensity and peak width, until being centred at $\sim 590\text{ cm}^{-1}$ at 1.3 V. The change in peak position is related to the position of oxidation; at lower potentials the surface is oxidised at step and defect sites, which accounts for the lower band position. The surface is then oxidised on the terrace sites at higher potentials, accounting for the increase in intensity. This was also observed when measuring the integrated intensity of the Raman bands, the peak intensity is maximised in agreement with the voltammetry data. A decrease in intensity is observed after the peak maximum at 1.3 V. This phenomenon is associated with the formation of multiple layers of oxide on the electrode surface.

A third peak at 340 cm^{-1} was observed (**Fig 3.1**), this was characterised as Au-O-Au bending.¹² It forms at potentials $> 0.7\text{ V}$ vs. Pd/H. The Au-O-Au forms as a result of the increased surface coverage of oxygen. The oxygen molecules are forced closer to each other as surface sites are occupied creating a bending mode.

Table 6.2 Raman peak positions from **Fig. 6.3b** and **6.4b**.

Assignment	Au-O-Au (bending)	Au-O	Au-OH
Peak position (cm^{-1})	353	543-580	800

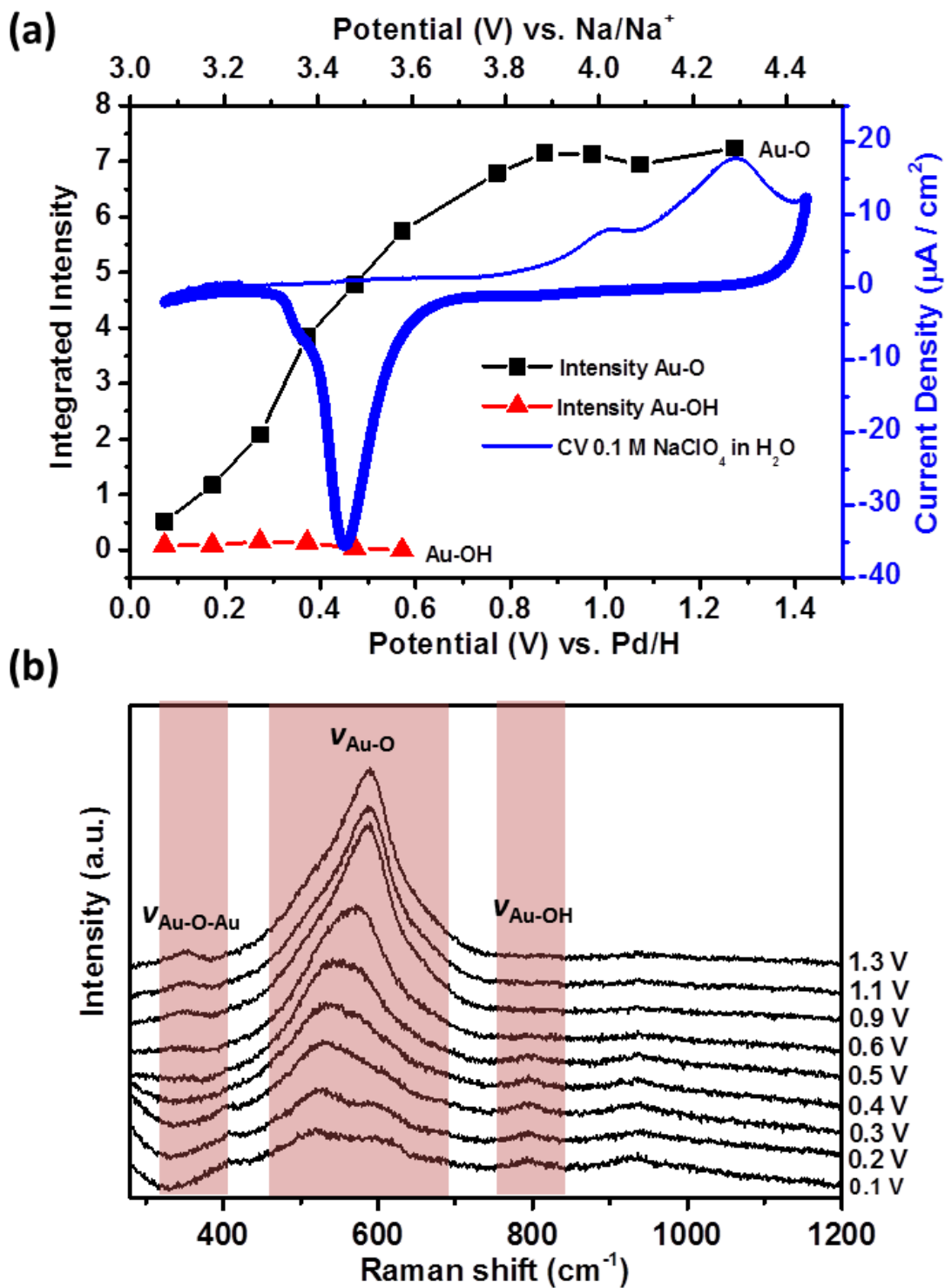


Figure 6.4 CV and Raman data for 0.1 M NaClO₄ in H₂O (purged with Ar) on a Au(111) half bead single crystal **(a)** Cyclic voltammogram (sweep rate 10 mV s⁻¹) with integrated intensities of Raman peaks at corresponding reduction potentials. **(b)** *In situ* SHINs spectra in the same electrolyte system. Potential measured vs. Pd/H.

The cyclic voltammetry for the reduction sweep, showed the presence of three peaks (**Table 6.1 + Fig. 6.4a**). Initially a wide, shallow reduction peak ranging from 0.9 V to 0.55 V. A second, sharp intense band was present at 0.46 V, this peak had a shoulder at 0.4 V. SHINERS was used to ascertain the origin of the species present at the different potentials on the Au(111) surface.

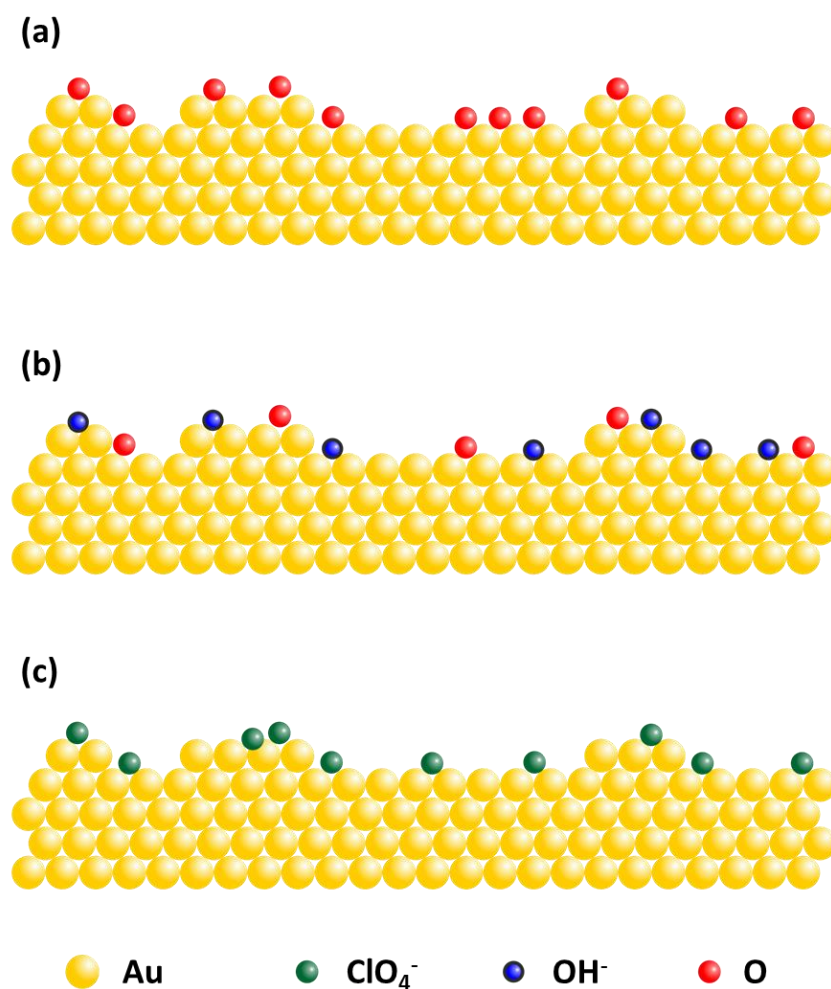


Figure 6.5 (a) Partial reduction of place exchanged O, (b) reduction of O and OH⁻, (c) complete reduction of O and adsorption of ClO₄⁻.

The SHINERS data showed that at potentials ranging from ~0.9 V until 0.55 V, partial reduction of place exchanged surface oxide starts to reduce Au-O to the OH⁻ intermediate (**Fig. 6.5a**). At lower reduction potentials (0.55 V to 0.2 V) the reduction of both oxide species starts to occur (**Fig. 6.5b + c**), this was observed in

the Raman due to the decrease in intensity of oxide and OH band. The complete desorption of OH, occurs at lower potentials than O, as can be observed in the integrated intensity of the Raman band, relative to the voltammetry data (**Fig. 6.4**). The adsorption of perchlorate ions (**Fig. 6.5c**), occurs as the oxide species are reduced from the electrode surface. These peaks were previously assigned by Li et al.⁸ in Na₂SO₄ electrolyte. Measuring the peak intensity of the *in situ* Raman data showed that it correlated well with the CV data (**Fig. 3.1a and 3.2a**) and confirmed the assumptions made.

6.5 The electrochemical response of moving from an aqueous to non-aqueous electrolyte

In order to understand the different electrochemical effects moving from an aqueous system to a non-aqueous system, solutions of 0.1 M NaClO₄/H₂O were prepared with the addition of increasing concentrations of MeCN from 1 mM to 100 mM. The results were initially studied using cyclic voltammetry (**Fig. 6.6 and Table 6.3**).

The addition of MeCN to the electrolyte has an inhibiting effect on the electrochemistry of the surface species (**Fig. 6.6**). In the oxidation sweep, a decrease in the intensity of the band at 1.0 V is observed with increasing MeCN concentrations. This band, without the presence of MeCN, was assigned to the oxidation of the hydroxide intermediate and oxidation of step and defect sites. The decrease in intensity of this peak would imply fewer step and defect sites are available, and/or the formation of the hydroxide intermediate is inhibited on the electrode surface, due to the presence of MeCN being strongly adsorbed at these sites.^{13, 14}

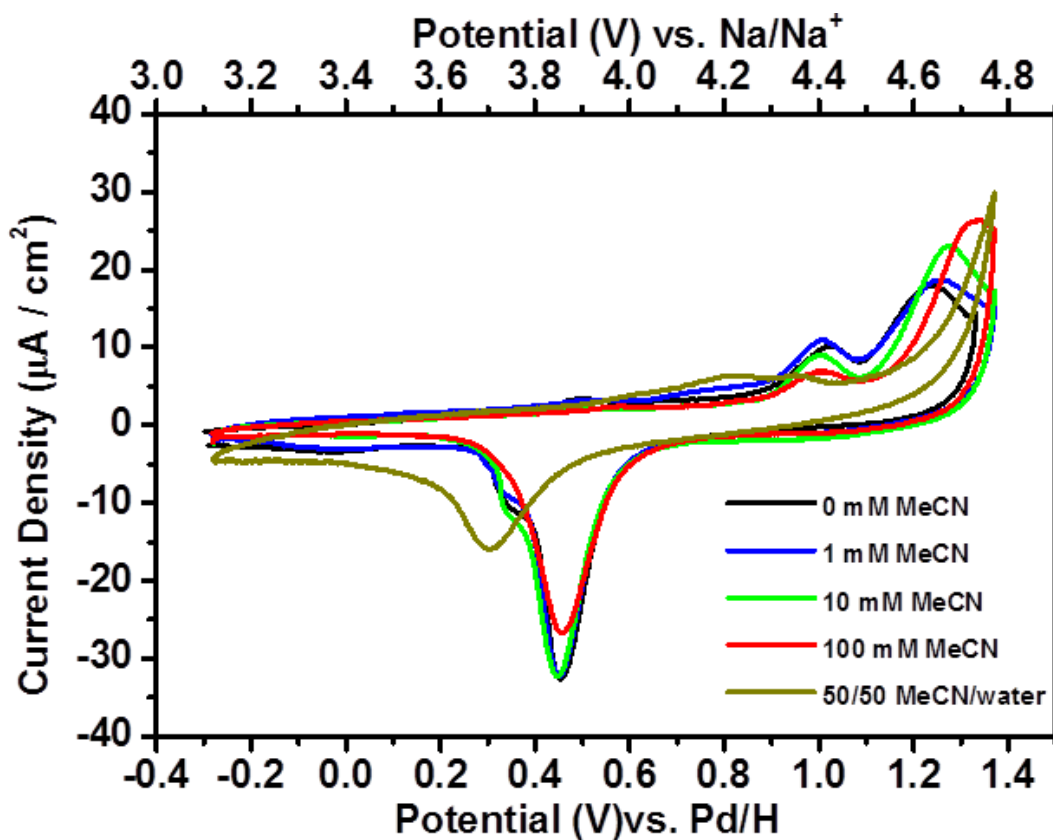


Figure 6.6 CV data for 0.1 M NaClO₄ in H₂O (purged with Ar) on Au(111) half bead single crystal with increasing concentration of MeCN. Sweep rate 10 mV/s.

Table 6.3 Peak position and assignment of cyclic voltammetry data from **Fig. 6.6**.

	Peak potential (V) vs. Pd/H				
	Ep ^{c1}	Ep ^{c2}	Ep ^{c3}	Ep ^{a1}	Ep ^{a2}
1 mM	0.49	1.02	1.25	0.45	0.32
10 mM	0.53	1.0	1.28	0.44	0.33
100 mM	0.59	0.99	1.33	0.45	-
50:50	0.8	0.94	> 1.38	0.30	-

The peak at 1.25 V is associated with the oxidation of sites on Au(111) terraces. At increasing MeCN concentrations, this band shifts to more positive potentials and increases in intensity. The shift in potential is indicative of a delay in the onset of oxidation. This suppression of the onset potential, due to the presence of MeCN competing with the oxidation on the surface is demonstrated strongly with a 50:50 (MeCN: H₂O) ratio (**Fig. 6.6**).

A similar response is observed in the reduction sweep, the increased suppression of the reduction peak at ~ 0.45 V with increasing MeCN concentration is an indication that the adsorption of MeCN is competing with the oxidation and reduction reactions taking place at the Au surface, inhibiting the adsorption of hydroxide and oxygen, also slowing the reaction kinetics.¹⁵ At equal concentrations of MeCN and water, the reduction of oxygen and hydroxide on the surface is severely inhibited.

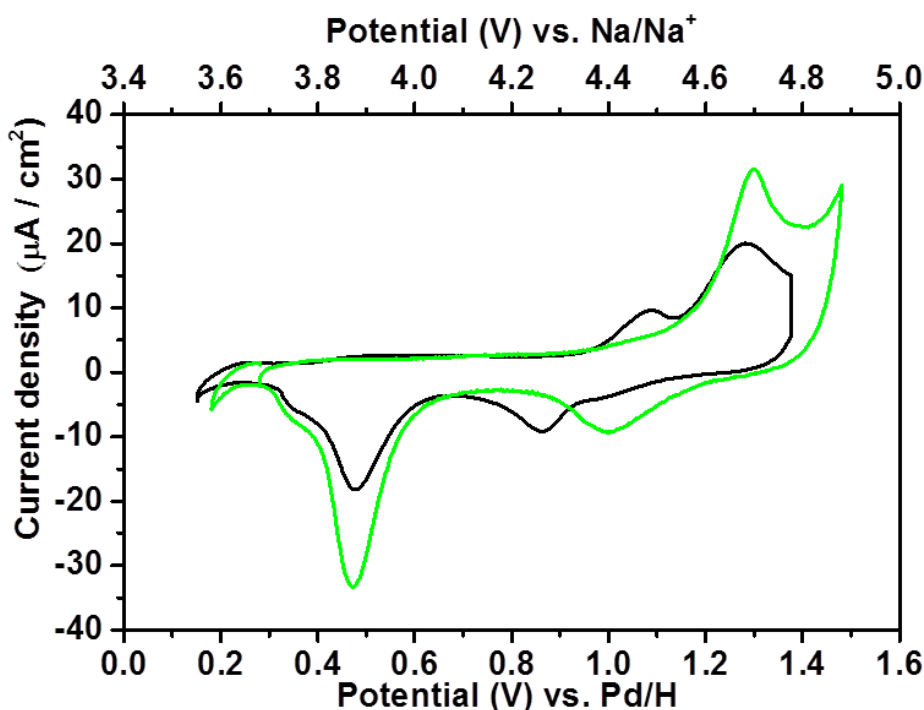


Figure 6.7 CV data for 0.1 M NaClO₄ in H₂O (saturated with oxygen after electrolyte purged with Ar, pH 9) on an Au(111) half bead single crystal with no MeCN (black), 100 mM MeCN (green). Sweep rate 10 mV/s.

In **Fig. 6.6**, all the CV's were taken in electrolytes purged with argon; however for experiments conducted in non-aqueous electrolytes, the electrolyte has to be saturated with oxygen prior to analysis. **Fig. 6.7** demonstrates the effect of purging the electrolyte with oxygen in an aqueous system. In the oxidation sweep a similar trend is observed, with and without the electrolyte having been purged with oxygen. On the reduction sweep, the addition of oxygen has a pronounced effect on the intensity of the reduction band at 0.9 V. The band at 0.9 V is associated with the partial reduction of O to OH⁻ on the electrode surface.⁸ The excess oxygen appears to promote this on the electrode surface. The increase in peak intensities with the addition of MeCN is attributed to the potential in the oxidation sweep having been driven to a more positive value.¹⁶

6.6 Using SHINERS to understand the electrochemical response of moving from an aqueous to non-aqueous electrolyte

The effect of increasing the MeCN concentration on the oxidation and reduction reactions was further analysed using SHINERS on the Au(111) surface, the SHINERS provided a large surface enhancement, allowing the products and intermediates to be studied *in situ*. The Raman data (**Fig. 6.8**) showed that increasing the concentration of MeCN increased the potential at which adsorption of hydroxide ions takes place. Initial OH⁻ adsorption occurred at 0.4 V with 1 mM MeCN (**Fig. 6.8a**), compared to 0.6 V for 100 mM MeCN (**Fig. 6.8c**). This agrees with the CV data showing that MeCN is inhibiting the reaction kinetics.

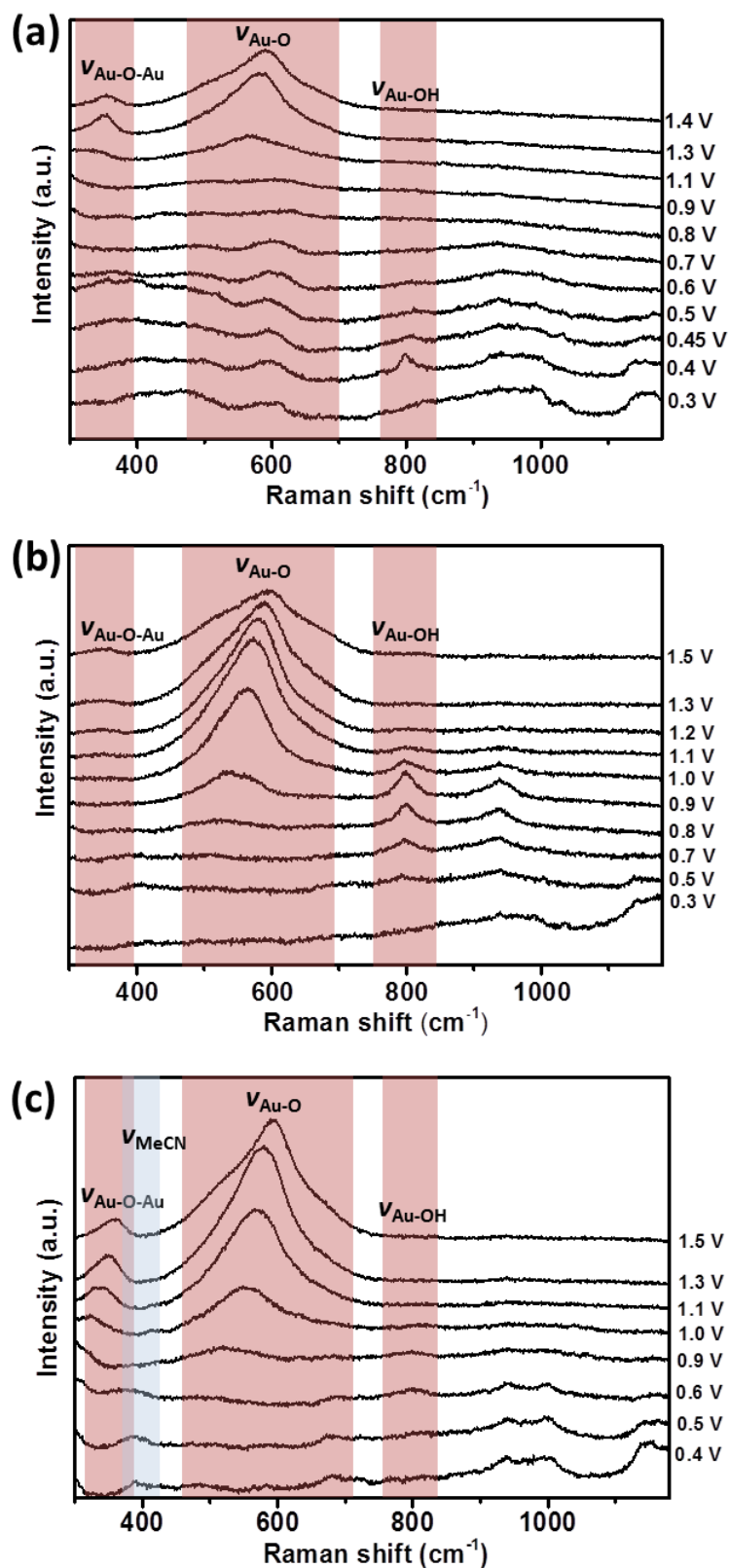


Figure 6.8 *In situ* SHINERS spectra for the oxidation sweep of 0.1 M NaClO₄ in H₂O (purged with Ar) on Au(111) half bead single crystal with (a) 1 mM, (b) 10 mM, (c) 100 mM MeCN. Potential measured vs. Pd/H.

MeCN peaks were observed during oxidation in the Raman spectra, however it would be useful to use a stronger MeCN raman mode (i.e. $C\equiv N_{\text{stretch}}$ at 2258 cm^{-1}) to conclusively detect MeCN on the electrode surface. It is likely that MeCN molecules are adsorbed on the gold surface, blocking the gold surface sites from the absorption of hydroxide ions and in turn the formation of Au-O. Therefore the higher the MeCN concentration, the more molecules blocking the surface, and the greater the over potential required to oxidise the surface.

The oxidation of 0.1 M NaClO_4 with 1 mM MeCN does not correlate with the rest of the results; a peak at 600 cm^{-1} (**Fig. 6.8a**) is oxidised from the surface before Au-O can form. The peak at $\sim 600\text{ cm}^{-1}$ is presently unassigned and is still present at -0.2 V vs. Pd/H in the cathodic scan (**Fig. 6.8 and 6.9**), indicating it may not be an oxidation product and more likely an impurity on the single crystal surface.

Further analysis is needed to understand this phenomenon. The reduction of oxygen from the Au(111) surface, without the addition of MeCN occurs via partial reduction of oxygen to form hydroxide on the surface (**Fig. 6.5b**). This does not appear to be the case with the addition of MeCN. In the cathodic scan, no adsorbed hydroxide is observed on the Au surface at any potential. A peak at 390 cm^{-1} is observed at $\sim 0.4\text{ V}$ and becomes more predominant with increasing MeCN concentrations (**Fig. 6.9**). The peak at 390 cm^{-1} has been assigned to the C-CN stretching mode of MeCN.¹⁷ The formation of the MeCN peak occurs at a similar potential to the hydroxide peak, when no MeCN was present. This indicates adsorbed MeCN inhibits the oxygen reduction reaction by blocking the formation of the hydroxide intermediate on the Au(111) surface.

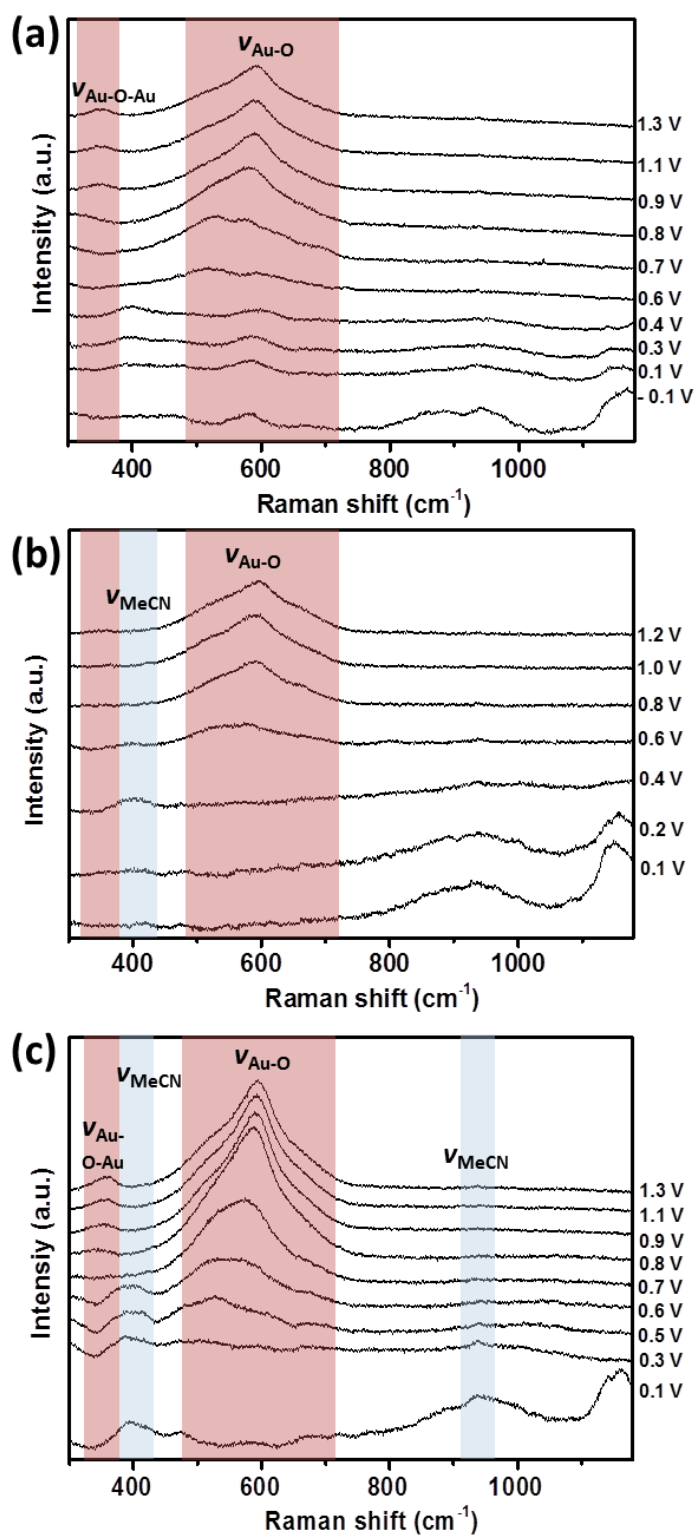


Figure 6.9 *In situ* SHINERS spectra for the reduction sweep of 0.1 M NaClO_4 in H_2O (purged with Ar) on Au(111) half bead single crystal with (a) 1 mM, (b) 10 mM, (c) 100 mM MeCN. Potentials vs. Pd/H.

The onset potential of gold oxide and adsorption of the hydroxide intermediate was shown to vary with the concentration of MeCN in the electrolyte (**Fig. 6.6**). When the concentration of MeCN was equivalent to that of water in the electrolyte the surface was strongly inhibited. *In situ* SHINERS was conducted to identify what was happening at the electrode surface (**Fig. 6.10**).

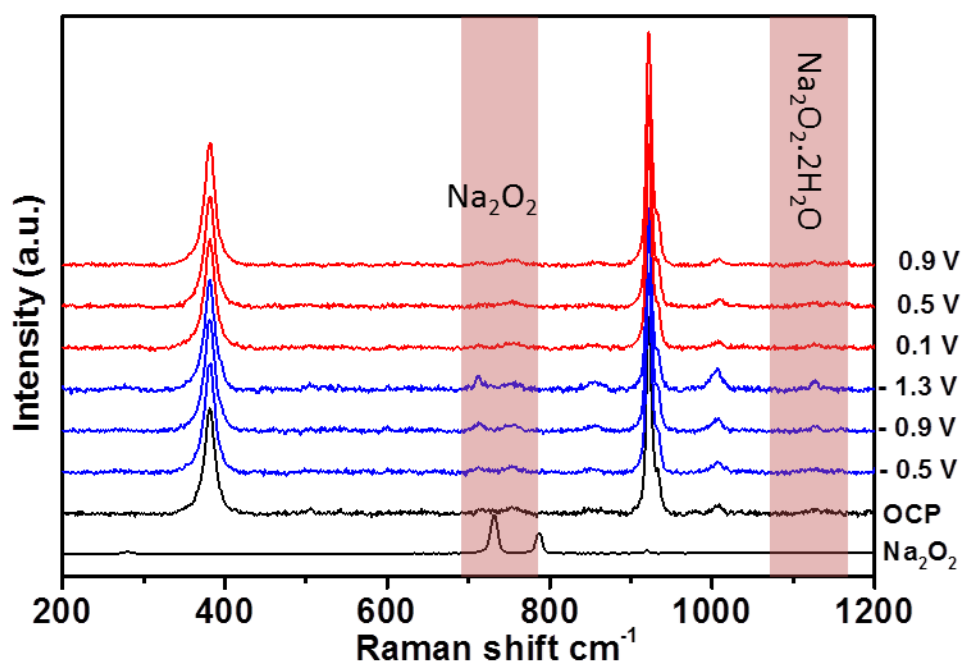


Figure 6.10 Raman spectra of 0.1 M NaClO₄ in water/acetonitrile (50:50) on Au(111) with SHINS. Potentials vs Ag/Ag⁺.

The OCP showed strong MeCN peaks (381 and 920 cm⁻¹) and a couple of perchlorate bands (1004 and 850 cm⁻¹).¹⁸ In the reduction sweep, the presence of a band at 1131 cm⁻¹ could possibly be attributed to the Na₂O₂·2H₂O, in agreement with Na₂O₂ formed on the electrode surface at 710 cm⁻¹, a second band is present in the spectra at 760 cm⁻¹, however this cannot be conclusively assigned to Na₂O₂ due to a perchlorate band forming in the same region. The possible peroxide peak is shifted from its position in the standard spectrum (**Fig. 6.10**), this phenomenon was also observed by Aldous and attributed to the formation of ion pairs with the salt.¹⁹ The presence of NaOH or Na₂CO₃ is not detected in the Raman spectra; however NaOH

may be visible at higher wavenumbers.²⁰ The MeCN appears to push the oxidation potential of the gold surface to higher potentials as Au-O is not visible in the potential range studied.

6.7 Understanding the ORR in an non-aqueous electrolyte

The electrochemical behaviour of NaClO₄ in non-aqueous media is significantly different compared with the aqueous mechanism on Au(111). In non-aqueous systems there have been multiple reports on the various products, formed via a multitude of reaction mechanisms.²¹⁻²⁵ **Fig. 6.11** displays the voltammetric response of 0.1 M NaClO₄ in MeCN (H₂O < 20 ppm).

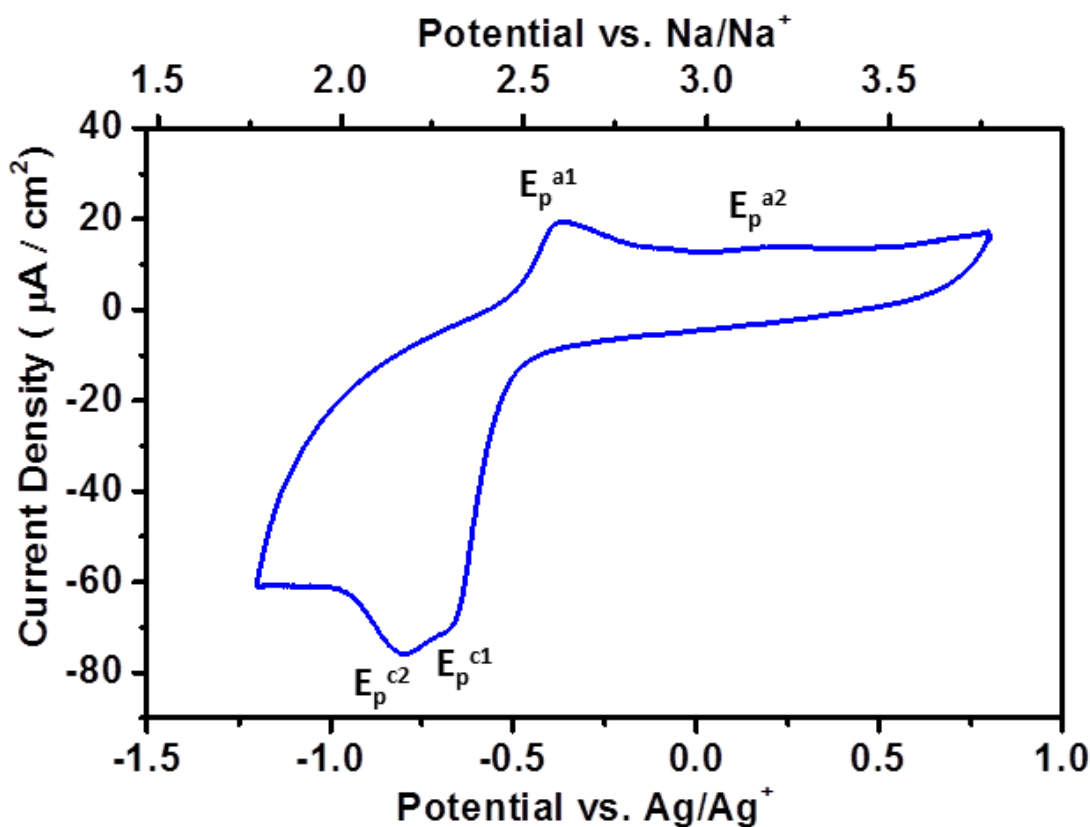


Figure 6.11 CV data for 0.1 M NaClO₄ in MeCN (saturated with oxygen after electrolyte purged, H₂O < 20 ppm) on Au(111) half bead single crystal. Sweep rate 10 mV/s.

The reduction and oxidation sweeps both have two significant peaks (**Fig. 6.11 and Table 6.4**), Ep^{c1} and Ep^{c2} in the reduction sweep. In the oxidation sweep, a strong band (Ep^{a1}) is followed by a shallow broad band (Ep^{a2}). The first reduction band has been assigned to the $1 e^-$ reduction of oxygen to superoxide on the Au electrode surface (**Eq. 6.1**), followed by the spontaneous formation of NaO_2 , in the presence of Na^+ ions on the electrode surface (**Eq. 6.2**). However the literature has shown this can be solvent dependent and may be short lived in MeCN.¹⁹ The second reduction band has been attributed to the second electron reduction to form Na_2O_2 (**Eq. 6.3**). In order to ascertain the exact nature of these species, spectroscopic studies are required.



In the oxidation sweep the oxidation peak Ep^{a1} is likely related to the oxidation of Na_2O_2 on the electrode surface, via a direct $2 e^-$ transfer. However this potential is more indicative of NaO_2 or O_2^- oxidation in the literature.²⁶ Thus more work is required to determine the species present in the oxidation sweep at Ep^{a1} and Ep^{a2} .

Table 6.4 Peak positions from CV in **Fig. 6.11**.

	Ep^{c1}	Ep^{c2}	Ep^{a1}	Ep^{a2}
Peak potential (V) vs Na/Na⁺	2.29	2.17	2.61	3.24

In situ SHINERS studies were conducted to help determine the intermediates and products formed under potential control. For the basis of this chapter, only the oxygen reduction reaction (ORR) has been studied spectroscopically (**Fig. 6.12**), future work will be conducted to study the oxygen evolution reaction (OER). The *in situ* SHINERS studies in the MeCN electrolyte, showed the growth of a number of peaks with decreasing reduction potentials (**Fig. 6.12**). A small peak at 1157 cm^{-1} from 2.54 V is observed, this can be assigned to the formation of NaO_2 on the electrode surface. At 2.54 V the formation of a Na_2O_2 is also observed on the electrode surface (715 cm^{-1}). Aldous et al.¹⁹ observed a similar phenomenon on a rough gold surface. They reported the presence of a second peak associated with Na_2O_2 at 760 cm^{-1} . A similar peak is observed in **Fig. 6.12**; likewise a band is present in the OCP related to perchlorate, therefore it cannot be conclusively assigned. The band at 715 cm^{-1} could also be attributed to the presence of Na_2CO_3 , as the standard has a peak at 699 cm^{-1} (**Fig. 6.14**); a very strong peak would be expected to accompany this band at 1070 cm^{-1} if this was the case. A small band is present, which could imply an amorphous layer of Na_2CO_3 . The growth of peroxide or carbonate is observed to increase, whilst the decrease in superoxide is also observed. Another band on the shoulder of the peak at 1010 cm^{-1} is apparent with decreasing reduction potentials. This is related to the interaction of sodium peroxide and the perchlorate ions.^{19, 27} The Raman spectra have showed that NaO_2 is observed on the electrode surface; however peroxide appears to be the main reduction product in the acetonitrile electrolyte.

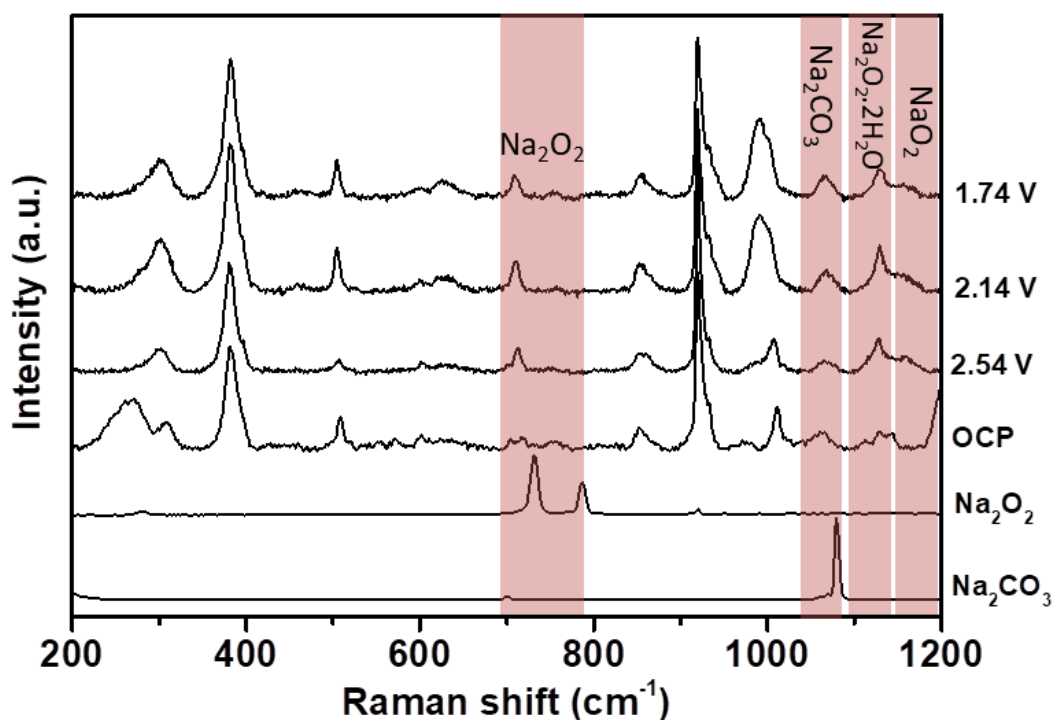


Figure 6.12 *In situ* SHINs spectra for the reduction sweep of 0.1 M NaClO₄ in MeCN (saturated with O₂, H₂O < 20 ppm) on an Au(111) half bead single crystal. (200 – 1200 cm⁻¹ wavenumbers). Potential measured vs. Na/Na⁺.

At 1130 cm⁻¹ a Raman band grows with increasing reduction potential, this band is also apparent in the OCP at a slightly lower potential. The presence of a band at 1136 cm⁻¹ in the literature has been attributed to the presence of Na₂O₂·2H₂O, formed as a result of water in the electrolyte. The peak at 1130 cm⁻¹ may be due to the formation of the di-hydrated species, due to trace water in the electrolyte. The peak may also be related to perchlorate on the electrode surface, again further studies are required to conclusively assign this band.

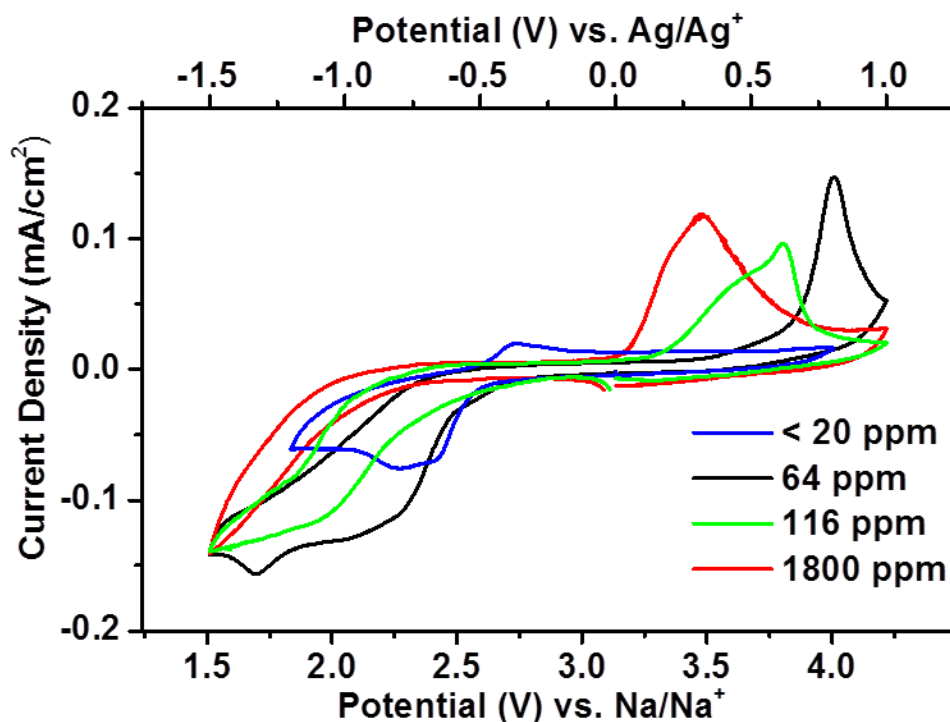


Figure 6.13 CV data for 0.1 M NaClO₄ in MeCN (saturated with oxygen after electrolyte purged on Au(111) half bead single crystal, with increasing H₂O concentrations. Sweep rate 10 mV/s.

Initial studies have been conducted to understand the effect of adding controlled amounts of water into the non-aqueous electrolyte and the impact on the reaction mechanism taking place (**Fig. 6.13**). The CV data shows a decrease in the onset of reduction with increasing water concentration. This indicates that water is inhibiting the adsorption at the electrode surface. The intensity of the first reduction band increases with 64 ppm of water, followed by small second reduction band at 1.7 V. The size of the first reduction band decreases with further increase in water concentration. This band was originally assigned to Na₂O₂ without the presence of water in the electrolyte; the addition of water may be causing the formation of the hydrated peroxy species, or hydroxide species. In order to understand the processes taking place at the surface, SHINERS studies have been undertaken.

Initial SHINERS studies with the addition of 120 ppm water into the electrolyte could not provide conclusive evidence of reaction products and intermediates (**Fig. 6.14**). However the presence of Na_2CO_3 could possibly be detected at 1070 cm^{-1} and 712 cm^{-1} , this could be associated with the decomposition of the electrolyte, which will be discussed later. The presence of $\text{Na}_2\text{O}_2 \cdot 2\text{H}_2\text{O}$ (1130 cm^{-1}) and NaOH may also be present at lower reduction potentials, which would agree with the reaction mechanism proposed by Medrano et al. (**Eq. 6.4 and 6.5**).²⁸

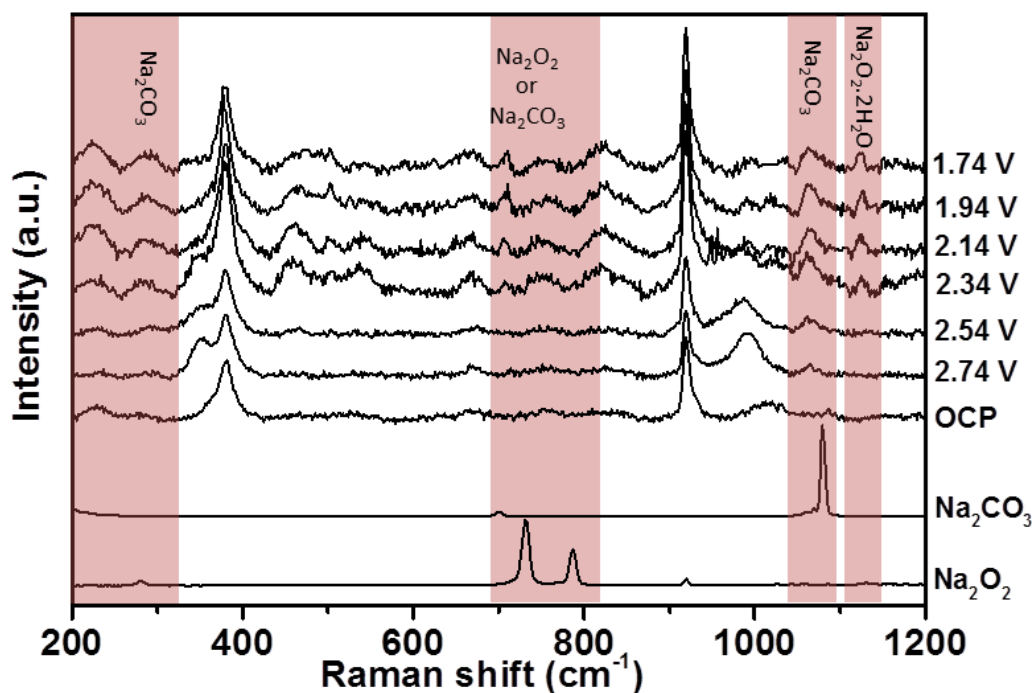
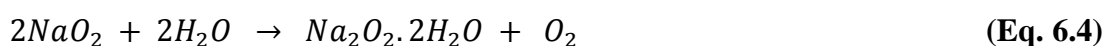


Figure 6.14 *In situ* SHINs spectra for the reduction sweep of 0.1 M NaClO_4 in MeCN (saturated with O_2 , $\text{H}_2\text{O} \sim 120\text{ ppm}$) on an Au(111) half bead single crystal. Lower wavenumbers ($200 - 1200\text{ cm}^{-1}$). Potentials vs. Na/Na^+ .

6.8 Solvent decomposition on the Au(111) surface

The Au(111) surface promotes the catalytic decomposition of MeCN, this agrees with reports on other precious metal surfaces.^{29, 30} The presence of the CN^- on the electrode surface is indicative of MeCN decomposition (**Fig. 6.15**). The CN^- band has a broad peak at 2130 cm^{-1} . The shape of this band is asymmetric in nature at lower potentials, this is indicative of two overlapping bands associated with the coordination of the cyanide ions with Na^+ at lower wavenumbers and MeCN at higher wavenumbers. A substantial increase in intensity of the band at 2130 cm^{-1} is observed at more negative potentials, with the band becoming centred at 2125 cm^{-1} . The increase in intensity is associated with the cyanide sodium interaction, this becomes more prevalent at lower potentials as Na^+ are attracted to the electrode surface,³⁰ when Na_2O_2 and NaO_2 are formed at the electrode surface.

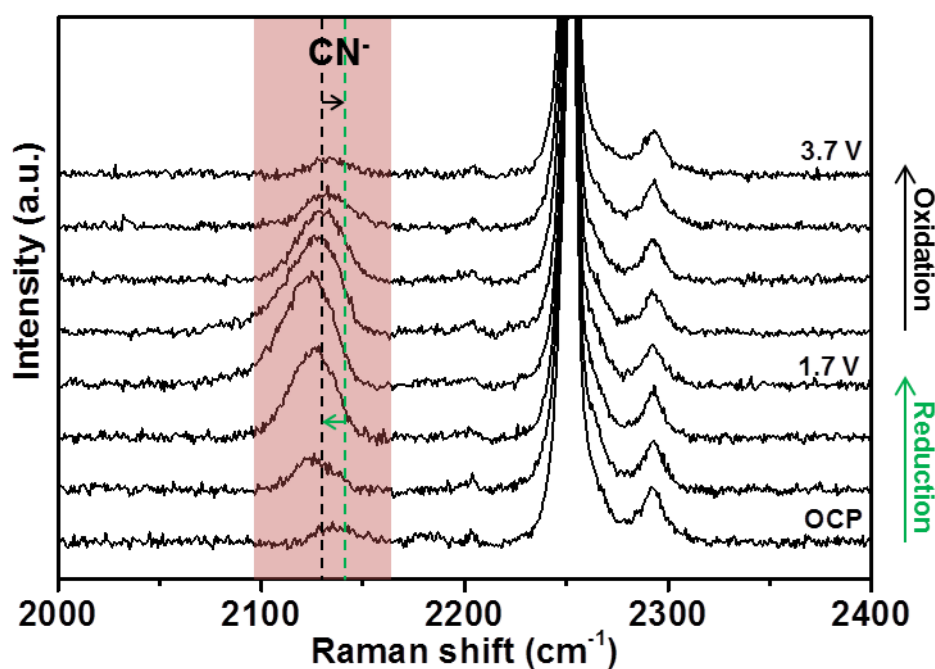


Figure 6.15 *In situ* SHINs spectra for the reduction sweep of 0.1 M NaClO_4 in MeCN (saturated with O_2 , $\text{H}_2\text{O} < 20\text{ ppm}$) on an Au(111) half bead single crystal. Higher wavenumbers ($2000 - 2400\text{ cm}^{-1}$). Potentials vs. Na/Na^+ .

The addition of water into the electrolyte has a pronounced effect on the shift observed in the cyanide band on the electrode surface associated with the decomposition of MeCN (**Fig 6.16**). A slight shift is observed with trace amounts of water (**Fig. 6.15**), this is related to a potential induced stark shift.^{31, 32} Electron donation occurs from the Au surface to the cyano group, decreasing the strength of the CN triple bond, thus reducing the frequency of the vibrational mode.³⁰

The addition of water has been reported to increase the presence of water in the double layer region at the electrode surface. This has been shown to inhibit the onset of cyanide adsorption on the surface to lower reduction potentials. It is hypothesised that the water interacts with the sodium species produced, either producing $\text{Na}_2\text{O}_2 \cdot 2\text{H}_2\text{O}$ or NaOH . These species would restrict electron transfer from the cyano ion to the sodium species. Therefore the C-N bond is associated with Au surface accounting for the stark shift (43 cm^{-1}).³¹

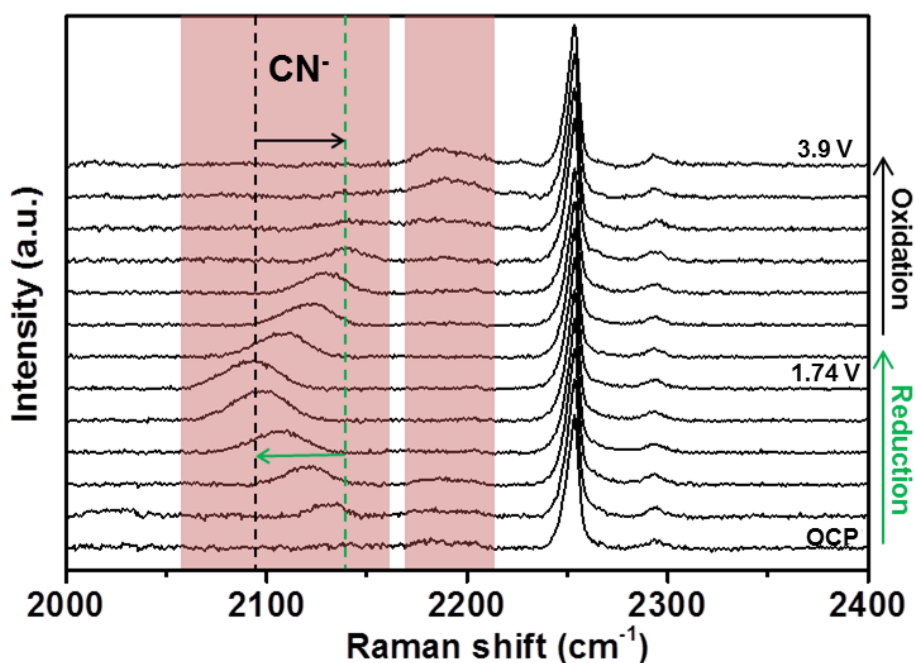


Figure 6.16 *In situ* SHINs spectra for the reduction sweep of 0.1 M NaClO_4 in MeCN (saturated with O_2 , $\text{H}_2\text{O} \sim 120 \text{ ppm}$) on an Au(111) half bead single crystal. Higher wavenumbers ($2000 - 2400 \text{ cm}^{-1}$).

6.9 Conclusions and future work

Overall this chapter has started to assess the changing reaction mechanism moving from an aqueous electrolyte to a non-aqueous electrolyte. In a aqueous system SHINERS has been able track the presence of the hydroxide intermediate in the oxidation and reduction reaction mechanisms on an Au(111) electrode. The addition of acetonitrile into the aqueous system had a passivating effect on the reaction mechanism, inhibiting the onset of oxidation and competing with the partial reduction via the hydroxide intermediate.

In the non-aqueous system, voltammetry and SHINERS studies identified sodium peroxide as the main reduction product, with small amounts of NaO_2 also being detected.

The addition of water to the non-aqueous electrolyte showed the possibility of NaOH and $\text{Na}_2\text{O}_2 \cdot 2\text{H}_2\text{O}$ being formed on the electrode surface. These results represent an initial investigation of single crystals and SHINERS, more work is required to fully understand the complete reaction mechanism with the addition of water. SHINERS of Au(111), in a completely dry electrolyte and the addition of larger volumes of water (500 ppm, 1000 ppm) would provide valuable insight into the processes taking place. A wider spectral range is also required to detect the presence of any sodium hydroxide species $\sim 3000\text{-}3500\text{ cm}^{-1}$.

The decomposition of the solvent was also detected on the Au(111) surface by the formation of the cyanide ion. A large stark shift was observed with the addition of water into the electrolyte,³³ which indicates water is interacting or inhibiting the cyanide at the electrode surface.

6. 10 References

1. P. G. Bruce, S. A. Freunberger, L. J. Hardwick and J.-M. Tarascon, *Nat. Mater.*, 2012, **11**, 19-29.
2. S. Meini, M. Piana, N. Tsiouvaras, A. Garsuch and H. A. Gasteiger, *Electrochem. Solid-State Lett.*, 2012, **15**, A45-A48.
3. T. Liu, M. Leskes, W. Yu, A. J. Moore, L. Zhou, P. M. Bayley, G. Kim and C. P. Grey, *Science*, 2015, **350**, 530-533.
4. T. Zhang and Z.-Y. Wen, *J. Phys. Chem. C*, 2017, **121**, 5968-5973.
5. J. Staszak-Jirkovský, R. Subbaraman, D. Strmcnik, K. L. Harrison, C. E. Diesendruck, R. Assary, O. Frank, L. Kobr, G. K. H. Wiberg, B. Genorio, J. G. Connell, P. P. Lopes, V. R. Stamenkovic, L. Curtiss, J. S. Moore, K. R. Zavadil and N. M. Markovic, *ACS Catal.*, 2015, **5**, 6600-6607.
6. J. Kim, H. Park, B. Lee, W. M. Seong, H.-D. Lim, Y. Bae, H. Kim, W. K. Kim, K. H. Ryu and K. Kang, *Nat. Commun.*, 2016, **7**, 10670.
7. C. Xia, R. Black, R. Fernandes, B. Adams and L. F. Nazar, *Nat. Chem.*, 2015, **7**, 496-501.
8. U. Zhumaev, A. V. Rudnev, J.-F. Li, A. Kuzume, T.-H. Vu and T. Wandlowski, *Electrochim. Acta*, 2013, **112**, 853-863.
9. L. A. Kibler, University of Ulm, 2003. PhD Thesis.
10. X. Wang and L. Andrews, *Inorg. Chem.*, 2005, **44**, 9076-9083.
11. F. Silva and A. Martins, *J. Electroan. Chem.*, 1999, **467**, 335-341.
12. A. Citra and L. Andrews, *J. Mol. Struct.: Theochem*, 1999, **489**, 95-108.
13. I. Srejcic, M. Smiljanic, Z. Rakocevic and S. Strbac, *Int. J. Electrochem. Sci.*, 2011, **6**, 3344-3354.

14. A. V. Rudnev, E. B. Molodkina, A. I. Danilov, Y. M. Polukarov and J. M. Feliu, *Electrochem. Commun.*, 2008, **10**, 502-505.
15. M. Smiljanic, I. Srejjic, V. Marinovic, Z. Rakocevic and S. Strbac, *Hem. ind.* , 2012, **66**, 327-333.
16. A. V. Rudnev, E. B. Molodkina, A. I. Danilov, Y. M. Polukarov, A. Berna and J. M. Feliu, *Electrochim. Acta*, 2009, **54**, 3692-3699.
17. G. Socrates, *Infrared and Raman Characteristic Group Frequencies: Tables and Charts*, Wiley, 2001.
18. I. A. Degen and G. A. Newman, *Spectrochim. Acta, Part A*, 1993, **49**, 859-887.
19. I. M. Aldous and L. J. Hardwick, *Angew. Chem.-Int. Edit.*, 2016, **55**, 8254-8257.
20. M. P. Krobok, P. G. Johannsen and W. B. Holzapfel, *J Phys. Cond. Matt.*, 1992, **4**, 8141.
21. S. Y. Sayed, K. P. C. Yao, D. G. Kwabi, T. P. Batcho, C. V. Amanchukwu, S. Feng, C. V. Thompson and Y. Shao-Horn, *Chem. Commun.*, 2016, **52**, 9691-9694.
22. I. Landa-Medrano, C. Li, N. Ortiz-Vitoriano, I. Ruiz de Larramendi, J. Carrasco and T. Rojo, *J. Phys. Chem. Lett.*, 2016, **7**, 1161-1166.
23. C. L. Bender, D. Schroder, R. Pinedo, P. Adelhelm and J. Janek, *Angew. Chem.-Int. Edit.*, 2016, **55**, 4640-4649.
24. H. Yadegari, Y. Li, M. N. Banis, X. Li, B. Wang, Q. Sun, R. Li, T.-K. Sham, X. Cui and X. Sun, *Energy & Environ. Sci.*, 2014, **7**, 3747-3757.
25. P. Hartmann, C. L. Bender, M. Vračar, A. K. Dürr, A. Garsuch, J. Janek and P. Adelhelm, *Phys. Chem. Chem. Phys.*, 2013, **15**, 11661-11672.
26. S. C. Ma, W. C. McKee, J. W. Wang, L. M. Guo, M. Jansen, Y. Xu and Z. Q. Peng, *Phys. Chem. Chem. Phys.* , 2017, **19**, 12375-12383.
27. J. M. Alia and H. G. M. Edwards, *Vib. Spectrosc.*, 2000, **24**, 185-200.

28. I. Landa-Medrano, J. T. Frith, I. Ruiz de Larramendi, I. Lozano, N. Ortiz-Vitoriano, N. Garcia-Araez and T. Rojo, *J. Power Sources*, 2017, **345**, 237-246.
29. A. I. and H. L., *J. Phys. Chem. Lett.*, 2014, **5**, 3924-3930.
30. P. Cao and Y. Sun, *J. Phys. Chem. B*, 2003, **107**, 5818-5824.
31. R. A. Gu, P. G. Cao, Y. H. Sun and Z. Q. Tian, *J. Electroan. Chem.*, 2002, **528**, 121-126.
32. W. Daum, F. Dederichs and J. E. Müller, *Phys. Rev. Lett.*, 1998, **80**, 766-769.
33. S. Baldelli, G. Mailhot, P. Ross, Y.-R. Shen and G. A. Somorjai, *J. Phys. Chem. B*, 2001, **105**, 654-662.

Chapter 7

Electrochemical Behaviour of Na, Li and TBA on Different Platinum Single Crystal Facets

7.1 Abstract

The results presented in this chapter report the preparation of different single crystal platinum facets (111, 110 and 100) for use in studying the electrochemistry of dioxygen in non-aqueous electrolytes. Specifically the fundamental reaction mechanisms involved in sodium-oxygen and lithium oxygen cells. A study on the electrochemical behaviour of different single crystal facets via cyclic voltammetry, demonstrated the (110) and (111) platinum facets promoted the production of sub-monolayers of Na_2O_2 and multilayers of NaO_2 as the main reduction products. The (111) and (110) facets also promoted the 1e^- oxidation of the surface Na_2O_2 . The addition of a supporting salt also showed an inhibiting effect on the reaction mechanism taking place. Investigation of a Na vs. Li system implied that each cation promoted a different electrochemical pathway, with possible 1e^- oxidation of Na_2O_2 to NaO_2 on specific crystal planes, however a direct 2e^- oxidation was observed with Li. The lithium reaction pathway also appears to be less dependent on the surface orientation, likely due to a build-up of Li_2O_2 on the electrode surface.

7.2 Introduction

The development of metal-oxygen batteries has been of particular interest due to their extremely high theoretical energy densities.¹ However, the reaction mechanisms are particularly complex due to the highly nucleophilic and sensitive reaction intermediates.^{2, 3} The Li-oxygen⁴ and Na-oxygen batteries have lots of problems preventing their development. In order to aid in the successful development, understanding what is happening at the electrode interphase is vital.

Single crystals are particularly useful for studying fundamental reaction mechanisms at the interphase. The ideal and controlled nature of using single crystal surfaces can provide information relating to adsorption properties⁵ such as adsorption sites⁶, chemisorption, physisorption, as well as surface coverages.⁵ Single crystals have predominantly been used for aqueous studies, due to the complex nature of preparing clean, ordered single crystal facets.⁷ There have only been a few non-aqueous single crystal studies, especially in relation to metal-air batteries, and they have been carried out on relatively unreactive gold surfaces.⁸

Studying the fundamental reaction mechanisms and the different behaviour observed between surface facets on platinum, may aid in the understanding and development of the metal-oxygen batteries and could identify any catalytic properties associated with the Pt surface.

7.3 Preparation of the platinum single crystal facets

In order to assure the quality of the results, it is important to check the quality of the single crystals used in this chapter. The crystallinity of the different platinum facets was checked by cyclic voltammetry in 0.1 M H₂SO₄ (see **introduction, Fig. 1.14**).⁷

7.4 Behaviour of NaClO₄ on different platinum single crystal facets

The electrochemical behaviour of 0.1 M NaClO₄ in DMSO on polycrystalline Pt and the (111), (100) and (110) single crystal facets of platinum were investigated using cyclic voltammetry (**Fig. 7.1**). Polycrystalline platinum (**Fig 7.1**) exhibits a reduction peak at 2.38 V, accompanied by a second peak / broad shoulder with a maximum at 2.18 V. In the oxidation sweep, a single broad peak is observed at 2.55 V with a very small shoulder at 2.37 V preceding the peak at 2.55 V.

The Pt(111) and (110) surfaces display substantially different electrochemistry (**Fig. 7.1**). Two peaks are observed in the reduction sweep on both (111) and (110) facets, a band at ~2.46 V followed by a second more intense band at ~2.28 V. In the oxidation sweep a sharp, intense band at 2.42 V (111) and 2.45 V (110) is observed. This peak occurs at the same potential as the shoulder on the polycrystalline electrode. A second broader oxidation peak at 2.62 V for both the (110) and (111) facets follows the bands at ~2.4 V.

The (100) surface displays a very broad reduction peak ~2.29 V (**Fig 7.1**), likely a result of two reduction processes overlapping. The oxidation behaviour displays a single oxidation peak at 2.62 V, a small shoulder may be present prior to the band at 2.62 V, however the intensity is negligible.

The overpotential for the onset of the first reduction process varies between the facets, Pt(110) has the largest overpotential, with Pt(poly) the smallest (overpotential trend, 110 > 111 > 100 > poly) (**Fig. 7.1b**). Likewise, the magnitude of the second reduction peak follows the reverse trend (poly > 100 > 111 > 110). This suggests the first reduction process is likely promoted on terrace sites, whereas the second process is promoted by step and defect sites.

The sharp bands in the oxidation scans are only prominent on the (111) and (110) crystal facets, implying the surface is having a contributing effect on the reaction mechanism taking place. It can be noted that there appears to be a direct relationship between the first and second oxidation band on the different facets. This may imply that the first oxidation process is a precursor to the second, with the first process being more prominent on the (110) and least on the (100).

Table 7.1 Oxidation and reduction peak positions from cyclic voltammetry data 0.1 M NaClO₄ in DMSO from **Fig. 7.1**.

	Ep^{c1} (a)	Ep^{c2} (b)	Ep^{a1} (c)	Ep^{a2} (d)
Pt(111)	2.47 V	2.28 V	2.42 V	2.65 V
Pt(110)	2.46 V	2.28 V	2.45 V	2.62 V
Pt(100)	2.29 V (broad)		2.43 V	2.62 V
Pt(poly)	2.38 V	2.18 V	2.37 V	2.55 V

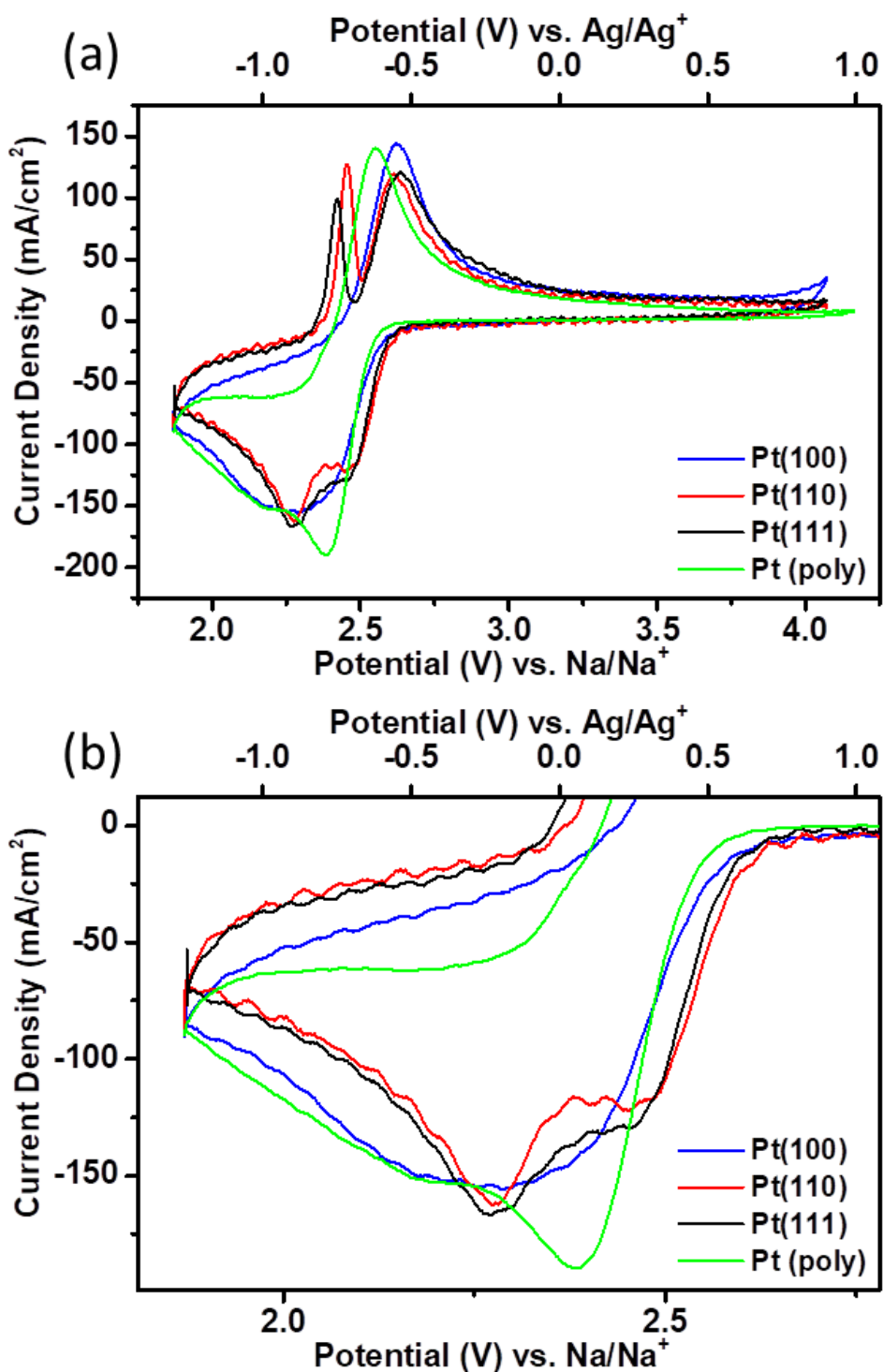


Figure 7.1 (a) CV's of 0.1 M NaClO₄ in DMSO (no TBA, saturated with O₂) on different platinum single crystal facets and polycrystalline platinum, Pt(poly), Pt(111), Pt(110), Pt(100). (b) Magnification of the reduction curve, demonstrating surface structure affects the overpotential for the onset of reduction. Sweep rate 50 mV/s. (NB. Oscillation in CVs a result of the flow of argon over cell causing small vibrations).

The electrochemistry of NaClO_4 on the platinum single crystals has shown significant variation between the different facets, especially the (100) compared with the (110) and (111) facets. These differences are likely a result of the interaction of oxygen with the facet surface, as oxygen is an integral part of the reduction and oxidation reactions taking place, as described later in the chapter.

It has been shown that under ultra-high vacuum (UHV) conditions (at 80 K) that the Pt(111) and (110) facets exhibit sticking probabilities between 0.6 - 0.5, compared to ~ 0.1 for the (100) plane.⁹ Further studies at 300K in UHV measuring the rate of O_2 adsorption showed the (100) facet to be considerably slower ($6 \times 10^{-14} \text{ cm}^{-2} \text{ s}^{-1}$) than on the (111) and (110) facets (0.14 and $0.23 \text{ cm}^{-2} \text{ s}^{-1}$) respectively.⁹ Furthermore, the Pt(100) surface at 80 K gave rise to, a surface coverage of $\sim 1.5\text{-}2 \times 10^{14}$ molecules of O_2/cm^2 .⁹ This is about a quarter of the coverage observed on (111) and (110) under the same conditions, ($6\text{-}7 \times 10^{14}$ molecules of O_2/cm^2). These values all represent O_2 not O_2^- , but a similar trend has been assumed in relation to surface activity for the superoxide species.¹⁰ These values suggest that the superoxide species have a much greater surface coverage and sticking probability on the (110) and (111) facets compared with the (100). This interpretation could afford an intrinsic reason for the voltammetric differences observed in the present study, which will be discussed later in the chapter.

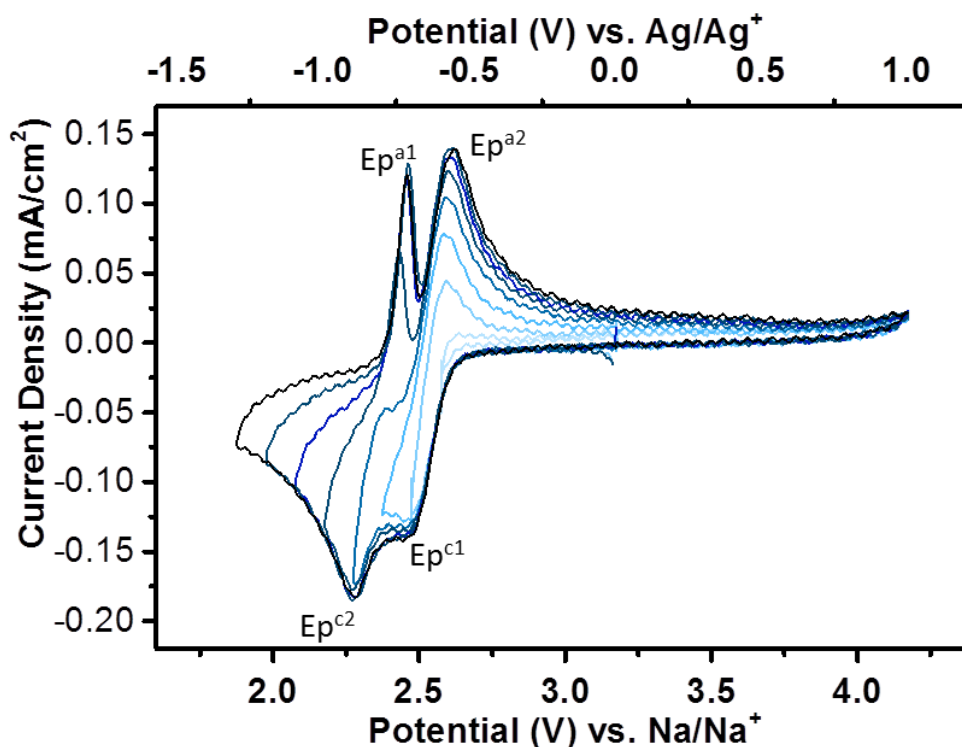


Figure 7.2 CV's of 0.1 M NaClO₄ in DMSO (no TBA, saturated with O₂) on Pt(111) driven to different potentials. Sweep rate 50 mV/s.

In order to elucidate the reaction mechanism taking place on Pt(111) in 0.1 M NaClO₄ / DMSO, the system was swept to increasing reduction potentials, and oxidised to track the resulting electrochemical responses (**Fig 7.2**). The voltammetry data indicated the initial reduction peak (Ep^{c1}) relates to the oxidation peak (Ep^{a2}), i.e. peaks Ep^{c1} and Ep^{a2} are a redox couple. At potentials below 2.4 V (second reduction peak (Ep^{c2}), the presence of the oxidation peak at 2.42 V was observed (Ep^{a1}). This grew with increasing reduction potentials, which implied Ep^{c2} and Ep^{a1} are also a redox couple. This result diverged from results published by Peng et al.¹¹ on a gold electrode, who demonstrated (Ep^{c1}) was related to (Ep^{a1}), and (Ep^{c2}) was associated with (Ep^{a2}).

The work by Peng et al.¹¹ and **Fig. 7.3** suggested that changing the metal surface from gold to platinum influences the reaction mechanism taking place. The Pt(100) surface was produced via cooling in CO, therefore Pt(100) has a 1x1 surface

structure. However, the Au(100) surface has a hex reconstructed surface, after applying a potential this structure will be lifted resulting in a large increase in defect sites. The presence of defects likely catalyse the second redox feature over the first, resulting a larger second reduction peak.

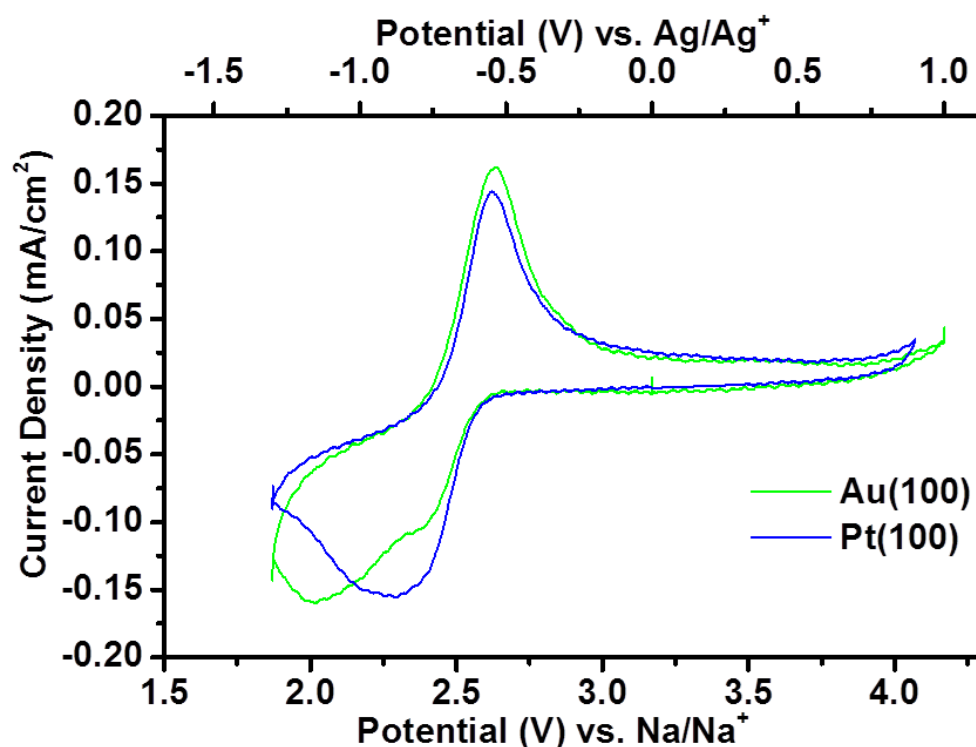
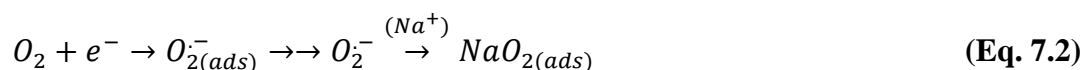


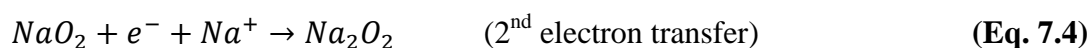
Figure 7.3 CV's of 0.1 M NaClO₄ in DMSO (saturated with O₂) on Au(100) (green), Pt(100) (blue). Sweep rate 50 mV/s.

The reaction mechanism taking place in the sodium-oxygen system has not been clearly identified in the literature with a variety of mechanisms being suggested.¹²⁻¹⁶ Thermodynamically both NaO₂ and Na₂O₂ are viable reduction products, with Na₂O₂ the slightly more stable discharge product with a free energy change (ΔG) of -449.7 kJ mol⁻¹ compared to -437.5 kJ mol⁻¹ for the superoxide species.¹⁷ However, it has been commonly suggested that NaO₂ is the predominant reduction species,^{2, 16, 18, 19} Studies have also demonstrated the Na₂O₂ is a possible product, but the species is usually formed in a hydrated state.^{12, 16, 20}

On all of the Pt surfaces, because of their high affinity for oxygen, we conclude that oxygen is first physisorbed into a precursor state onto the electrode surface (**Eq. 7.1**). It then follows that the initial reduction band at ~ 2.47 V should be assigned to the $1 e^-$ reduction of oxygen to form a superoxide species ($O_2 \rightarrow O_2^-$) on the electrode surface (**Eq. 7.2**). This is consistent both with surface science and electrochemical studies of molecular adsorption of oxygen on platinum.⁹ The superoxide ion would then undergo a spontaneous chemical reaction in the presence of Na^+ to form NaO_2 (**Eq. 7.2**).



The identification of the second reduction peak around 2.28 V cannot be conclusively assigned from the voltammetry data alone. It was suggested by Peng et al that the direct reduction of surface adsorbed O_2 to NaO_2 ¹¹ on an Au surface (**Eq. 7.3**) was occurring. Alternatively, it is hypothesised that adsorbed $NaO_{2(ads)}$ undergoes second electron reduction or disproportionation of $NaO_{2(ads)}$ to Na_2O_2 (**Eq. 7.4 or 7.5**) on platinum. The coadsorption of superoxide on the electrode surface with sodium allows the peroxide to form.



It has previously been shown that the (100) facet has a lower sticking probability and surface coverage of oxygen, the activity of the (100) facet has also been shown to be less active in aqueous media for the oxygen reduction reaction by Attard et al.²¹ This could account for less O_2^- and proportionally less NaO_2 on the surface. The presence of less NaO_2 may result in the formation of smaller NaO_2 islands on the

electrode surface. Comparatively on the Pt(111) and Pt(110) facets, greater coverage of NaO₂ may influence growth of larger NaO₂ islands due to more nucleation sites. This may promote more peroxide growth on these facets relative to the (100) and polycrystalline surfaces. The size of the NaO₂ structure affects the thermodynamic stability of NaO₂. Growth of structures larger than 10 nm are consequently thermodynamically less stable than Na₂O₂ formation.²² The possible thermodynamic preference for peroxide formation may account for the second electron reduction of NaO₂ to Na₂O₂ at the edge of the NaO₂ islands. This reaction has been reported to be sluggish¹¹; therefore, the Pt surface may have a catalytic effect on the reaction mechanism.

The oxidation mechanism for NaClO₄ in DMSO is quite complicated and not fully understood. A substantial change in the voltammetry between the different facets implies a reaction mechanism that is surface and facet dependent. A preliminary explanation has been provided but without further spectroscopic data, the mechanism can only be theorised.

The initial sharp oxidation peak has been assigned to the 1 e⁻ oxidation of adsorbed Na₂O₂ to NaO₂ (**Eq. 7.6**). The presence of this peak is dependent on the Na⁺ concentration in the electrolyte. At low concentrations only small amounts of Na₂O₂ are oxidised from the surface as determined from the surface coverage (θ) of the peroxide species on the (111) facet (**Table 7.2**). At higher Na⁺ concentrations the surface coverage of Na₂O₂ increases substantially, 0.02 for 1 mM to 0.41 for 100 mM, also observed visibly in the peak intensities from the voltammetry data (**Fig. 7.4a**).



The voltammetry data strongly implies that the peroxide is a surface adsorbed species, as it is directly related to the amount of adsorbed NaO₂ on the surface. At low concentrations the size of the 1st oxidation peak is considerably smaller in relation to the 2nd oxidation peak. The difference in peak size decreases with increasing concentration, which is also displayed in the surface coverage of the different species (**Table 7.2 and Fig 7.4**), implying that surface NaO₂ on the electrode surface is converted into peroxide on the surface. This phenomenon holds true for low concentrations, where only small amounts of surface NaO₂ is formed, limited by Na being consumed by O₂, promoting predominantly free superoxide that is oxidised at Ep^{a2}.

Table 7.2 Charge and surface coverage of oxidation species from cyclic voltammetry data of different NaClO₄ concentrations in DMSO, calculated for the Pt(111) facet.

NaClO ₄ concentration	Ep ^{a1}		Ep ^{a2}	
	Q (μC/cm ²)	θ	Q (μC/cm ²)	θ
100 mM	98.80	0.41	508	2.17
50 mM	43.80	0.18	374	1.56
10 mM	23.94	0.10	552	2.3
1 mM	4.80	0.02	824	3.4

However, at higher Na⁺ concentrations the formation of NaO₂ is not limited by the availability of Na⁺ cations. Thus, more surface NaO₂ will be formed; subsequently more peroxide will be formed and therefore less free superoxide. This

is demonstrated in the charge of Ep^{a2} (**Table 7.2**) where the oxidation of O_2^- and NaO_2 overlap (**Eq. 7.7 and 7.8**). Either O_2^- or NaO_2 is the dominant species depending on the concentration of Na, i.e. at low concentration O_2^- is preferred, whereas at higher concentrations NaO_2 is preferred.



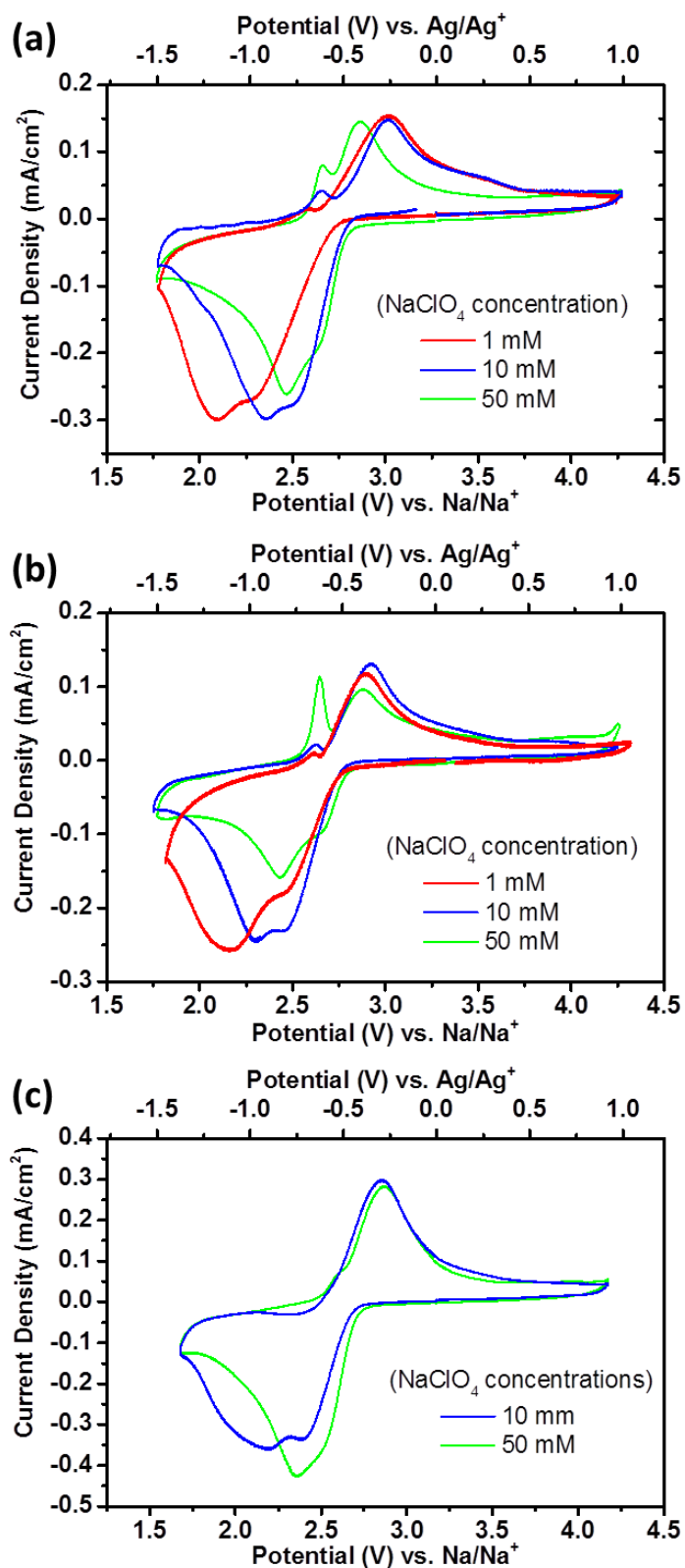


Figure 7.4 CV's of different NaClO₄ concentrations in DMSO (saturated with O₂) on (a) Pt(111), (b) Pt(110), (c) Pt(100). Sweep rate 50 mV/s.

A similar trend is observed between the different platinum facets, the (111) and (110) facets displayed the greatest affinity for peroxide formation, which was observed throughout the concentration studies relative to the (100) surface (**Fig. 7.4**). This was further demonstrated by the surface coverages of 0.1 M NaClO₄ in DMSO of the Ep^{al} peak, with sub monolayer coverages of 0.78, 0.41 and 0.05 for (110), (111) and (100) respectively.

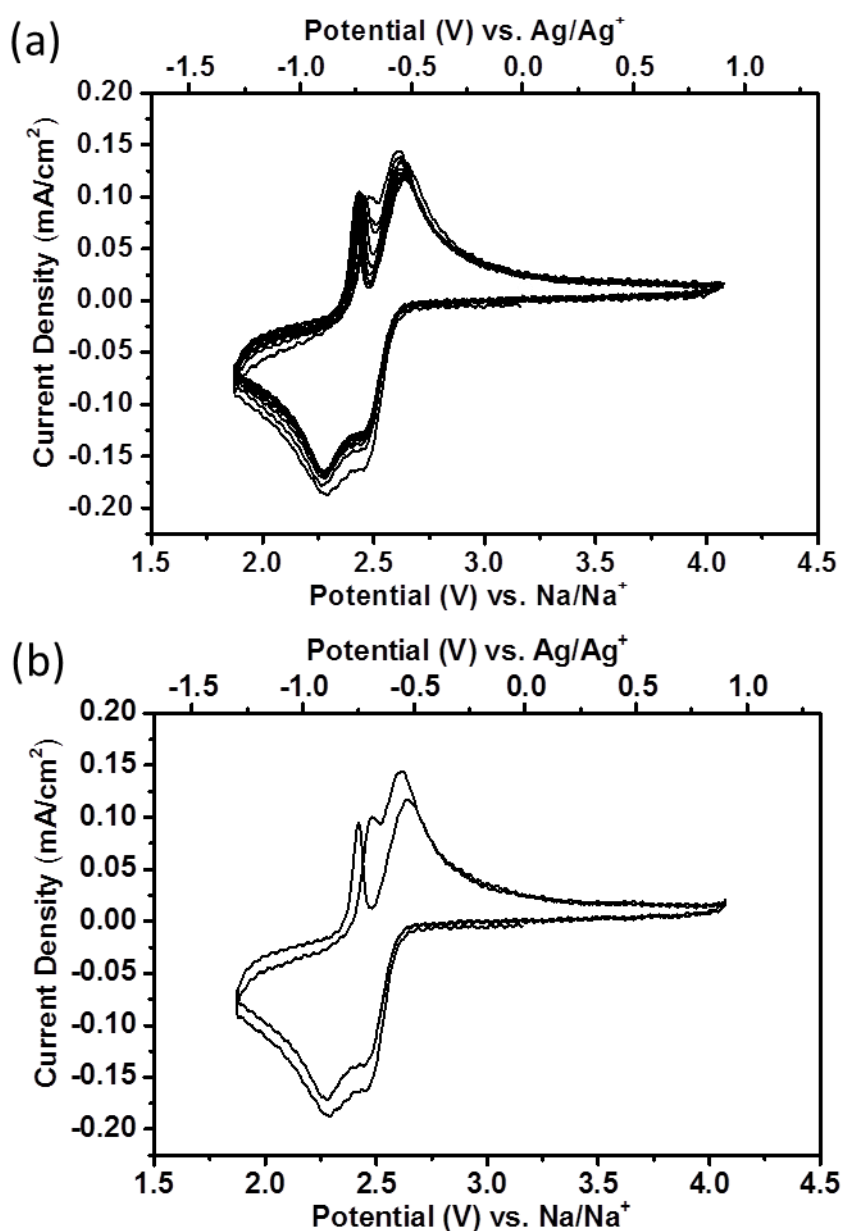


Figure 7.5 (a) CV's of 0.1 M NaClO₄ in DMSO (saturated with O₂) on Pt(111) 10 cycles, (b) CV showing 1st and 10th cycle. Sweep rate 50 mV/s.

In order to assess the reversibility of the reaction mechanism, the reaction was cycled on the Pt(111) surface (**Fig. 7.5a**). This demonstrated that the reaction mechanism was reasonably reversible in the DMSO electrolyte with minimal reduction in peak intensities after the 1st cycle, once the protective bromide layer was stripped (**Fig. 7.5b**). The work presented by Peng et al.¹¹ indicated that sulphoxide adsorption may also be occurring in conjunction with Na products. This may be having an influence on the mechanism and further work is required to understand this.

7.5 Effect of the tetrabutylammonium cation on the reaction mechanism on different Pt single crystal facets without sodium

The addition of a supporting salt (TBAClO₄) without the presence NaClO₄ has a strong inhibiting effect on the reversibility of the superoxide redox couple on the different platinum surface facets. The CV's of 0.1 TBAClO₄ in DMSO (**Fig. 7.6**) showed a partial reduction peak, followed by a sharp tail. The intensity of the reduction peak was most pronounced on the (100) facet compared to the (110) and (111) facets, which display similar intensities and peak shapes to each other. A negative shift in the onset potential of reduction of O₂ to O₂⁻ on the (100) facet relative to the other facets was observed, this trend also occurred on (100) without the presence of TBA. The delay in reduction on the Pt(100) facet implies that the 1 e⁻ reduction of O₂ to O₂⁻ is inhibited by the surface. Attard et al.²³ observed a shift in onset potential of oxide formation in aqueous perchloric acid between the (110), (111) and the (100) facets.²³ This delay was attributed to the adsorption of perchlorate ions on the electrode surface. On the (111) and (110) facets, perchlorate is specifically adsorbed, however on the (100) surface perchlorate is non-specifically

adsorbed.²³ Thus it is possible the perchlorate is having a similar effect in the non – aqueous media.

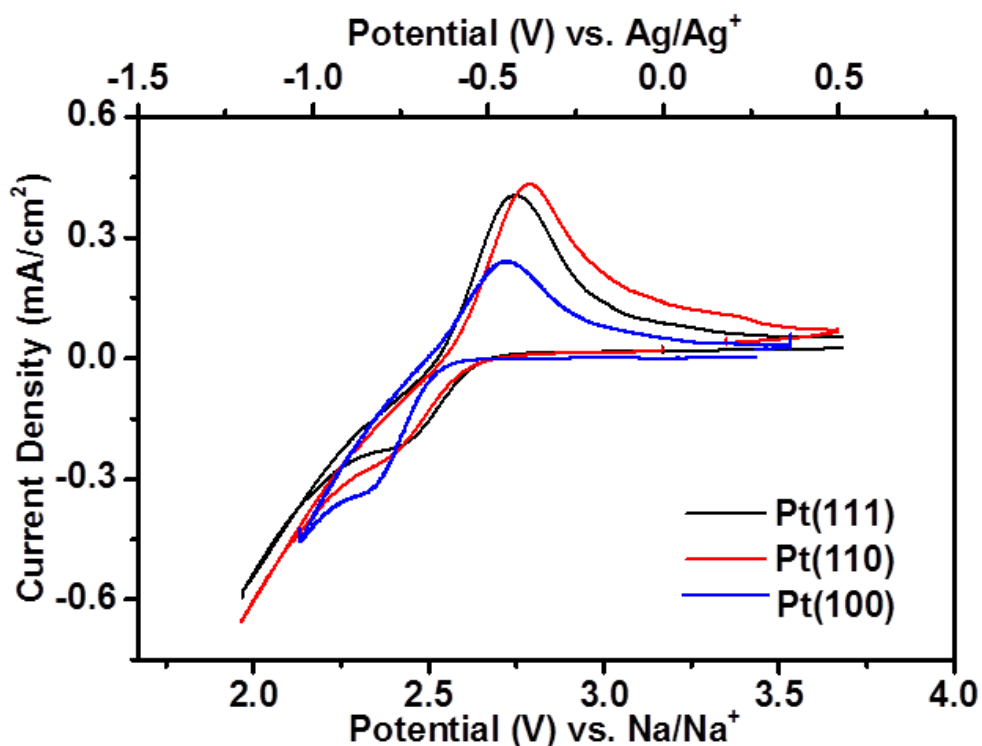


Figure 7.6 CV's of 0.1 M TBAClO₄ in DMSO (no Na⁺, saturated with O₂) on different Pt single crystal facets. Sweep rate 50 mV/s.

Each platinum facet undergoes an initial reduction band accompanied by a catalytic tail, these tails increase in intensity in the reduction regions that were measured. This result signifies that the surface is not being passivated as the current continues to increase; alternatively, continuous production of O₂⁻ is occurring. Unlike the superoxide being reduced directly on the electrode surface (O₂⁻_(ads)) as in the initial reduction band, the TBA is stabilising the produced O₂⁻ in solution, via the hard soft acid base theory as mentioned in chapter 4.²⁴⁻²⁶ The O₂⁻ is then continually solvated into solution due to the highly solubilising nature of DMSO (Gutmann donor number 29.8²⁷). The TBA⁺ has been reported to have a blocking effect on the surface for the adsorption of oxygen. Aldous²⁸ and Deng²⁹ showed that the TBA is adsorbed onto the electrode surface, with the orientation potential dependent (**Fig.**

7.7). The TBA group re-orientates with decreasing potential, at lower potentials, the nitrogen group is held closely to the surface through 1 alkyl chain³⁰. This leads to the availability of surface sites for oxygen adsorption being reduced.

The oxidation sweep on each of the Pt facets shows a single oxidation band, associated with the $1 e^-$ oxidation of the O_2^- to O_2 . The oxidation band on Pt(100) is less intense as the surface was reduced to a less negative potential. However, this indicates that on oxidation the solution species are oxidised at the surface, as O_2^- is removed, O_2^- in solution can migrate to the electrode surface.

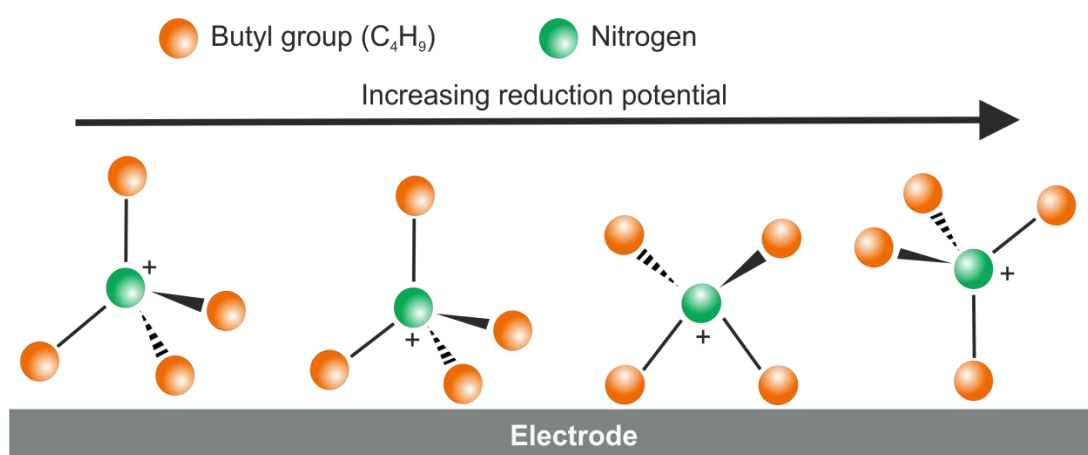


Figure 7.7 Schematic of the potential dependent rearrangement of TBA cation on the electrode. Recreated from Aldous.²⁸

7.6 Effect of the tetrabutylammonium cation on the reaction mechanism on different Pt single crystal facets with sodium

The addition of 0.05 mM NaClO₄ into 0.1 M TBAClO₄/DMSO electrolyte had a different electrochemical response (**Fig 7.8**), in comparison to an electrolyte without the presence of TBA⁺. In the preceding section TBA⁺ was shown to have an inhibiting effect on the adsorption of the oxidation species on the electrode surface, instead promoting solvation of the oxygen species upon reduction. An inhibiting effect is also observed with the addition of NaClO₄ into the electrolyte (**Fig. 7.8**). The sharp oxidation band at ~ 2.45 V is substantially less intense with the presence of TBA⁺ in the electrolyte. This phenomenon is likely a result of the TBA⁺ inhibiting the formation of peroxide on the electrode surface, a reduction in the intensity of the second reduction band on all of the facets relative to the CV without TBA⁺ provides further evidence of this. A likely explanation for the reduced coverage of Na₂O₂ on the electrode surface is the TBA cation supports the O₂⁻ in solution and therefore NaO₂ in solution. This promotes the second electron transfer or disproportionation to happen and be solubilised into solution. A further indication of Na₂O₂ being solubilised is the prevention of surface passivation, which occurs without TBA⁺. The reduction current does not reach zero, which implies the surface is still active at these reduction potentials; this is not the case without TBA⁺ where the current becomes negligible in the reduction sweep.

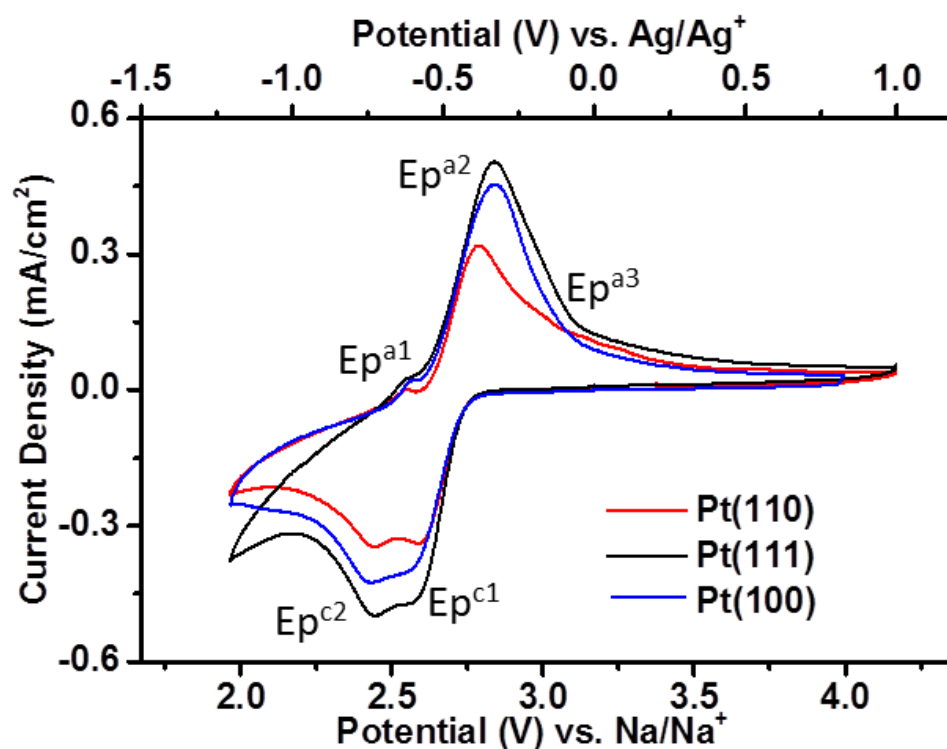


Figure 7.8 CV's of 50mM NaClO₄ in 0.1 M TBAClO₄ in DMSO (saturated with O₂) on different Pt single crystal facets. Sweep rate 50 mV/s.

The potential window opening of 0.1 M NaClO₄ in 0.1 M TBAClO₄/DMSO demonstrated the relationship between reduction and oxidation peaks (**Fig. 7.9**). A similar trend was observed with the addition of the TBA salt to the same system without the supporting salt. On Pt(111) peaks Ep^{c1} and Ep^{a2} are related redox processes. Peak Ep^{c2} and Ep^{a1} are also related, however with decreasing potential a third oxidation peak (Ep^{a3}) grows in intensity. This third peak is not observed without the addition of the supporting salt. Ep^{a3} is attributed to the oxidation of Na₂O₂ in solution,¹¹ this coincides with the reduction in intensity of the initial oxidation band (Ep^{a1}), assigned to the 1e⁻ oxidation of Na₂O₂, which has inhibited the presence of TBA⁺ on the electrode surface; thus promoting the formation of the solution species.

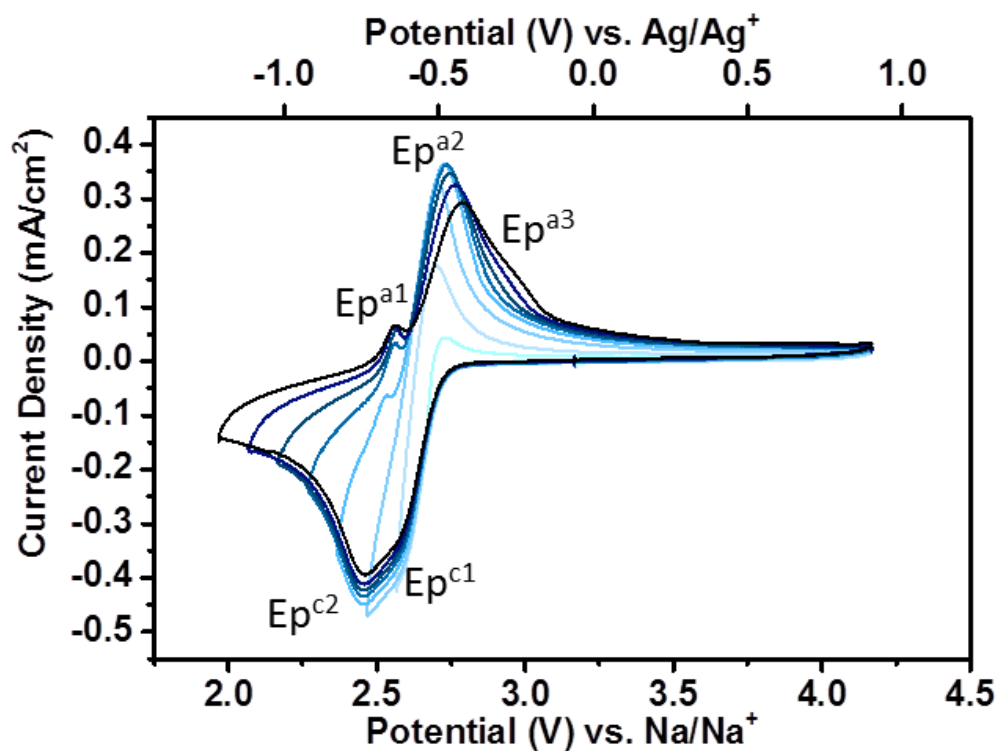


Figure 7.9 CV's of 0.1 M NaClO₄ in 0.1 M TBAClO₄ in DMSO (saturated with O₂) on Pt(111) driven to different potentials. Sweep rate 50 mV/s.

Fig. 7.10 shows cycling of the electrolyte system with the presence of TBA⁺ has reasonable reversibility after the first couple of cycles, once the bromide has been stripped from the surface. A similar trend was observed without the presence of TBA⁺, with no build-up of peroxide on the electrode surface. The limited reduction in intensity of the all the peaks implied that minimal amounts of side reactions were occurring, i.e. minimal carbonates or other degradation species which are notoriously difficult to oxidise within this potential window.

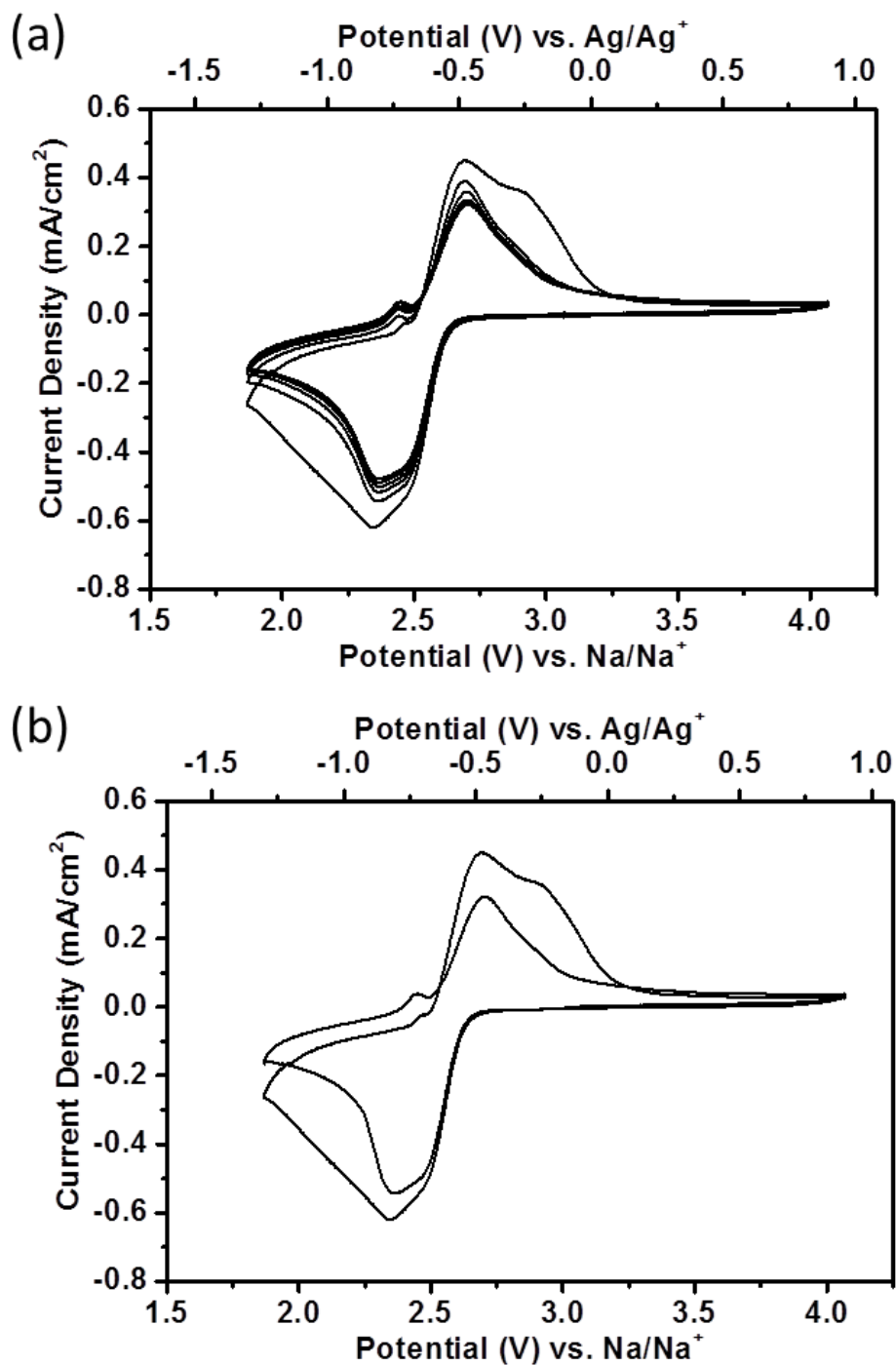


Figure 7.10 CV's of 0.1 M NaClO₄ in 0.1 M TBAClO₄ in DMSO on Pt(111) (a) cycled 10 times, (b) 1st and 10th cycle. Sweep rate 50 mV/s.

7.7 Concentration effects on the reaction mechanisms in the presence of TBA⁺ and Na⁺ cations

The reaction mechanism in the presence of both Na⁺ and TBA⁺ in DMSO appears to be concentration dependent. In electrolytes without any Na⁺ present, the TBA⁺ has an inhibiting effect on the electrode surface as it competes with O₂ for adsorption sites. Thus forcing O₂⁻ to be produced in solution via an outer sphere electron transfer mechanism (see experimental).³¹ The TBA⁺ also acts to stabilise the O₂⁻ in solution, as mentioned previously. The addition of 1 mM NaClO₄ sees a large increase in current response on all of the facets in both the oxidation and reduction scans (**Fig. 7.11a**). This increase in current response, implies that small amounts of sodium ions catalyse superoxide formation in solution. This could be the result of Na⁺ co-adsorbing with the superoxide in a preferential orientation on the electrode surface, creating more available surface sites for adsorption. A catalytic tail is still observed with addition of 1 mM NaClO₄. The presence of this catalytic tail implies that free O₂⁻ is still being produced and solubilised into solution in the presence of TBA⁺ on the electrode surface. The presence of free O₂⁻ is likely a result of all the Na⁺ being consumed in the reduction reaction.

Upon a further increase in Na⁺ concentration (**Fig. 7.11b+c**), the NaO₂ competes with the TBA⁺ on the electrode surface, with free O₂⁻ being spontaneously driven to NaO₂. The 1st oxidation peak at ~2.45 V is seen to increase in intensity with increasing Na⁺ concentration, as more peroxide is formed and oxidised off the electrode surface. However, the presence of TBA⁺ is still inhibiting the electrode surface, producing peroxide in solution which is oxidised at potentials ~2.9 V, after the second oxidation peak.

The addition of TBA^+ as a supporting salt to the $\text{NaClO}_4/\text{DMSO}$ has a substantial inhibiting effect on the reaction compared to the same reaction without the addition of the supporting salt. The reaction mechanism has been theorised to change from Na_2O_2 being produced on the electrode surface and predominantly oxidised via a 1 e^- transfer to NaO_2 without the presence of TBA^+ . Instead, in the presence of TBA^+ , surface based Na_2O_2 is inhibited, therefore solubilised peroxide is produced. This was demonstrated by a comparison of the surface coverage of peroxide on the Pt(111) showing a significant decrease without TBA^+ 0.41 of a monolayer relative to 0.07 with TBA^+ in the electrolyte. It being implied the peroxide is being formed in solution, then likely oxidised via direct oxidation to Na and O_2 at a more positive oxidation potential.

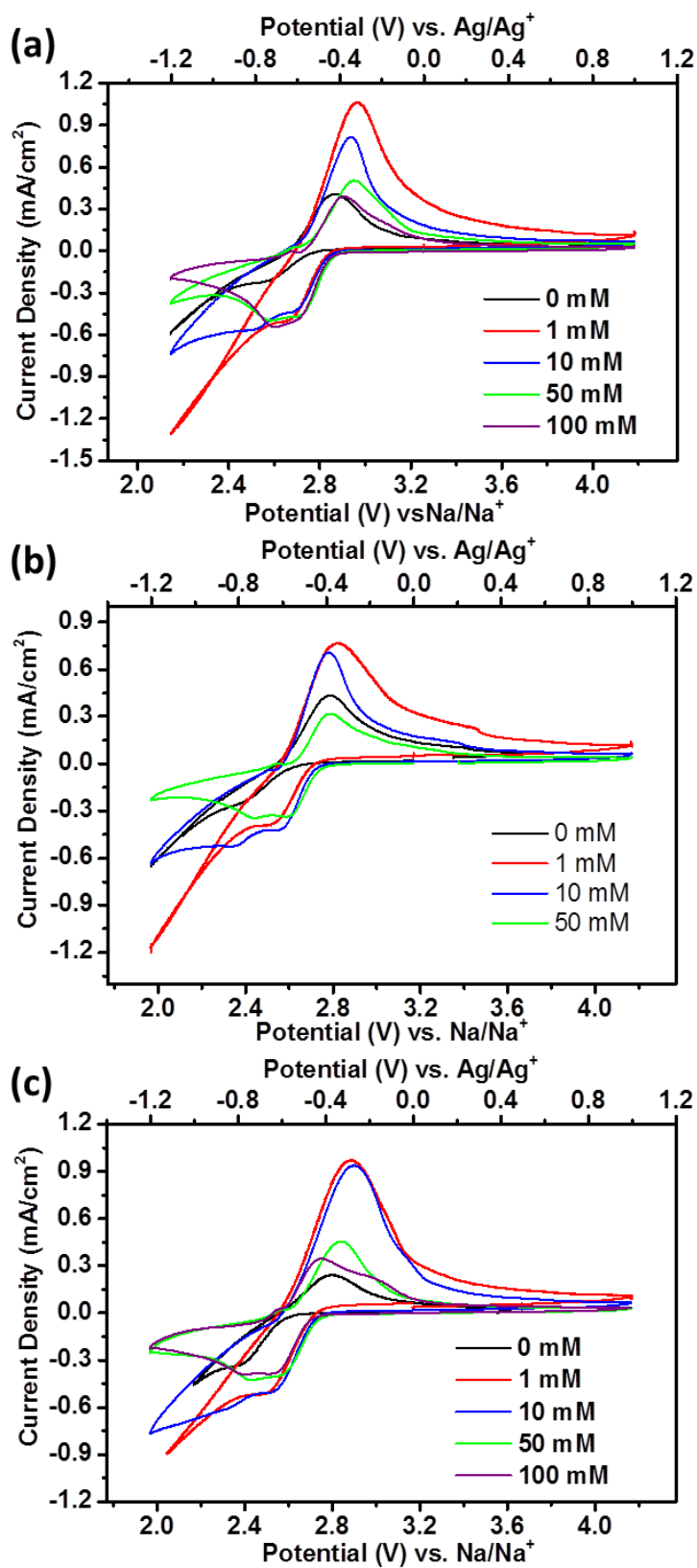
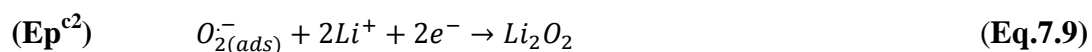


Figure 7.11 CV's of different NaClO₄ concentrations in 0.1 M TBAClO₄ / DMSO (saturated with O₂) on (a) Pt(111), (b) Pt(110), (c) Pt(100). Sweep rate 50 mV/s.

7.8 Comparing the behaviour of LiClO₄ and NaClO₄ on different platinum single crystal facets

A notable change in the electrochemistry is observed when sodium cations were swapped for lithium (**Fig 7.12a**). A single broad reduction peak was observed in the reduction sweep with lithium, this may be the overlapping of two electrochemical processes. Initially the reduction of O₂ to O₂⁻ (**Eq. 7.8**), followed by O₂⁻ to Li₂O₂ in the presence of Li⁺ (**Eq.7.9**). Bruce et al³² suggested a spontaneous reaction to form LiO₂ on Au does not occur due to the highly solvating nature of DMSO or if it does the lifetime of the LiO₂ is too short to be detected, therefore on platinum it is predicted O₂⁻ is also formed in solution where it can undergo disproportionation to form Li₂O₂ (**Eq. 7.9**), which precipitates onto the electrode surface. This behaviour varies in sodium, where 2 reduction peaks are observed (**Fig 7.12a**), linked with the formation of surface NaO₂ and Na₂O₂. The window opening with Li on Pt(111) (**Fig. 7.12b**) demonstrates the reduction band with decreasing potential Ep^{c1} is converted into Ep^{c2}, which oxidise at Ep^{a1} and Ep^{a2}, in agreement with O₂⁻ being reduced to Li₂O₂ in the presence of Li⁺.



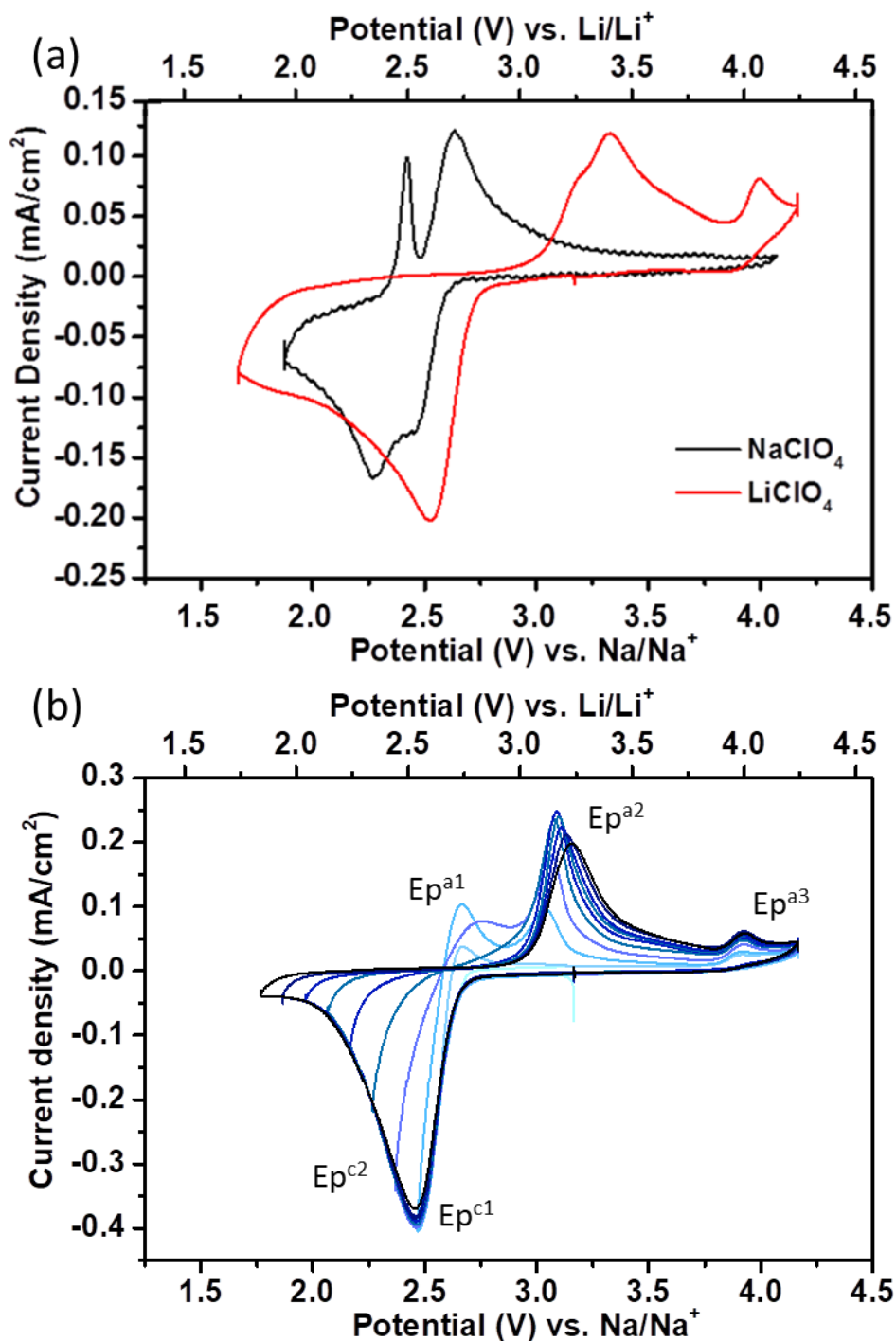


Figure 7.12 CV's of (a) 0.1 M LiClO_4 (red) and 0.1 M NaClO_4 (black) in DMSO (no TBA, saturated with O_2) on Pt(111). Sweep rate 50 mV/s, (b) 0.05 M LiClO_4 in DMSO (no TBA, saturated with O_2) on Pt (111). Sweep to different potentials to determine peak relationships. Sweep rate 50 mV/s.

The oxidation sweeps with Na and Li cations are significantly different. Sodium has two oxidation peaks which have been assigned earlier to the $1 e^-$ oxidation of Na_2O_2 to NaO_2 , preceded by the oxidation of NaO_2 and O_2^- depending on Na^+ concentration. However, the presence of multiple oxidation peaks are detected with Li^+ , a broad peak at ~ 3.25 , which appears to have a couple of overlapping peaks, followed by another peak at 4.0 V or 4.1 V depending on Li^+ concentration (**Fig. 7.12a + b**). The potential window opening shows that Ep^{a1} is related to Ep^{c1} but as the potential is reduced, the intensity of Ep^{a1} decreases as it is transformed into Ep^{a2} , strongly implying O_2 to O_2^- is the initial step in the reaction mechanism. The overlapping oxidation bands around 3.25 V and 3.45 V are attributed to the oxidation of Li_2O_2 ; unlike sodium where a $1 e^-$ oxidation of the peroxide species occurs, a direct $2 e^-$ oxidation of peroxide to Li^+ and oxygen is hypothesised in agreement with other results.^{33,34} The appearance of a couple of peaks in this region could imply that oxidation of LiO_2 may also be occurring, and could be a result of LiO_2 being formed on the electrode surface,³⁴ however this is debatable, so more work is required to understand the oxidation processes.

The oxidation peak Ep^{a3} which occurs at 4.1 V is likely the result of the oxidation of a decomposition product.³⁵ This peak is observed when superoxide is observed and grows in intensity, with increasing reduction potentials.

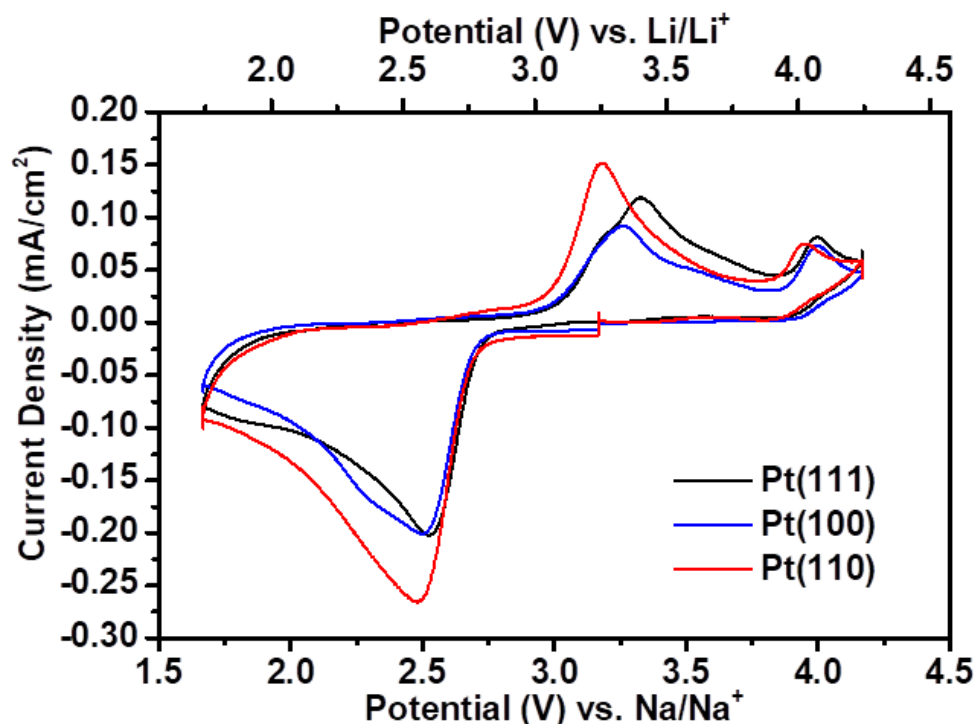


Figure 7.13 CV's of 0.1 M LiClO₄ in DMSO (no TBA, saturated with O₂) on different Pt single crystal facets. Sweep rate 50 mV/s.

A comparison of the different platinum facets with 0.1 M LiClO₄ in DMSO did not show a similar trend to that associated with sodium (**Fig. 7.13**). The onset of reduction was still slightly shifted to a more negative potential with the (100) facet relative to the other facets. However, the (110) surface displayed a different electrochemical response to the other two facets. The (110) facets had a more intense reduction band, probably related to the greater surface coverage associated with this facet. It could prevent less bulk O₂⁻ being formed and inhibit the disproportionation to Li₂O₂. In the oxidation sweep the (110) has a more intense oxidation band associated with either free superoxide or oxidation of surface bound lithium superoxide.

7.9 Conclusions and future work

Overall this chapter has demonstrated the successful preparation of the (110), (100) and (111) low index platinum single crystal facets, for use in non-aqueous studies. Initial studies showed that without the addition of a supporting salt it is probable that the oxidation of sodium peroxide produced in the reduction sweep, is promoted via $1 e^-$ oxidation on the (111) and (110) facets. This phenomenon is not as pronounced on the (100) facet, likely related to the limited surface coverage associated with the facet. The addition of TBA as a supporting salt directly inhibits the reduction of sodium species on the electrode surface, promoting NaO_2 to be produced in solution.

A study of the different electrochemical behaviour, when using sodium or lithium cations in the electrolyte displayed significant mechanistic differences. The sodium mechanism probably utilised a $1e^-$ oxidation of the peroxide. In comparison, in the presence of lithium, a $2 e^-$ oxidation of the peroxide occurred. The presence of decomposition products may also have been detected in the lithium system.

The results in this chapter are all based on the voltammetry data produced, therefore all the reaction mechanisms can only be theorised. In order to prove or disprove the proposed schemes, it is necessary to undertake further work.

Voltammetry studies using higher concentrations of NaClO_4 would provide interesting data on the preference between NaO_2 and Na_2O_2 formation on the Pt facets. It is likely peroxide formation may be favoured at greater concentrations, as the surface coverage increased dramatically from 1 mM to 100 mM but more investigation is required to understand this. Further work on the behaviour of lithium on the different facets would also help to elucidate the reaction mechanisms taking place.

In situ Raman studies using SHINERS, and AFM studies would be invaluable in ascertaining the species present on the electrode surface in relation to potential.

Further theoretical work to develop the understanding of the interactions of TBA and Na on the electrode surface would also be of interest in gaining a better insight into the reaction mechanism taking place.

7.10 References

1. D. Sharon, D. Hirshberg, M. Afri, A. A. Frimer, M. Noked and D. Aurbach, *J. Solid State Electrochem.*, 2017, **21**, 1861-1878.
2. S. Y. Sayed, K. P. C. Yao, D. G. Kwabi, T. P. Batcho, C. V. Amanchukwu, S. Feng, C. V. Thompson and Y. Shao-Horn, *Chem. Commun.*, 2016, **52**, 9691-9694.
3. P. G. Bruce, S. A. Freunberger, L. J. Hardwick and J.-M. Tarascon, *Nat. Mater.*, 2012, **11**, 19-29.
4. N. Imanishi, A. C. Luntz and P. G. Bruce, *The Lithium Air Battery: Fundamentals*, Springer, 2014.
5. O. Hazzazi, PhD Thesis, University of Cardiff, 2003.
6. O. A. Hazzazi, G. A. Attard, P. B. Wells, F. J. Vidal-Iglesias and M. Casadesus, *J. Electroan. Chem.*, 2009, **625**, 123-130.
7. L. A. Kibler, University of Ulm, 2003. PhD Thesis.
8. J. Staszak-Jirkovský, R. Subbaraman, D. Strmcnik, K. L. Harrison, C. E. Diesendruck, R. Assary, O. Frank, L. Kobr, G. K. H. Wiberg, B. Genorio, J. G. Connell, P. P. Lopes, V. R. Stamenkovic, L. Curtiss, J. S. Moore, K. R. Zavadil and N. M. Markovic, *ACS Catal.*, 2015, **5**, 6600-6607.
9. V. A. Sobyenin, G. K. Boreskov, A. R. Cholach and A. P. Losev, *React. Kinet. Catal. Lett.*, 1985, **27**, 299-304.
10. R. G. Jungst and E. S. Meeting, *Power Source Modeling: Proceedings of the International Symposium*, Electrochemical Society, 2005.
11. S. C. Ma, W. C. McKee, J. W. Wang, L. M. Guo, M. Jansen, Y. Xu and Z. Q. Peng, *Phys. Chem. Chem. Phys.*, 2017, **19**, 12375-12383.

12. C. L. Bender, D. Schroder, R. Pinedo, P. Adelhelm and J. Janek, *Angew. Chem.-Int. Edit.*, 2016, **55**, 4640-4649.
13. I. M. Aldous and L. J. Hardwick, *Angew. Chem.-Int. Edit.*, 2016, **55**, 8254-8257.
14. C. Xia, R. Black, R. Fernandes, B. Adams and L. F. Nazar, *Nat. Chem.*, 2015, **7**, 496-501.
15. P. Hartmann, M. Heinemann, C. L. Bender, K. Graf, R.-P. Baumann, P. Adelhelm, C. Heiliger and J. Janek, *J. Phys. Chem. C.*, 2015, **119**, 22778-22786.
16. I. Landa-Medrano, J. T. Frith, I. Ruiz de Larramendi, I. Lozano, N. Ortiz-Vitoriano, N. Garcia-Araez and T. Rojo, *J. Power Sources*, 2017, **345**, 237-246.
17. H. Yadegari, Q. Sun and X. Sun, *Adv. Mater.*, 2016, **28**, 7065-7093.
18. P. Hartmann, C. L. Bender, M. Vračar, A. K. Dürr, A. Garsuch, J. Janek and P. Adelhelm, *Phys. Chem. Chem. Phys.*, 2013, **15**, 11661-11672.
19. P. Hartmann, C. L. Bender, M. Vračar, A. K. Dürr, A. Garsuch, J. Janek and P. Adelhelm, *Nat. Mater.*, 2013, **12**, 228-232.
20. I. Landa-Medrano, C. Li, N. Ortiz-Vitoriano, I. Ruiz de Larramendi, J. Carrasco and T. Rojo, *J. Phys. Chem. Lett.*, 2016, **7**, 1161-1166.
21. G. A. Attard and A. Brew, *J. Electroan. Chem.*, 2015, **747**, 123-129.
22. S. Kang, Y. Mo, S. P. Ong and G. Ceder, *Nano Lett.*, 2014, **14**, 1016-1020.
23. G. A. Attard, A. Brew, K. Hunter, J. Sharman and E. Wright, *Phys. Chem. Chem. Phys.*, 2014, **16**, 13689-13698.
24. C. Ó'Laoire, Northeastern University, 2010.

25. C. O. Laoire, S. Mukerjee, K. M. Abraham, E. J. Plichta and M. A. Hendrickson, *J. Phys. Chem. C.*, 2010, **114**, 9178-9186.
26. C. O. Laoire, S. Mukerjee, K. M. Abraham, E. J. Plichta and M. A. Hendrickson, *J. Phys. Chem. C.*, 2009, **113**, 20127-20134.
27. V. Gutmann, *Coord. Chem. Rev.*, 1976, **18**, 225-255.
28. I. M. Aldous and L. J. Hardwick, *J. Phys. Chem. Lett.*, 2014, **5**, 3924-3930.
29. Z. Deng and D. E. Irish, *J. Phys. Chem.*, 1994, **98**, 9371-9373.
30. W. R. Fawcett, M. Fedurco and M. Opallo, *J. Phys. Chem. C.*, 1992, **96**, 9959-9964.
31. N. M. Markovic, *Nat. Mater.*, 2013, **12**, 101-102.
32. L. Johnson, C. M. Li, Z. Liu, Y. H. Chen, S. A. Freunberger, P. C. Ashok, B. B. Praveen, K. Dholakia, J. M. Tarascon and P. G. Bruce, *Nat. Chem.*, 2014, **6**, 1091.
33. A. I. Belova, D. G. Kwabi, L. V. Yashina, Y. Shao-Horn and D. M. Itkis, *J. Phys. Chem. C.*, 2017, **121**, 1569-1577.
34. F. S. Gittleson, W.-H. Ryu and A. D. Taylor, *ACS Appl. Mater. Interfaces*, 2014, **6**, 19017-19025.
35. V. S. Dilimon, D.-G. Lee, S.-D. Yim and H.-K. Song, *J. Phys. Chem. C.*, 2015, **119**, 3472-3480.

Chapter 8

Conclusions and Future Work

8.1 Conclusions

The use of a variety of electrochemical and spectroscopic techniques have been used throughout this thesis in order to further the understanding of the fundamental reaction mechanisms and pathways associated with Li-oxygen and Na-oxygen batteries.

The synthesis, characterisation and analysis of shell isolated nanoparticles for enhanced Raman spectroscopy (SHINERS) was outlined in chapter 3, providing a base for the development of SHINERS as a technique to be utilised for analysing interactions at the electrode surface in battery applications.

The electrochemical stability and behaviour of SHINS was compared with that of SERS in chapter 4, to ascertain whether any additional or adverse effects occurred as a result of the presence of SHINERS. SHINERS were demonstrated as a reliable and practical alternative to SERS, to study electrochemical reactions upon typically Raman inactive surfaces. SHINERS were used to track the oxygen reduction reaction mechanisms on a variety of polycrystalline electrodes, the results demonstrated platinum had the strongest interaction with the superoxide species, favouring a flat O-O conformation at less negative potentials. The interaction of superoxide with the carbon surface was weak, however a weak interaction was observed through a distortion in the vibrational stretching mode of the graphitic ring.

The effect of solvent on the reaction mechanism for the Li-O₂ chemistry was also studied. The surface solution mechanism had previously been described in the

literature; however the results in chapter 4 demonstrated the reaction pathway is both surface and solvent dependent, with the glassy carbon having a stabilising effect on the production of LiO_2 .

The effect of surface morphology on the enhancement of the SHINs was studied in chapter 5. The enhancement was shown to drop with increased surface roughness; however the enhancement on very rough surfaces was observed to be ca 1×10^3 , which was still sufficient to provide an adequate Raman signal.

The effect of varying the carbon morphology from EPPG to BPPG was shown in chapter 5, the degradation of the carbon surface was observed on both surfaces. However, the more electrochemically active EPPG surface experienced a greater stabilisation of superoxide on the surface.

A more practical battery electrode (a composite electrode comprising of carbon black and binder) was studied. The results demonstrated the degradation of the carbon black electrode in the presence of the lithium species, with Li_2CO_3 being observed on oxidation, due to degradation of the electrode surface.

The results presented in chapter 6 focus on the effect of moving from an aqueous electrolyte to a non-aqueous electrolyte on a Au(111) single crystal surface. The addition of trace amounts of MeCN into an aqueous system inhibited the oxidation of the surface, preventing the formation of the hydroxide intermediate. The MeCN preferentially absorbed on step and defect sites and pushed the oxidation of the gold surface to higher potentials from 1.25 V to ~ 1.35 V vs. Pd/H.

The addition of trace amounts of H_2O into the non-aqueous system, promoted the degradation of the electrolyte, with the cyanide band being detected in the Raman. The presence of carbonates was also detected on the electrode surface.

Chapter 7 studied the electrochemically effects of varying the platinum single crystal surface facet on the reaction mechanism in the Na-O₂ system with DMSO as a solvent. A method for the successful preparation of the different platinum facets for use in a non-aqueous environment was presented.

The results on the different platinum facets demonstrated the (110) and (111) surfaces to have a higher coverage of absorbed oxygen, this resulted in the increased production of Na₂O₂ relative to the polycrystalline and (100) due to catalytic nature of the electrode surface. In the oxidation sweep a 1 e⁻ oxidation of Na₂O₂ to NaO₂ was possibly observed. The electrochemical impact of adding a supporting salt (TBAClO₄) was measured. The salt inhibited the absorption of oxygen on the electrode surface, instead an outer sphere electron transfer mechanism has been proposed in the presence of the salt, with more solution based products being observed.

8.2 Future work

This thesis has provided a preliminary investigation into the application of SHINERS for studying battery systems. To develop this technique is it important to optimise the distribution of the nanoparticles on the electrode surface. This will provide a more uniform enhancement across the whole coated area, which would allow more quantifiable SHINERS measurements. The distribution of the particles upon more porous electrode materials may be controlled via different size and shape nanoparticles. Larger particles may provide greater enhancement upon these surfaces. The shape of the particles may also allow the surface plasmon to be tuned to provide optimum enhancement at different laser wavelengths.

Chapter 4 and 5 focus on varying the electrode surface and solvent, it would provide a greater understanding of the reaction mechanisms to further study

alternative carbon surfaces, e.g. boron doped diamond, and alternative solvents, e.g. diglyme. Understanding the reaction steps in the charging mechanism will also aid in providing a better understanding of the reaction pathways.

Chapter 6 focuses on how the reaction mechanism varies between aqueous and non-aqueous systems; initial studies have shown clear comparisons between the systems. However, a better spectro-electrochemical study across a broader range of MeCN and H₂O concentrations, would allow clearer elucidation of the processes taking place.

Finally, chapter 7 provides an electrochemical study of the Na-O₂ system on different platinum single crystals. However, the assignment of the data is only speculative. In order to accurately assign the data, a thorough Raman study via SHINERS needs to be conducted in order to provide comprehensive evidence of the peak assignments made from the electrochemical data.

Summary of papers and conference presentations

Tom Galloway

Email: tomgalloway@hotmail.co.uk

Thesis title: **Shining Light on Electrode Interfaces**

Supervisor: Prof. Laurence J. Hardwick

Education

01/10/13 – 30/09/17: PhD in Chemistry, Stephenson Institute for Renewable Energy

Aims

- To develop in situ Raman spectroscopy techniques for the evaluation of the reaction mechanisms and film formation on practical electrode surfaces
- To study the electrochemistry of oxygen in both aqueous and non-aqueous media.
- To combine electrochemical and spectroscopic studies in order to understand the structure-function relationship in oxygen reduction and evolution reactions, and the extent of electro-catalysis within these systems

Publications

- **Galloway, T. A.**; Hardwick, L. J., Utilizing in Situ Electrochemical SHINERS for Oxygen Reduction Reaction Studies in Aprotic Electrolytes. *J. Phys. Chem. Lett.* 2016, **7** (11), 2119-2124. (**Chapter 4**).
- **Galloway, T. A.**; Cabo-Fernandez, L.; Aldous, I. M.; Braga, F.; Hardwick, L. J., Shell Isolated Nanoparticles for Enhanced Raman Spectroscopy Studies in Lithium-Oxygen cells. *Faraday Discuss.* **2017**, DOI: 10.1039/C7FD00151G. (**Chapter 5**).
- **Galloway, T. A.**; Attard, G.; Hardwick, L. J., in preparation (2017). (**Chapter 7**).

Conferences, presentations and courses attended

- ECS UK North West student chapter conference, University of Liverpool, 8th June, 2017. Presentation, titled '*Shining Light on Electrode Interfaces*'. **(Chapter 3 and 4)**
- Johnson Matthey Academic Conference (JMAC), Loughborough University, 11-12th April, 2017. Presentation, awarded runner up, titled '*Shining Light on Electrode Interfaces*'. **(Chapter 5)**
- 229th ECS Meeting, 29th May-2nd June, 2016, San Diego. Presentation, titled '*Utilizing in situ electrochemical SHINERS for oxygen reduction reaction studies in aprotic electrolytes*'. **(Chapter 3 and 4)**
- SIRBATT Workshop 'Controlling Lithium Battery Interfaces', 27th May, 2016, Orlando, Florida. Poster presented. **(Chapter 3, 4 and 5)**
- Brazil-Warwick meeting, 1st February, 2016, Warwick University. Presentation, titled '*Utilising SHINERS for the study of oxygen electrochemistry in the lithium-oxygen battery*'. **(Chapter 4)**
- UK-Korea symposium on lithium and sodium batteries, Royal society of chemistry, London, 18th January, 2016. Poster presented. **(Chapter 4)**
- Lithium ion batteries workshop, University of Loughborough, 10th April, 2015. Poster presented. **(Chapter 6)**
- STFC Early Career Researchers conference, 18th March, 2015. Poster presented, awarded best poster, titled '*Surface enhanced Raman spectroscopy of oxygen electrochemistry in aqueous and non-aqueous electrolytes*'. **(Chapter 6)**
- Electrochemistry North West, University of Liverpool, 23rd June, 2014. Poster Presented, awarded best poster, titled '*In situ spectroscopic studies of the electrochemistry of di-oxygen in non-aqueous li-oxygen battery electrolytes*'.
- Johnson Matthey Academic Conference (JMAC), Loughborough University, 15-16th April, 2014. Poster presented.
- Advances in li-battery research workshop, University of Liverpool, 10-11th April, 2014. Poster presented.